Interfaces in Metal-Oxygen Batteries
Adsorbate formation and influence on oxygen reduction

Dissertation

zur

Erlangung des Doktorgrades (Dr. rer. nat.)

der

Methamatisch-Naturwissenschaftlichen Fakultät

der

Rheinischen Friedrich-Wilhelms-Universität Bonn

vorgelegt von

Andreas Köllisch-Mirbach

aus

Troisdorf, Deutschland

Bonn 2024

Angefertigt mit Genehmigung der Mathematisch-Naturwissenschaftlichen Fakultät
der Rheinischen Friedrich-Wilhelms-Universität Bonn

Vorsitz: Prof. Dr. Thomas Bredow

Gutachterin/Betreuerin: Prof. Dr. Barbara Kirchner

Gutachter: Prof. Dr. Helmut Baltruschat

Tag der Promotion: 07.06.2024

Erscheinungsjahr: 2024

Publications

Parts of this thesis have already been published in international, peer-reviewed journals:

[3] A. Koellisch-Mirbach, P. P. Bawol, I. Park, H. Baltruschat, *ChemElectroChem* **2022**. DOI: *doi.org/10.1002/celc.202200159*

[2] A. Köllisch-Mirbach, I. Park, M. Hegemann, E. Thome, H. Baltruschat, *ChemSusChem* **2021**, *14*, 2564. DOI: *https://doi.org/10.1002/cssc.202100364*

[1] A. Koellisch-Mirbach, T. Lohrmann, P. H. Reinsberg, H. Baltruschat, *Journal of Electroanalytical Chemistry (1959)* **2020**, *875*, 114560. DOI: *https://doi.org/10.1016/j.jelechem.2020.114560*

Additionally, chapter 8 is a part of a manuscript, which is also prepared for submission to a journal.

Complete list of publications

[7] A. Koellisch-Mirbach, P. P. Bawol, I. Park, H. Baltruschat, *ChemElectroChem* **2022**. DOI: *doi.org/10.1002/celc.202200159*

[6] A. Köllisch-Mirbach, I. Park, M. Hegemann, E. Thome, H. Baltruschat, *ChemSusChem* **2021**, *14*, 2564. DOI: *https://doi.org/10.1002/cssc.202100364*

[5] M. Hegemann, P. P. Bawol, A. Kollisch-Mirbach, H. Baltruschat, *Electrocatalysis* **2021**, *12*, 564-578. DOI: *https://doi.org/10.1007/s12678-021-00669-4*

[4] P. P. Bawol, A. Koellisch-Mirbach, C. J. Bondue, H. Baltruschat, P. H. Reinsberg, *ChemSusChem* **2021**, *14*, 428. DOI: *https://doi.org/10.1002/cssc.202001605*

[3] A. Koellisch-Mirbach, T. Lohrmann, P. H. Reinsberg, H. Baltruschat, *Journal of Electroanalytical Chemistry (1959)* **2020**, *875*, 114560. DOI: *https://doi.org/10.1016/j.jelechem.2020.114560*

[2] P. H. Reinsberg, A. Koellisch, P. P. Bawol, H. Baltruschat, *Phys. Chem. Chem. Phys.* **2019**, *21*, 4286-4294. DOI: *https://doi.org/10.1039/C8CP06362A*

[1] P. H. Reinsberg, A. Koellisch, H. Baltruschat, *Electrochim. Acta* **2019**, *313*, 223-234. DOI: *https://doi.org/10.1016/j.electacta.2019.05.014*

Selection of conference contributions

Conference: 116th AGEF Symposium: Triboelectrochemistry (Bonn, 2021)

Format: Oral

Title: Sulfate adsorption on Au(111) electrodes – Influence of the potential on the force distance curves

Conference: 239th ECS Meeting (Digital Meeting, 2021)

Format: Invited

Title: ORR in Ca^{2+} containing DMSO on Pt and Au electrodes – Reaction Mechanism studied by DEMS, AFM, XPS and varied surface structure

Conference: ISE 71st Annual Meeting (Belgrade online, 2020)

Format: Poster

Title: Oxygen reduction reaction on rough massive gold electrodes – Surface roughness as adjusting screw (RRDE and DEMS approach in Ca^{2+}/Li^{+} containing dimethyl sulfoxide)

Conference: ISE 70th Annual Meeting

Format: Poster

Title: The mechanism of Li_2O_2-monolayer formation and reoxidation – The effect of electrode roguhness

Danksagung

Hiermit möchte ich mich bei all denen bedanken, die mich während der Promotion unterstützt haben. Vor allen anderen gilt mein Dank Prof. Dr. Helmut Baltruschat. Trotz der doch sonderbaren Umstände während der Pandemiezeit habe ich eine hervorragende Betreuung erfahren dürfen. Zu jedem Zeitpunkt konnte ich mich ohne Bedenken an ihn wenden, wenn es um die Diskussion von Auswertung und Interpretation der Messdaten ging. Ich möchte ferner hervorheben, dass ich stets die Möglichkeit hatte meine eigenen Interessen bezüglich der Forschungsthemen zu verfolgen.

Bei Prof. Dr. Thomas Bredow bedanke ich mich hiermit für die freundliche Übernahme des Vorsitzes der Promotionskommission. Weiterhin bedanke ich mich hiermit bei den weiteren Mitgliedern der Promotionskommission Prof. Dr. Barbara Kirchner für die Übernahme der Rolle als Betreuerin und Prof. Dr. Thorsten Geisler-Wierwille für die Übernahme der Rolle des Gutachters. Ferner bedanke ich mich bei allen Kollegen der Abteilung Elektrochemie für die wissenschaftliche Zusammenarbeit. In diesem Kontext gilt besonderer Dank Dr. Philip H. Reinsberg, Dr. Pawel P. Bawol und Inhee Park, für wertvolle Gespräche bezüglich wissenschaftlicher Fragestellungen.

Weiterer Dank gilt auch Carole Rossignol für ihre Hilfe bei organisatorischen Problemen und Elke Thoma für Ihre Unterstützung im Labor. Dank gilt auch Cara Tabea Lohrmann, deren Messung im Rahmen ihrer Masterarbeit Einzug in diese Arbeit gefunden hat. Ebenfalls möchte ich mich bei den Werkstätten des Instituts für Physikalische und Theoretische Chemie für die gute Zusammenarbeit und die Hilfe bei der Konstruktion neuer elektrochemischer Zellen bedanken.

Ohne mein soziales Umfeld wäre die Arbeit ebenfalls nicht zustande gekommen, sodass sich mich bei meinen guten Freunden Markus und Jan bedanken möchte, die mir immer guten Freizeitausgleich ermöglicht haben.

Meiner Familie danke ich für die ständige und uneingeschränkte Unterstützung in jeglicher Situation.

Zuletzt bedanke ich mich bei meiner geliebten Frau Katharina für den emotionalen Rückhalt und die ständige Motivation. Das Arbeiten an dieser Dissertation fiel mir durch Sie deutlich leichter, da Sie stets ein offenes Ohr hatte, wenn ich von fehlgeschlagenen Messungen frustriert war.

Abstract

This study deals to a large extent with the formation of adsorbates during the oxygen reduction reaction in organic electrolytes on gold and platinum surfaces. The mainly used methods are voltammetry (also at rotating ring disc electrodes), differential electrochemical mass spectrometry and atomic force microscopy. However in this context, a novel electrochemical cell with low electrolyte volume was developed, that shows a comparable performance to the frequently used H-cell. It will be shown, that the novel cell has several advantages over the H-cell. The novel cell was used in the context of investigations on the applicability of hydrate melt electrolytes for metal-air batteries. Concerning these investigations it will be shown, that hydrate melt electrolytes are in fact inapplicable for this type of application. The electrolyte's electrochemical potential window, in which it can be operated, proved to be very small, other than expected from the reduced solvent activity.

However, aprotic alternatives are proposed, that showed extraordinarily high concentrations. The key part of this work deals with the oxygen reduction in DMSO. For the Li^+ case it was found, that an adsorbate is formed during the oxygen reduction, which to large extent (almost completely) deactivates the electrode. This however was not the case for Ca^{2+} containing DMSO. In this case, the formed CaO_2/CaO adsorbate only inhibits further peroxide formation (peroxide is the main reaction product in the case of the ORR in Ca^{2+} containing DMSO). Superoxide can still be formed through or on top of the adsorbate. This is true at least for Au and Pt electrodes. The formation of the adsorbate in both cases is a competitive reaction to the formation of dissolving peroxide. Knowing this, a detailed mechanism is proposed for the oxygen reduction on Au and Pt electrodes in Ca^{2+} containing DMSO. Regarding older data, furthermore a correlation was found between the tendency of the oxide species formed during the ORR to bind to the electrode surface or to the alkaline earth metal cation (ion-pairing) and the contribution of dissolving peroxide to the ORR current density. This allowed for proposing a more generalized ORR mechanism for all alkaline earth metal cations, concerning the ORR in DMSO for several electrode materials. Additionally upon investigating the adsorbate formation during the ORR in Ca^{2+} containing electrolytes, an astonishing observation was made in 0.1 M LiCl + 0.1 M $CaCl_2$ electrolyte. $CaCl_2$ is nearly insoluble in DMSO, but as LiCl is added to the solution in a stoichiometric amount (or in excess), $CaCl_2$ completely dissolves, indicating the formation of a $[CaCl_3]^-$ complex. Furthermore, the ORR in this system hints to the presence of an autocatalytic reaction at the disc electrode in an RRDE experiment, which would have to be confirmed.

Organic electrolytes often strongly adsorb on electrode surfaces. In addition, a layering, i.e. an ordering perpendicular to the electrode surface, was revealed by recording force separation curves via AFM. Therefore in order to model such layers which are probably caused by hydrophobic interactions, a layer of sodium dodecylsulfonate (SDS*) was examined in comparison to the observations from literature made for the alkylsulfate and alkylthiolate systems. It will be shown that the flat adsorbed SDS*, on Au(111) electrodes, undergoes a phase transition to a condensed state as the electrode is charged positively. During this phase transition, friction shows a maximum for low normal loads. At higher normal loads, one observes a smooth transition from low to high friction as the condensed layer is formed.

Contents

List of Figures

List of Tables

List of Abbreviations

AFM	Atomic Force Microscopy
AT	Alkylthiol
CE	Counter electrode
Cp*	Decamethylferrocene
CV	Cyclic voltammogram
DMSO	Dimethyl sulfoxide
MS	Mass spectrometer
OER	Oxygen evolution reaction
ORR	Oxygen reduction reaction
Otf	Triflate, trifluoromethanesulfonate
RE	Reference electrode
RRDE	Rotating ring disk electrode
SDS	Sodium dodecylsulfate
SDS*	Sodium dodecylsulfonate
TBA	Tetrabutylammonium
TG	Tetraglyme, tetraethylene glycol dimethyl ether
TFSI	Trifluoromethanesulfonimide
UHV	Ultra High Vacuum
WE	Working electrode
XPS	X-Ray Photoelectron Spectroscopy
FSC	Force separation curve

1 Introduction

This Thesis deals with two topics. On the one hand, it deals with electrode processes occurring in metal-O_2 batteries and the formation of adsorbates on electrodes in non-aqueous electrolytes. Thus, this chapter provides the motivation for further research in the field of battery technologies beyond Li-ion systems. Since, on the other hand, a part of this thesis addresses the formation of an adsorbate in aqueous electrolytes, a short overview of a similar system is given. Finally, this chapter aims at establishing a connection between these two topics.

As this thesis consists to a large extent of manuscripts, which were published in peer reviewed journals, each manuscript resembles a separate chapter and provides a separate introduction.

1.1 Motivation

The motivation of finding novel Battery systems, which are cheap and don't require rare materials like lithium has once again grown a lot due to public attention to the climate change and its consequences. Since Charles David Keeling established a direct connection between the consumption of fossil fuels and the increase of CO_2 in the earth's atmosphere, mankind has to avoid fossil fuels in general. As alternatives concerning power supply, there is nuclear fission, which causes problems for timescales far beyond imagination and additionally the construction of nuclear fission power plants takes several years, which is most likely beyond the estimated deadline for irreversible climate changes. A nuclear alternative is nuclear fusion, which might take decades to become economically relevant, as concerning Europe the first serious experimental reactor (ITER = International Thermonuclear Experimental Reactor) is still in construction. This highlights the importance of renewable energies, such as wind power, solar power and hydropower, as the technologies are well established and the construction of the corresponding power plants requires much less time compared to the nuclear alternatives. The huge disadvantage in these power plants is the on-demand energy production. As a result, the storage of energy is a topic even for future generations. Where pumped storage systems are geographically unavailable one has to rely on either energy storage in large battery stacks or on the conversion of energy to renewable fuels (Power to X) e.g. hydrogen. The fact that any conversion goes in hand with additional energy losses, makes large scale batteries very attractive. Concerning mobility, electrification of road and railway traffic is also required. Many car manufacturers provide electric cars nowadays. As the energy density is very important for this battery application, further research in novel battery technologies is highlighted. Also for mobile devices (e.g. smartphones) the energy density (especially volumetric) is an important factor and motivates further research.

1.2 Battery context

Nowadays batteries too large extent rely on Li-ion technologies, which led to a Nobel Prize in Chemistry for the work of John B. Goodenough, M. Stanley Whittingham and Akira Yoshino in 2019. Though this technology is well established and provides a sufficient energy density to find application in powering cars, better solutions have to be found as lithium is extremely rare and its mining goes in hand with severe environmental problems. The hunt for alternatives led to further research in the field of alkaline metal ion batteries, thus speaking of Na-ion batteries and K-ion batteries. As sodium and potassium are heavier than Lithium while carrying the same charge, the theoretical gravimetric energy density of these two alternatives is expected to be less. A way to generally increase the energy density of the battery is to replace the cathode by an air electrode, which results in a metal-O_2 battery. To increase the energy density even further scientists started to investigate alkaline earth metals as charge carrier, leading to divalent metal-O_2 batteries. Such metal air batteries are topic of this thesis. However, researchers also tried to avoid flammable organic electrolytes and thus investigated hydrate melt electrolytes[1, 2] as a special type of water in salt electrolyte.

1.3 Friction context

As most of the experiments in this thesis dealt with DMSO and a strong interaction of adsorbed DMSO with Au electrodes was observed (utilizing AFM), we checked the literature and for DMSO already a lot of work was done, so as for alkylsulfates and alkylthiols. However, no literature was found for alkylsulfonates. As the adsorption behavior of alkylsulfonates remained untouched throughout the years, while alkylthiols and alkylsulfates were investigated very detailed, we decided to address this lack in literature. Alkylsuflates (AS) and alkylthiols (AT) are known to form well-ordered structures at Au(111) electrodes. As an example for AS, sodiumdodecylsulfate (SDS) forms a hemimicellar (hemicylindrical) structure at low coverage and undergoes a phase transition upon positively charging the electrode, to form a condensed, disordered bilayer [3]. While as an example for AT, hexanethiol forms a $(\sqrt{3} \times \sqrt{3})R30°$ structure (vertically oriented alkyltails) at high coverage and forms a row like structure (horizontally oriented molecules) as the coverage decreases with time in UHV[4].

2 Experimental methods

This chapter provides a short overview over the methods used in this thesis. For a more detailed theoretical description of the observed phenomena, these in electrochemistry commonly used textbooks are recommended:

- Allen J. Bard, Larry R. Faulkner, *Electrochemical Methods: Fundamentals and Applications*, 2000. ISBN: 978-0-471-04372-0.
- Carl H. Hamann, Andrew Hamnett, Wolf Vielstich, *Electrochemsitry*, 2007. ISBN: 978-3-527-31069-2.

Note that all labware in this study was carefully cleaned with chromic acid and rinsed with Milli-Q water to ensure the cleanliness required for electrochemical experiments. Furthermore, the cleaned labware was stored in concentrated KOH solution before being rinsed again by Milli-Q water and used for the desired experiment.

2.1 Cyclic voltammetry

Cyclic voltammetry describes an electroanalytical method where the current (i) is monitored as a function Potential (E) applied to an electrode (the so called working electrode = WE). In this thesis the current is rather normalized to the geometrical electrode Area (A_{geo}) and thus given as the current density (j).

Three electrode arrangement

Usually the three-electrode arrangement is used in electrochemistry to investigate reactions at a working electrode (WE), which often serves as the electrocatalyst. Additionally, a counter electrode (CE) and a reference electrode (RE) are immersed into the electrolyte. A so-called potentiostat is connected to all electrodes to control the current between WE and CE, while no current flows between WE and RE. In this thesis, usually an H-cell was used to perform electrochemical experiments (if not stated otherwise).

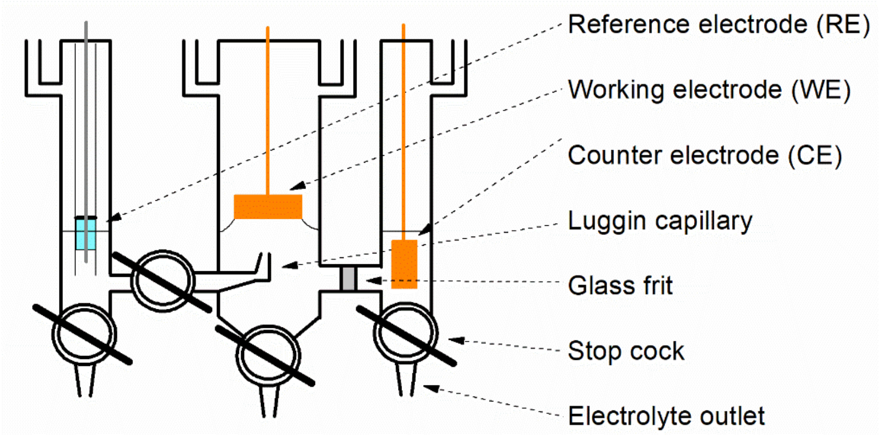

Figure 1 shows a sketch of an electrochemical glass cell (H-cell). The cell consists of separated compartments for the WE, CE and RE.

Figure 1 shows a sketch of an H-cell used in this thesis, where all electrode compartments are separated by either a closed stopcock or a glass frit. Note that the CE surface area should always be larger compared to the surface area of the WE, otherwise (in rare cases) current limitations might occur at the CE and be misinterpreted as limitations at the WE.

The voltammogram

The potential applied to the WE is of triangular shape if plotted against the time (t). The slope in consequence is the so called sweep rate (v). The voltammogram thus is a plot of current density vs electrode potential at constant sweep rate.

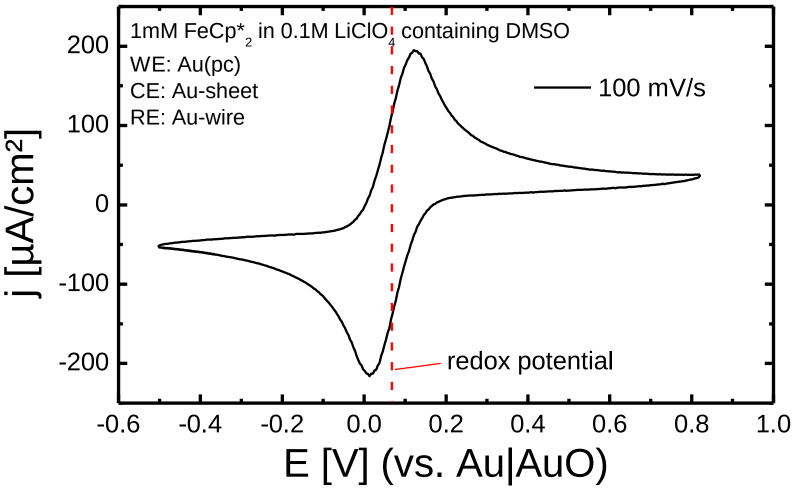

Figure 2 shows an exemplary redox couple (decamethylferrocene = FeCp*) in $LiClO_4$ containing DMSO on polycrystalline Au at 100 mV/s vs Au|AuO. CE was a gold sheet and RE was a gold wire immersed into the electrolyte. The dashed red line denotes the center of the redox couple.

Regarding Figure 2 one observes in cathodic direction (from positive to negative potential) that the current density (absolute) increases to a maximum close to 0 V vs Au|AuO. This is the reduction peak of the iron centre of the FeCp* complex. Continuing in cathodic direction the absolute current density decreases to a constant value, which corresponds to the diffusion limited formation of the reduced species. Starting now in anodic direction (from negative to positive potential) the current density is close to the diffusion limited value until approaching the redox potential. Then the current density increases to an anodic peak corresponding to the oxidation of the reduced species. After the peak the current density decrease to the value corresponding to the diffusion limited oxidation of the reduced species. The overall shape is typical for a diffusion controlled process. The peak itself originates in the fact that the surface concentration of the reacting species quickly drops from the bulk concentration to 0, while the thickness of the Nernstian diffusion layer (δ_N) is growing as the potential passes the peak. This is shown more clearly below.

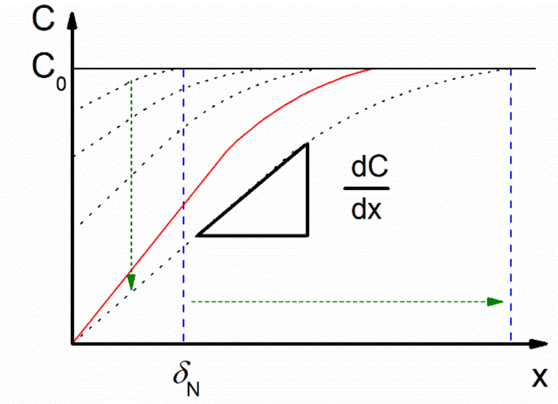

Figure 3 shows the plot of reactant concentration vs distance (x pointing perpendicularly away from the electrode surface). The plot highlights the growth of the Nernstian diffusion layer and the change of the concentration profile with increasing potential. The dashed blue line denotes the thickness of the Nernstian diffusion layer. The dotted black lines denote the concentration profile. The solid black line denotes the bulk concertation (C_0) of the reactant. The green arrows indicate the change with increasing potential. The slope is given as the concentration gradient. The solid red line denotes the point in time for maximum concentration gradient.

Figure 3 shows the change in concentration profile with increasing potential. The important parameter in this figure is the slope $\frac{dC}{dx}$, as the current density is directly proportional to it:

$$j = \frac{zFD}{A}\left(\frac{dC}{dx}\right)_{x=0} \tag{1}$$

With j as the current density, z as the number of transferred electrons, F as the Faraday constant, D as the diffusion coefficient, A as the electrode surface area and $\frac{dC}{dx}$ as the concentration gradient. As the slope in Figure 3 shows a maximum at a certain potential value, this will in consequence result in a peak in current density.

The other possibility for a peak in a voltammogram corresponds to a surface controlled process. There the peak originates from the deposition of a species at the electrode, which results in electrode blocking and thus depletion of the current, as the electrode is saturated. To separate these two possibilities (diffusion or surface control), one records voltammograms at different sweep rates. For a diffusion controlled process the reaction charges should increase with increasing sweep rate, while they should stay constant for a surface controlled process.

Determination of the electrode roughness factor

Many investigations in this thesis required the knowledge of the exact electrode surface area. In the supporting information of ref. [5] is a detailed description of the calculation for Pt and Au electrodes. In general the electrode roughness is determined using a surface controlled process, such as the hydrogen adsorption (for Pt) or the adsorption of oxide species (for Au). As the current (i) is monitored during the adsorption, it is possible to obtain the charge (q_{ML}) for one monolayer by integration of the current over time (until the potential is reached, where the monolayer adsorption is finished):

$$q_{ML} = \int_{ads.\ start}^{ads.\ end} i\ dt \tag{2}$$

To obtain the electrode roughness factor (f_R), q_{ML} is divided by the mono layer charge for an electrode roughness of 1 (q_{ML}^{*}):

$$f_R = \frac{q_{ML}}{q_{ML}^{*}} \tag{3}$$

While q_{ML}^{*} either is obtained empirically and documented in literature or it is obtained via the calculated metal atom density at the surface, assuming a certain relation between adsorbed molecules/atoms and metal surface atoms.

2.2 The Rotating Ring Disc Electrode (RRDE)

The rotating ring disc electrode (RRDE) allows for the electrochemical formation of a product at the disc electrode and the further examination of soluble reaction products at a second electrode (the ring electrode). This is achieved by using a rotating cylindrical electrode, which introduces convection by its rotation.

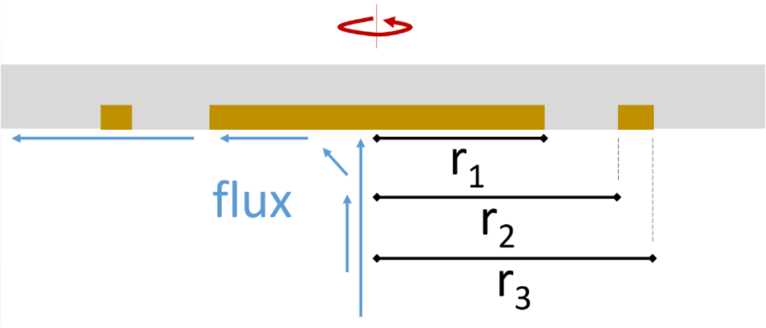

Figure 4 shows a sketch of the RRDE, where the red arrow indicates the electrode rotation, the blue arrows indicate the flux, r_1 is the radius of the disc electrode, r_2 is the inner radius of the ring electrode and r_3 is the outer radius of the ring electrode.

As the reactant reaches the disc electrode, it undergoes a potential induced reaction (e.g. reduction). If soluble species are formed during this reduction, they move to the ring electrode as a result of the flux. At the ring electrode the soluble reaction products can undergo further potential induced reactions (e.g. reoxidation). Assuming the following reaction at the disc and ring electrode:

$$A + ze^- \rightarrow B \tag{4}$$

With A as a reactant, that is reduced at the electrode, z as the number of transferred electrons and B as the product. The current at the disc electrode (i_{disc}) then is given by

$$i_{disc} = zFDA\left(\frac{c_0 - c_s}{\delta_N}\right) \tag{5}$$

With c_0 as bulk concentration and c_s as surface concentration of A. In the RRDE setup, δ_N is given by

$$\delta_N = 1.61D^{-\frac{1}{3}}\nu^{\frac{1}{6}}\omega^{-\frac{1}{2}} \tag{6}$$

Where ν is the kinematic viscosity of the solvent and ω is the angular velocity. For a disc electrode of the radius r_1 and a ring electrode of inner radius r_2 and outer radius r_3 this gives for the disc current and ring current (i_{ring})

$$i_{disc} = 0.62\pi r_1^2 zFD^{\frac{2}{3}}\nu^{-\frac{1}{6}}\omega^{\frac{1}{2}}(c_0 - c_s) \tag{7}$$

$$i_{ring} = 0.62\pi(r_3 - r_2)^2 zFD^{\frac{2}{3}}\nu^{-\frac{1}{6}}\omega^{\frac{1}{2}}(c_0 - c_s) \tag{8}$$

Assuming a different reaction at the ring electrode such as the reoxidation of B via

$$B \rightarrow ze^- + A \tag{9}$$

The ring current is given by

$$i_{ring} = Ni_{disc} \tag{10}$$

Where the collection efficiency (N) is the proportionality constant. The collection efficiency can be either calculated [6] or it can be determined empirically by using a system of well-known stoichiometry.

Calculation of the superoxide share

This thesis to a large extend deals with the oxygen reduction reaction in alkaline metal and alkaline earth metal cation containing DMSO. Thus, the formation and detection of the oxygen reduction products need to be addressed. In this sub chapter, the calculation of the superoxide share will be examined under convection. In a RRDE setup, oxygen is reduced to superoxide and/or peroxide depending on the electrode potential and cation. Assuming two subsequent 1-electron transfer steps, the reaction at the disc electrode will be given as

$$O_2 + e^- \rightarrow O_2^- \tag{11}$$

$$O_2^- + e^- \rightarrow O_2^{2-} \tag{12}$$

If the ring potential is positive enough, the generated soluble oxygen reduction products (mostly O_2^-) will be reoxidized at the ring electrode via

$$O_2^- \rightarrow O_2 + e^- \tag{13}$$

Assuming solely these reaction to be relevant, the share of superoxide ($\chi_{O_2^-}$) to the oxygen reduction product distribution can be calculated from the disc and ring current during a RRDE experiment. The current at the disc and electrode is given by

$$i_{disc} = 2F\frac{dn_{O_2}}{dt} - F\chi_{O_2^-} = F(2 - \chi_{O_2^-})\frac{dn_{O_2}}{dt} \tag{14}$$

$$i_{ring} = FN\frac{dn_{O_2^-}}{dt} = FN\chi_{O_2^-}\frac{dn_{O_2}}{dt} \tag{15}$$

With $\frac{dn_{O_2}}{dt}$ and $\frac{dn_{O_2^-}}{dt}$ as oxygen and superoxide consumption. Rearranging and combining equation (14) and (15) further gives

$$\frac{dn_{O_2}}{dt} = \frac{i_{disc}}{F(2-\chi_{O_2^-})} = \frac{i_{ring}}{FN\chi_{O_2^-}} \tag{16}$$

Thus the expression for the superoxide can be written as

$$\chi_{O_2^-} = \frac{2i_{ring}}{Ni_{disc} + i_{ring}} \tag{17}$$

In this picture, the share of peroxide is directly given as

$$\chi_{O_2^{2-}} = 1 - \chi_{O_2^-} \tag{18}$$

2.3 Differential Electrochemical Mass Spectrometry (DEMS)

Utilizing voltammetry and special setups as the RRDE, electrochemists were enabled to study the electrochemistry of reactants reacting at an electrode. The methods shown so far can provide an idea of the reactions at the electrodes. But a direct connection to a reaction product is difficult to provide clearly. Differential electrochemical mass spectrometry provides this possibility. It allows for direct detection of volatile species formed at porous electrodes via connection to a mass spectrometer. The electrolyte is separated from the vacuum via a hydrophobic porous PTFE membrane. Depending on the application, an electrocatalyst (usually Au and Pt) is sputtered onto the membrane, so that the membrane can act as an electrode. The first approach to combine electrochemistry with a mass spectrometry was made by Bruckenstein and Gadde in 1971 [7], though the setup suffered from bad time resolution. In 1984 Wolter and Heitbaum improved the vacuum system and introduced the differential electrochemical mass spectrometry (DEMS) [8]. The superior time resolution allows for a plot of the mass spectrometer response (ion current) vs potential, the so called mass spectrometric cyclic voltammogram (MSCV).

In the Baltruschat group several cells were developed to increase the range of possible applications of the DEMS system. Thus the DEMS system could be applied to investigate single crystalline electrodes [5, 9-26], battery applications [27, 28] and DEMS could be combined with a convective system in a generator collector approach [29], with IR spectroscopy[30] and with a quartz microbalance [31]. In this thesis the DEMS was used to investigate battery applications (for metal-O_2 batteries), while the dual thin-layer cell was used (convective conditions). Thus, the dual thin-layer cell will be the only cell discussed in the context of DEMS.

The vacuum system

In general the vacuum system used during this thesis is similar to the system mentioned above[8]. A schematic drawing of the DEMS system is shown in Figure 5. The vacuum system is differentially pumped by two turbo molecular pumps with a pumping speed of 200 l/s (TPU1) and 50 l/s (TPU2). TPU1 reduces the pressure close to the ion source to 10^{-5}-10^{-4} mbar and TPU2 reduces the pressure in the analyser to 10^{-6}-10^{-5} mbar. This low pressure provides a sufficient free mean path for the analyte in the quadrupole.

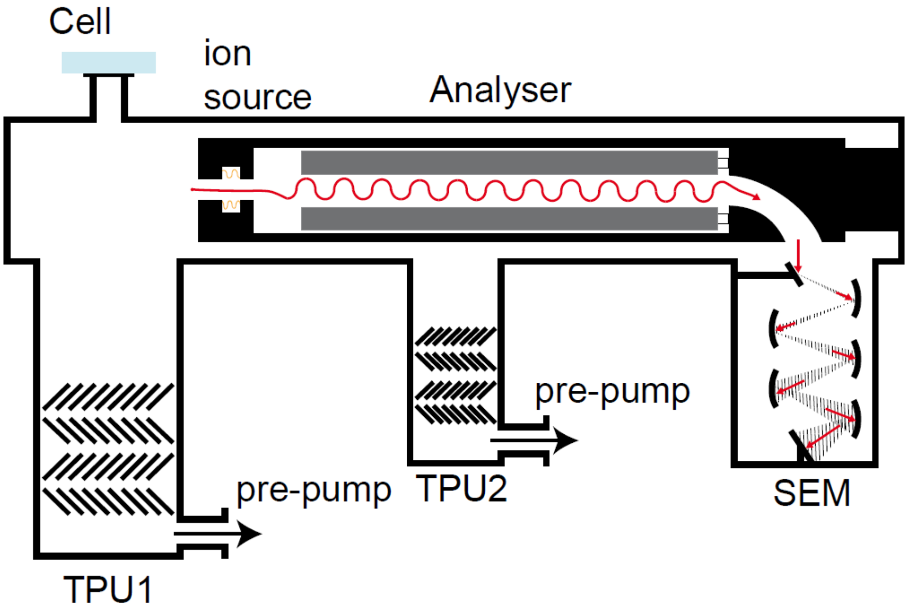

Figure 5 shows the schematic vaccum system of the DEMS. The TPUs denote the turbo molecular pumps and the SEM denotes the secondary electron multiplier. Taken from [149].

The dual-thin-layer cell

The dual thin-layer cell is shown schematically in Figure 6. The working principle has not changed regarding the original cell presented in 1999[31], though the cell was improved by increasing the number of capillaries from 4 to 6 to optimize the flow. A shown in Figure 6, the electrolyte enters the cell via the electrolyte inlet next to the WE compartment. The volume of both electrolyte compartments (at the WE and close to the MS) is given by the thickness of the added Teflon spacers and can thus be adjusted. After the electrolyte reached the WE compartment, it enters the compartment close to the MS through the six capillaries. This compartment is separated from the MS via the porous PTFE membrane. The electrolyte then leaves the cell via the electrolyte outlet on the right side. In this setup it is required to use 2 CEs to avoid electronic oscillations. Note that CE1 is connected to a 1.1 MΩ resistance to minimize the ohmic potential drop between WE and RE.

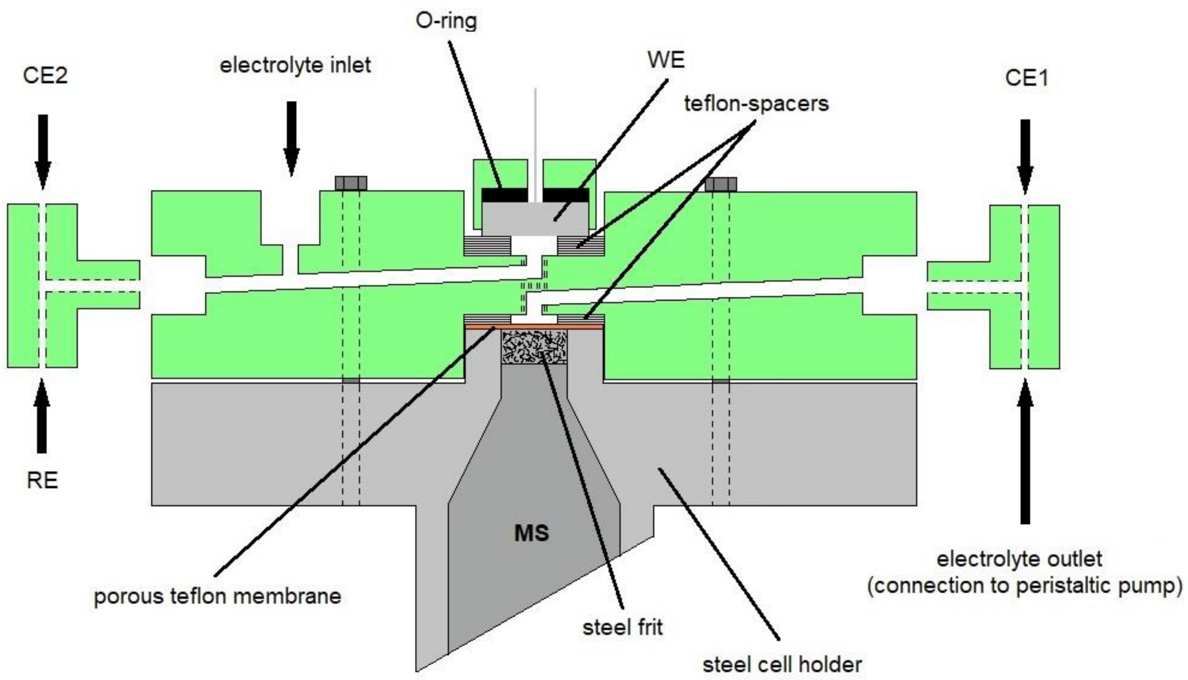

Figure 6 shows a schematic drawing of the dual thin-layer cell (side view). Modified after Bondue et al. [29].

The electrolyte-vacuum interface

The porous, hydrophobic PTFE membrane serves as the phase boundary between electrolyte and vacuum and thus separates the cell from the mass spectrometer. Figure 7 shows a schematic drawing of the boundary between electrolyte and MS vacuum. Note that Figure 7 shows a sputtered PTFE membrane. For a setup like in Figure 6, the membrane is not sputtered with an electrocatalyst.

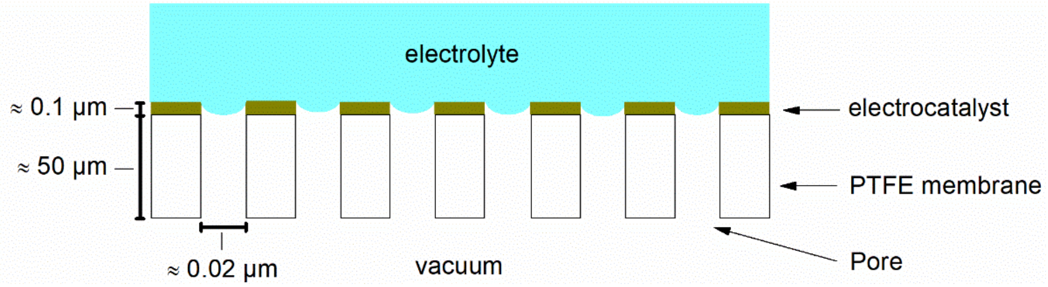

Figure 7 shows a schematic of the sputtered PTFE membrane.

To on the one hand separate the electrolyte from the vacuum system and on the other hand be permeable for volatile species (the analyte), the pore radius has to be below the critical pore radius (r_{crit}). The critical pore radius is given by

$$r_{crit} < -\frac{2\sigma\cos(\gamma)}{p_0} \tag{19}$$

With σ as surface tension of the electrolyte, γ as the contact angle between the electrolyte and the PTFE membrane and p_0 as the atmospheric pressure. However a pore diameter of 20 nm was found to be practicable. For the case of a sputtered PTFE membrane electrode, the delay between analyte formation at the electrode and detection at the MS, is reduced dramatically. However, this approach is still limited by the evaporation of the solvent at the electrolyte-vacuum interface. The flux of the solvent molecules into the vacuum was estimated by Wolter and Heitbaum based on the molecular flow of the evaporated solvent within the pores giving [8]:

$$q = 3.1 * 10^4 \frac{r}{l}(p_1 - p_2) \tag{20}$$

With l as the thickness of the membrane and $p_1 - p_2$ as the pressure difference in the pores. Assuming l = 50 µm, r = 10 nm and for $p_1 - p_2$ = 31.7 mbar (the vapor pressure of water), the flux through a pore is given by [32]:

$$q_{H_2O} \approx 393 \,\frac{mbar\ cm}{s} \tag{21}$$

Now the maximal allowed membrane are $A_{membrane}$ can be calculated via

$$q_{H_2O} A_{membrane} \alpha = p_{max} S \tag{22}$$

With α = 50 % as porosity, S = 200 l/s as the pumping speed and p_{max} = 10^{-6} bar as the pressure in the vacuum system, $A_{membrane}$ is estimated to be in the range of 1 cm^2. In this thesis the PTFE membranes have an area of 0.283 cm^2 acting as boundary and thus are below the upper limit of 1 cm^2.

Calibration for the calculation of z

DEMS allows for the potential resolved calculation of the number of transferred electrons (z) of a reaction at the electrocatalyst by correlating the faradaic current (i_F) measured at the electrode to the ion current response (i_{ion}) of the MS. The faradaic current is directly proportional to the ion current:

$$i_{ion} = K_{MS} \frac{i_F}{z} \tag{23}$$

With K_{MS} as the proportionality constant. Thus K_{MS} can be obtained by calibration to a reaction, where z is known. Figure 8 shows such a calibration experiment after baseline corrections.

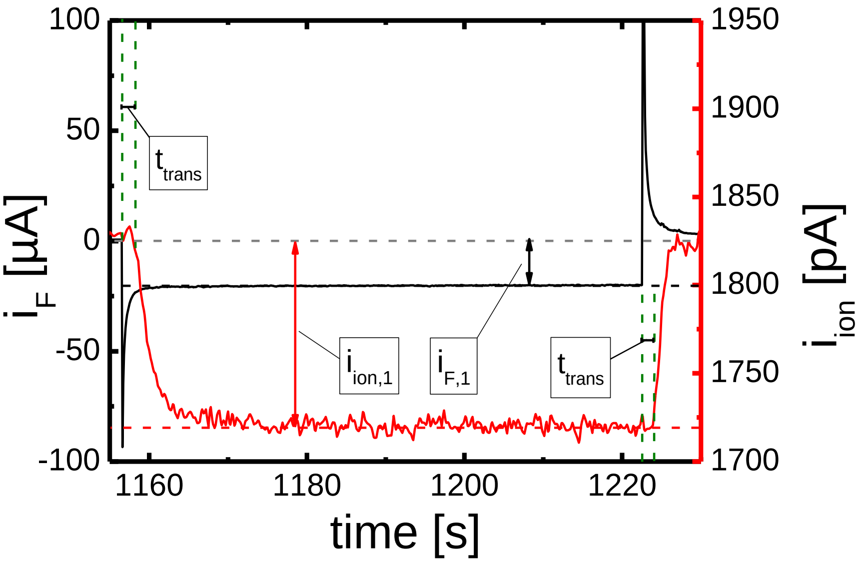

Figure 8 shows an exemplary calibration experiment. Plotted is the faradaic current (black) and the ion current (red) vs the time. The transfer time (t_{trans}) is shown together with the average faradaic current ($i_{F,1}$) and the average ion current ($i_{ion,1}$) of the MS. The model process in this case is the oxygen reduction of O_2 to superoxide on Au in 0.5 M $KClO_4$. Therefore the WE potential was set to 1.19 V vs Ag|Ag^+.

Via this calibration experiment, the proportionality constant K_{MS} is calculated via:

$$K_{MS} = \frac{z\, i_{ion,1}}{i_{F,1}} \tag{24}$$

Then K_{MS} can be used to correlate any current related to an electrochemical reaction at the electrocatalyst to the MS ion current response to give the number of transferred electrons (z) during the reaction at the electrocatalyst:

$$z = K_{MS} \frac{i_F}{i_{ion}} \tag{25}$$

2.4 Single crystal preparation

Before any experiment, the electrodes have to be checked for cleanliness. Thus in case of Pt and Au electrodes, the electrodes were cycled in 0.1 or 0.5 M H_2SO_4 and the voltammetry was checked. If the electrodes showed the well-known voltammetric shape in this system, the electrodes were either used to conduct an experiment, were roughened or annealed. Figure 9 - Figure 11 show typical voltammograms for Pt(111), Pt(100) and Au(111).

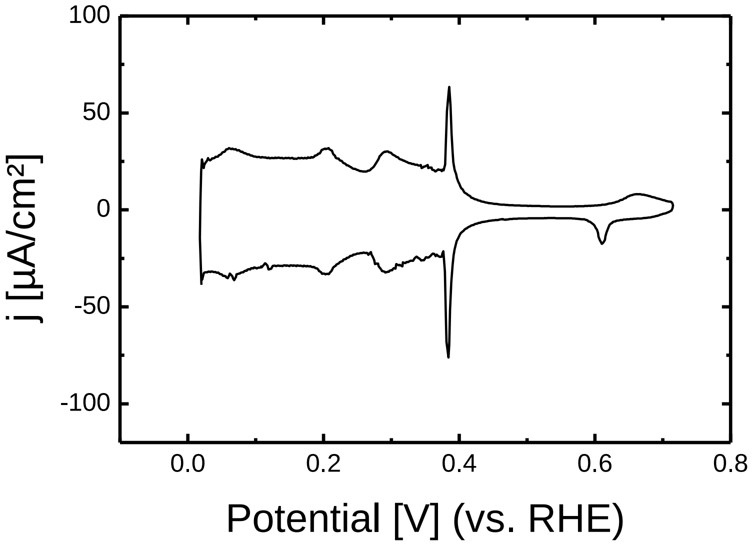

Figure 9 shows a typical voltammogram of Pt(111) in Ar-saturated 0.1 M H_2SO_4. RE was an RHE and CE was a PT-sheet. The experiment was conducted in an H-cell. The sweep rate was 50 mV/s.

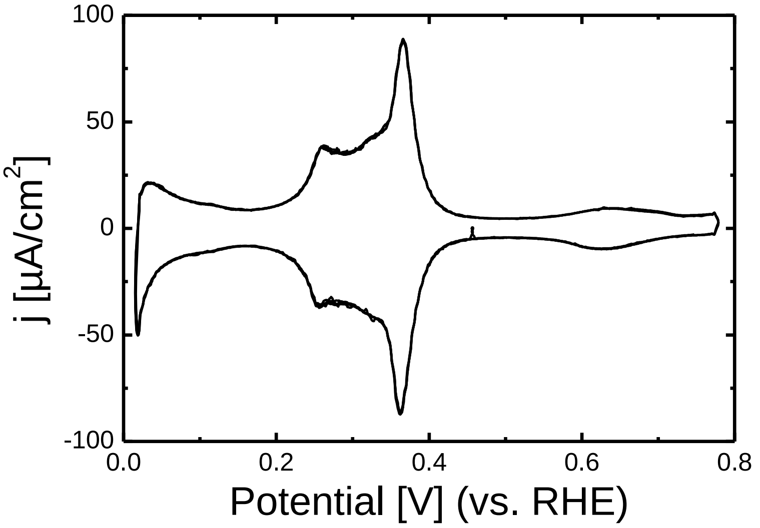

Figure 10 shows a typical voltammogram of Pt(100) in Ar-saturated 0.1 M H_2SO_4. RE was an RHE and CE was a PT-sheet. The experiment was conducted in an H-cell. The sweep rate was 50 mV/s.

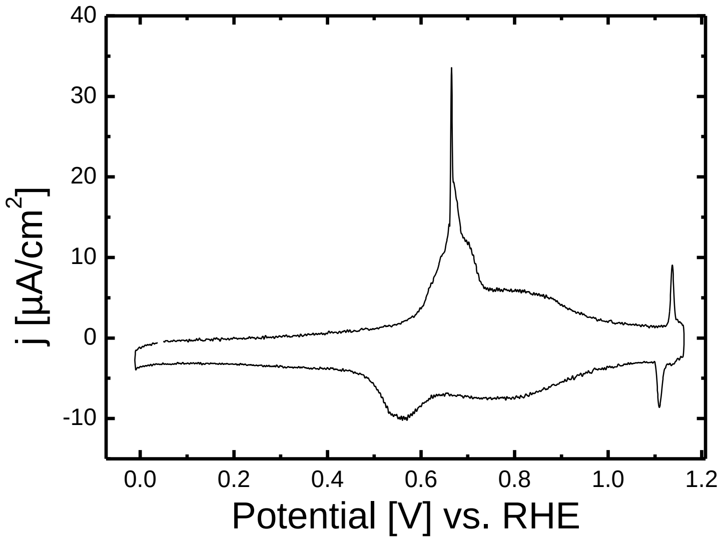

Figure 11 shows a typical voltammogram of Au(111) in Ar-saturated 0.1 M H_2SO_4. RE was an RHE and CE was a Au-sheet. The experiment was conducted in an H-cell. The sweep rate was 50 mV/s.

However, if the electrodes do not show the expected voltammetric shape, they were cleaned as described below.

Cleaning of Au electrodes:

The electrode is oxidized (electrochemically in 0.5 M H_2SO_4) until the electrode surface was covered with a gold oxide layer (visible as red colour). Afterwards the gold oxide layer is removed chemically by dissolution in concentrated hydrochloric acid.

Cleaning of Pt electrodes:

The platinum electrodes were immersed several times alternately into concentrated nitric acid and a solution of ammonia in water.

Then the electrode is checked again by voltammetry and this procedure is repeated until the electrode shows the well-known voltammetric shape. [33, 34]

Preparation of Au single crystalline electrodes:

After the cleaning procedure the Au electrodes were either flame annealed or annealed in a N_2-purged induction heat cell afterwards. After the annealing, the crystals cooled down (in the same cell where they were inductively heated for the case of inductively heated crystals) above N_2-saturated Milli-Q water.[33, 34] After the electrodes reached room temperature, they were characterized in H_2SO_4 once every day prior to an experiment to proof the setup. When the setup showed good performance, the electrodes were again prepared and transferred to the experimental setup.

Preparation of Pt single crystalline electrodes:

After the cleaning procedure the electrode is transferred to and annealed in an induction heat cell purged by N_2 (for Pt(111) and Pt(pc)) or 5% H_2 + 95% Ar (for Pt(100)) (see Figure 94). Afterwards, the crystals cooled down above N_2-saturated Milli-Q water.[33, 34]. The cooldown period varied between 4 and 6 minutes depending on the thickness of the single crystals and the gas flow. Then a KBr solution was added to the cell to give a concentration of 20 mM KBr and the single crystal was contacted to this solution (Note that there was no contact to ambient air so far); the bromine adsorbate protects the surface against ambient air and contaminants. The bromine layer was stripped electrochemically at negative potentials once every day prior to an experiment to confirm cleanliness and surface order (see Figure 94). The electrode then was prepared again and transferred to the cell containing the organic electrolyte. Ref. [35, 36] were used as model to develop this exact procedure and adjusted to fit the needs of this study.

The single crystals used for AFM experiments were prepared by flame annealing.

2.5 Electrode roughening

This thesis uses the electrode roughness as additional adjusting screw to investigate electrode processes. This chapter deals with the procedure to roughen massive Au and Pt electrodes. As in chapter 2.4, the electrodes at first had to be cycled in H_2SO_4 to check for cleanliness. But the roughening requires a further step prior to the actual roughening. The electrodes have to be polished before they are roughened. This establishes on the one hand similar starting conditions regardless of the history of the electrode and on the other hand this step is required to properly roughen Pt electrode. It seemed that Pt electrodes can only be roughened properly when the electrode is smooth initially. Thus an even better option to the polishing is the annealing, as done for the single crystalline electrodes (see chapter 2.4). In practice this means that if one tries to roughen an already rough Pt electrode (using the method described below), the electrode roughness will hardly increase.

Roughening of Au electrodes:

The electrode was immersed in Ar-saturated 0.5 M H_2SO_5 and a potential of above 2.5 V was applied (forming the gold oxide) for a certain time before the formed gold oxide was reduced electrochemically in the same cell. Increasing the applied potential or the time at high potentials increases the resulting electrode roughness.

Roughening of Pt electrodes:

The electrode was immersed into Ar-saturated 0.5 M H_2SO_4 and an alternating potential (at 1.4 kHz) between 0 V and 2.6 V vs RHE was applied to the electrode. After the dedicated time, the platinum oxide species were reduced until the current drops to zero. An increase in the treatment duration leads to an increase in the resulting electrode roughness.

An example for a the CV of a roughened Au electrode is shown below in Figure 12

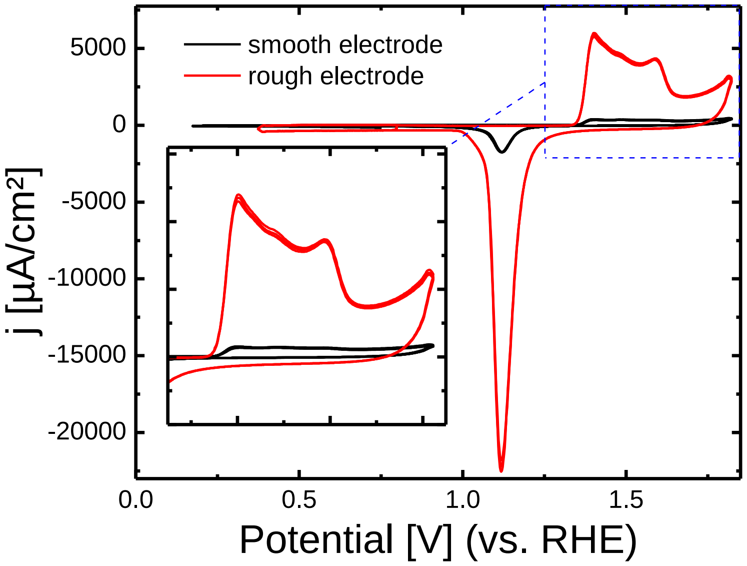

Figure 12 show the voltammetry of smooth (black) and rough (red) Au in 0.1 M H_2SO_4 vs RHE, with Au wire as CE. The inset shows a magnification of the relevant region for the determination of surface roughness in case of Au. Note that the current in this voltammogram is normalized to the geometrical surface area of the electrode.

2.6 Atomic Force Microscopy (AFM)

In 1986, Binnig and Quate initiated the development of the AFM systems used nowadays [37]. However, at the current date AFM is common technique to probe the surface of a substrate. In atomic force microscopy a sharp tip (only several atoms at the apex) is brought in contact with a surface. The tip is attached to a cantilever, which also acts as mirror to reflect a laser beam. The reflexion of the laser beam is detected by a photodetector and is measured as a signal in volts. This signal is then processed in a feedback system. As the cantilever will bend when it is moved towards the surface (much like a spring) or across the surface, the reflexion will move along the photodetector. The photodetector is separated into 4 regions (A, B, C and D). Thus the intensity of the reflexion can be tracked as the reflexion moves across the photodetector. So the exact tilt of the cantilever can be tracked in any direction with respect to the displacement (utilizing piezoelectric elements for movements in nm range). This finally enables imaging of the surface. A schematic of the AFM principle is given in Figure 13.

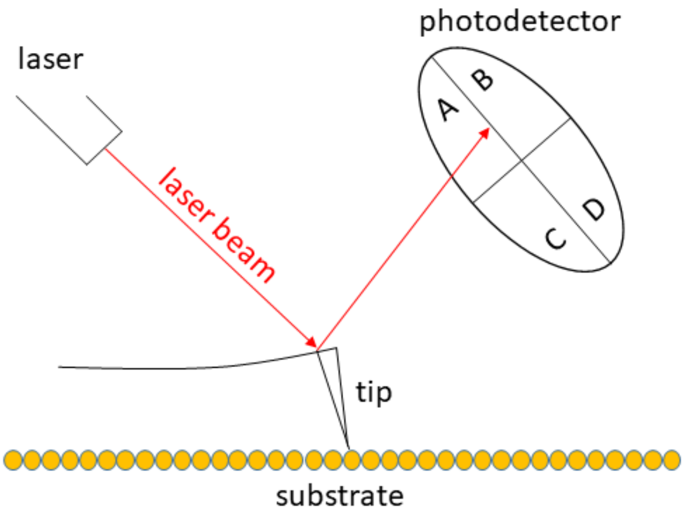

Figure 13 shows a schematic of the AFM working principle.

As the cantilever approaches the substrate in an AFM experiment, the tip at some point experiences an attractive force (bending the cantilever towards the surface) depending on the charge situated on the tip and the substrate (thus sometimes no attractive force is observed). As the tip approaches closer to the surface it passes layers of electrolyte or even the electrochemical double layer. At some point the force required for further penetration of these layers exceeds the attractive force that the tip experiences. At this transition point, there is a maximum in "negative" deflection. When the tip physically contacts the surface, the cantilever starts to bend upwards (according to Hooke's law) due to the repulsive force. Approaching the cantilever closer to the surface, the deflection of the laser beam is dominated by the force constant of the cantilever in normal direction. Thus a force separation curve (FSC) can be calculated, where the force is calculated from the deflection of the laser beam. A schematic for a FSC is shown in Figure 14.

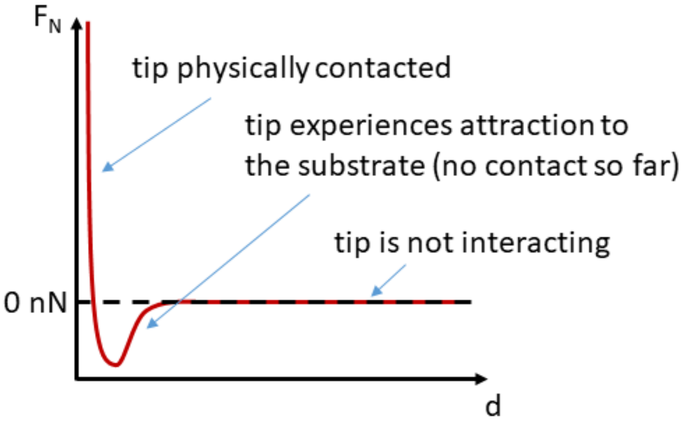

Figure 14 shows a schematic for a FSC in an AFM experiment. F_N denotes the normal force and d denotes the distance between the tip and the surface. The slope caused by the normal force constant of the cantilever is subtracted resulting in a steep increase in force (to infinity) as the tip contacts to the surface.

In this study AFM was used in combination with electrochemistry in a three-electrode arrangement similar to the H-cell. Therefore a home-built EC-AFM cell was used. The cell is shown in Figure 15.

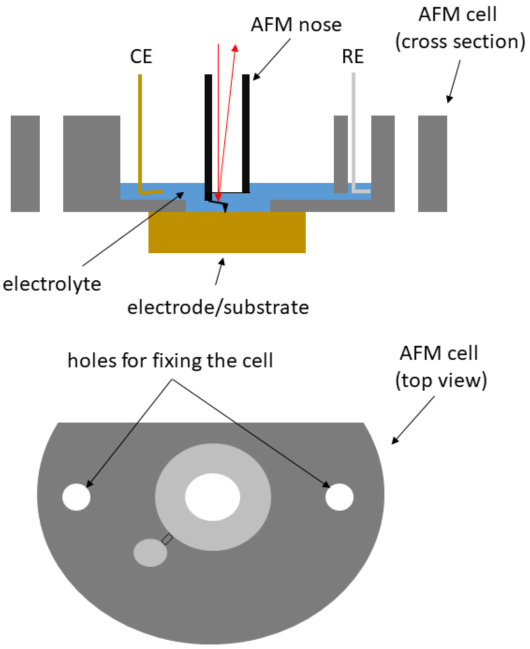

Figure 15 shows a sketch of the EC-AFM cell used in this study. The cell body is made of KEL-F and consists of two compartments. The larger compartment is the WE compartment, where the electrode is pressed against. This compartment is filled with electrolyte establishing the contact to the CE, which is also immersed into this compartment. The WE compartment is connected to the RE compartment via a capillary. Through this capillary, the RE is contacted to the other electrodes via the electrolyte. The red arrows indicate the laser beam pathway.

Calculation of the force

To calculate the forces in an AFM experiment from the deflection in Volts, one needs the force constants of the cantilever for normal (k_N) and lateral/torsional motion (k_L/k_Φ). Where k_L and k_Φ can be interconverted via:

$$k_\mathrm{L} = \frac{k_\Phi}{{l_\mathrm{L}}^2} \tag{26}$$

Where l_L denotes the length of lever causing the torsion (distance between tip apex and centre of rotation), which is typically given by:

$$l_\mathrm{L} = h + \frac{1}{2} t_\mathrm{C} \tag{27}$$

Here h denotes the height of the tip and t_C denotes the thickness of the cantilever, which are usually given by the provider. The force constants are obtained via the Sader method[38, 39]. Therefore the cantilever has to be driven by a vibration (usually caused by a piezo electric system) to show its simplest normal and torsional mode. Note that one has to separate normal from lateral deflection, to evaluate this. However, this gives a plot of deflection amplitude with respect to the frequency. For both cases (normal and torsional) the peak with largest intensity is assumed to be the simplest vibrational mode. Fitting the theoretical behavior for a driven harmonic oscillation (effectively a lagrangian) to the shape of the signals, one obtains the quality factor f_{Q} of the harmonic oscillation. The signal ($I_{(\omega)}$) is given by:

$$I_{(\omega)} = I_0 + \frac{\frac{A}{{f_{\mathrm{Q}}}^2} * \omega^4}{(\omega^2 - {\omega_{\mathrm{R}}}^2)^2 + \left(\frac{\omega * \omega_{\mathrm{R}}}{f_{\mathrm{Q}}}\right)^2} \tag{28}$$

Where I_0 is the signal offset (typically: $I_0 = 0$), ω_{R} is the resonance frequency, ω is the frequency and A is the amplitude. Then f_{Q} and ω_{R} are further processed via an online calibration tool (https://ampc.ms.unimelb.edu.au/afm/calibration.html) to give the normal and torsional force constant. In addition to the force constants, the deflection sensitivity (S_{N}) is required, which correlates the Signal of the photodetector (in Volts) to the piezoelectric displacement. This is usually done by calculating the slope in a force separation curve (FSC) in an interval, where the tip is physically contacted to the substrate. Thus the normal and lateral force is obtained via:

$$F_{\mathrm{N}} = k_{\mathrm{N}} * S_{\mathrm{N}} * (U_{\mathrm{N}} - U_0) \tag{29}$$

$$F_{\mathrm{L}} = \frac{3}{2} * \frac{h}{L} * k_{\mathrm{L}} * S_{\mathrm{N}} * U_{\mathrm{L}} \tag{30}$$

While F_{L} denotes the lateral force U_{N} denotes the deflection in normal direction, U_0 denotes the deflection offset, U_{L} denotes the deflection in lateral direction and L denotes the length of the cantilever. The friction force (F_{fric}) is then further calculated via:

$$F_{\mathrm{fric}} = \frac{F_{\mathrm{L,retrace}} - F_{\mathrm{L,trace}}}{2} \tag{31}$$

Where $F_{\mathrm{L,trace}}$ is the lateral force calculated from the trace (left to right) and $F_{\mathrm{L,retrace}}$ is the lateral force calculated from retrace (right to left).

3 Solvent in salt electrolytes:

3.1 A novel cell in battery geometry

The H-cell (see chapter 2.1) is a well-established tool to investigate the electrochemistry at a working electrode. But as a battery has a rather compact design with a thin electrolyte layer (where anode and cathode are separated by a membrane and arranged parallel to minimize resistance and to ensure a homogeneous current contribution) electrochemistry might be different. Electrolytes, which are topic of research (especially at high salt concentrations) might be very rare and not easily available in large amounts (if commercially available at all). To simulate battery conditions/geometry and to be able to use expensive electrolytes, a novel low-volume cell for electrochemical investigations was constructed (see Figure 16).

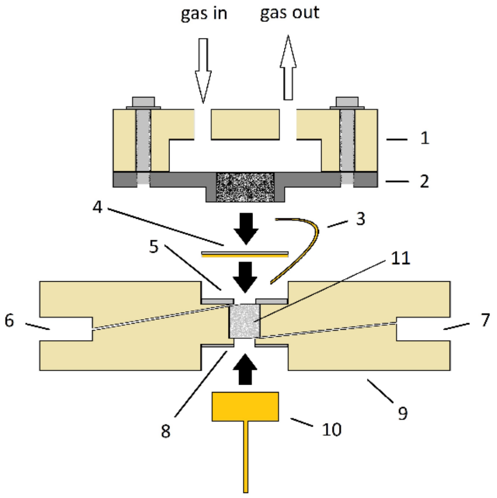

1: Teflon body of the gas chamber
2: Steel plate with steel frit (middle)
3: Wire for electrical contact
4: Sputtered Teflon membrane
5: Teflon spacer (thick)
6: Electrolyte outlet / Contact to RE
7: Electrolyte inlet
8: Teflon spacer (thin)
9: KEL-F cell body with glass frit (middle)
10: WE / CE (depends on the purpose)
11: Glas fritt

Figure 16 shows a schematic of the novel cell. The thick Teflon spacer has a thickness of 1 mm and the thin Teflon spacer has a thickness of 50 µm. The total size is comparable to the size of the DEMS cell by Bondue et al. [29]

This novel cell has several advantages compared to an H-cell.

Low volume:

The cell has a small volume of approximately 60 µl (neglecting the capillaries). This makes investigations regarding expensive electrolytes (such as TFSI salts) less cost intensive. Furthermore electrolytes will not have to be prepared in larger amounts, which makes dangerous electrolytes such as $Mg(ClO_4)_2$ in organic solvents less problematic to prepare. Due to the low volume to surface ratio, less problems with contaminants (such as H_2O) are expected.

Versatile:

The cell can be connected any type of massive or membrane-like electrode. This allows for voltammetric investigations on massive and porous (for gas diffusion) electrodes as well as e.g. the connection to a DEMS. The glass frit furthermore blocks diffusion of reaction products from CE to WE compartment (at least to some extent).

Parallel electrode geometry:

The parallel arrangement of WE and CE together with the low electrolyte volume minimizes the electrolyte's resistance and result in a homogeneous current distribution. Furthermore the geometry resembles battery geometry and allows for a more direct comparison.

The cell already found application in the LuCaMag project (03EK3051A) in the framework of the "Vom Material zur Innovation"-initiative. There it was used for investigations in the oxygen reduction reaction in aqueous, highly concentrated $CaCl_2$ (up to 6.5 M) in the context of Hydrate-Melt electrolytes.

Performance

The new thin layer cell was compared to an H-cell by checking the redox couple of decamethyleferrocene (FeCp*) in DMSO. As conducting salt 0.1 M $LiClO_4$ was used for the new cell and 0.1 M $KClO_4$ for the H-cell. Note that the cation has no significant influence on the FeCp* redox couple.

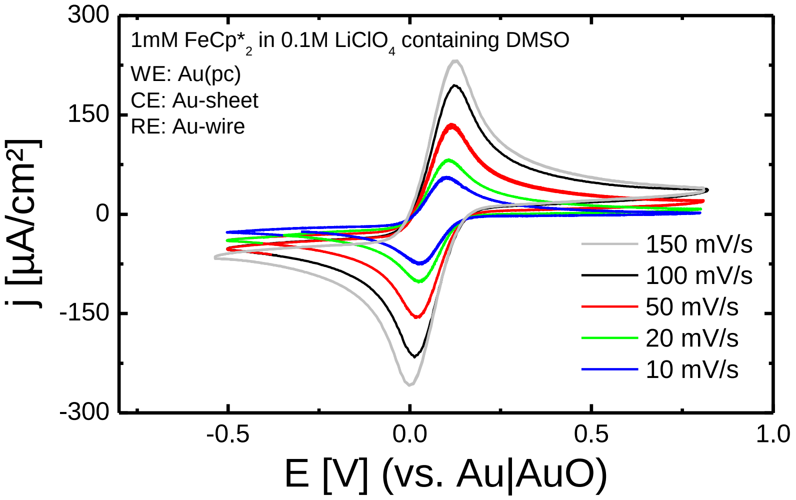

Figure 17 shows the FeCp* redox couple in 1 mM FeCp* + 0.1 M $LiClO_4$ containing DMSO on polycrystalline Au in the novel cell. The colorcode indicates the current density response for different sweep rates.

Figure 17 shows the FeCp* redox couple in the new thin layer cell and demonstrates that the new cell seems to perform well. As the system is known as well-performing reference system which shows a diffusion controlled process, we compared the behavior of diffusion limited current density vs square root of sweep rate for the new cell to the H-cell. These two plots should overlap to prove the performance of the new cell. The plot itself should give a linear behavior assuming a diffusion controlled process.

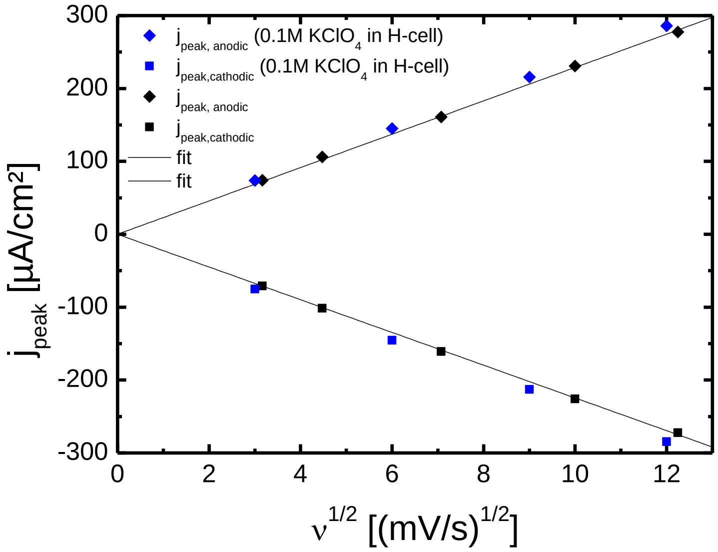

Figure 18 shows the plot of peak current density vs square root of sweep rate for the new cell (corresponding to the experiment in Figure 17, black) and for the H-cell (with $KClO_4$ as conducting salt, blue). The solid line corresponds to the best linear fit.

Figure 18 shows the Randles-Sevcik plot for a reversible process to comparison of the Experiments for the new cell to the H-cell. As the test system is well-known to show high reversibility, the experimental data should nicely follow the theoretical behavior of:

$$j_\mathrm{p} = 0.4463\ C\ z^{3/2}\ F^{3/2}\ (vD/RT)^{1/2} \tag{32}$$

The plot shows a very similar behavior for H-cell and the new cell, both showing nicely a linear behavior as theory predicts. This proves the new cell to be an interesting alternative depending on the conditions required to perform the experiment as discussed above.

Chemicals and Devices

Decamethylferrocene ($Me_{10}Fc$, 97%, SIGMA-ALDRICH), lithium perchlorate ($LiClO_4$, battery grade, SIGMA ALDRICH), potassium perchlorate ($KClO_4$, ≥99%, SIGMA-ALDRICH), dimethyl sulfoxide (DMSO, 99.7%, over molecular sieve, Acros Organics). For purging and electrolyte saturation argon (99.999%, Air liquide) was used. All non-aqueous electrolytes were prepared and stored in a GS glovebox.

The $KClO_4$ salt was dried under reduced pressure at 180 °C to decrease the water content further.

The water content in the electrolytes was monitored using a C20 Metler Toledo (coulometric KF titrator with a diaphragm electrode). The samples for water content determination were extracted from the used electrolyte after the experiments. The cells (H-cell and low volume cell) were connected to a bipotentiostat (Tacussel Bipad B1).

3.2 Investigating the system of highly concentrated $CaCl_2$ in H_2O

In solvent in salt electrolytes all the solvent is bound to salt, reducing its activity to a minimum, thus potentially increasing the electrolyte's potential window. A rather simple solvent in salt electrolyte is the hydrate melt. Depending on the effective increase in potential window for "aqueous" electrolytes a battery application might become more attractive. In this chapter $CaCl_2$ servers as model system as both Ca^{2+} and Cl^- both tend to bind water. In the context of this thesis the possible application of this system (and similar systems) will be discussed in the battery context. Thus the following parameters were examined:

- Conductivity
- Oxygen solubility and diffusion coefficient
- Potential window

Furthermore the oxygen reduction in highly concentrated $CaCl_2$ was investigated utilizing cyclic voltammetry in quiescent solution and under convection (RRDE).

Investigations

Conductivity:

The conductivity of $CaCl_2$ was determined at concentrations of 0.5 M, 4.0 M and 6.5 M.

Table 1 Conductivity of $CaCl_2$ for several concentrations at T = 298K.

C [mol/l]	Λ_{298K} [mS/cm]
0.5	90.8
4.0	236.0
6.5	141.8

Table 1 shows that the conductivity of $CaCl_2$ increases from 0.5 M to 4.0 M and decreases from 4.0 M to 6.5 M. This indicates that the water is bound, decreasing its activity and thus decreasing the conductivity.

Oxygen solubility and diffusion coefficient:

The oxygen solubility and the diffusion coefficient were determined as described in ref. [40, 41]. This method allows for simultaneous determination of the diffusion coefficient and the solubility of gaseous species via a transient in the mass signal after a pressure jump in a thin layer cell of well-defined thickness. The method was limited to a concentration of 2.0 M due to the detection limit of the mass spectrometer.

Table 2 Oxygen diffusion coefficients and solubility at 900 mbar O_2 partial pressure for several $CaCl_2$ concentrations.

C_{CaCl2} [mol/l]	0.0	0.5	1.0	2.0
$D_{O_2}^{900\ mbar}$ [cm²/s]	$20.1*10^{-6}$	$16.7*10^{-6}$	$13.6*10^{-6}$	$0.9*10^{-6}$
$C_{O_2}^{max}$ [mmol/l]	1.27	0.65	0.45	0.20

Table 2 shows a decreasing oxygen diffusion coefficient for increasing $CaCl_2$ concentration. On the one hand a decreasing oxygen diffusion leads to a low current at the air electrode. On the other hand this also decreases oxygen diffusion to the negative electrode.

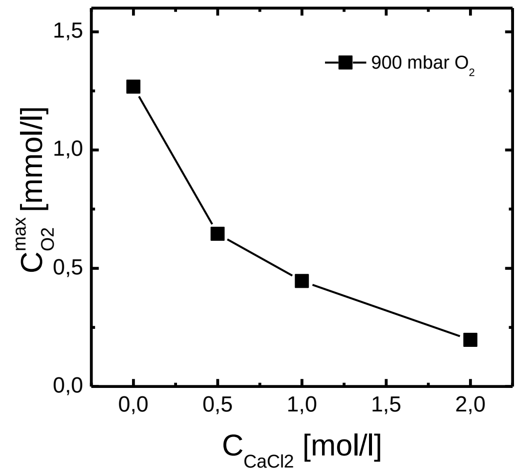

Figure 19 shows the plot of the oxygen solubility vs. the $CaCl_2$ concentration at 900 mbar O_2 partial pressure.

Figure 19 shows the plot of the oxygen solubility vs. the CaCl2 concentration at 900 mbar O2 partial pressure.shows the same trend. The higher the concentration, the lower the oxygen solubility. If one extrapolates the data to concentrations as high as 6.5 M, the oxygen solubility decreases to some µmol/l.

<u>Potential window:</u>

The potential window of aqueous $CaCl_2$ was examined at several concentrations in argon saturated Milli-Q water at 50 mV/s at Au and Glassy-Carbon electrodes in an H-cell. CE was a gold sheet and as RE a silver wire in saturated KCl was used.

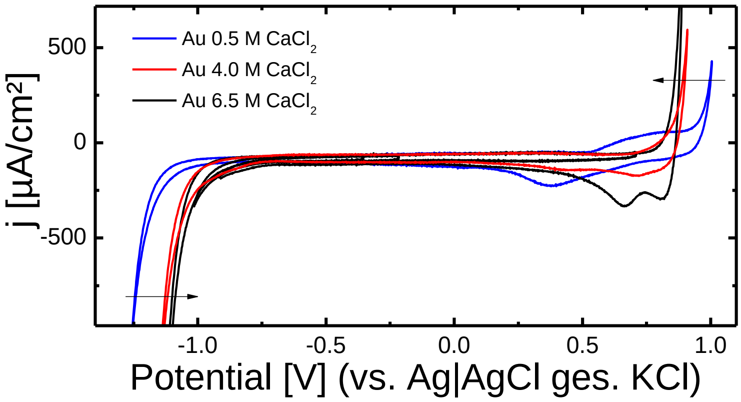

Figure 20 shows the voltammetry of Au in argon saturated, aqueous $CaCl_2$ at 50mV/s vs Ag|AgCl (in sat. KCl). CE was an Au sheet. The arrows indicate the shift of the potential limits with increasing salt concentration.

Figure 20 shows that the potential window decreases in cathodic direction as well as in anodic direction with increasing $CaCl_2$ concentration for the Au case. In cathodic direction this trend can be explained by the increased acidity of the bound water, fostering hydrogen evolution. In anodic direction the trend might be explained by the increasing Cl^- concentration, which might foster the formation of $[AuCl_n]^{n-}$ complexes. This would contradict a practical battery application.

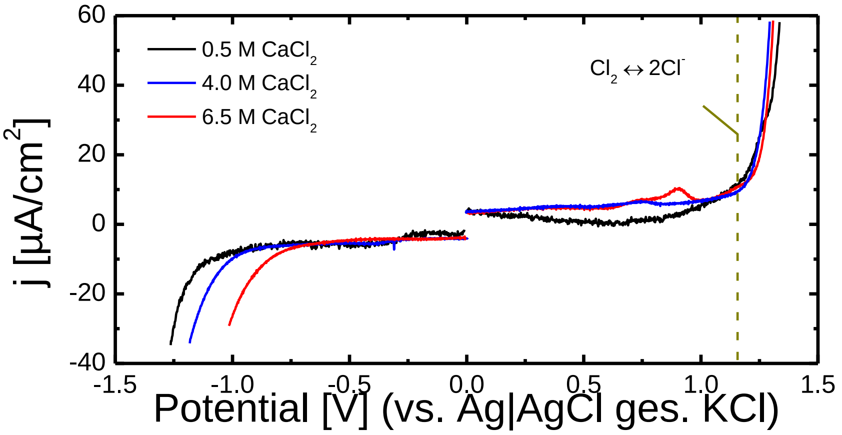

Figure 21 shows the voltammetry of Glassy-Carbon in argon saturated, aqueous $CaCl_2$ at 50mV/s vs Ag|AgCl (in sat. KCl). CE was an Au sheet. The dashed line refers to the theoretical potential for the $Cl_2/2Cl^-$ redox couple.

Regarding Figure 21 an effect similar to the Au case is observed for Glassy-Carbon in cathodic direction. In anodic direction the trend seems to solely depend on the conductivity as the effect of complex formation is furthermore unexpected for Glassy-Carbon.

<u>Oxygen reduction:</u>

Initially the oxygen reduction in $(\mathrm{Ar}^{80\%}/\mathrm{O}_2^{20\%})$ saturated, resting electrolyte at $CaCl_2$ concentrations of 0.5 M, 4.0 M and 6.5 M was investigated.

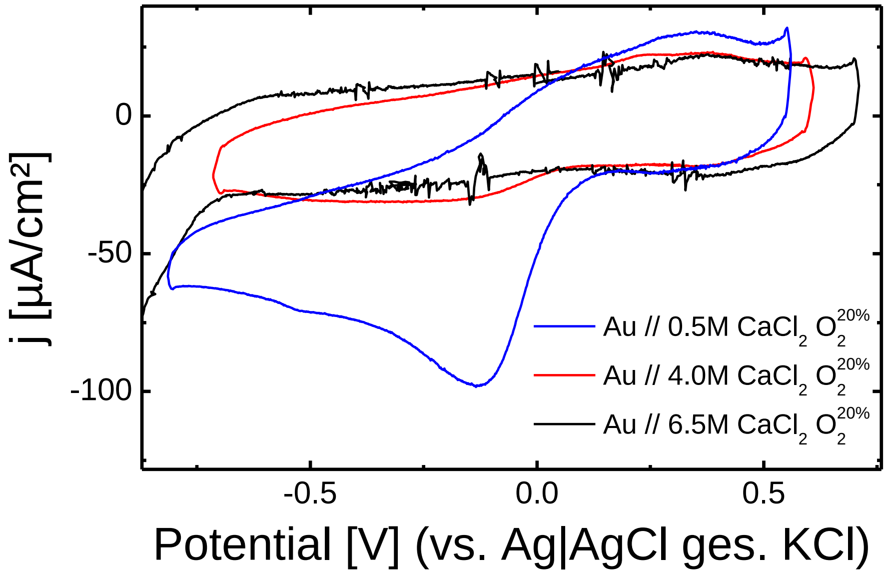

Figure 22 shows the voltammetry in quiescent solution of ($Ar^{80\%}/O_2^{20\%}$) saturated, aqueous CaCl$_2$ of varying concentrations on Au at 50 mV/s vs Ag|AgCl (in sat. KCl) with an Au sheet as CE.

Figure 22 shows that the oxygen reduction current density (starting at 0.2 V in cathodic direction) decreases with increasing salt concentration as expected. This is a direct consequence of the decreasing oxygen diffusion coefficient and oxygen solubility with increasing salt concentration.

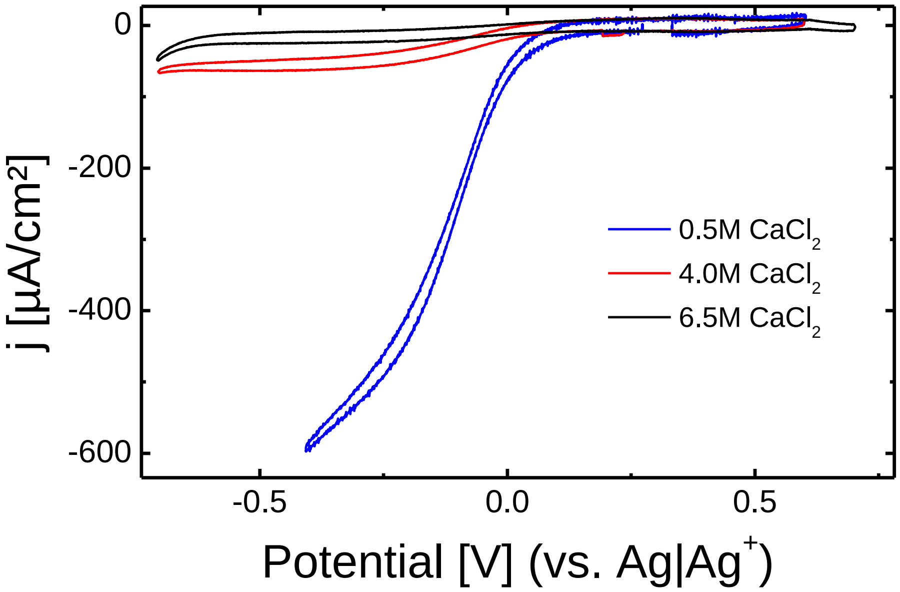

Figure 23 shows the voltammetry at 16 Hz rotation frequency of ($Ar^{80\%}/O_2^{20\%}$) saturated, aqueous CaCl$_2$ of varying concentrations on Au at 50 mV/s vs Ag|AgCl (in sat. KCl) with an Au sheet as CE

Under convection the difference in current density is accordingly more pronounced. During the experiments, we observed that a change in current density with increasing rotation frequency at high concentrations was hardly visible. Thus further RRDE investigations were excluded. Though it is noteworthy, that the Au electrode was not blocked by oxygen reduction species and that the ring current was extremely low. This makes water as ORR main product the most probable.

To compensate for the low oxygen diffusion coefficients, additional experiments were performed using a novel cell described in chapter 3.1 in a gas diffusion setup. As WE served a sputtered Au membrane electrode.

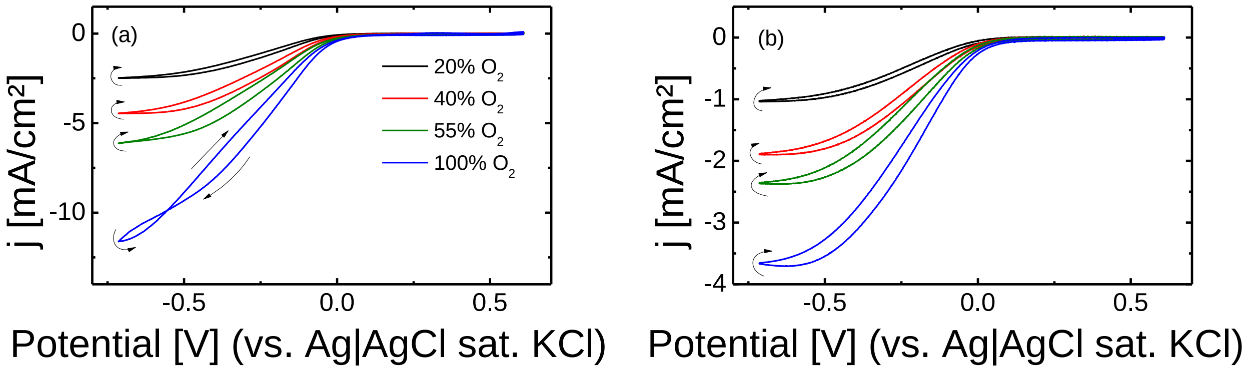

Figure 24 shows the voltammetry of aqueous $CaCl_2$ for quiescent solution on Au (sputtered membrane electrode) for $CaCl_2$ concentrations of 4.0 M (a) und 6.5 M (b) and varying O_2 partial pressures at 50 mV/s vs Ag|AgCl (in sat. KCl). CE was an Au sheet. The arrows indicate the sweep direction

As expected, Figure 24 shows a significant increase in current density compared to the RRDE case. This supports the interpretation that the small current densities are caused by the low oxygen diffusion and solubility in highly concentrated $CaCl_2$. However, also in this system we observe a decrease in current density with increasing $CaCl_2$ concentration (comparing Figure 24a with Figure 24b). To further investigate on this, the diffusion limited current density was plotted against the oxygen partial pressure. In theory one should observe a linear behavior (referring to Henry's law and Fick's law).

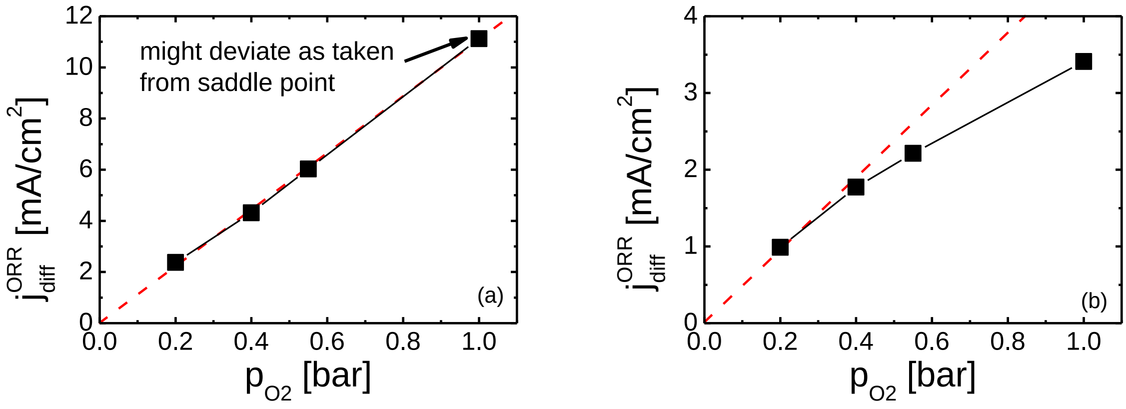

Figure 25 shows the plot of diffusion limited current density vs O_2 partial pressure for aqueous $CaCl_2$ at concentrations of 4.0 M (a) and 6.5 M (b). The red line indicates the theoretical behavior.

Figure 25 shows this plot. For 4.0 M $CaCl_2$ the theoretical behavior matches the experimental observations. For a concentration of 6.5 M $CaCl_2$ a deviation from the theoretical behavior was observed. This deviation increases with increasing O_2 partial pressures. A possible explanation for this observation is that the oxygen reduction is further limited by diffusion of H^+ to the electrode (assuming H_2O as main reduction product).

In conclusion hydrate-melt electrolytes seem to be inapplicable for oxygen battery applications due to their narrow potential window (especially limited in cathodic direction), as one aims at maximizing the battery voltage. As for the case of Ca or Mg metal deposition at the anode could not be achieved, intercalation might be an option as anode process. But even in this case suitable intercalation compounds that work above the potential of hydrogen evolution still have to be developed, as to my knowledge those do not exist at the present day.

As an alternative to hydrate-melt electrolytes other solvent in salt electrolytes are suggested. By investigating the solubility behavior of several DMSO and TG containing electrolytes, we identified the following electrolytes as possible candidates due to their high concentration:

- $Ca(TFSI)_2$ ● 1 TG ● 1 DMSO (liquid at room temperature)
- $Ca(TFSI)_2$ ● 4 DMSO (liquid at room temperature)
- $Ca(TFSI)_{1.6}(Otf)_{0.4}$ ● 2 TG (liquid at room temperature)

Where the image below shows the preparation of $Ca(TFSI)_2$ ● 4 DMSO (Figure 26c) from DMSO (Figure 26a) and $Ca(TFSI)_2$ (Figure 26b). Note that these electrolytes show a high viscosity.

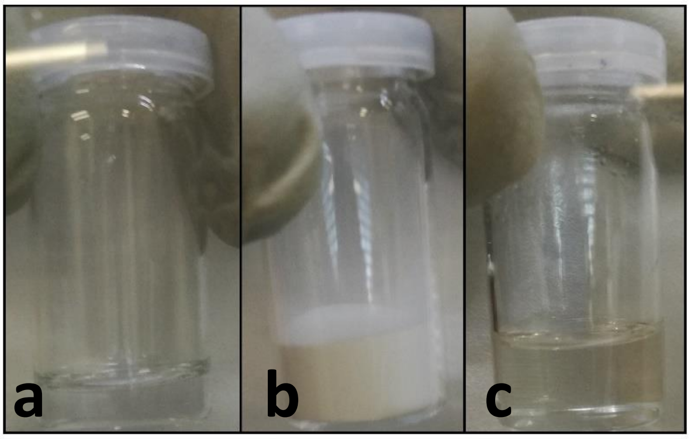

Figure 26 shows the preparation of $Ca(TFSI)_2$ ● 4 DMSO (c) from DMSO (a) and $Ca(TFSI)_2$ (b).

Note that increasing the concentration to regimes, where the cation ligand sphere cannot be saturated solely by the solvent, ion-pairing has to be taken into account. Thus concerning metal deposition not only the stability of the anion towards strong reduction potentials but also the stability of the ion-paired anion has to be taken into account. Theoretical calculations [42, 43] have shown that ion-paired

TFSI is destabilized (cleavage of the C-S bond) concerning reductive potentials. Thus a reduction is expected to be possible, while intermediary formed M^+ (M = Mg in this case) causes reduction of the TFSI anion within the complex, breaking the S-C bond and restoring M^{2+}. Intercalation of the divalent cation instead of plating it might solve this problem[44-46], while a lot of research still is required to identify proper intercalation compounds.

Chemicals and Devices

Dimethyl sulfoxide (DMSO ,99.7%, over molecular sieve, Acros Organics), tetraethylenglycoldimethylether (TG, 99%, Acros Organics), calcium chloride dihydrate ($CaCl_2$ $2H_2O$, 99%, Merck), calcium trifluoromethanesulfonate ($Ca(Otf)_2$, 98%, abcr), calcium bistrifluoromethanesulfonimide ($Ca(TFSI)_2$, >97%, TCI). For purging and electrolyte saturation argon (99.999%, Air liquide) and oxygen (99.9995%, Air liquide) were used. The gases were mixed and the flow was controlled via electronic flow meters (F-201C-UA-22-V, Bronkhorst, MFT-V12C Union Carbide), while the flow meters were calibrated for the specific gases. All non-aqueous electrolytes were prepared and stored in a GS glovebox.

The $Ca(TFSI)_2$ and $Ca(Otf)_2$ salts were dried under reduced pressure at 180 °C to decrease the water content further.

The conductivity of the electrolytes was measured via the Metler Toledo SevenCompact.

The water content in the electrolytes was monitored using a C20 Metler Toledo (coulometric KF titrator with a diaphragm electrode). The samples for water content determination were extracted from the used electrolyte after the experiments. The cells (H-cell and low volume cell) were connected to a bipotentiostat (Tacussel Bipad B1).

4 The mechanism of Li_2O_2-film formation and reoxidation – influence of electrode roughness and single crystal surface structure

Andreas Koellisch-Mirbach*, Tabea Lohrmann*, Philip Heinrich Reinsberg* and Helmut Baltruschat*

*Institut für Physikalische und Theoretische Chemie, Universität Bonn, Römerstraße 164, D-53117 Bonn, Germany

Reproduced and adapted with permission of

A. Koellisch-Mirbach, T. Lohrmann, P. H. Reinsberg, H. Baltruschat, *Journal of Electroanalytical Chemistry (1959)* **2020**, *875*, 114560.

Summary and statement to work contributions:

The work presented in this article is based on a previous master thesis by A. Koellisch-Mirbach (A. Koellisch-Mirbach, *Oxygen reduction in Non-Aqueous Electrolytes: Influence of the Surface Structure of the Electrocatalyst* (Master thesis), **2019**). In addition to the results obtained in this Master's thesis, Pt(100) was investigated in the same context and valuable interpretations and conclusions were added. The chapter *"Determination of the apparent transfer coefficient α' for OER"* were part of the Master thesis (Determination of Apparent Transfer Coefficients of the Oxygen Reduction and Evolution Reaction in Aprotic Solvents) of Tabea Lohrmann.

The presented work addresses the oxygen reduction reaction (ORR) and oxygen evolution reaction (OER) in Li^+-containing dimethyl sulfoxide (DMSO) on Pt single and poly crystalline electrodes. Furthermore the influence of electrode roughness on ORR and OER is investigated on platinum and gold electrodes. Rotating ring disc electrode (RRDE) investigations in a generator collector arrangement and differential electrochemical mass spectrometry (DEMS) investigations, both show a direct proportionality between the amount of formed Li_2O_2 and the electrodes roughness factor. Thus a complete blocking of the electrode surface occurs irrespective of the electrode material or surface roughness. Correlating the amount of formed Li_2O_2 with the real electrode surface area additionally hints the formation of one monolayer in case of polycrystalline platinum electrodes (Pt(pc)) and the formation of two monolayer in case of polycrystalline gold electrodes (assuming 1 to 1 adsorption of Li_2O_2 per electrode surface atom). Also in case of polycrystalline gold electrode, the superoxide formation is visibly (in a voltammogram) separated from the peroxide formation and occurs at more positive potentials. Comparing the gold and platinum electrodes, on gold electrodes the amount of evolved CO_2, monitored by DEMS, indicates a lower degree of electrolyte degradation. Thus, the ORR on gold electrodes leads to less side product formation. Regardless of the electrode material, the electrochemical generation of peroxide largely exceeds that of superoxide. The amount of formed superoxide seems to solely depend on the time until peroxide formation becomes dominant. The constant amount of formed superoxide with respect to increasing electrode roughness further implies that both, the superoxide formation onset and the peroxide formation onset, are shifted similarly. The single crystalline electrode surface structure on platinum electrodes also influences the ORR and OER. The ORR on Pt(100) leads to the formation of 2 monolayers of Li_2O_2, while the ORR on Pt(111)/Pt(pc) only one monolayer is formed. However, the ORR and shape of the voltammograms is rather independent on the atomic surface structure, apart from a shifted onset-potential by approximately 45 mV for Pt(100). This shift towards more negative potentials hints a decreased rate in case of Pt(100). Concerning a practical battery application, the amount of Li_2O_2, which can be formed is too small due to the surface limitation. During the OER, Li_2O_2 is reoxidized to mainly O_2 with 2 e^- per molecule. For the case of high electrode roughness, superoxide is detected during the Li_2O_2 oxidation. Furthermore ac voltammetry investigations show an apparent transfer coefficient (α') of 0.3. This value hints a rate determining first charge transfer and thus agrees well with the detection of superoxide during Li_2O_2 reoxidation. The finding of superoxide during the OER is almost certainly not an effect of electrode roughness itself, but rather an effect of increased sensitivity, as more peroxide is reoxidized during OER. The main difference in CV-shape between Pt(111), Pt(pc) and Pt(100) is visible in the anodic scan direction. It is shown, that the shape of the CV and the amount of formed peroxide strongly depends on the atomic surface structure. For Pt(100) two monolayers are formed, while in case of Pt(111) and Pt(pc) only one monolayer is formed. This strong dependence suggests that the peroxide layer has to be regarded as an adsorbate. It is further noteworthy, that such a thin layer of peroxide is formed on all catalysts and atomic surface structures investigated in this work

Own manuscript contributions:

- Design of the experiments
- Performing the experiments
- Data evaluation
- Interpretation of the results
- Writing the manuscript

Acknoledgements

The authors gratefully acknowledge the financial support by the German Federal Ministry of Education *via* 11 the LiBaLu-project in the framework “Vom Material zur Innovation”-initiative (03XP0029A).

5 Electrochemical Reduction of O_2 in Ca^{2+}-containing DMSO: Role of Roughness and Single Crystal Structure

Andreas Koellisch-Mirbach*, Inhee Park*, Martina Hegemann*, Elke Thome* and Helmut Baltruschat*

*Institut für Physikalische und Theoretische Chemie, Universität Bonn, Römerstraße 164, D-53117 Bonn, Germany

Reproduced and adapted with permission of

A. Köllisch-Mirbach, I. Park, M. Hegemann, E. Thome, H. Baltruschat, *ChemSusChem* **2021**, *14*, 2564.

Copyright © Wiley Ltd.: DOI: **https://doi.org/10.1002/cssc.202100364**

Summary and statement to work contributions:

In this work, I. Park contributed by performing and evaluating the atomic force microscopy experiment (Figure 67 + Figure 78). My role concerning this experiment was to put the results into the context of the other results of this work and to improve the interpretations. The same holds for one experiment performed by M. Hegemann (Figure 75a) and E. Thome (determination of a diffusion coefficient). However in these cases the experiments were evaluated and interpreted by myself.

This study sheds some light on the fundamental reaction mechanism of the oxygen reduction reaction (ORR) in calcium cation (Ca^{2+}) containing dimethyl sulfoxide (DMSO). The ORR was investigated on well ordered (single crystalline) electrode surfaces, on annealed polycrystalline electrode surfaces and on deliberately roughened electrode surfaces. Cyclic voltammetry, differential electrochemical mass spectrometry (DEMS), a rotating ring disc electrode (RRDE) approach in a generator collector arrangement and atomic force microscopy (AFM) were used to provide insights into the fundamental electrode processes of the ORR.

This study shows that during the early ORR, slightly soluble calcium peroxide (CaO_2) is the main product on gold electrodes. In parallel to this reaction a competing side reaction leads to the formation of surface calcium oxide (CaO) and or CaO_2 until a monolayer is completed. This monolayer is completely closed on smooth annealed gold electrodes, which leads to the depletion of further oxygen reduction. However, on rough gold electrodes the CaO/CaO_2 layer is more defective and thus allows for continuous formation of superoxide through or on top of the CaO/CaO_2 layer. The CaO_2, which either forms via two subsequent 1 e^- transfer steps or by disproportionation of superoxide may be deposited on top of the CaO/CaO_2 adsorbate layer and is visible as bulk deposit in AFM measurements. These AFM experiments further demonstrated the slow dissolution of peroxide particles with time. For the case of smooth polycrystalline electrodes a severe deactivation of the ORR was observed, while deliberately roughened electrodes (covered with the CaO/CaO_2 adsorbate) allow for a diffusion limited superoxide formation. On single crystalline electrodes the peroxide formation is more pronounced, which is most likely due to a decreased stability of the CaO/CaO_2 adsorbed on the surface or due to kinetically hindered formation compared to the polycrystalline surfaces. Apart from that, the atomic electrode surface structure only has a minor influence on the ORR in presence of convection. The fundamental processes remain similar regardless of the electrode surface roughness, as the peroxide formation is a diffusion limited process under the measurement conditions. Thus for an electrode surface roughness factor (f_R) of 50, the formation of the formation of the CaO/CaO_2 adsorbate would take 50 times as long as for a roughness factor of 1.

In RRDE experiments it is shown that superoxide and peroxide are formed at the disc electrode and are reoxidized at the ring electrode in a generator collector arrangement. However, the reoxidation kinetics of the dissolved peroxide are sluggish (visible as a high reoxidation potential), which is most likely due to the formation of ion pairs of peroxide with the Ca^{2+} cation. This setup further demonstrated that the reoxidation of the formed soluble peroxide can be fostered by increasing the electrode surface roughness (as already mentioned for the ORR) and thus the effective rate. Correlating the ORR half wave potential shift with the electrode surface roughness, we were able to estimate the apparent transfer coefficient α_{app}. The thus obtained results confirm the results of the usual Tafel analysis and indicate an equilibrated first 1 e^- transfer.

This study once again shows that the electrode surface roughness is an important factor to be addressed as it strongly affects the product distribution of electrochemical reactions and proves the variation of the electrode surface roughness as a valuable tool for investigations on the reaction kinetics.

Own manuscript contributions:

- Design of the experiments
- Performing the experiments
- Data evaluation
- Interpretation of the results
- Writing the manuscript

Acknoledgements

The authors gratefully acknowledge the Federal Ministry of Education and Research (BMBF) for funding this work. This work was part of the MeLuBat project (03CP0110D) and the LuCaMag project (03EK3051A) in the framework of the “Vom Material zur Innovation”-initiative. Open access funding enabled and organized by Project DEAL.

6 Towards a generalized ORR mechanism in M^{2+} containing DMSO – Oxygen reduction and evolution in Ca^{2+} containing DMSO on atomically smooth and rough Pt

Andreas Koellisch-Mirbach*, Pawel, Peter Bawol*, Inhee Park* and Helmut Baltruschat*

*Institut für Physikalische und Theoretische Chemie, Universität Bonn, Römerstraße 164, D-53117 Bonn, Germany

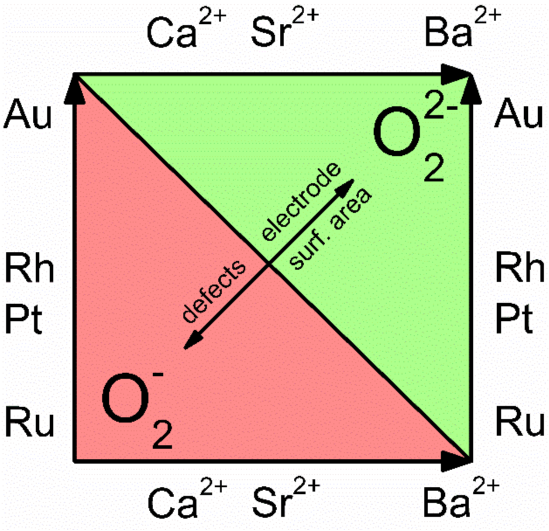

Reproduced and adapted with permission of

Koellisch-Mirbach, A., Bawol, P.P., Park, I. and Baltruschat, H. (2022), *Towards a generalized ORR mechanism in M2+ containing DMSO – Oxygen reduction and evolution in Ca2+ containing DMSO on atomically smooth and rough Pt*. ChemElectroChem. Accepted Author Manuscript.

Summary and statement to work contributions:

In this work, P. P. Bawol assisted during performing and evaluating the XPS experiment (Figure 83). I. Park performed and evaluated the in situ STM experiment (Figure 95), where it was my role to put the corresponding results into the context of the other results of this work and to improve the interpretations.

The ORR and OER in Ca^{2+} containing DMSO is investigated on atomically smooth, single crystalline (Pt (111) and Pt(100)) and deliberately roughened Pt electrode surfaces. The investigation of single crystalline Pt electrodes involved the protection of the single crystalline electrode surface against ambient conditions. This was achieved by an adsorbed layer of bromide, which is completely stripped from the surface prior to the ORR onset, as demonstrated by cyclic voltammetry.

The ORR on atomically smooth and rough Pt electrodes initially leads to the formation of calcium peroxide as main product. The formed peroxide forms a closed layer similar to the results observed on Au electrodes. After the completion of this layer, superoxide is the main reduction product. However, on Pt electrodes the formation of the calcium peroxide adsorbate layer is completed much faster than on Au electrodes. Additionally the adsorbate layer is formed faster on rough electrodes compared to atomically smooth electrodes. This hints a lower stability of the calcium peroxide adsorbate on atomically smooth Pt electrodes. As the main ORR product in this case is peroxide, the formation of dissolving peroxide is likely as already observed for Au electrodes.

It is furthermore noteworthy that superoxide is formed through or on top of the calcium peroxide adsorbate layer. This in consequence allows for a continuous discharge in the battery context.

The variation of the electrode roughness provided a deeper understanding of the general ORR mechanism in M^{2+} containing DMSO. The formation of adsorbed alkaline earth metal oxide and or peroxide seems to be the limiting factor for continuous peroxide formation for several electrode materials in DMSO. This study indicates that the ORR product distribution depends in the electrode surface-oxide interaction. In a battery context this finding predicts a continuous discharge, with peroxide as main product, without deactivation for electrode materials with low oxide interaction. In consequence this means that for electrodes with a high electrodes material oxide interaction a fast adsorbate formation is expected. These findings fit to observations made in earlier publications by the Baltruschat group. [47, 48]

For battery applications peroxide is favored due to its higher theoretical energy density (2 electrons per O_2 molecule transferred) compared to superoxide (1 electron per O_2 molecule transferred). This highlights electrode materials with extraordinarily low oxide interaction as interesting candidates. The ORR product distribution additionally is affected by several other factors. This study highlights three factors with strong influence. First would be the electrode roughness as on rough electrodes the adsorbate layer completion requires more absolute charge due to the increased real surface area. Second is the atomic surface structure, as on atomically smooth electrodes the adsorbate formation is slow due to thermodynamic or kinetic instability of the adsorbate attached to the electrode surface. The third factor would be the use of Additives like ORR mediators, as they lead to oxygen reduction at some distance of the electrode and thus avoid the formation of the adsorbate some extent. This shows, that minimizing the electrode oxide interaction, minimizing the electrode surface defects and maximizing the real electrode surface area, are key points to foster the formation of dissolving peroxide and as a result should increase the battery performance in such systems.

Own manuscript contributions:

- Design of the experiments
- Performing the experiments
- Data evaluation
- Interpretation of the results
- Writing the manuscript

Acknoledgements

The authors gratefully acknowledge the Federal Ministry of Education and Research (BMBF) for funding this work. This work was part of the MeLuBat-project (03XP0110D) and the LuCaMag-project (03EK3051A) in the framework of the “Vom Material zur Innovation”-initiative

7 The unexpected dissolution of $CaCl_2$ in DMSO

As this thesis deals with the oxygen reduction reaction of alkaline metal and alkaline earth metal cation containing DMSO, several electrolytes were identified to be interesting for future investigations (see the end of chapter 3). However the LiCl/$CaCl_2$ mixed electrolyte in DSMO electrolyte showed an astonishing behavior. Although $CaCl_2$ is nearly insoluble in DMSO, the 1 to 1 addition of $CaCl_2$ to 0.1 M LiCl in DMSO leads to complete dissolution of $CaCl_2$. In ref. [49] the authors proposed the formation of $CaCl_3^-$ for $CaCl_2$ + isophthalic acid chloride + m-phenylenediamine in dimethyl acteamide. The LiCl/$CaCl_2$ mixed electrolyte system in DSMO is certainly interesting and further investigations are highly recommended, as there are hardly any publications dealing with "stable" $CaCl_3^-$. As this system was discovered during the end of this thesis, further investigations were not possible.

Investigations

In the context of this thesis the oxygen reduction in 0.1 M LiCl + $CaCl_2$ containing DMSO was investigated. Note that this experiment could not be reproduced due to a lack of time, but at least encourages further investigations.

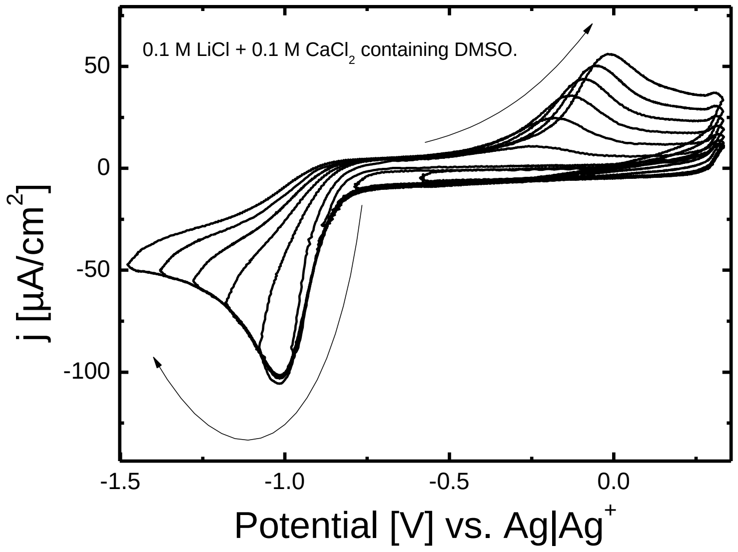

Figure 27 shows the potential window opening experiment of the (20% O_2 / 80% Ar)-saturated 0.1 M LiCl + 0.1 M $CaCl_2$ mixed DMSO electrolyte on a Pt electrode. Sweep rate was 50 mV/s, RE was a silver wire immersed into 0.1 M $AgNO_3$ and CE was a Pt-sheet. The arrows indicate the evolution of the voltammogram with increasing lower potential limit.

Figure 27 shows a potential window opening experiment in cathodic direction for the LiCl/$CaCl_2$ mixed DMSO system. From a comparison to the pure Li^+ and Ca^{2+} cases (see chapters 4 and 6), it is reasonable to assume that the observed currents correspond to the ORR and OER. Starting in cathodic direction the ORR starts close to -0.8 V vs Ag|Ag$^+$. The ORR current density increases to a peak and decreases after the peak to a diffusion limited value, indicating a diffusion controlled process rather than a surface limited process. In anodic direction the current density increases to a peak, which growth with more negative potentials applied to the electrode. This indicates a direct correlation to the ORR and suggests OER to be the most plausible reaction referring to the anodic peak. It is interesting that the dominant OER peak for the Li^+ system is located at roughly -0.5 V vs Ag|Ag^+ and for the Ca^{2+} at 0.25 V vs Ag|Ag^+ (both as perchlorate salts), whereas in the case of the mixed electrolyte of the chlorides, the dominant peak is close to 0 V vs Ag|Ag^+.

A further astonishing observation was made as the ORR was investigated in this system under convection.

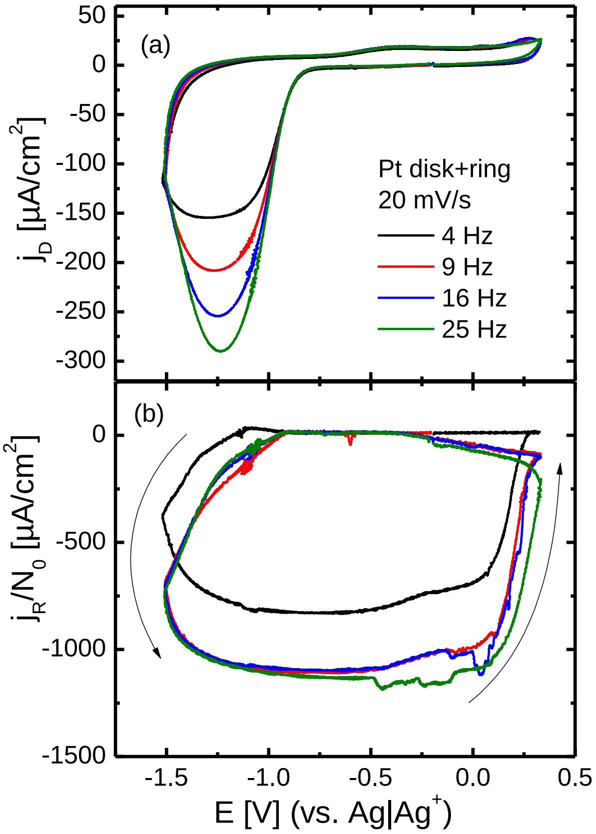

Figure 28 shows the cyclic voltammetry of a Pt/Pt thin gap electrode in (20% O_2 / 80% Ar)-saturated 0.1 M LiCl + 0.1 M $CaCl_2$ containing DMSO vs Ag|Ag^+ with a Pt sheet as CE. Sweep rate was 20 mV/s, E_{ring} = 0.3 V and varying rotation frequency using a usual H-cell. Disk current density is shown in (a). The ring current (b) is normalized to the collection efficiency N_0 and the geometrical surface area of the disk electrode for 1 to 1 comparability. The arrows indicate the sweep direction.

Figure 28 shows the experiment under convective conditions. The disc current in this figure is not unreasonable and shows most likely the oxygen reduction in cathodic direction and the reoxidation of adsorbed oxide species in anodic direction. Astonishing is the behavior of the ring current: On the one hand the current density is negative, which means that the process at the ring electrode is a reduction;

on the other hand the absolute ring current density is very large (about 1 mA/cm^2 for 9-25 Hz). The reduction process at the ring electrode starts as the ORR at the disc electrode starts and only stops after the disc potential reaches the value for the reoxidation of the oxide species. This highly indicates the formation of a catalytically active species at the disc electrode during the ORR. Thus on the ring electrode we would observe the reduction of a reaction product formed during the auto catalytic process at the disc electrode. As the ring potential is fairly positive, and as $\mathrm{CaCl_3^-}$ is expected to be rather unstable, the most plausible product detected at the ring is Cl_2. From my view, the most plausible explanation would be an autocatalytic reaction of chloride with oxygen to chlorine and peroxide. To get a clear picture of this mechanism DEMS experiments are required. However, this result wasn't reproduced due to missing time, but further research is highly recommended.

Chemicals and Devices

Dimethyl sulfoxide (DMSO,99.7%, over molecular sieve, Acros Organics), calcium chloride ($CaCl_2$, 99.99%, ultra dry, abcr), lithium chloride (LiCl, ≥98%, Sigma Aldrich). For purging and electrolyte saturation argon (99.999%, Air liquide) and oxygen (99.9995%, Air liquide) were used. The gases were mixed and the flow was controlled via electronic flow meters (F-201C-UA-22-V, Bronkhorst, MFT-V12C Union Carbide), while the flow meters were calibrated for the specific gases. All non-aqueous electrolytes were prepared and stored in a GS glovebox.

The H-cell was connected to a bipotentiostat (Tacussel Bipad B1).

8 The Electrochemistry of Sodiumdodecylsulfonate on Au(111) in sulfuric acid – Voltammetry, Adsorbate structure and Friction

8.1 Abstract

This study deals with the adsorption of sodiumdodecylsulfonate (SDS*) on the single crystalline Au(111) surface in 0.1 M sulfuric acid. As demonstrated by cyclic voltammetry and atomic force microscopy (AFM), the SDS* adsorbate shows a transition from a flat adsorbed phase to a condensed phase with increasing electrode potential. These observations are similar to those on sodiumdodecylsulfate (SDS) [4, 50, 51], where a condensed, disordered bilayer was found [3]. For the SDS* we found a well-ordered structure of the condensed layer and thus were able to suggest a structure for the condensed layer. Comparing the condensed and the flat phase, the condensed phase shows lower friction at low normal loads (tip follows corrugation) and higher friction at high normal loads (tip compresses/penetrates the layer).

8.2 Introduction

As opposed to sodiumdodecylsulfonate (SDS*), the adsorption of the similar sodiumdodecylsulfate (SDS) on electrode surfaces has been studied in detail.[4, 50, 51] SDS surface species form well-known and highly reproducible structures depending on their coverage[4, 50, 51]. For SDS at low coverage a hemimicellar phase was found, where the SDS molecules (in direct contact to the electrode) adsorb flat at the Au(111) surface where the unpolar alkyl tails point towards each other, while the head groups arrange in a $\sqrt{3} \times \sqrt{7}$ structure stabilized by bridging water molecules adsorbed at the surface[50], similar to the well-known sulfate structure on Au(111)[52]. At a larger coverage (electrochemically induced by increasing the potential and thus the surface charge) a condensed, disordered bilayer is formed at a surface charge of 40 $\mu C/cm^2$, a total layer charge of 77 $\mu C/cm^2$ and a thickness of 1.98 – 21.3 nm, showing that the layer has to be interdigitated with the sulfate groups pointing towards the electrode and the bulk electrolyte[4]. Concerning alkylthiol (AT) at low coverages a row-like structure was observed with periodicity of $\sqrt{3} \times p$ with p as an integer factor multiplied by the Au(111) lattice constant of 0.288 nm. [53] For higher coverages the $(\sqrt{3} \times \sqrt{3})R30°$ structure is typically observed[54]. This phase is also called “standing up” phase as the alkyl tails are pointing towards the bulk electrolyte with a typical angle of 30° to the surface normal. By physically removing the SDS with a STM tip the authors of [51] were even able to establish Cu nanostructures at the surface of Au(111), similar to Cu deposition at Pt(111) after removal of adsorbed ethane [55] and tip induced nanostructuring [56, 57]. However, up to the present study the adsorption behavior of alkylsulfonates on Au(111) remained unexamined as well as the friction behavior on SDS*. Thus this study investigates

SDS* modified Au(111) electrodes in 0.1 M H_2SO_4. We will demonstrate, that SDS* molecules adsorb horizontally on the electrode at low coverage and undergo a phase transition as a positive potential is applied to the electrode similar to SDS and also phospholipides[58]. The thus formed phase shows an increased thickness compared to the other state indicating the formation of a “standing up” phase similar to both the SDS and the AT case. In this study we will address the differences between SDS* and SDS/AT concerning voltammetry structure and friction. The approach to investigate friction in the present study is similar to the approach in ref. [59], where also a frictional transition was observed for pyridine on the Au(111) surface. The friction behavior in diluted H_2SO_4 was already investigated in detail with respect to the normal load and applied electrode potential[60] and furthermore during silver UPD [61]. This work is also motivated by the finding of layered structures in organic solvents.[62]

8.3 Experimental

In this study a Au(111) single crystalline electrode was used (1cm diameter; 0.785 cm^2 geometrical area). Before any experiment the Au electrode was cycled in 0.1 M H_2SO_4 before it was annealed by flame. After cooling down above Ar-saturated Milli-Q water in Ar atmosphere a water droplet was attached to the electrode and the electrode was transferred to the H-cell. Then it was checked weather the electrode shows the well-known voltammogram or not. If further cleaning was required, the electrode was electrochemically oxidized in 0.5 M H_2SO_4 at 10V until a red layer of gold oxide covered the surface. Afterwards, the gold oxide was removed chemically in hydrochloric acid. After the cleaning the electrode was cycled again. This procedure was repeated until the voltammogram showed the well-known shape.

Cleaning:

The H-cell was cleaned in chromic acid (at least 1 hour placed in a chromic acid bath), extensively rinsed with Milli-Q water and afterwards the working electrode compartment was rinsed with the target electrolyte once directly before the experiment. The AFM cell with the corresponding reference and counter electrodes was cleaned by first boiling 0.1 M H_2SO_4 and boiling Milli-Q water afterwards.

Chemicals:

Sodium dodecylsulfonate ($Na(C_{12}H_{25})SO_3$, 99%, Acros Organics), sulfuric acid (H_2SO_4, 95-97%, EMSURE). For purging and electrolyte saturation argon (99.999%, Air liquide) and oxygen (99.9995%, Air liquide) were used. The gases were mixed and the flow was controlled via electronic flow meters (F-201C-UA-22-V, Bronkhorst, MFT-V12C Union Carbide), while the flow meters were calibrated for the specific gases.

Setup:

The experiments were conducted in either an H-Cell using a *PINE* Bipotentiostat, or in a homemade AFM cell (Note: The conversion factor between the Pt|PtO reference used in the AFM cell and the RHE used in the H-cell was typically 0.935 V). The AFM is an Agilent 5500 AFM, which is combined with a glass chamber (the chamber was purged with Ar). As Tips we used silicon tips (PPP-FM (hard cantilever) / PPP-CONTSC (soft cantilever), NANOSENSORS) with a tip radius below 10 nm. The normal force constants (typically: hard cantilever ≈ 1.5 N/m and soft cantilever ≈ 0.05 N/m) and lateral force constants (typically: hard cantilever ≈ 50 N/m and soft cantilever ≈ 5 N/m) were determined via measuring the normal and torsional resonance frequency and proceeding with the Sader method [38, 39]. The lateral force constant is obtained by dividing the torsional force constant by the square of the distance between tip apex and the centre of rotation (usually this distance equals $\text{"tip height"} + 0.5 * \text{"cantilever thickness"}$). Images were usually corrected by a global or local plane.

8.4 Results and Discussion

Voltammetry

Starting with the voltammetry of 1 mM SDS* in 0.1 M H_2SO_4 (see Figure 29) in anodic direction (electrode contact established at open circuit), one observes a peak (A1’) close to 0.8 V vs RHE. The peak is followed by a shoulder before current density (j) increases again to a smaller peak around 1.1 V vs RHE. In subsequent cycles A1’ shifts negative (A1) and shows decreased peak current density (j_{peak}) in the second cycle before j_{peak} of A1 increases during subsequent cycles. During and after the second cycle a further peak in j appeared (A2) which might correspond to the shoulder positive of A1’. In cathodic direction C1’ is visible in the first cycle, while in subsequent cycles C1’ is split into C1 and C2 similar to A1’, albeit with a negligible potential shift.

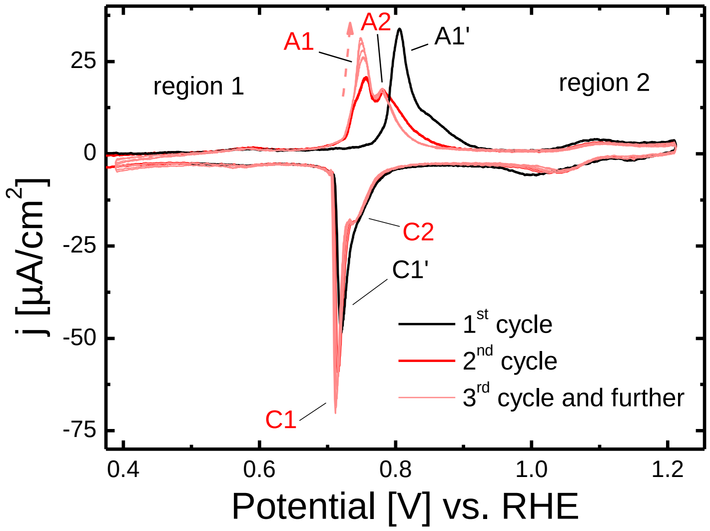

Figure 29 The voltammetry of 1 mM SDS* in 0.1 M H_2SO_4 on Au(111) at 50mV/s vs RHE as reference electrode (RE) and with a gold sheet as counter electrode (CE). The electrolyte was Ar-saturated. The first recorded cycle after contacting the electrode (at potentials negative of A1) to the electrolyte (black) and the subsequent cycles (red) are shown. Peaks in anodic and cathodic direction are marked. Region 1 corresponds to potentials negative of A1/A1' and C1/C1' respectively and region 2 corresponds to potentials positive of A1/A1' and C1/C1'. The red arrow indicates the evolution of A1 with time.

It is noteworthy that the voltammetry strongly deviates from the voltammetry of Au(111) in 0.1 M H_2SO_4 (see Figure 41), as this indicates the specific adsorption of the sulfonate on Au(111). The voltammetry to some extent is similar to the observations on Au(111) in SDS containing 0.1 M H_2SO_4 [51]. In this reference, the authors show a similar anodic peak shift to negative potentials upon cycling. They ascribe the anodic peak (from 2nd cycle on) to the transition of a hemimicellar adsorbed SDS film to a condensed SDS film (actually a disordered bilayer) as it was already earlier observed in ref [50]. The shift then was explained by the transition of a randomly oriented SDS adsorbate in the first cycle in region 1 to a hemimicellar state in region 1 for all subsequent cycles, which stabilizes the unreconstructed surface. The increase in A1 with increasing cycle number in consequence might be due to the continuous ordering of the layer formed in region 1 (assuming a phase transition rather than adsorption at the bare electrode). Structural investigations will show such a behavior also for the SDS* later on in this study. Note that in a window opening experiment in both anodic and cathodic direction one observes, that a rise in A1 gives rise to C1, a rise in A2 gives rise to C2 and vice versa (see Figure 43).

To further investigate the processes in A1', A1, A2 and the corresponding cathodic peaks, charges were calculated and are shown in Table 3.

Table 3 shows the charges evaluated for A1 + A2 (Q_{A1+A2}) and C1 + C2 (Q_{C1+C2}).

cycle	Q_{A1+A2} [µC/cm^2]	Q_{C1+C2} [µC/cm^2]
1	32.9	26.9
2	30.0	28.3
3	29.6	28.1
4	30.0	29.0
5	30.5	28.7
6	30.4	28.7

Regarding Table 3 the charges in A1‘+shoulder, A1+A2 and the corresponding cathodic charges show values around 30 µC/cm^2. The charges in anodic direction are slightly larger compared to the cathodic charges which might be due to imperfections in the integration limits. The anodic charge in the first cycle seems further to be slightly larger compared to the subsequent cycles and the cathodic charge during the first cycle is smaller compared to the subsequent cycles. The average charge however is far below the value for a 1 to 1 adsorption of SDS* per Au(111) surface atom (222µC/cm^2) [63]. The value is furthermore below the values for $\sqrt{3} \text{ x } \sqrt{3}$ and $\sqrt{3} \text{ x } \sqrt{7}$ structures. This indicates a phase transition of an adsorbed species or the adsorption of a less dense layer compared to $\sqrt{3} \text{ x } \sqrt{7}$ sulfate adsorption. In [4], the authors found a charge density of 40 µC/cm^2 for the condensed SDS layer. They furthermore found (via neutron reflectivity experiments) a total layer charge of -77 µC/cm^2 and suggested a condensed bilayer in region 2. In a further publication [3] it was found that the bilayer structure is not commensurate. In case of linear akylthiols the $\sqrt{3} \text{ x } \sqrt{3}$ structure is the high density structure [54], while the density of the structure decreases with storage time in UHV [53]. In ref [53] the authors found a low density row like structure for alkylthiols. Thus concerning the SDS*, a phase transition of the SDS*-adsorbate from a less dense to a more dense state seems plausible and will be discussed later in this study. The presence of a surface limited process is further confirmed by the independence of peak current on sweep rate (see Figure 44).

Structure

To get further insights into the actual adsorption behavior of SDS* on the electrode with respect to the electrodes potential, the electrode surface was investigated in-situ via AFM.

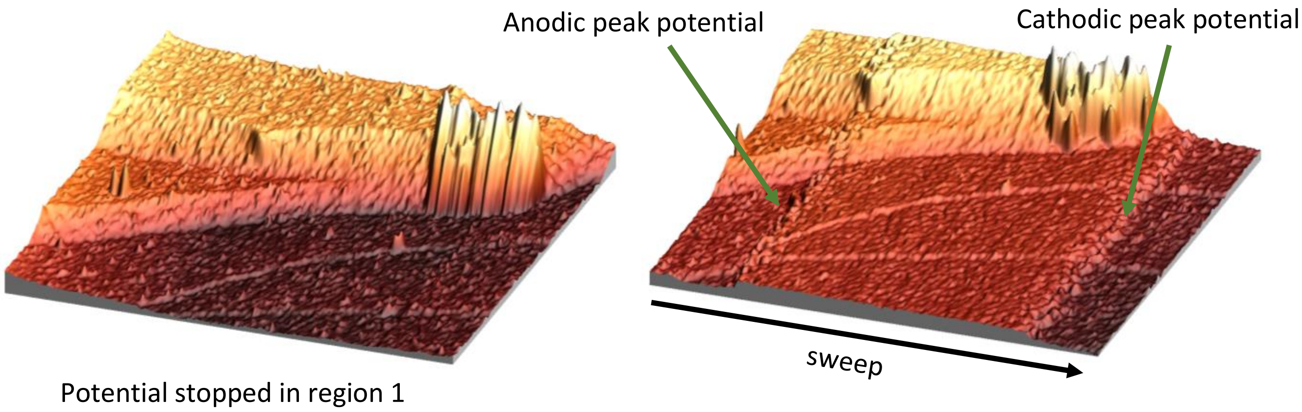

Figure 30 shows 1 × 1 µm large topographic 3D AFM images of the Au(111) electrode in 1 mM SDS* containing 0.1 M H_2SO_4 in region 1 at -0.340 V vs Pt|PtO, using a soft cantilever with k_{lat} = 7.4 N/m and k_{normal} = 0.05 N/m (left side) and during a potential sweep (right side). The green arrows indicate the potential of A1 and C1. Tip velocity was 22.4 nm/s, normal load was close to 0.5 nN. Potential limits for the sweep were -0.380 V (0.555 V) and 0.175 V (1.110 V) vs. Pt|PtO (vs. RHE. The anodic peak potential was at -0.168 V and the cathodic peak potential at -0.222 V both vs. Pt|PtO.

The left side of Figure 30 shows a topographic image of the Au(111) electrode in 1 mM SDS* containing 0.1 M H_2SO_4 and serves as reference to compare it to an image, where the potential was swept. In the right image a height increase is clearly visible as the potential passes the anodic peak potential (A1+A2), which is followed by a height decrease as the potential passes the cathodic peak potential (C1+C2). This might indicate the adsorption of SDS on the electrode surface or it indicates the transition from a flat adsorption state to a condensed state as observed for SDS [4, 50, 51]. Note that the slight tilt of the image is due to the local plane correction of the images, as defects/steps are present in the images. These defects/steps serve as marker to prove, that the position of the scan did not change significantly.

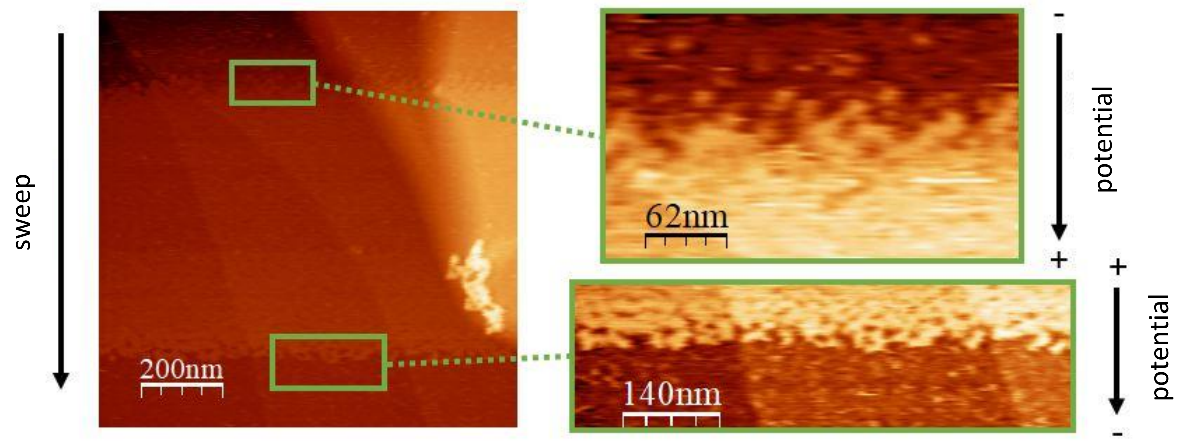

Figure 31 shows a 2D version of the right image of Figure 30. Both images on the right side are magnifications of the regions, where the potential passes the anodic and cathodic peak. The corresponding friction images are shown in Figure 49.

Figure 31 provides a closer look at what happens as the potential passes the anodic and cathodic peak potentials. In both cases, the formation of an increasing number of domains are visible, which ultimately collapse; obviously both states are present during the transition. The height change for a normal load of close to 0 nN is in the range of 1.5 nm. This indicates the formation of a layer (or interdigitated bilayer) of vertically oriented SDS* molecules similar to the SDS and AT cases [4, 50, 51] [54], where the authors observed a transition from a flat adsorption state (actually hemimicells in case of SDS) to a state, where the molecules are oriented vertically. Due to the hemimicellar phase for SDS, the height in that case changed only by 0.6 nm [4]. To further investigate the structure, we recorded topographic images and friction images at very low normal loads.

In region 1 we observed a periodicity at a length of b = 1.94 nm in one direction and a periodicity of a = 0.39 nm in the other direction, while the vectors are split by α = 71° (see Figure 32 a-c). This hints one flat adsorbed SDS* molecule per cell. Under the reasonable assumption of one transferred electron per SDS* molecule this leads to a charge density of 22.5 µC/cm^2. At this point we can exclude that A1 + A2 refers to an adsorption of SDS on the bare Au(111) electrode. Note, that for the SDS* case we didn’t observe hemimicells in region 1 in contrast to observations for SDS [4, 50], though for both, the SDS case[51] and the SDS* case the critical micellar concentration (cmc) was not attained referring to the cmc in pure water (SDS: 8.36 mM and SDS*: 10.75 mM, both at 298.15K)[64]. But we observe a row like structure similar to alkylthiols at low coverage on Au(111) [53]. This might refer to a stabilizing effect of water molecules in the $\sqrt{3} \times \sqrt{7}$ orientation in case of the SDS [50]. Figure 32 shows a different situation for the SDS* case. The missing, bridging oxygen atom between the sulfur atom and the carbon atom, seems to lead to a different local structure, so that the stabilizing effect vanishes.

We could not clearly identify the structure with respect to the Au(111) surface, we observed three preferable directions of the rows with a 120° angle (two of these three orientations are visible in Figure 32a) between the three orientations. The distance between two alkyltails along the row is 0.39 nm $\approx \frac{\sqrt{7}}{2} * a_{Au(111)}$.

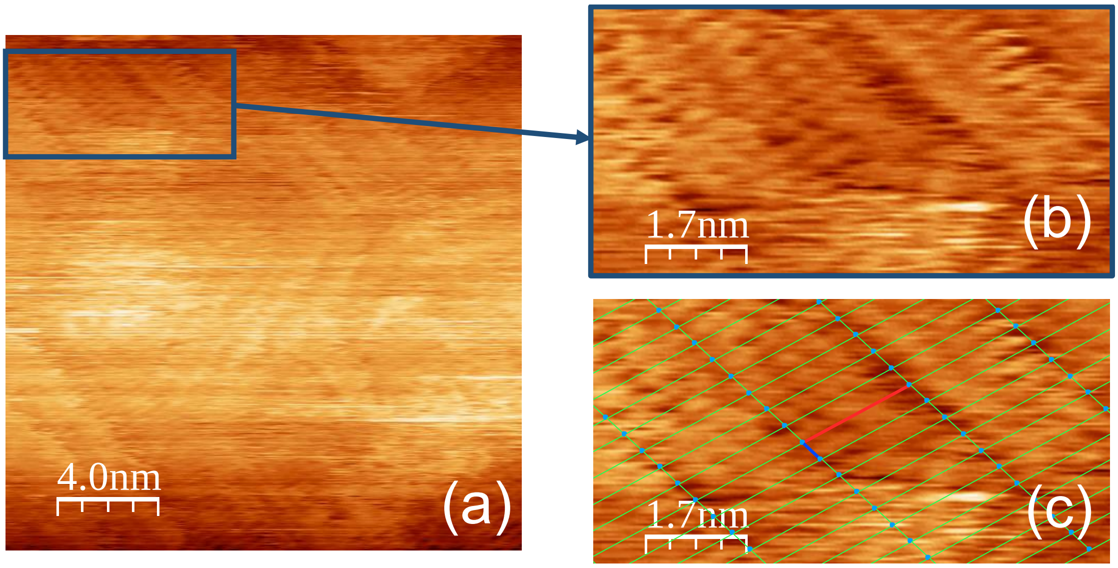

Figure 32 shows a 20 × 20 nm large topographic image (a) of the SDS* modified Au(111) surface in 1 mM SDS* containing 0.1M H_2SO_4 at E= -370 mV vs Pt|PtO (region 1). The image was recorded at a tip velocity of 0.45 nm/s and a normal load of close to 0 nN. (b) shows a magnification as indicated by the blue arrow and widnow. (c) shows the lattice suggested for the observed row-like structure. A soft cantilever was used.

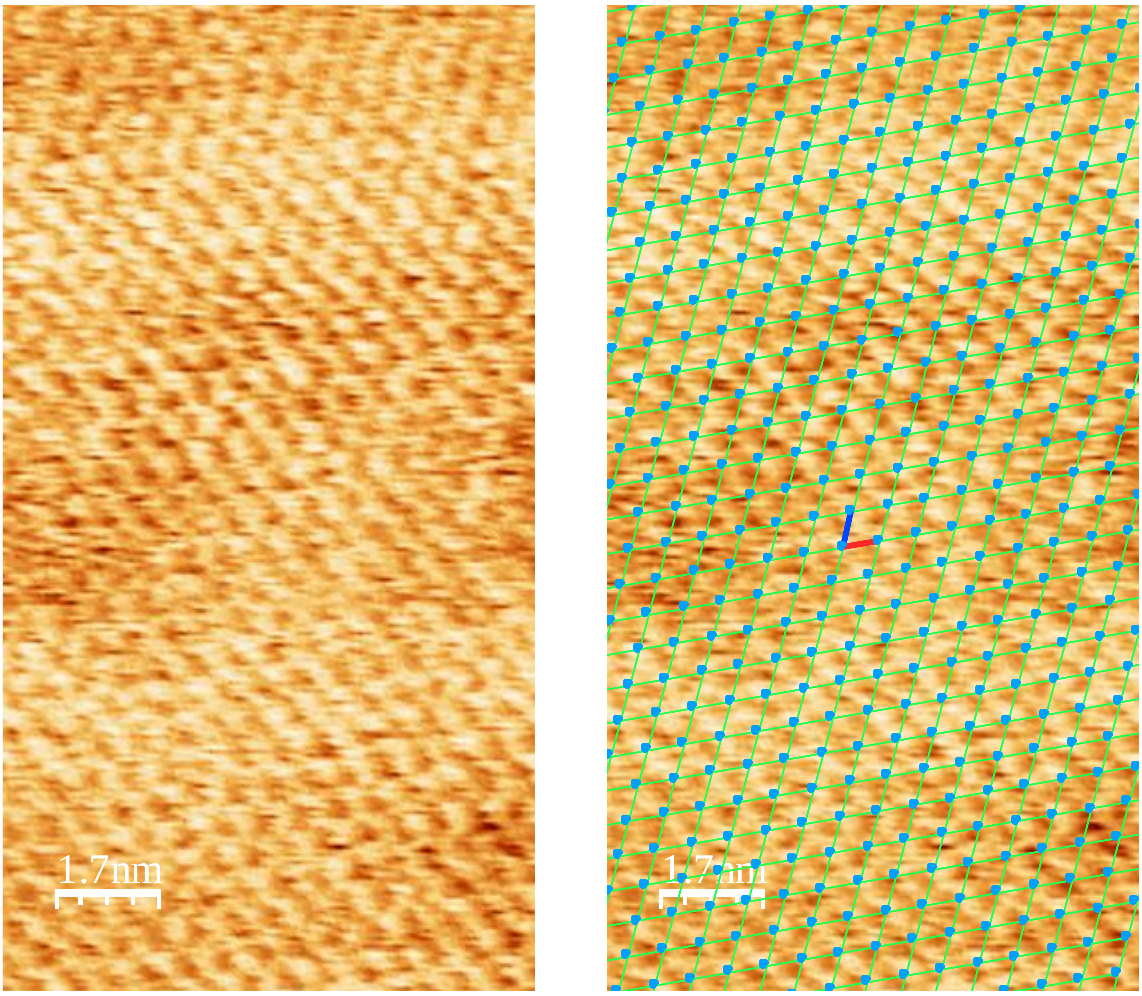

Figure 33 shows a part of an actual 30 × 30 nm friction image (see Figure 45), where the potential was swept similar to Figure 30. Only the part, where the condensed layer is present is shown. The tip velocity was 0.67 nm/s and the normal load was approximately 0 nN. In the right part of the figure a unit cell was included. Vector a = blue vector b = red angle between a and b ≈ 64.9°. A soft cantilever was used. Potential was stopped at 0.1 V vs Pt|PtO, k_{lat} = 7.4 N/m and k_{normal} = 0.05 N/m.

Figure 33 shows the structure of the condensed layer (region 2), which proved to be stable up to a normal load of 2 nN. The unit cell has values of a = 0.57, b = 0.58 and α = 65.2° (indicating a 2 × 2 structure). Assuming again one molecule per unit cell, a charge density of 53.8 $\mu C/cm^2$ is calculated assuming again a single charge transfer per unit cell. Subtracting the charge density in region 1 from the charge density in region 2 leads to a value of 31.4 $\mu C/cm^2$, which fits to the observed charge density of A1+A2 and C1+C2 in Table 3. Combining this with the thickness increase during A1+A2, we conclude, that in the SDS* case during A1+A2 the flat adsorbed SDS* molecules orient vertically, allowing further SDS* adsorption until a condensed layer is formed. To get further insights, the image was FFT filtered, selecting the brightest signals (see Figure 47).

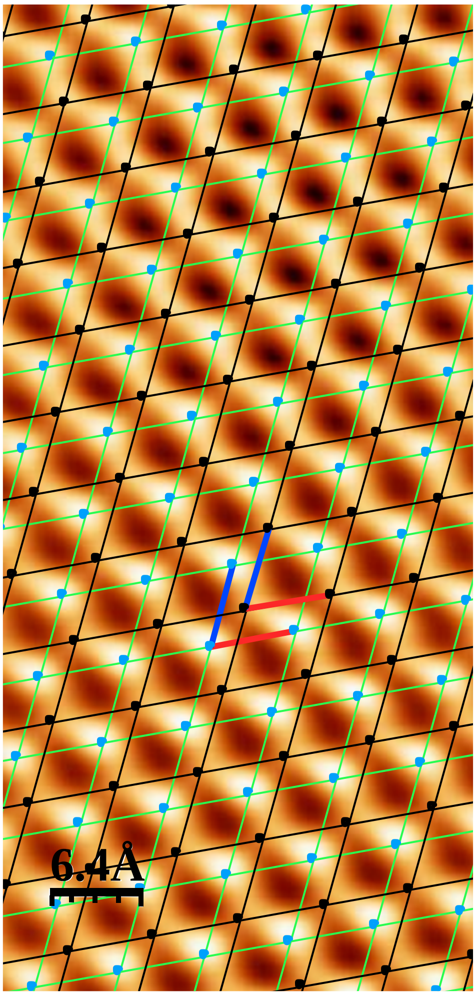

Figure 34 shows an FFT filtered version of a part of Figure 33. The green cells denote the actual unit cell and the black cells denote the signals referring to the SDS* layer directly attached to the electrode.

Figure 34 shows an FFT filtered part of Figure 33 (magnified). The image shows, that an additional signal with lower intensity (as indicated by the black cells) is observed within the unit cell (green cell), showing the same periodicity as the main signals. This suggests two possibilities, which have to be addressed. First of all, this might indicate that the observed structure actually is a honeycomb structure. However this can be quickly excluded, as a honeycomb structure with the observed distances, an adsorption of SDS* via the three oxygen atoms on the gold surface would result in huge repulsive forces as the sulfonate head groups would have to be packed extremely dense (0.33 nm distance, which is below the size of a sulfate ion). The next possibility is the formation of a bilayer as for the SDS case. Then this observation would just show the end of the alkyltail of the SDS* molecule adsorbed at the Au(111) surface, which in consequence means, that the brighter signals refer to the layer, countering the adsorbed layer. Another explanation assuming the formation of a bilayer is given in Figure 35, ascribing the observation of the other signal to a fixed sulfonate group, where the oxygen atoms show honey comb orientation.

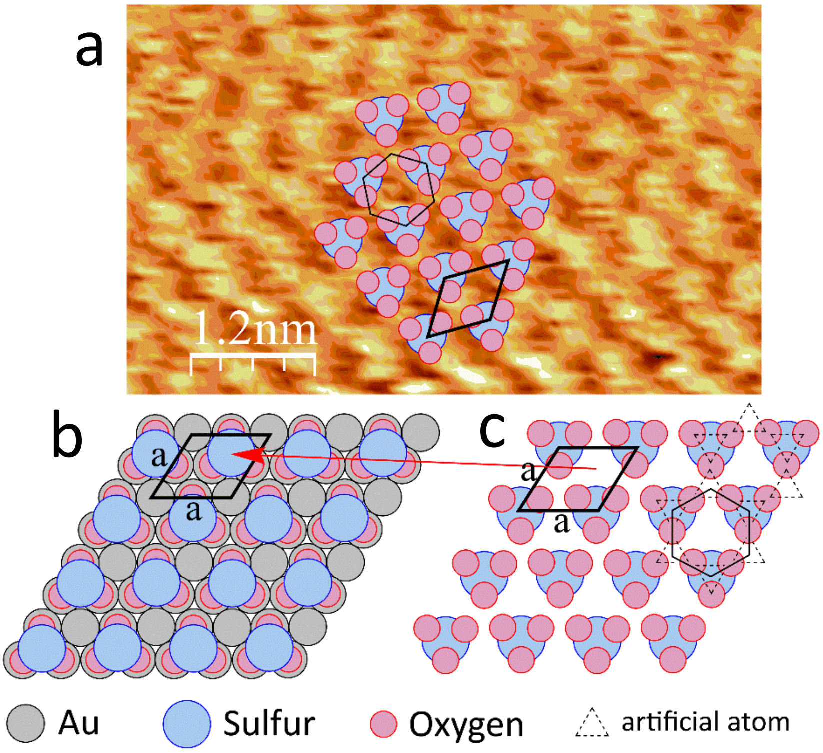

Figure 35 shows the suggested structure for the condensed SDS* bilayer. Note that for clarity the alkyl chain connected to the sulfur atom is not shown. The AFM friction image (a) is a small section of Figure 33. The structure inset in (a) resembles the structure of the counter layer (c). It is furthermore shown the layer directly adsorbed on the electrode (b) and the counter layer (c). A soft cantilever was used.

Figure 35 shows a structural suggestion (2 × 2 structure) for the SDS* condensed bilayer. In Figure 35a a small section of Figure 33 is shown with the inset showing the SDS* counterlayer, as it is the counterlayer where the tip scans over. The sulfur atoms form a hexagonal lattice with a lattice constant corresponding to twice the lattice constant of the Au(111) structure. This effectively results in a ratio of 1 SDS* molecule per 4 Au surface atoms regarding the adsorbed SDS layer, while accounting for the counterlayer this ratio will increase to 2 SDS* molecules per 4 Au surface atoms. The suggested formation of the bilayer further explains the observation of voids in Figure 33 - Figure 35. However, the alkylchains have to be closely packed assuming the formation of the bilayer, as referring to the observed lattice constant the inter-chain distance is in the range of 0.33 nm. To further investigate the formed layer, the dependence of layer height for the condensed layer was investigated with respect to the applied normal load.

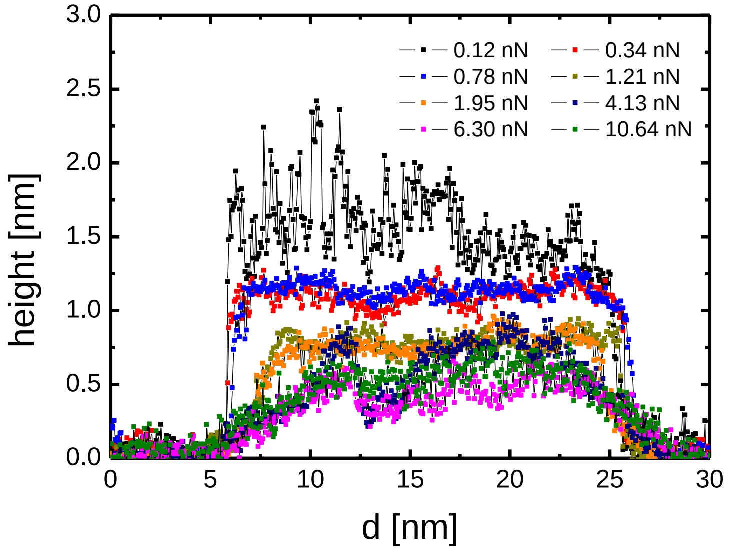

Figure 36 shows a line in y direction of topographic images (30 × 30 nm) at several normal loads during a potential scan. The scan direction was along the y direction of the image, which is the x axis in this plot. The tip velocity was 0.67 nm/s, k_{lat} = 7.4 N/m and k_{normal} = 0.05 N/m. A soft cantilever was used. The potential window can be seen in Figure 37.

Figure 36 shows the measured height of the condensed layer (with respect to the height of the flat layer) during a sweep for several normal loads. The measured height corresponds to the relative layer thickness of the condensed layer with respect to the flat adsorbed state. The height thus is lower than the actual distance from the Au surface to the upper edge of the layer. The Thickness of the condensed layer thus equals approximately 1.9-2.1 nm assuming that the layer is not desorbed but compressed to a thickness of approximately 0.4 nm referring to the inter chain distance regarding the flat state (the thickness of the condensed is similar to the SDS case[4]). A similar thickness is observed in the force separation curve (see Figure 46), where furthermore a similar stability up to 2 nN normal load could be observed sometimes. Figure 36 additionally shows that the condensed layer can be compressed by the cantilever. Note that at normal forces above 4 nN, the tip became unstable, which might result in deviations of the force constant.

Now the question arises, if a normal layer could achieve the observed thickness, especially as a 2 × 2 layer should result in a strong tilt of the SDS* molecules to obtain a dense packing similar to alkanethiols in $\sqrt{3} \times \sqrt{3}$ structure[54]. Using the data from [50] the length of a SDS* molecule is estimated to be approximately 1.68 nm, which is slightly less than the observed thickness. However, as we account for a typical tilt of 30-40° normal to the surface for a single layer, this would lead to a thickness of 1.29-1.45 nm. As we rather underestimated the measured thickness of the layer (we could not apply truly 0 nN), this strongly hints the formation of a bilayer.

Friction

The friction was investigated with respect to the electrode potential and applied normal load.

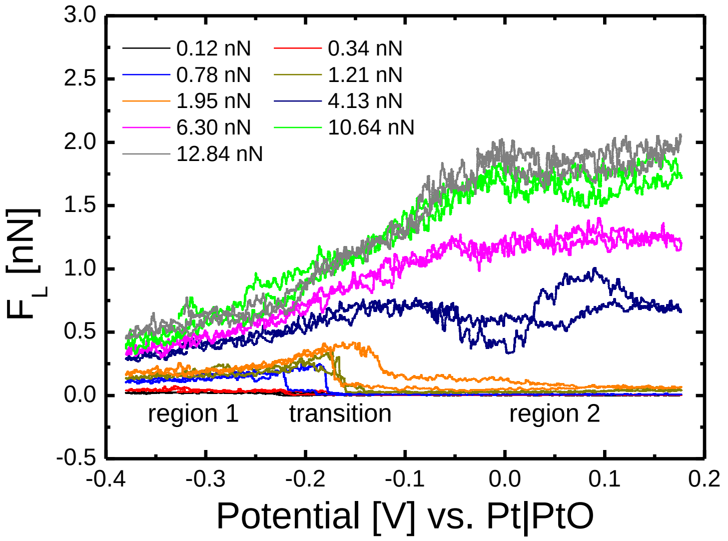

Figure 37 shows the friction force vs the applied electrode potential during a voltammetric scan. This image corresponds to Figure 36 and thus has the same conditions.

Figure 37 shows the friction force with respect to the applied electrode potential and normal load. Note that the hysteresis in the curves (e.g. orange curve) is a result of the hysteresis of the voltammetric peaks (the anodic peak is more positive). Overall the friction force increases with increasing normal load. For normal loads up to 2 nN the friction force in region 1 is larger compared to region 2. This goes in hand with the observation of a well ordered structure in region 2 at low normal loads. The tip thus follows the corrugation without larger energy dissipation. This seems to be different in region 1 (indicating that the adsorbate is more easily distorted by the tip in region 1). During the transition at low normal loads, the friction force rises to a maximum. We assign this to the restructuring of the adsorbate layer, as the structural disorder during the transition from flat to condensed state causes additional dissipation. At normal loads above 2 nN the condensed layer is distorted and is expected to be penetrated by the tip (at least partially, see Figure 36). This causes an increase in friction force, thus increasing the friction force in region 2 above the friction force observed in region 1. Also the maximum in friction force during the transition vanishes at larger normal loads as the magnitude of dissipation is dominated by the contribution of the condensed layer to the surface coverage. Thus as during the transition only domains are formed (see Figure 31), which increase in size with increasing potential, we would expect a continuous increase in friction force with increasing potential until the condensed layer is complete. The wave shape for a normal load 4.13 nN in Figure 37 might be due to the fact that 4 nN is barely sufficient to penetrate or strongly distort the condensed layer.

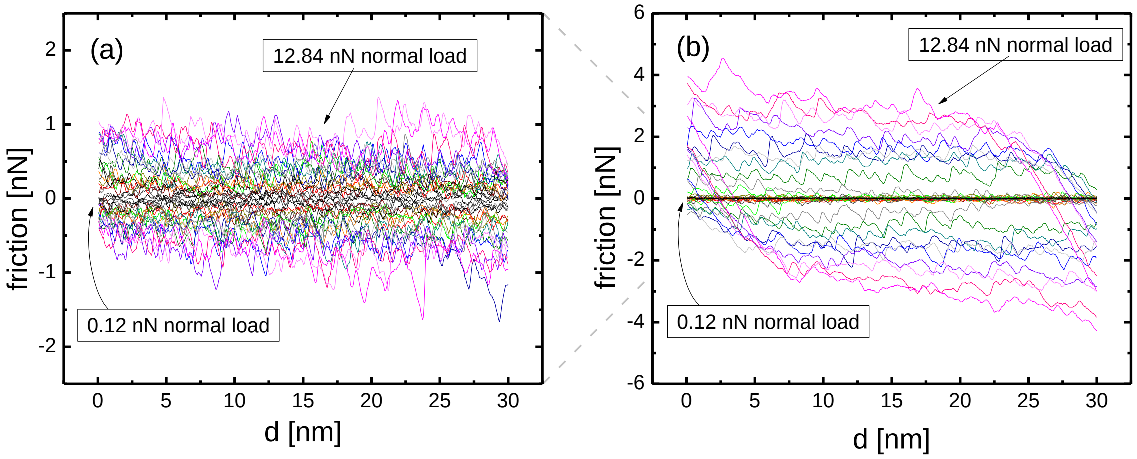

Figure 38 shows the friction loops for increasing and decreasing normal load in region 1 at -0.370 V vs. Pt|PtO (a) and region 2 at 0.170 V vs. Pt|PtO (b). This figure corresponds to Figure 36 and Figure 37 and thus has the same conditions.

Figure 38 shows the friction loops for increasing normal loads in region 1 (Figure 38a) and region 2 (Figure 38b). The overall friction is larger for region 2 compared to region 1 at normal loads above 2 nN and lower for normal loads below 2 nN, which is in good agreement with the observations in Figure 37. In region 2 one observes a slope over several nm for normal loads large enough to distort/penetrate the condensed layer. This slope seems to be constant (at least very similar) for all normal loads, where it is observed. The slope amounts to 0.45 N/m and thus is one magnitude smaller than the expected lateral force constant of the cantilever (7.39 N/m obtained from calibration) and of the effective force constant for the atomic corrugation on I-modified Au(111) (4.36 N/m) [65]. This indicates that the observed slope of 0.45 N/m refers to an effective force constant (k_{eff}), which is dominated by a process with a lower force constant:

$$k_{\mathrm{eff}} = \left(\frac{1}{k_{\mathrm{L}}} + \frac{1}{k_{\mathrm{L}}^{\#}}\right)^{-1} \tag{33}$$

Where $k_{\mathrm{L}}^{\#}$ is the force constant of the additional “spring”. As k_{L} and k_{eff} are known, this additional force constant can be calculated via:

$$k_{\mathrm{L}}^{\#} = \left(\frac{1}{k_{\mathrm{eff}}} - \frac{1}{k_{\mathrm{L}}}\right)^{-1} \tag{34}$$

Thus giving a value of 0.48 N/m. However, as soon as the tip starts to slide over the surface, this effect vanishes and thus indicates a connection to the tip back bending after reversion of the scan direction. With the total distance the tip moved until it starts to slide (d_{s}), the “compression” (d_{add}) of the additional spring (meaning the additional distance that the tip moved without deflection) is obtained via:

$$d_{\mathrm{add}} = \frac{d_{\mathrm{s}}}{1 + \frac{k_{\mathrm{L}}^{\#}}{k_{\mathrm{L}}}} \tag{35}$$

Note that equation (35) is derived from the connection of springs in series (equal force at each spring).

Thus d_{add} is calculated to be 4 nm. This distance is in the range of twice the length of a streched SDS* molecule and might thus correspond to the layer being compressed and stretched parallel to the surface upon reverting the scan direction before the tip starts to actually slide. (see Figure 39).

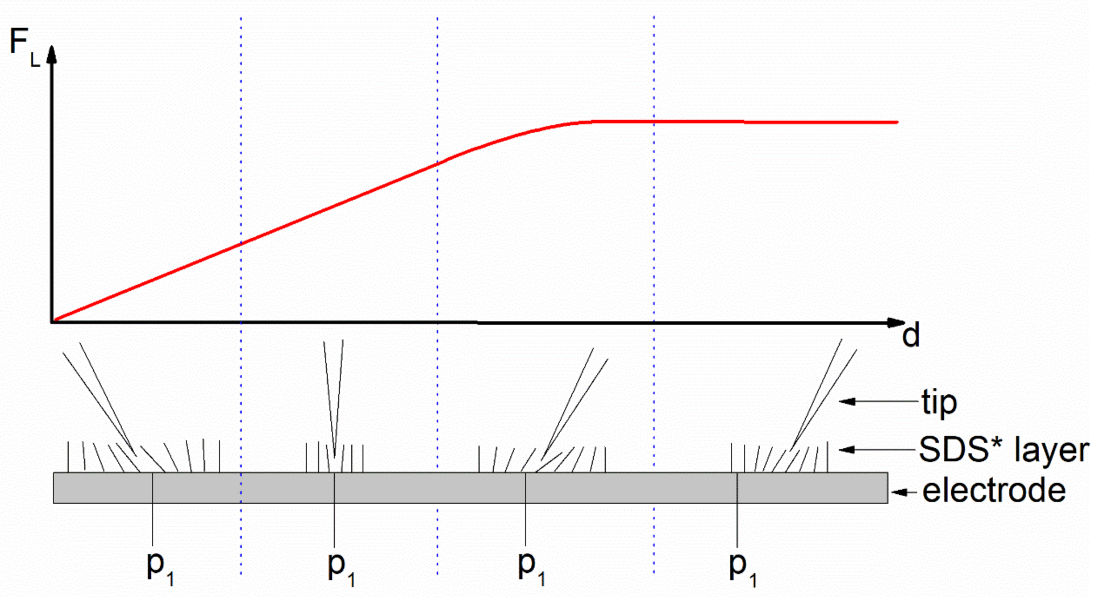

Figure 39 show a schematic for the suggested mechanism that causes the observations in Figure 38. p_1 denotes a fixed point at the electrode surface (acting as reference point in this schematic). Shown is the bending of the tip and the lateral compression of the SDS* layer while initiating a change in slide direction.

Figure 39 shows a schematic for the underlying mechanism of the observations in Figure 38. Initially the tip is tilted to the left from the previous scan into the left direction. Upon moving to the right side the tip is bend to neutral position and the lateral force is at 0 nN. Continuing further to the right, the tip is tilted to the right side until the SDS* is fully stretched. Then the tip starts to slide showing a seemingly constant friction force.

Assuming the tilting of the layer being the cause of the additional “spring” is furthermore reasonable as the slope is only observed for the case, where the SDS* molecules are oriented vertically. Calculating $k_{\mathrm{L}}^{\#}$ from a similar experiment using a hard cantilever at ≈30 nN normal load (see Figure 40b and Figure 50) we obtained a value of 0.61 N/m, which is very similar to the soft cantilever. However, a moderate deviation is expected, as $k_{\mathrm{L}}^{\#}$ (if calculated like here) depends on the contact area of the tip front and the SDS* layer in sliding direction.

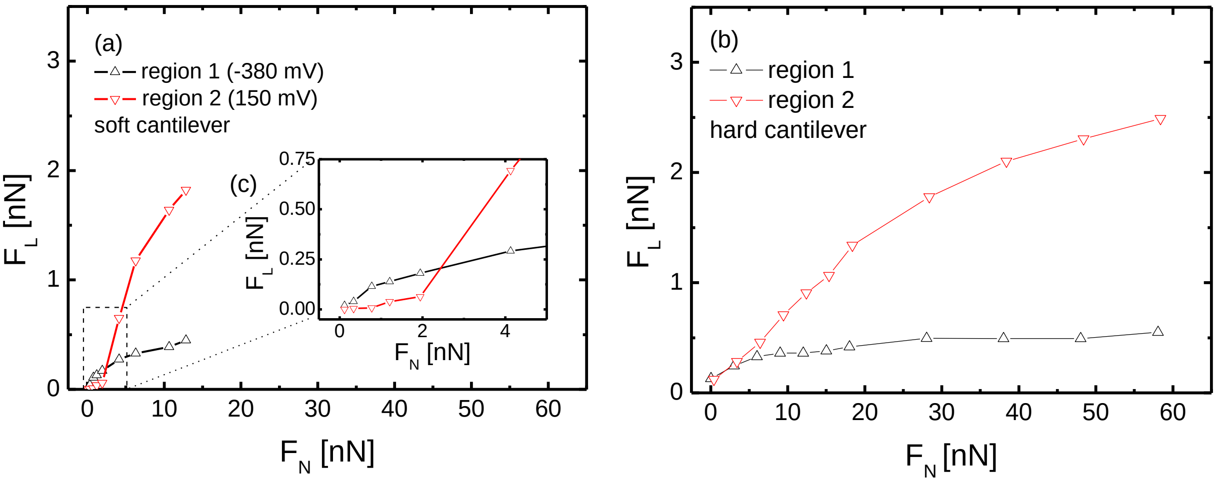

Figure 40 Friction vs normal load curves for a soft cantilever (a, k_{lat} = 7.4 N/m and k_{normal} = 0.05 N/m) and a hard cantilever (b, , k_{lat} = 22.3 N/m and k_{normal} = 1.6 N/m). The tip velocity for the corresponding 30 × 30 nm images was 0.67 nm/s. The applied potential in region 1 was -0.380 V vs. Pt|PtO and in region 2 0.150 V vs. Pt|PtO.

Figure 40 shows the plot of Friction force vs normal load for a soft cantilever (a) and for a hard cantilever (b). Regarding low normal loads, for both the soft and hard cantilever we observe that initially the friction is lower in region 2 compared to region 1. As the normal load increases and the tip penetrates or strongly distorts the condensed layer, we again observe that the friction in region 2 becomes larger than the friction in region 1. This we attribute to a lateral force offset, which is caused by either the continuous compression of the layer, or the continuous desorption of the adsorbed SDS* molecules (thus SDS* molecules will re-adsorb behind the tip), as the tip slides over the surface.

Using the hard cantilever, much higher normal loads were achievable, showing that the slope in region 2 decreases with increasing normal load (at higher normal loads, see Figure 40b). We actually went to even higher normal loads in a different experiment (see Figure 48), where we observed a plateau for high normal loads (above 100 nN). This indicates, that at a certain normal load the situation underneath the tip in region 1 and region 2 are similar, just with a different force offset in lateral direction. This means that the tip might have penetrated the layers completely in both cases and slides over the Au(111) surface, continuously desorbing the SDS* molecules at its front, while SDS* readsorbs behind the tip. This further means, that the dissipation would correlate to the stability of these to adsorption states (flat and condensed). Differences between hard and soft cantilevers in the lateral and normal force are certainly caused by slight differences in the contact area (sharpness of the tip).

8.5 Conclusion

In the context of this work it was found that SDS* forms a flat adsorbate phase (a = 0.39 nm; b = 1.94 nm; α = 71°), which results in a charge of 22.4 µC/cm^2. We suggest that the SDS* molecules are oriented in an interdigitated way to avoid strong repulsion of the polar head groups. The observation of a row-like structure rather indicates similarities to alkylthiols than alkylsulfates, which form hemimicells. Further studies are necessary to clarify the exact structure. The friction in this state was also investigated, showing a moderate increase in friction for increasing normal load at low normal loads. Above 6 nN normal load friction attained a plateau and shows an almost constant value of 0.5 nN up to the maximum measured normal load of 130 nN, which one might describe as super lubrication.

However, as a more positive potential is applied to the electrode, the SDS* molecules orient vertically, which allows for further SDS* molecules to adsorb. This is on the one hand visible as two peaks in a voltammogram (approximately 30 µC/cm^2 during the transition) and on the other hand as a height increase in topographic AFM images (approximately by 1.6 nm). During the transition domains of both phases were observed, which led to a maximum in friction at low normal loads, as the SDS* layer was disordered (domains of region1 and region 2 are present simultaneously) during the transition. Concerning the voltammetry, we cannot give an accurate explanation for the observation of two separated peaks, but we suggest that during A1 the SDS* molecules orient vertically to allow for a larger coverage. Then as a maximum in coverage for the resulting structure is attained, the SDS* layer reorganizes in A2 to form the structure observed in this study for region 2.

In region 2 the SDS* molecules form a condensed phase (a = 0.57; b = 0.58; a = 64.9°) with a surface charge of 53.8 µC/cm^2 determined from the structure. This is in good agreement with the charge observed for the transition (30 µC/cm^2 from voltammetry) added to the charge calculated from the structure in region 1 (22.4 µC/cm^2) giving 52.4 µC/cm^2. The lattice parameters of the observed structure further indicate a 2×2 structure. Regarding the measured height of the condensed layer, we suggest that the condensed layer is a bilayer. This would result in a very densely packed layer as the distance between the alkylchains (geometrically calculated) is 0.33 nm referring to a 2×2 structure. For low normal loads region 2 shows atomic corrugation and friction is close to 0 nN. As the tip start to penetrate/strongly distort the layer, friction increases and reaches a plateau above 100 nN normal load.

Overall this shows a very interesting behavior and further studies are necessary, as many questions remained unanswered. This work provides an idea of how alkylsulfonates adsorb on Au(111) surfaces in 0.1 M H_2SO_4 and how they change their structure as a positive electrode potential is applied.

8.6 Supporting Information

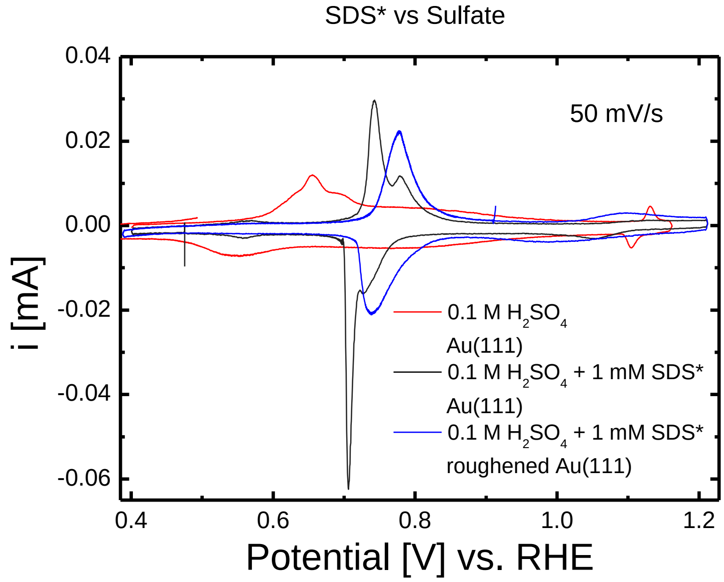

Figure 41 shows the voltammetric comparison of Au(111) in 0.1 M H_2SO_4 (red) and Au(111) in 1 mM SDS* containing H_2SO_4 (atomically smooth = black; roughened = blue) at 50 mV/s vs RHE. CE was a Au-sheet. The measurement was conducted in an H-cell. All electrolytes were Ar-saturated.

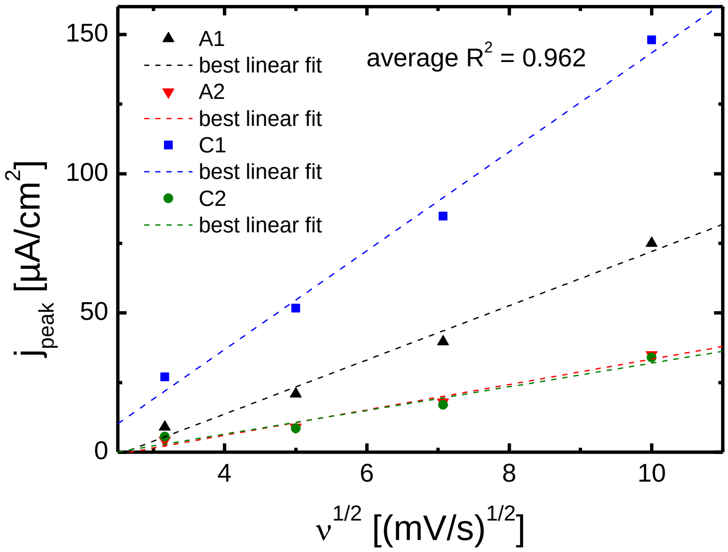

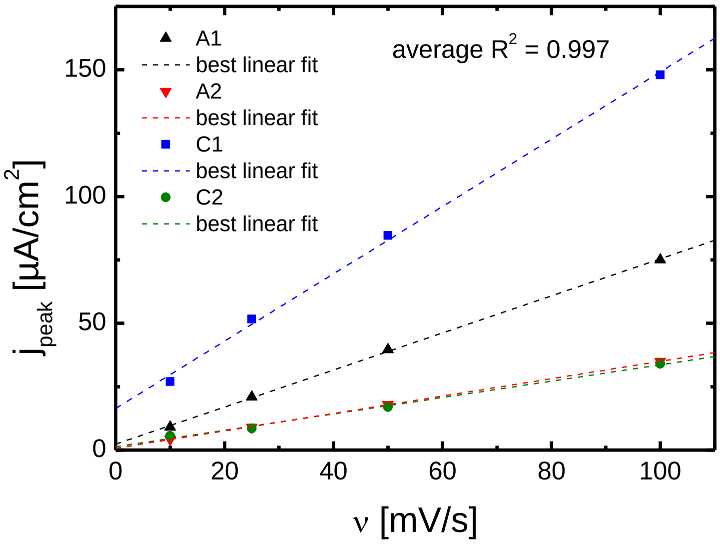

Figure 42 shows the voltammetric peak current dependence on sweep rate. Data is shown in triangles (for A1 and A2) squares (C1) and circles (C2). The dashed lines demonstrate the best linear fit and R^2 is the correlated error squared.

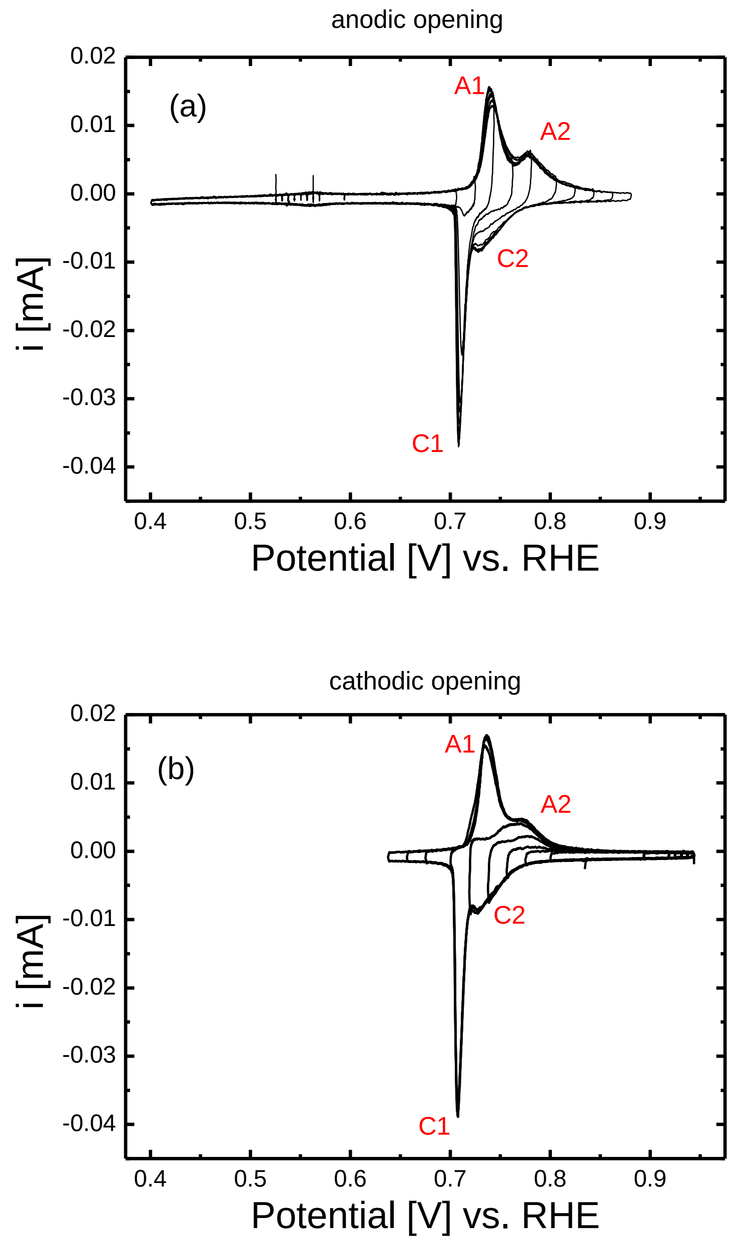

Figure 43 shows the voltammetry of 1 mM SDS* in 0.1 M H_2SO_4 on Au(111) at 50mV/s vs RHE as reference electrode (RE) and with a gold sheet as counter electrode (CE). The electrolyte was Ar-saturated. (a) shows the consecutive opening of the upper limit cycle by cycle. (b) shows the consecutive opening of the lower limit cycle by cycle.

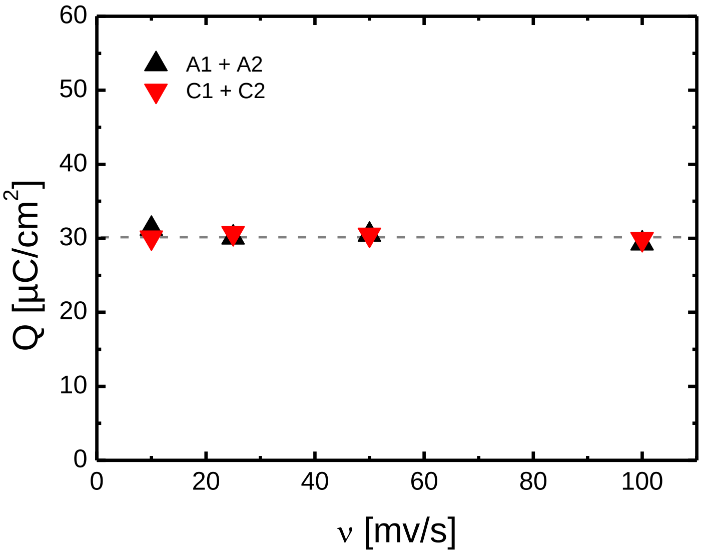

Figure 44 shows the charge density for several sweeprates calculated via integration of the peaks A1 + A2 and C1 + C2 from the voltammogramm.

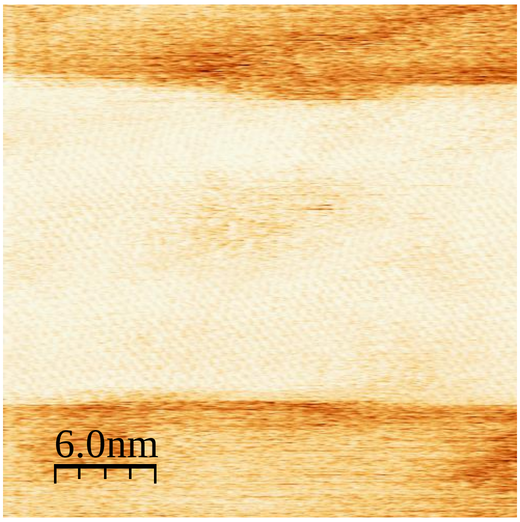

Figure 45 shows a friction image (trace) of a potential sweep (along y axis) for 1 mM SDS* containing 0.1 M H_2SO_4. The image shows from top to bottom the transition from the flat adsorbed phase to the condensed phase and back.

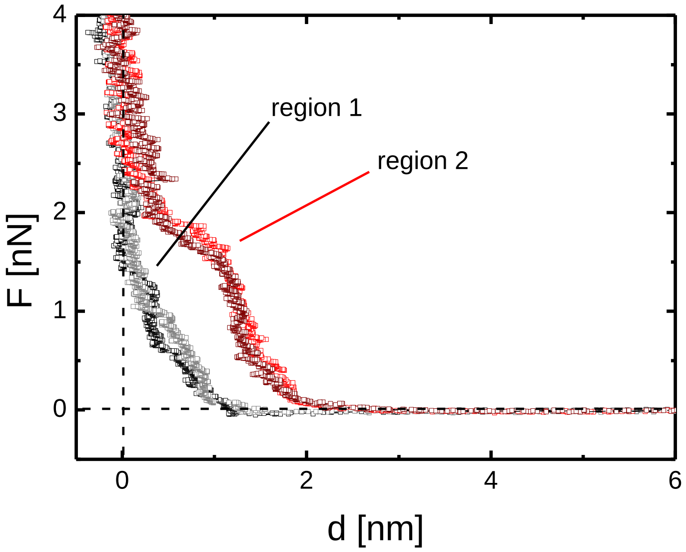

Figure 46 shows the force separation curve (approach) for region 1 (black, grey) and region 2 (red, brown) in 1 mM SDS* containing 0.1 M H_2SO_4.

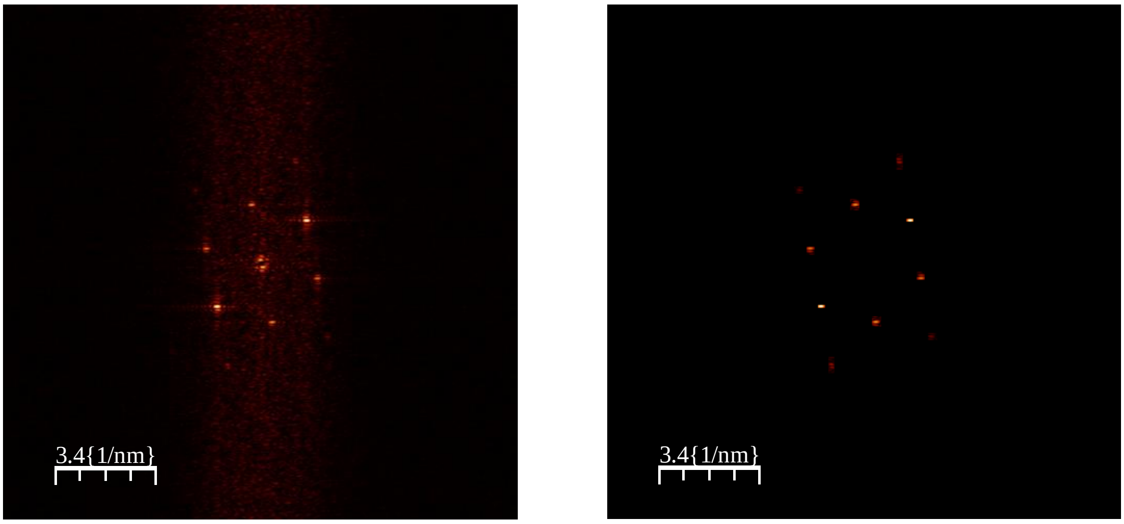

Figure 47 shows the FFT filtering and selection of the most dominant signals concerning the condensed layer structure observed in Figure 33.

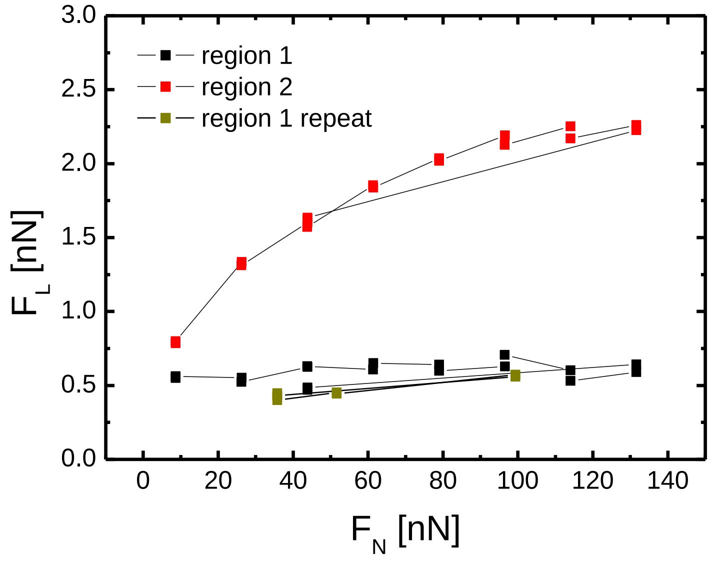

Figure 48 Friction vs normal load curves for a hard cantilever. The tip velocity for the corresponding 20 × 20 nm images was 0.45 nm/s, k_{lat} was 85.2 N/m and k_{normal} was 1.8 N/m.

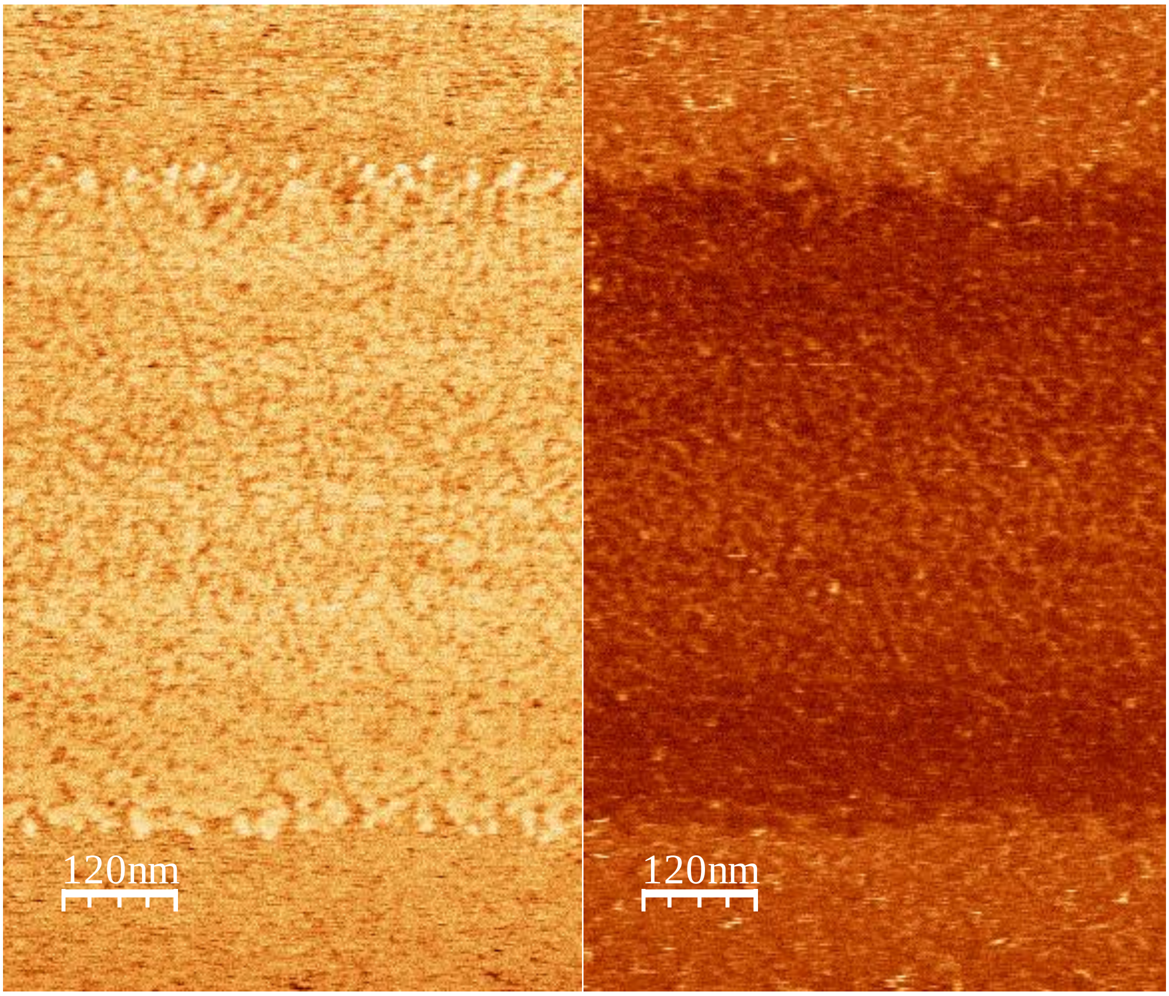

Figure 49 Friction images corresponding to Figure 30. Left side = trace and right side = retrace. The images here are cut on the right side and thus are missing the dominant feature of the image in Figure 30. This was done to increase contrast.

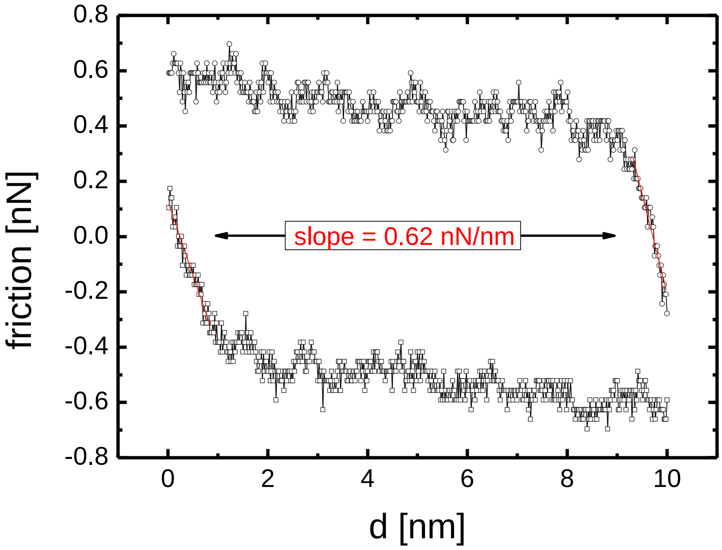

Figure 50 shows the friction loop for approximately 30 nN normal load in region 2 at 0.170 V vs. Pt|PtO (b). This figure corresponds to Figure 40b and thus has the same conditions.

9 Summary and Outlook

The novel cell

Electrochemical experiments often require a very specific framework of equipment, to achieve the necessary conditions. Furthermore some required compounds or materials are rarely found on the commercial market due to high production cost and thus suffer from high cost for the end user as well. In the context of this study a novel cell was developed (adapted from the thin layer cell[29]) to tackle the cost of expensive salts/electrolytes for the purpose of research. It was shown, that the novel cell showed good performance for a reversible model system in comparison to the frequently used and well-established H-cell. We have pointed out several advantages of the novel cell compared to the H-cell and already used the cell in the context of a BMBF project. The limits regarding experimental application of this cell are not reached yet and we recommend its use, especially for the case of costly solvent in salt electrolytes.

Solvent in salt electrolytes

Solvent in salt electrolytes in the battery context are of special interest, as the salt acts as an important, active species in this case. The cation of the salt as charge carrier is either being intercalated into the electrode material or plated/deposited on it upon charging of the battery. Thus increasing the concentration is a straight forward approach to decrease the content of inactive (note that the solvent often strongly influences the electrochemical reaction, which however is not meant with active in this context) material in the battery. A special case of a solvent in salt electrolyte is the hydrate melt, where H_2O acts as solvent. Water containing electrolytes often suffer from a low electrochemical potential window due to the electrochemical decomposition of H_2O (mainly hydrogen and oxygen evolution). In solvent in salt electrolytes, the concentration of the solvent is strongly decreased so that all (or at least most of) the solvent is bound to the cation and/or anion. This in consequence affects the stability of the solvent molecules.

This thesis dealt with the possible application of hydrate melt electrolytes in metal-O_2 batteries in the context of a BMBF project. Upon the investigations of a simple model system, several trends were found to contradict an application for these type of electrolytes in a battery context. It was found that the hydrate melt electrolyte's window of stability (electrochemical window) is too small in cathodic direction to allow for metal deposition. We actually found that with increasing salt concentration (effectively decreasing the water activity), the hydrogen evolution is shifted to more positive potential, opposing the desired trend. Obviously, the activity of the proton is increased due to coordination of the water to the cation. However, three solvent in salt electrolytes were suggested, which might be worth a closer investigation. It is highlighted, that the use of alkaline earth metal cations (at least magnesium) in these kinds of electrolytes is difficult, as from literature[42, 43] a decomposition mechanism is known affecting many ligands (regardless of ion-paired anion or solvent) of the cations, upon the trial of plating the alkaline earth metal, via a single electron transfer to the cation. This leads to an M^+ transition state, which destabilizes the ligands and causes decomposition reactions for many of these. Thus one has to not only consider the solvent stability but also the stability of the anion (especially at high concentrations due to increased ion-pairing).

Metal-O_2 batteries

The oxygen reduction reaction is the target reaction at the positive electrode in metal-O_2 batteries. However, this reaction obeys several problems, which vary depending on the chosen electrolyte and electrode material. For several electrolytes, superoxide is the number one problem, as this highly reactive compound might decompose the solvent. This, in the worst case, leads to blocking of the electrode by decomposition products. Blocking of the electrode is a very general problem regarding the oxygen reduction reaction, as the reduction products often stay on the electrode surface and suffer from a poor conductivity, which limits the battery capacity by the electrode surface area. As discussed in chapter 4, in Li^+ containing DMSO the oxygen reduction reaction path can be solution mediated, which allows for continuous discharge (as the adsorbate formation in this case seems to be rather a side reaction). This exemplary shows, that there are solutions to be found for these problems. Thus investigations on the oxygen reduction in alkaline metal and alkaline earth metal cation containing DMSO were carried out, and it was found, that the formation of a MO_2/MO adsorbate seems to be not only present for all alkaline earth metal cations during the ORR in DMSO, but also plays a directing role in whether superoxide or peroxide formations is dominant. Furthermore, as the adsorbate formation is hindered (e.g. by kinetics) dissolving peroxide is formed, which would allow for a continuous discharge of a battery with two e^- per oxygen molecule compared to one (superoxide). Finally a more generalized mechanism for the ORR in alkaline earth metal cation containing DMSO was proposed based on the findings concerning the crucial role of the CaO_2/CaO adsorbate formation. A correlation was established between the tendency of the oxide species to rather bind to the electrode surface or to the alkaline earth metal cation (e.g. as ion-pair) and the share of dissolving peroxide. This strongly indicates, that the adsorbate formation plays a crucial role for all alkaline earth metal air battery systems. Several parameters were identified, that affect the adsorbate formation. Thus to achieve a large contribution of dissolving peroxide during the ORR in alkaline earth metal cation containing DMSO, the electrode oxide interaction has to be minimized, electrode surface defects have to be avoided and the real surface area of the electrode has to be maximized. This suggests the use of systems like gold nanoparticle electrodes, which are certainly not applicable for battery applications, but might act as model systems to further investigate the nature of the observed trends and to (maybe) provide more applicable suggestions as electrode materials.

However, as the adsorbate formation was investigated, a system with very astonishing behavior was found. For the system of 0.1 M LiCl + 0.1 M $CaCl_2$ in DMSO it was not only found that the $CaCl_2$ dissolves completely in DMSO, which is not the case, when no LiCl is present in solution. In fact it is also highly indicated, that during the oxygen reduction reaction on a Pt electrode under convection, a autocatalytically active surface species is formed, which causes a negative ring current response at positive ring potentials, which indicates most likely chlorine reduction. This certainly is worth further investigation and needs confirmation.

Sodium dodecylsulfonate adsorption on Au(111)

As this thesis has once again shown, that the electrochemical interface strongly affects the electrochemical reactions at the electrode (in this context the oxygen reduction reaction), it is important to being able to model and influence the structure and composition of this interface. In chapters 4-6 it was shown, that the peroxide/oxide adsorbate strongly affects the reaction path and even leads to complete depletion of the reaction in some cases. It is also noteworthy, that regarding ionic liquids (as “extreme case” of solvent in salt electrolytes) show a strictly layered structure perpendicular to the electrode surface. This highlights the importance to investigate possibilities to influence or even design the electrochemical interface by e.g. AFM-tip induced nanostructuring of the electrode using sodiumdodecylsulfate (SDS) [56, 57]. This thesis investigated sodiumdudecylsulfonate (SDS*) as alternative and as a first step aims at a structural comparison. Due to the fact, that (to our knowledge) there is hardly any literature addressing this system, we decided to initiate investigations in this system, while similar systems like alkylsulfates and alkylthiolates are common research topics nowadays. In this thesis the transition from a flat adsorbed SDS* layer to a condensed, compressible SDS* layer with vertically oriented molecules was observed in positive scan direction during cyclic voltammetry and a structure for the condensed layer was provided utilizing AFM techniques. The condensed layer showed a clear structuring in AFM experiments at low normal loads using a soft cantilever. Furthermore an indication was found, that the condensed layer is a bilayer similar to the case of SDS. Finally the friction on both adsorbate layer structures was investigated and overall showed very low friction coefficients at low normal loads and when the condensed layer was fully compressed. This system showed many similarities to alkylsulfate and alkylthiolate systems but also several differences, proving it to be a comparably interesting system for research. We highly recommend experiments in alkaline solution, as then the adsorption of SDS* on the bare electrode might be observed, as more negative potentials are achievable at lower H^+ concentrations

10 Appendix

10.1 The mechanism of Li_2O_2-film formation and reoxidation – influence of electrode roughness and single crystal surface structure

10.1.1 Abstract

In this work, the role of the electrode surface structure on oxygen reduction reaction (ORR) and oxygen evolution reaction (OER) in lithium ion containing dimethyl sulfoxide (DMSO) was elucidated for Pt single crystal electrodes and deliberately roughened polycrystalline gold and platinum electrodes. Both rotating ring disk electrode (RRDE) measurements and results obtained by differential electrochemical mass spectrometry (DEMS) show that the amount of insoluble Li_2O_2 formed is proportional to the roughness factor and corresponds to one or two monolayers if referenced to the true surface area. The amount of soluble LiO_2 is independent of roughness, although the formation of the passivating Li_2O_2 layer takes longer.

On gold electrodes less side products are formed as compared to platinum electrodes. It was furthermore found that ORR on single crystalline Pt(100) leads to two monolayers of Li_2O_2, while in case of Pt(111)/Pt(pc) only one monolayer was reoxidized.

The shape of the reoxidation peaks in the anodic potential scan is independent of roughness, but it depends not only on the electrode material (Au or Pt) but also on the atomic surface structure[66]. Since Tafelslopes cannot be determined directly by usual methods for such surface confined reactions, we used ac voltammetry to determine the apparent transfer coefficient (α’) and gain some insight into the reoxidation mechanism; the obtained α' of 0.3 hints to a rate determining first charge transfer. This agrees well with the detection of superoxide during oxidation of Li_2O_2 on the surface.

10.1.2 Introduction

Lithium ion batteries are reliable and commonly used these days, but for many applications one would like to have batteries with a higher energy density than the typical value of $0.91\frac{kJ}{g}$.[67] So, Li-O_2 batteries are of special interest due to their high theoretical energy density (13.8 $\frac{kJ}{g}$).[68, 69] The main product during discharge in Li-O_2 cells is Li_2O_2 and not Li_2O for organic electrolytes. [70-79] A lot of fundamental research concerning the oxygen reduction has already been performed. [70, 72, 75, 77, 80-88] The mechanism of oxygen reduction reaction (ORR) is strongly dependent on the electrode material and the electrode surface.[68] In principle two mechanisms are proposed for the ORR in Li^+ containing organic electrolytes. The first one is surface mediated and leads to a fast surface passivation by a thin layer of peroxide, while the second one is solution mediated and thus does not lead to a quickly passivated surface.[89]

	Surface mediated	Solution mediated	
(36)	$Li^+ + e^- + O_{2\,(sol)} \rightarrow LiO_{2\,(surf)}$	$Li^+_{(sol)} + e^- + O_{2\,(sol)} \rightarrow Li^+_{(sol)} + O^-_{2\,(sol)}$	(40)
(37)	$Li^+ + LiO_{2\,(surf)} + e^- \rightarrow Li_2O_{2\,(ads)}$	$Li^+_{(surf)} + O^-_{2\,(surf)} \rightarrow Li^+_{(sol)} + O^-_{2\,(sol)}$ [90]	(41)
(38)	$2LiO_{2\,(surf)} \rightarrow Li_2O_{2\,(surf)} + O_2$	$2\left(Li^+_{(solv)} + O^-_{2\,(solv)}\right) \rightarrow Li_2O_2 + O_2$	(42)
(39)	$2Li^+ + 2e^- + O_2 \overset{\text{Au}}{\rightarrow} 2Li_2O_2$ [90]	$2Li^+_{(solv)} + O^-_{2\,(solv)} + e^- \rightarrow Li_2O_2$	(43)

Key for the solution-mediated mechanism is the stability of superoxide in solution. Using dimethyl sulfoxide (DMSO) as electrolyte enhances the solution mediated pathway by increasing the lifetime of superoxide in solution.[72] This is caused by the strong solvation of Li^+-ions by DMSO, related to its large donor number ($125\ \frac{kJ}{mol}$)[91]. This has been explained by the stabilization of superoxide in a complex with a soft acid such as TBA^+ or strongly solvated Li^+-ions using the HSAB concept.[72], but in [92] it is shown that this is a misconception of the HSAB concept and that rather the polarity of the solvent or an additive plays a role. Instead of reaction (40), one may as well consider reaction (36) and (41), since electron transfer is occurring in close vicinity of the electrode surface and probably is also promoted by the presence of Li^+ ions similar to proton coupled electron transfer. The superoxide in solution will then disproportionate to finally form Li_2O_2, which grows as micrometer-sized particles.[80, 89, 93, 94] Regarding the surface mediated mechanism, the superoxide disproportionation on the surface can't be distinguished from the direct oxygen reduction to peroxide.[90] Concerning the fact, that both small superoxide molecules have to be adsorbed on the surface for the surface disproportionation to occur, it is hard exclude a pathway with electron transfer via the electrode surface.

A further problem in Li-O_2 cells is the decomposition of the electrolyte, which in case of organic electrolytes is indicated by CO_2 generation during charging. It was proposed, that the CO_2 evolved at positive potentials has its origin in a parasitic reaction of the electrolyte (e.g. DMSO) with Li_2O_2. [75, 95] The parasitic reaction forms carbonates and these carbonates, or more accurate, the carbonate oxygen is then oxidized during charging via:

$$2Li_2CO_3 \rightarrow 4Li^+ + 4e^- + 2CO_2 + {}^1O_2 \tag{44}$$

Here it was unclear for a long time, why no evolved oxygen was detected. Later, by directly investigating the oxidation of lithium carbonate it was shown, that the formed oxygen is highly reactive singlet oxygen, which immediately reacts with the solvent, [96, 97] thus explaining the problems of its detection. It was further shown, that singlet oxygen is also generated in the ORR during the superoxide disproportionation. [96, 98]

The thin layer of Li_2O_2 formed in the surface mediated reduction is a surface limited reaction; current transients in chronoamperometric ORR experiments on Au display a typical nucleation and growth behavior.[99] The kinetics of the oxygen evolution from Li_2O_2 has been much less studied than the oxygen reduction. For gold electrodes in 0.1 M Li^+-containing DMSO saturated with $O_2^{10\%}/Ar^{90\%}$-mixtures at 10mV/s, the ORR under convection starts with a shoulder attributed to LiO_2 formation, followed by a peak attributed to Li_2O_2 formation and thus resulting in electrode passivation by Li_2O_2.[100] The reoxidation of the deposited Li_2O_2 seems to take place during two steps as indicated by the two anodic peaks attributed to the OER[68, 100-102], Liu and Ye found, that initially the oxidation takes place at the Au|Li_2O_2 interface and the remaining particles get oxidized at higher overpotentials[102], while another group found, that at low overpotentials amorphous Li_2O_2 is oxidized and at higher overpotentials crystalline Li_2O_2 is decomposed.[103] Here, a fundamental question is whether the two electrons are transferred simultaneously or consecutively. Since the amount of Li_2O_2 on the surface is limited, one cannot easily measure Tafel slopes for this reaction. For such systems, in particular for adsorbate systems and reactions changing with time due to a non-steady-state surface coverage by reactants or intermediates, we had introduced a method to determine the apparent transfer coefficient (and thus the reciprocal Tafel slope) by ac-voltammetry, [104-106] a method that similarly was used for hydrogen evolution.[107] Here we apply this method to the oxidation of the Li_2O_2 layer.

It has already been described for carbon electrodes, that the surface structure of the electrode has a large impact on the ORR/OER and side product formation.[66] While it has also been described for Au and Pt that the surface structure influences the coulombic efficiency and number of transferred electrons during the ORR in a differential electrochemical mass spectrometry (DEMS) measurement[68]. For Na it was already shown that the surface orientation directly affects the voltammetry. [36] This role of the surface structure, notably surface roughness and single crystal structure, will be investigated in this work for Li^+ electrolytes using rotating ring disc (RRDE) and DEMS experiments. In a forthcoming paper, we will examine the role of roughness in Ca2+ containing electrolytes.[108] The examination of the role of the electrode roughness is quite important since fundamental studies are usually performed at relatively smooth electrodes, whereas batteries contain rough, nano- and mesostructured electrodes. Experimental results on well oriented single crystal electrode surfaces are a prerequisite for any comparison with theoretical quantum chemical calculations since these can be done exclusively for such ideal surfaces.

10.1.3 Experimental

Electrodes: All non-RRDE electrodes in this study were 1 cm in diameter resulting in a geometrical surface area of 0.785 cm^2. The RRDE disk electrodes had a diameter of 0.5 cm resulting in a geometrical surface area of 0.196 cm^2 and were exchange disk electrodes, allowing de-/ and reconstruction of the complete electrode. The gold ring electrode is separated from the disk electrode by a Teflon ring. The collection efficiency (*N*) is 0.25.

RRDE setup: The RRDE investigations were conducted in a usual H-Cell inside a glovebox under argon atmosphere. The DMSO and all chemicals except the silver nitrate were stored inside the glovebox. The WE, Ce and RE were connected to a PINE potentiostat (MODEL AFCBP1), while the electrode rotator was connected to a GAMRY rotation control (RDE710). CE were gold/platinum sheets depending on the WE-material, while as reference a silver wire was immersed into 0.1 M $AgNO_3$ containing DMSO.

DEMS setup: The We, CEs and the RE of the Dual Thin Layer flow through cell were connected to a home built bipotentiostat and the electrolyte outlet of the cell was connected to a peristaltic pump (SPETEL Perimax). The thin electrolyte compartment of the working electrode and the compartment of the porous Teflon membrane (serving as the interface to the vacuum) were defined by a Teflon spacer of 200 µm (WE compartment) and 100 µm (Membrane compartment) thickness and a diameter of 6 mm, leaving an accessible electrode area of 0.283 cm^2. RE was a silver wire in 0.1 M $AgNO_3$ containing DMSO, while CEs were gold/platinum wires depending on the WE-material. More Detailed information about the DEMS setup and Dual Thin Layer Cell can be found elsewhere.[48, 109-112]

Electrode Cleaning: For cleaning the electrodes were cycled in 0.5 M H_2SO_4 until the well-known CV shape could be observed. If contaminations are observed during the scan, the electrodes were cleaned further. In case of gold, the electrode was oxidized in 0.5 M H_2SO_4 until the surface was reddish. Afterwards, the formed gold oxide was removed in concentrated hydrochloric acid. In case of platinum, the electrode was immersed alternately into concentrated nitric acid and a solution of ammonia in water several times. Regardless of the electrode material, the voltammetry was checked after these advanced cleaning procedures to exclude remained contamination.[33, 34]

Electrode roughening: For adjustment of the roughness factor (f_R) in case of gold, the electrode was annealed (cooldown in N_2 above milli-Q water) or polished to start at a low roughness factor. Afterwards the electrode was rinsed with milli-Q water, immersed in argon saturated 0.5 M H_2SO_4 and a potential > 2.5 V was applied for a given time before the formed oxide layer was reduced. Variation of applied potential and treatment duration leads to different f_R. The determination of f_R is further explained in the supporting information (Figure 59 + Figure 60). In case of platinum, the electrode was annealed (cooldown in N_2), immersed in argon saturated 0.5 M H_2SO_4 and a fast switching potential (ca. 1.4 kHz between 0 V and 2.6 V) was applied to the electrode. After the dedicated treatment duration, the oxidized platinum species were reduced until the reduction current was close to 0. Variation of the upper potential limit and treatment duration leads to different f_R. At this point one has to mention that the roughening procedure for gold results in a somewhat inhomogeneous f_R over the electrode surface. Thus f_R for the accessible area in DEMS measurements is overestimated for gold.

Preparation of single crystals: The single crystals were cleaned as described above and annealed in an induction heat cell afterwards. To obtain a well ordered (111)/(100)-surface, the cell was saturated with N_2 in case of Pt(111) and with ($Ar^{95\%}H_2{}^{5\%}$) in case of Pt(100) during the annealing procedure (150 s at yellow heat) and also during cooling down of the crystal above milli-Q water.[33, 34] After cooling down for 10 minutes, the electrode was characterized in 0.5 M H_2SO_4 or protected by bromide from 1 mM KBr solution for transport. The method of bromide protection in ref. [36] allows for save transport of Pt single crystal electrodes through ambient without losing surface integrity and was used as model for the procedure used in this study (note that we avoided using CO during the procedure). After bromide protection, the electrode was rinsed with water.

AC-voltammetry: The quasi-continuous recording of the apparent transfer coefficient α' as a function of the potential (or time) was achieved by superimposing a small ac-voltage (u_{ac} = 3 mV) to the potential ramp during cycling voltammetry. (For the measurement of these AC-voltammograms a potentiostat model 273A (EG & G, Princeton applied research) was used together with a lock-in amplifier (5210, EG & G).) This can be expressed as following:

For an irreversible reaction with

$$i = zF\, k'(E) f(\theta) \tag{45}$$

and

$$k'(E) = k_0 \exp\left(\frac{\alpha' F E}{RT}\right) \tag{46}$$

the apparent transfer coefficient is given by

$$\alpha' = \frac{RT}{F}\frac{\partial \ln i}{\partial E} = \frac{RT}{F}\frac{1}{i}\frac{\partial i}{\partial E} \tag{47}$$

and related to the Tafel slope b according to

$$b = \frac{\partial E}{\partial \lg i} = \frac{2.3\,\partial E}{\partial \ln i} = \frac{RT}{F}\frac{1}{\alpha'} \tag{48}$$

The term $\frac{\partial i}{\partial E}$ corresponds to the ratio of the small ac current amplitude and small amplitude of the ac potential and can be therefore be rewritten as $\frac{i_{ac}}{u_{ac}}$. The amplitude u_{ac} and frequency (here, 5 to 10 Hz) have to be chosen such that the coverage (θ), which in our case is the surface coverage by peroxide, and thus the function $f(\theta)$, describing the dependence of the rate on the coverage, remain practically constant within the ac period. Then, its contribution to the derivative of the current is negligible. For i_{ac} only its real part (free of the contributions of capacitive processes) is used. Furthermore, u_{ac} was corrected for the electrolyte resistance, which had been determined independently by impedance measurements as described in ref.[105]

10.1.4 Results & Discussion

Rotating Ring Disk Electrode (RRDE) investigations

It is well known, that Li_2O_2 forms a passivating layer during ORR on gold surfaces, while predominantly during the ORR onset soluble LiO_2 is generated at low overpotentials. The influence of the electrode roughness on the reaction was now studied using the RRDE. Generated LiO_2 dissolves into the electrolyte and thus can be detected at the ring electrode. Furthermore the share of superoxide ($\chi_{superox.}$) can be calculated via

$$\chi_{superox.} = \frac{2 * j_{ring}}{N * j_{disk} + j_{ring}} \tag{49}$$

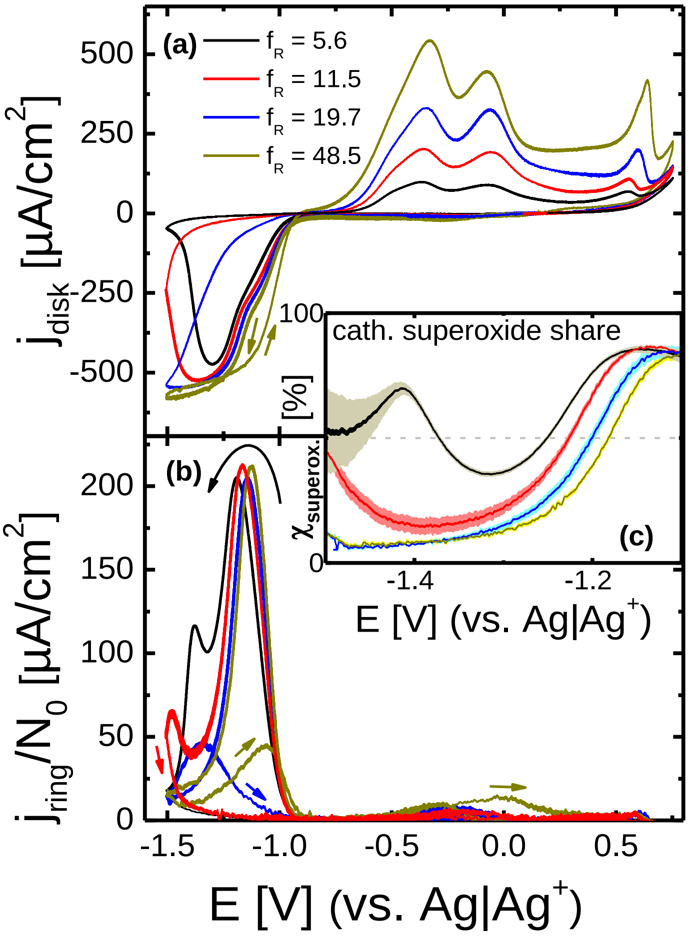

Figure 51 CVs for Au disk (a) and ring (b) electrodes with different f_R and calculated superoxide share (c) at 20 mV/s and 9 Hz in ($Ar^{80\%}O_2^{20\%}$)-saturated 0.1 M $LiClO_4$ containing DMSO vs Ag|Ag$^+$. Disk-current is normalized to the geometrical surface area and ring-current is normalized to the theoretical collection efficiency and (N_0) and geometrical surface area of the disk electrode. Ring potential was held at 0.3 V. The Potential axis refers to the swept disk potential. Shown data is smoothed using Savitzky-Golay method. Arrows indicate the sweep direction.

Figure 51 shows the cyclic voltammetry of the roughened, polycrystalline gold electrodes in ($\mathrm{Ar}^{80\%}\mathrm{O}_2^{20\%}$)-saturated 0.1 M $LiClO_4$ containing DMSO vs Ag|Ag$^+$ at 20 mV/s and 9 Hz. The ring potential was set to 0.3 V for detection of the generated superoxide at the disk electrode. The disc current is normalized to the geometrical surface area and the ring current is normalized to both the collection efficiency and the geometrical surface area of the disk electrode. As seen in Figure 51a, the disk current increases at -0.9 V in cathodic direction due to the generation of LiO_2, and then increases further due to switching from LiO_2 to Li_2O_2 formation. With increasing electrode roughness, LiO_2 and Li_2O_2 formation shift to more positive potentials due to the increase of the apparent rate constants. For $f_R \leq 11.5$, the Li_2O_2 formation diminishes due to electrode deactivation before reversal of the potential. Regarding the anodic sweep, the generated Li_2O_2 is reoxidized starting at approximately -0.8 V depending on f_R. During the anodic sweep, two peaks for the Li_2O_2 reoxidation (-0.33 V and 0.08 V) and one peak for the carbonate oxygen oxidation (CO_2-evolution proven by DEMS, Figure 54c) are observed. Considering the fact, that the amount of Li_2O_2 during the ORR on gold electrodes for this system amounts to approximately 2 monolayers, the first peak might be due to oxidation of the second layer, while the second peak in anodic direction occurs due to oxidation of the Li_2O_2 layer directly on top of the gold surface, thus requiring a larger overpotential for oxidation.[68] Another explanation for the two peaks is given by Liu and Ye, as they concluded from infrared absorption spectroscopy and SERS measurements that the oxidation of Li_2O_2 initiates at the Au|Li_2O_2 interface (first peak); Oxidation of the remaining particles would then occur at higher overpotentials (second peak).[102] Furthermore it has been suggested that at low overpotentials amorphous Li_2O_2 is oxidized and at higher overpotentials crystalline Li_2O_2 is decomposed.[103] It is notable, that the peak potential above 0.5 V (CO_2-evolution as will be shown below, cf. [68, 100]) shifts to more positive potentials with increasing roughness.

Figure 51b shows the ring current normalized to the collection efficiency and geometrical surface area of the disk electrode. The ring current during the cathodic sweep increases at -0.9 V due to the oxidation of soluble LiO_2 generated at the disk electrode. The first peak in cathodic direction occurs due to the maximum in LiO_2 formation at the disk electrode and so directly refers to the shoulder in Figure 51a. In the rising part the current at a given potential is higher for high roughness factors (and thus the half wave potential is shifted to more positive potentials) due to the increased apparent rate constant for superoxide formation. After the first peak in ring current (the peak current fits to the expected diffusion limited current), the ring current (and the LiO_2 formation rate at the disc) decreases to a minimum, due to the increasing rate of Li_2O_2 formation. Continuing the sweep, the ring current increases to a second peak, which is attributed to the decrease in rate of peroxide formation, as the disk electrode deactivates (low f_R) [68]. For larger f_R, the second peak in the ring current is shifted in time and thus to the anodic sweep, because more Li_2O_2 is deposited on the disk electrode before it deactivates; for the largest f_R the electrode does not even deactivate. In this case, the second peak in ring current is shifted to the onset/depletion of peroxide formation. (Note: the maximum disc current is limited by diffusion and thus independent of roughness). During the OER, the ring current at around 0 V indicates the formation of a soluble, oxidizable species for high f_R (see Figure 51b), which most probably corresponds to the superoxide intermediate being formed in the reverse of reaction (2). A similar observation had already been made for the OER on Vulcan Carbon thin films on glassy carbon electrodes in Li^+ containing DMSO in an RRDE measurement.[113]

For further insight, the cathodic superoxide share was calculated as shown in Figure 51c. The superoxide share refers to the amount of superoxide related current relative to the total current at the disc; a share of 100% means, that only LiO_2 is formed. Starting from -1.1 V, in cathodic direction, the share is around 85% and then decreases to a minimum due to the maximum in Li_2O_2 formation at the disk electrode. As the disk electrode deactivates, the superoxide share increases again for $f_R \leq 11.5$ due to the early electrode deactivation. The yield in Figure 51c directly correlates with the first peak in ring current (and the shoulder in disc current) and thus follows the same behavior. For increasing electrode roughness, this peak in I_{ring} shifts to more positive potentials due to increasing real surface area and thus increasing effective rate constant.

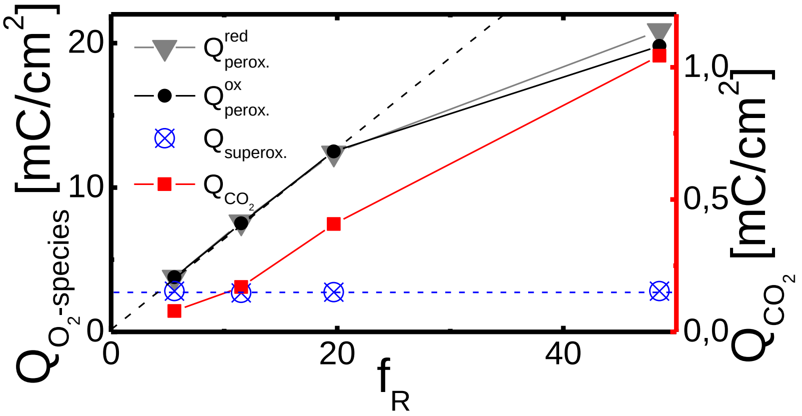

Figure 52 Calculated reduction and reoxidation charges (obtained from integration of the faradaic current normalized to the geometric surface area) of O_2-species and CO_2-evolution for increasing Au(pc) electrode roughness conducted in 0.1M $LiClO_4$ containing ($Ar^{80\%}O_2^{20\%}$)-saturated DMSO at 20mV/s and 9Hz. $Q^{red}_{perox.}$, $Q^{ox}_{perox.}$ and Q_{CO_2} refer to the integration of the disk current while $Q_{superox.}$ refers to the integration of the ring current.

For all experiments, the currents were integrated to investigate the reaction charges. The calculated charge densities for the respective reactions are shown in Figure 52. The charges corresponding to the ORR and Li_2O_2 reoxidation are in excellent agreement; both and also the charge ascribed to CO_2-evolution increase linearly with increasing electrode roughness (except the values for $Q^{red}_{perox.}$ and $Q^{Ox}_{perox.}$ for the largest f_R), whereas the charge corresponding to the LiO_2 reoxidation at the ring electrode is independent of electrode roughness. This reflects the fact that the rate of superoxide formation in the peak is diffusion limited; the higher amount in the onset region for higher roughness is counterbalanced by the earlier deactivation. The last value for $Q^{red}_{perox.}$ and $Q^{Ox}_{perox.}$ does not fit to the linear behavior, because the electrode with this roughness is not saturated with Li_2O_2 as already indicated in the CV (Figure 51).

Determination of the apparent transfer coefficient α' for OER

In order to obtain a little more insight into the mechanism of oxygen evolution from Li_2O_2, we determined the apparent transfer coefficient α' from ac voltammetric measurements at a polycristalline Au electrode. A corresponding voltammogram together with the real and imaginary part is shown in the supporting information (Figure 61). The calculated α' is shown in Figure 53 as a function of potential for three different frequencies together with the dc current during the anodic scan. In a wide potential range between -0.35 V and 0.25 V, i.e. over the positive side of the first and over the whole second peak it is around 0.3 (corresponding to a Tafel slope of 200 mV); its independence of frequency and potential confirm the reliability of this value. Note that although the dc current for OER is decreasing with the cycle number due to a less positive anodic potential limit (resulting in electrode deactivation), the apparent transfer coefficient α' remains constant. This is in the range of typical transfer coefficients for a one electron transfer and we have thus to conclude that the first charge transfer is rate limiting. The superoxide (LiO_2) thus formed (reverse of reaction (2)) is then oxidized to O_2 in a very fast follow up reaction or dissolved to a small extend. The simultaneous transfer of two electrons can be excluded since that would result in an apparent transfer coefficient of about 1 ($\alpha' = 2\alpha$) or at least 0.6. (At the onset of OER the α'-values are larger at the lower frequencies. This might be taken as an indication that here the direct 2 e^- transfer also plays a role. However, at the onset α' is the result of the ratio between two small numbers and thus not reliable. Also, the dependence on frequency indicates that at the onset other pseudocapacitive effects might play a role which could not be corrected for.)

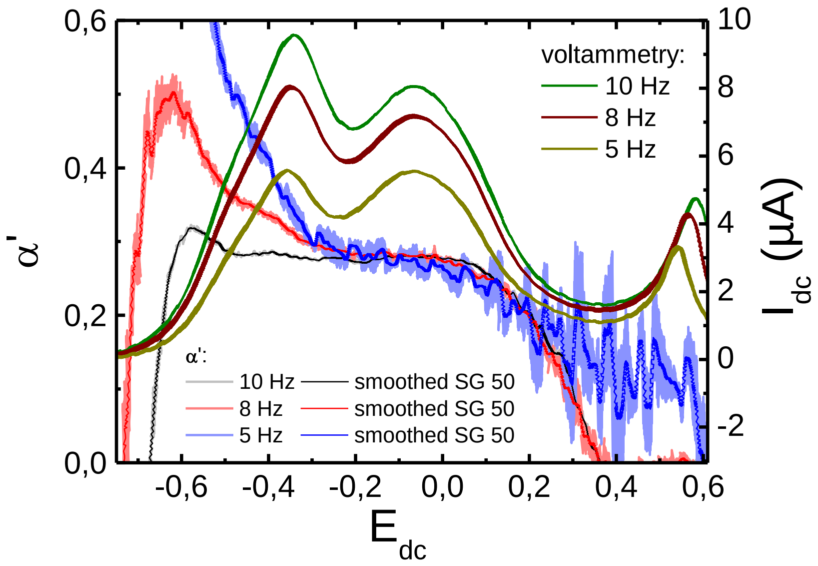

Figure 53 Apparent transfer coefficient as a function of the applied dc potential for a 0.1 M $LiClO_4$ solution in DMSO. The black, red and blue curves describe the apparent transfer coefficient for a frequency of 10 Hz, 8 Hz and 5 Hz. Green, brown and dark yellow are the corresponding dc currents from the anodic sweep of the voltammogram (10 mV/s). Data noted with SG 50 (darker colors) are smoothed using Savitzky-Golay method with 50 points of window.´

Differential Electrochemical Mass Spectrometry (DEMS) investigations

Differential electrochemical mass spectrometry gives insights into the product distribution and thus clearly shows the amount of consumed and generated oxygen. Furthermore, it provides the number of transferred electrons during the ORR and OER, enabling the confirmation of the calculated superoxide share.

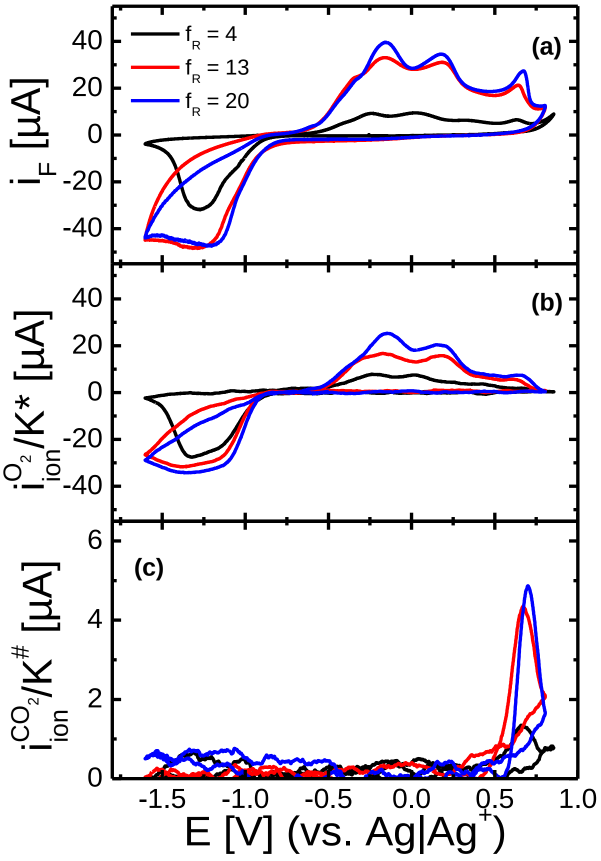

Figure 54 CVs and MS-CVS of Au(pc) in ($Ar^{80\%}O_2^{20\%}$)-saturated 0.5 M $LiClO_4$ containing DMSO at 10 mV/s and 3.2 µl/s flow rate (a). Potential dependent ion current normalized to the oxygen calibration constant for mass 32 (b) and mass 44 (c).The color-code indicates the electrode roughness. Data is smoothed using Savitzky-Golay method.

Figure 54a shows the cyclic voltammetry of roughened polycrystalline gold electrodes in 0.5 M $LiClO_4$ containing DMSO at 10 mV/s and 3.2 µl/s flow rate vs Ag|Ag$^+$. The electrolyte was saturated with ($\mathrm{Ar}^{80\%}\mathrm{O}_2^{20\%}$). Also the ion current for m/z = 32 (O_2, Figure 54b) and 44 (CO_2, Figure 54c) are plotted against the potential in the mass spectrometric CV (MSCV). In this study, the ion currents are normalized to the oxygen/CO_2 calibration constant (K* and K$^\#$, see equation (*56* and (*57* for reasons of comparability to the faradaic current. The cyclic voltammogram obtained using the thin layer flow through DEMS cell (Figure 54a) is comparable to the one obtained from RRDE setup (Figure 51a), while the current for the lowest f_R remains below the diffusion limited current because of the lower sweep rate and different cell geometry. The MS-CV for m/z = 32 (after background subtraction for O_2 dissolved in the electrolyte) nicely confirms the cathodic oxygen reduction and anodic Li_2O_2 reoxidation, while the MS-CV for mass 44 confirms the evolution of CO_2 ($E \geq 0.5$ V). The observed trends with increasing electrode roughness are similar to those observed for the RRDE setup. Furthermore, the number of transferred electrons, the oxidation charges and the reduction charges were calculated. The values are shown in Figure 55 for different electrode roughness values.

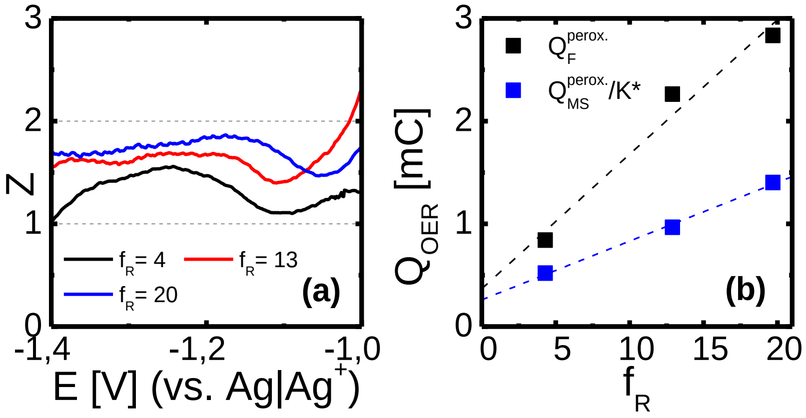

Figure 55 Calculated number of electrons transferred per O_2 during the ORR (a) and reoxidation charges during OER as a function of the roughness factor (F_R) (b), from CV (Q_F) and DEMS (Q_{MS}); the latter were converted to faradaic charges by division by the oxygen calibration constant K*.

It is clearly visible, that the number of transferred electrons increases in the relevant region up to a value of 1.85 electrons per O_2 for the electrode surface with highest roughness factor. This mirrors the behavior observed at the RRDE setup and, in combination with the linear increase of OER charges, leads to the conclusion, that the amount of deposited Li_2O_2 is proportional to the surface area, as one would expect. Also the number of transferred electrons during OER is close to two (as directly seen from the difference in slopes in Figure 55b, where the OER charge from MS is divided by the oxygen calibration constant allowing a direct comparison), identifying Li_2O_2 as deposit. At this point one has to note, that in this setup, the superoxide is transported out of the cell and therefore is not reoxidized at the WE.

We conducted a similar experiment for platinum as electrode material. Figure 56 shows the cyclic voltammetry of platinum electrodes with varying electrode roughness in ($\mathrm{Ar}^{80\%}\mathrm{O}_2^{20\%}$)-saturated 0.5M $LiClO_4$ containing DMSO at 10mV/s and 5µl/s flow rate vs Ag|Ag$^+$. The ion currents divided by K* referring to mass 32 (O_2, Figure 56b) and mass 44 (CO_2, Figure 56c) are plotted versus the potential, while division by K* allows again easier comparison.

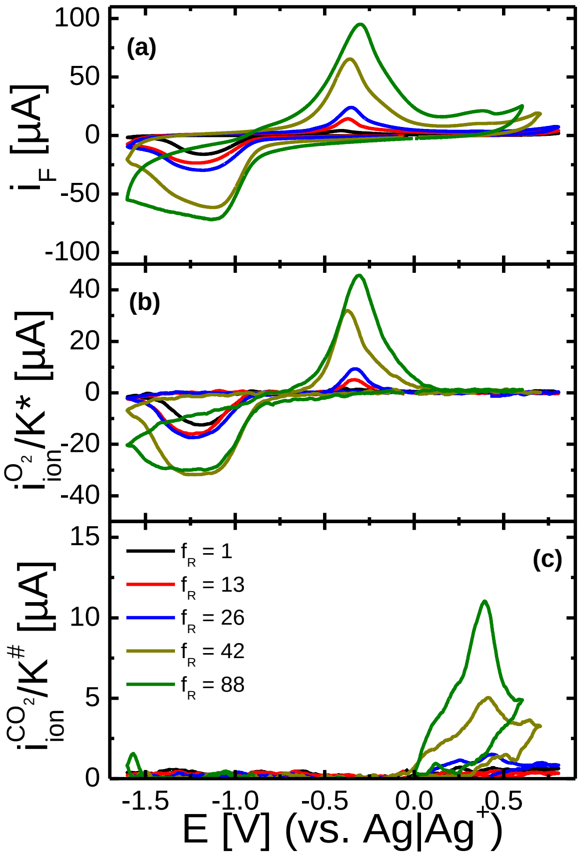

Figure 56 CVs and MS-CVS of Pt(pc) in ($Ar^{80\%}O_2^{20\%}$)-saturated 0.5 M $LiClO_4$ containing DMSO at 10 mV/s and 5 µl/s flow rate (a). Potential dependent ion current normalized to the oxygen calibration constant for mass 32 (b) and mass 44 (c).The color-code indicates the electrode roughness. Data is smoothed using Savitzky-Golay method.

As for gold, starting in cathodic direction, the faradaic current increases at approximately -0.85 V due to the ORR being paralleled by oxygen consumption, visible in the ion current for mass 32. Going more negative, the faradaic current starts to decrease due to electrode deactivation, while smoother electrodes deactivate faster. The ion current shows, that even the electrode with the largest roughness factor (f_R = 88) starts to deactivate during the cathodic sweep. A diffusion limited current is already observed for a roughness factor of 42, before electrode deactivation. For lower electrode roughness factors, electrode deactivation occurs before diffusion limitation is reached. Staring from -1.6 V in anodic direction, only for f_R = 88 oxygen reduction continues. Differently from gold, at more positive potentials the reoxidation of deposited Li_2O_2 is observed in only one large peak as observed before [68]. One further difference to gold is, that the ion current peak referring to CO_2-evolution slightly shifts to more negative potentials. The absence of evolved oxygen during CO_2-evolution, is explained by the generation of highly reactive O_2^1 in parallel to CO_2 evolution[97], which immediately reacts with the electrolyte, preventing it's detection via MS, as described in detail in the introduction.

The potential dependent number of transferred electrons (Figure 57a) and the reaction charges (Figure 57b) were calculated for varying electrode roughness factors and shown in Figure 57.

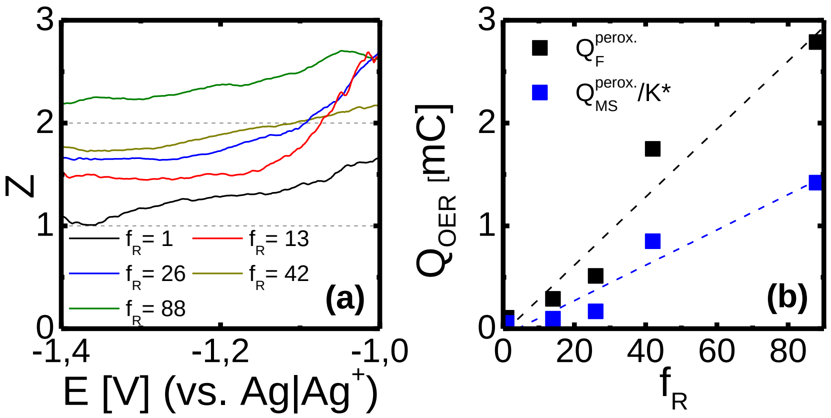

Figure 57 Calculated number of electrons transferred per O_2 during the ORR (a) and reoxidation charges with respect to the roughness factor (f_R) (b).

Similar to Au(pc), the number of transferred electrons approaches a value of two for increasing electrode roughness, indicating, that predominantly Li_2O_2 is formed during the ORR for larger roughness factors. One also observes, that the reoxidation charges increase monotonically with increasing electrode roughness, as one would expect for the surface limited deposition of an insoluble species. Indicated by the ratio of charges obtained from faradaic current and ion current (see Figure 57), the number of transferred electrons during OER is close to two (see equation (*55*), identifying Li_2O_2 as deposit also on Pt (The abrupt change in Figure 57b from f_R = 26 to f_R = 42 might be caused by a varied thickness of the thin layer cell as defined by the compressible Teflon spacer).

The influence of the atomic surface structure of well-ordered Pt surfaces on the ORR is remarkable as shown by DEMS in Figure 58, where Pt(111), Pt(100) and smooth (annealed, f_R = 1) Pt(pc) were compared.

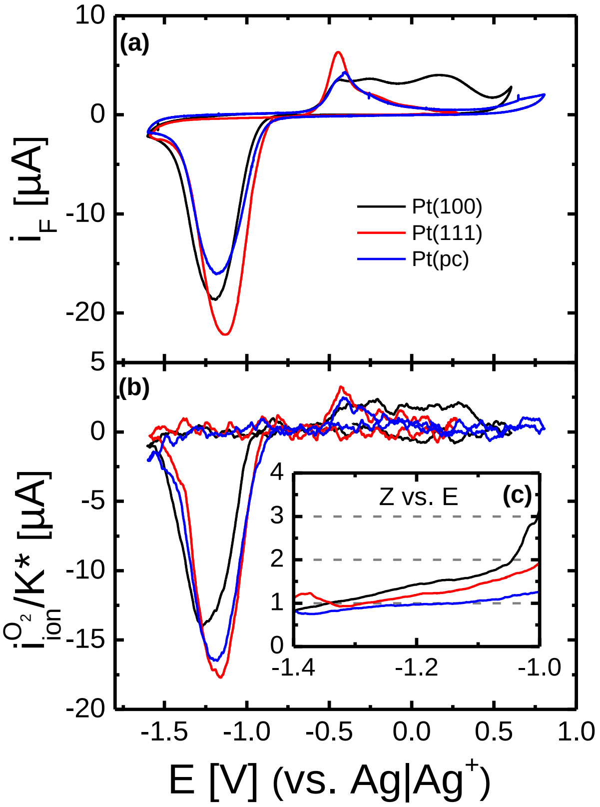

Figure 58 CVs and MS-CVs of Pt(hkl) in ($Ar^{80\%}O_2^{20\%}$)-saturated 0.5 M $LiClO_4$ containing DMSO at 10 mV/s and 5 µl/s flow rate (a). Potential dependent ion current normalized to the oxygen calibration constant for mass 32 (b). Potential dependent number of transferred electrons (c). Data in (c) are smoothed using Savitzky-Golay method. Data for Pt(111) in (a) had to be corrected due to electronic problems (see Figure 63-Figure 65 for original data of Pt(hkl)).

Figure 58a shows the cyclic voltammetry of Pt(111), Pt(100) and Pt(pc) in ($\mathrm{Ar}^{80\%}\mathrm{O}_2^{20\%}$)-saturated 0.5 M $LiClO_4$ containing DMSO at 10 mV/s and 5 µl/s flow rate vs Ag|Ag$^+$. The ion current for mass 32 (O_2; Figure 58b) and the number of transferred electrons (Figure 58c) are also plotted versus the potential. Again the cathodic sweep is dominated by the ORR in one large peak visible in CV and MSCV. In case of Pt(100) the ORR occurs at more negative potential compared to Pt(111) and Pt(pc). The number of transferred electrons (Figure 58c) quickly goes to one for more negative potentials, demonstrating again that at the peroxide covered surface, which is rapidly formed at these extremely smooth surfaces, LiO_2 is the product. The anodic part of the CV shows the reoxidation of deposited Li_2O_2. In case of Pt(111) and Pt(pc) the reoxidation occurs in one peak corresponding to approximately one monolayer Li_2O_2, cf. Table 4. The reoxidation of Li_2O_2 in case of Pt(100) occurs in two separated peaks corresponding to slightly more than two monolayers Li_2O_2 (see Table 4).

For the single crystalline surfaces, the number of reoxidized layers of deposited Li_2O_2 was calculated (Table 4), where one monolayer is defined by a one to one ratio of Li_2O_2 units to platinum surface atoms.[101]

Table 4 Calculated number of reoxidized layers of deposited Li_2O_2 on single crystalline Pt and polycrystalline Pt and Au surfaces. One monolayer (ML) of Li_2O_2 here is defined as the amount of reoxidation charge corresponding to two electrons per metal surface atom (480 µC/cm² for Pt(111), 420 µC/cm² for Pt(100) and Pt(pc) and 390 µC/cm² for Au(pc) derived from [114]). Q_F^{OER} is the reoxidation charge of Li_2O_2 obtained from integration of the faradaic current. Q_{MS}^{OER} is the reoxidation charge of Li_2O_2 obtained from integration of the ion current referring to mass 32.

Pt(hkl)			**ML(O_2^{2-}) from Q_{MS}^{OER}**	**ML(O_2^{2-}) from Q_F^{OER}**
Pt(111)			1.2	1.2
Pt(100)			2.4	2.8
Pt(pc)			0.9	0.9
Electrode material	**f$_R$**	**Setup**	**ML(O_2^{2-}) from Q_{MS}^{OER}**	**ML(O_2^{2-}) from Q_F^{OER}**
Pt	1	DEMS	0.9	0.9
Pt	13	DEMS	0.12	0.19
Pt	26	DEMS	0.11	0.17
Pt	42	DEMS	0.34	0.35
Pt	88	DEMS	0.27	0.27
Au	4,3	DEMS	2.2	1.77
Au	12,9	DEMS	1.36	1.59
Au	19,7	DEMS	1.29	1.3
Au	5,6	RRDE	-	1.74
Au	11,5	RRDE	-	1.68
Au	19,7	RRDE	-	1.63
Au	48,5	RRDE	-	1.05

Table 4 shows, that in case of Pt(111) only one monolayer of Li_2O_2 is deposited until the electrode deactivates, while in case of Pt(100) at least two layers can be deposited. Concerning the shape of the anodic reoxidation of Li_2O_2 in case of Pt(100), it is similar to the case of polycrystalline gold, where about 2 layers of Li_2O_2 are deposited for a roughness factor of 1.[68] Concerning the polycrystalline electrodes, it is notable, that rough platinum electrodes show a coverage per real electrode area of below 0.5 ML. (Here, for normalization we used the common value of 210 µC/cm^2 [114]. More recent values given in literature, e.g. 230 µC/cm^2 as proposed in ref. [115] will change the values for Pt(pc) only slightly (changes < 10 %)). Thus electrode saturation with Li_2O_2 is not attained, while also rough gold electrodes show a value around 1.5 ML. Even for the highest roughness factor of nearly 50, for which no blocking of the ORR is observed even in the anodic sweep of the voltammogram, the coverage still is above one. The large difference in OER charge might refer to the increased CO_2 generation on Pt as compared to gold. If CO_2 is generated as proposed by eq. (*44*, carbonate could be the reason for the faster electrode blocking and thus lower coverage of Li_2O_2 on Pt.

10.1.5 Conclusions

We expect that a complete blocking of the surface is occurring at sufficiently low potentials or longer times irrespective of the surface roughness. On rough Pt and Au surfaces, the generation of peroxide largely exceeds that of superoxide in cyclic voltammetric experiments since ORR is diffusion limited and more peroxide can be deposited on a rough surface. On the other hand, the ORR and the shape of the voltammograms does not depend much on the atomic surface structure, except for a shifted onset-potential by ≈ 45 mV and thus a decreased rate in case of Pt(100). The amount of Li_2O_2 which can thus be formed is limited by the electrode area and therefore too small for practical battery applications. Gold is somewhat special in this context because blocking only occurs negative of a clearly defined transition potential, but not only is gold too expensive for practical applications, but also in a battery the potential during discharge cannot be so clearly defined to avoid potentials of surface mediated Li2O2 formation and drive the reaction towards the solution path, in which larger Li2O2 particles are formed by disproportionation of the superoxide. Possibilities to foster this reaction path are the use of additives, which enhance superoxide formation probably by slowing down the second electron transfer[92], or the use of redox mediators for the oxygen reduction. [116-122] Apart from these practical aspects, it is interesting to note that such a thin layer of peroxide, resembling an adsorbate layer, is formed on all catalysts and all atomic surface structures. As has been shown in the past, this is even true for glassy carbon electrodes, and electrodes covered by a usually passivating layer of Se.[68]

In the anodic process, oxygen is formed with 2 electrons per molecule, in agreement with Li_2O_2 being the solid reduction product. For electrodes with a high roughness factor, we could detect formation of superoxide during peroxide oxidation. This is almost certainly not an effect of the roughness itself, but due to the increased absolute amount of superoxide formed, leading to the higher sensitivity. This finding of superoxide as an intermediate of peroxide oxidation corroborates the finding of a rate determining first charge transfer found in ac-voltammetric measurements. The difference in amount of evolved CO_2 between Au and Pt indicates a lower degree of electrolyte degradation and side product formation in case of Au.

The dependence of the CV-shape during peroxide oxidation and the dependence of the amount of peroxide formed once again shows, that the electrochemistry is strongly affected by the structure of the electrode surface. The strong dependence of the peroxide oxidation process on the atomic surface structure of the Pt single crystal electrodes suggests that the peroxide layer has to be regarded as an adsorbate. The large difference in OER shape between Pt(111) and Pt(100) needs further investigation. Especially regarding the two broad anodic peaks in case of Pt(100). This observation opens up new questions concerning comparability to Au electrodes, where a similar coverage of Li_2O_2 is found and mechanisms are already proposed.[68, 102] The different behavior of Pt(100) compared to Pt(111) might be the result of a more open surface structure of the formed Li_2O_2 as the surface structure of Pt(100) already is more open compared to Pt(111), allowing the deposition of further layer of Li_2O_2 (at least one additional layer). Regarding massive electrodes this study has once again shown that surface roughness has a considerable effect on the reaction kinetics.

10.1.6 Supporting information

Calculation of the roughness factor

The real surface area (A_{real}) of an electrode and the theoretical/geometrical surface area of the same electrode (A_{geo}) often differ strongly related to the roughness of the electrode. The ratio between A_{real} and A_{geo} is called the roughness factor (f_R) and is given by

$$f_R = \frac{A_{real}}{A_{geo}} \tag{50}$$

The current of an electrode reaction is proportional to A_{real}, so that $f_R$can directly be calculated from a CV via the ratio of the real charge (Q_{real}) and the geometrical charge (Q_{geo})

$$f_R = \frac{Q_{real}}{Q_{geo}} \tag{51}$$

While Q_{geo} is available from the theoretical number of atoms on the surface or an empirical value for a given potential interval.

Gold electrodes:

For polycrystalline gold electrodes an empirical value (390 µC/cm^2) for Q_{geo} in the oxygen region in 0.5 M H_2SO_4 is known and well accepted.[114]

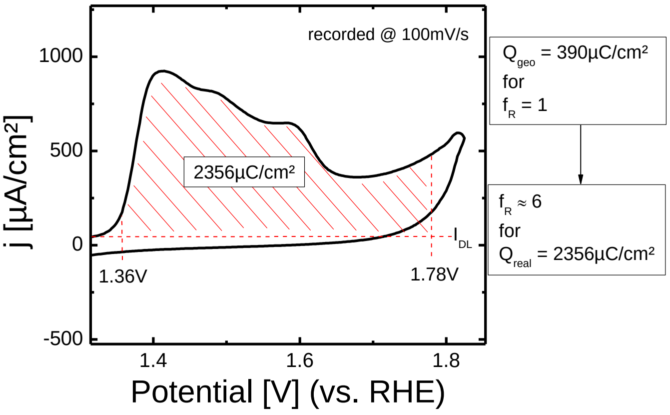

Figure 59 The important region for the integration to obtain the roughness factor. In this case the oxygen UPD region on polycrystalline gold.

Figure 59 shows an exemplary calculation of f_R from a CV, where Q_{real} is available via integration of the relevant region of the CV

$$Q_{real} = \int j v_s^{-1} dE \tag{52}$$

With v_s as sweep rate given by

$$v_s = \frac{dE}{dt} \tag{53}$$

The Baseline for the Integration is given by the current (i_{DL}), which is needed for charging the double layer.

Platinum electrodes:

For polycrystalline platinum electrodes an empirical value (210 µC/cm^2) for Q_{geo} in the hydrogen region in 0.5 M H_2SO_4 is known and well accepted.[114]

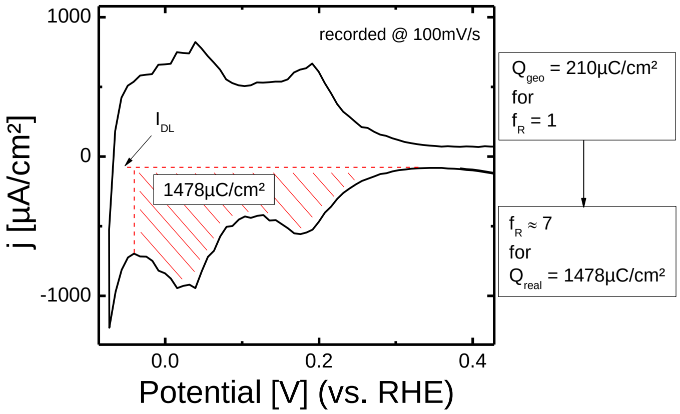

Figure 60 The important region for the integration to obtain the roughness factor. In this case the hydrogen UPD region on polycrystalline platinum.

Figure 60 shows an exemplary calculation of f_R from a CV, where Q_{real} is available via integration of the relevant region of the CV. The procedure is the same as for the gold electrode.

Calculation of the number of transferred electrons in DEMS measurements

Differential electrochemical mass spectrometry allows the potential resolved calculation of the number of transferred electrons (z) by correlating the faradaic current (i_F) at the electrode with the ion current (i_{ion}) of the mass spectrometer. Faradaic and ion current are proportional, with K^* as the constant of proportionality. The ion current is given by

$$i_{ion} = K^* \frac{i_F}{z} \tag{54}$$

So that the number of transferred electrons is given by

$$z = K^* \frac{i_F}{i_{ion}} \tag{55}$$

While K^* is obtained by calibration via a well-known reaction, for example the ORR in tetrabutylammoniumperchlorate (TBAClO$_4$) containing DMSO, where only superoxide is formed ($z = 1$).[72, 77, 101] Thus K^* is given by

$$K^* = \frac{i_{ion}}{i_F} \tag{56}$$

The ionization probability P_x^{ion} for species *x* then further provides the conversion of K^* (which refers to oxygen) to the calibration constant $K^{\#}$ for CO$_2$ via

$$K^{\#} = \frac{P^{ion}_{CO_2}}{P^{ion}_{O_2}} * K^{*} \tag{57}$$

While the fraction gives

$$\frac{P^{ion}_{CO_2}}{P^{ion}_{O_2}} \approx 1.4 \tag{58}$$

AC-voltammetry

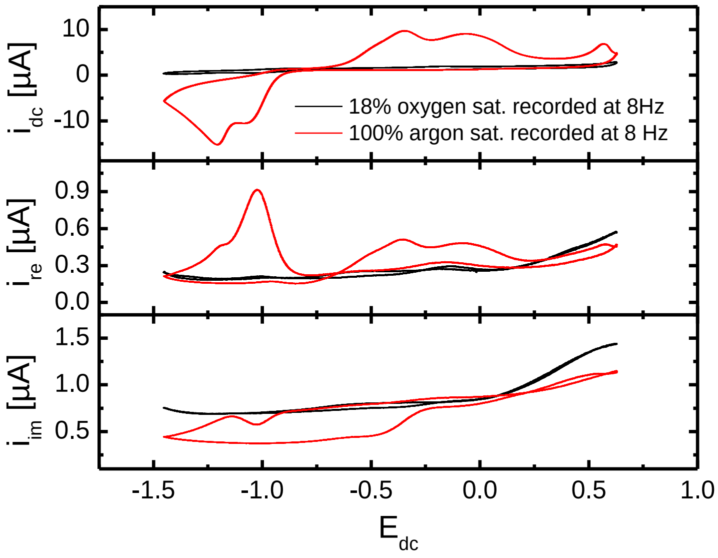

Figure 61 ACV for 0.1 M $LiClO_4$ in DMSO recorded at a frequency of 8 Hz for the ac signal (sweep rate: 8 mV/s, current range: 100 µA, sensitivity of lock-in amplifier: 300 mV, temperature: 27 °C). The black curve was recorded in absence of oxygen, the red curve for mixture of 18% oxygen with argon.

Stable CV for Pt single crystals

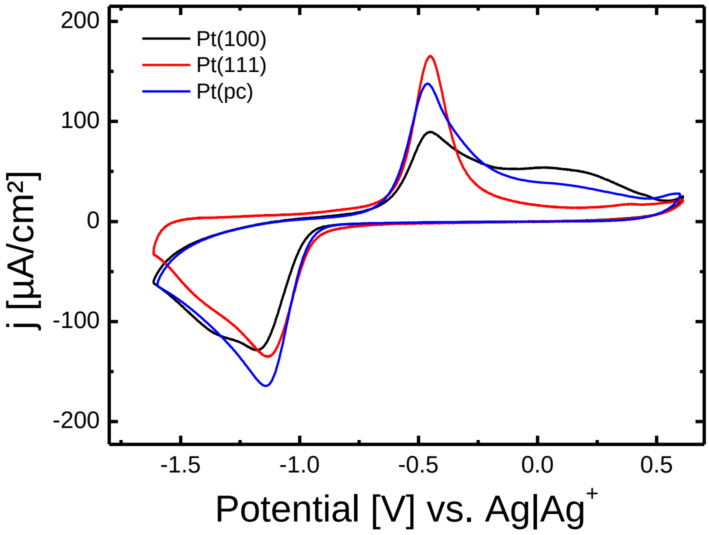

Figure 62 Stable cyclic voltammograms of Pt(111) and Pt(100) in 0.1 M $LiClO_4$ containing DMSO at 50 mV/s in a usual H-Cell. CE was a Pt-sheet and RE was a Ag-wire immersed into 0.1 M $AgNO_3$ containing DMSO.

Original Data of Pt(hkl) and Pt(pc) in DEMS Experiments

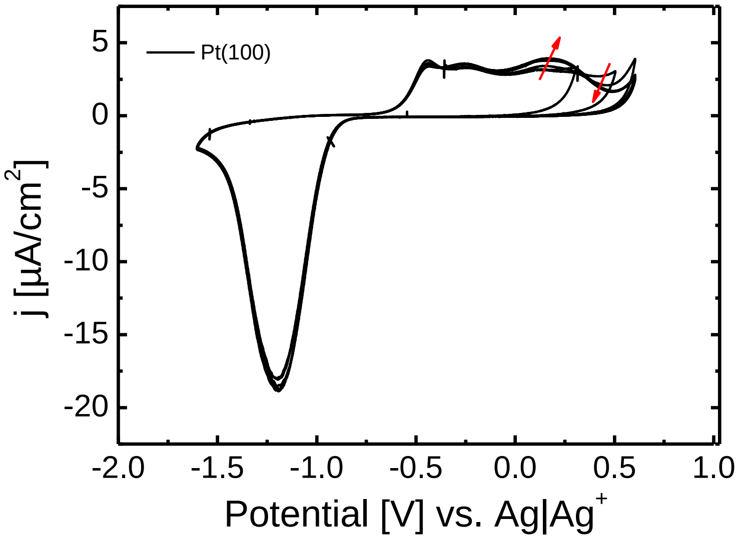

Figure 63 Consecutive CVs of Pt(100) in ($Ar^{80\%}O_2^{20\%}$)-saturated 0.5 M $LiClO_4$ containing DMSO at 10 mV/s and 5 µl/s flow rate. Red arrows indicate trend with increasing upper limit. The last five cycles (upper limit kept constant) are almost overlapping.

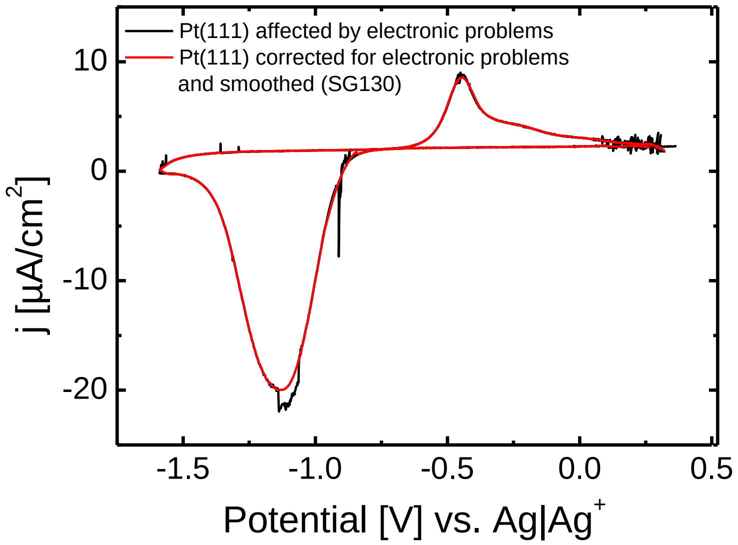

Figure 64 Second CV of Pt(111) in ($Ar^{80\%}O_2^{20\%}$)-saturated 0.5 M $LiClO_4$ containing DMSO at 10 mV/s and 5 µl/s flow rate. Red curve shows the same measurement as black curve (original data), while a correction was made for the electronic problems at approximately -1.1 V. Furthermore red curve is smoothed using Savitzky-Golay method. Electronic problems during first cycle were too large for a reasonable correction.

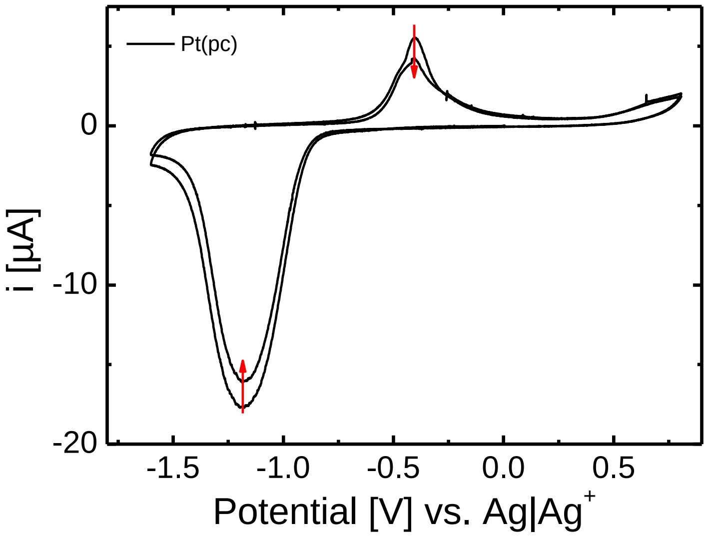

Figure 65 First and Second cycle of Pt(pc) in ($Ar^{80\%}O_2^{20\%}$)-saturated 0.5 M $LiClO_4$ containing DMSO at 10 mV/s and 5 µl/s flow rate. Red arrows indicate trend with increasing cycle number.

The critical role of CO_2

As shown in ref. [123] CO_2 has to be avoided, as it is incompatible with Li_2O_2. In this study CO_2-contaminations were carefully avoided by using purging gases with high purity. The CO_2 generated from carbonate oxidation only reaches negligible levels under the measurement conditions.

Chemicals

Table 5 Chemicals.

Chemical compound (specification)	**Provider**	**Sum formula**
Potassium perchlorate (for analysis)	EMSURE	$KClO_4$
Silver nitrate (99%)	CHEMPUR	$AgNO_3$
Dimethyl sulfoxide (99.7, extra dry)	ACROS ORGANICS	C_2H_6OS
Potassium bromide for analysis (99%)	ACROS ORGANICS	KBr
Lithium perchlorate (battery grade)	SIGMA ALDRICH	$LiClO_4$
Argon (99.999%)	Air liquide	Ar
Oxygen (99.9995%)	Air liquide	O_2
Nitrogen (99.999%)	Air liquide	N_2
Argon/Oxygen (80% / 20%)	Air liquide	$Ar^{80\%}/O_2^{20\%}$

10.2 Electrochemical Reduction of O_2 in Ca^{2+}-containing DMSO: Role of Roughness and Single Crystal Structure

10.2.1 Abstract

This work compares the oxygen reduction reaction (ORR) in Ca^{2+} containing dimethyl sulfoxide (DMSO) at well-ordered and rough electrode surfaces using cyclic voltammetry, differential electrochemical mass spectrometry (DEMS), rotating ring disk electrode (RRDE) and atomic force microscopy (AFM). Slightly soluble CaO_2 is the main product during early ORR on gold electrodes; after completion of a monolayer of CaO and/or CaO_2, which is formed in parallel and in competition to the peroxide, only superoxide is formed. When the monolayer is completely closed on smooth annealed Au no further reduction occurs, whereas on rough Au a defect – rich layer allows for continuous formation of superoxide. CaO_2 formed either via two subsequent 1 e^- transfer steps or by disproportionation of superoxide may be deposited on top of the CaO/CaO_2 adsorbate layer. The slow dissolution of the peroxide particles is demonstrated by AFM.

While a smooth CaO/CaO_2 covered electrode shows severe deactivation, and a CaO/CaO_2 covered rough electrode allows for diffusion limited superoxide formation, on single crystals peroxide formation is more pronounced. The reason is most likely the lack of nucleation sites for the blocking CaO/CaO_2 layer.

RRDE investigations showed sluggish reoxidation kinetics of the dissolved peroxide most likely due to ion pairing with Ca^{2+}. Utilizing an unusual approach we were able to estimate the apparent transfer coefficient α_{app} via variation of the electrode roughness, confirming the result of the usual Tafel analysis and indicating an equilibrated first 1 e^- transfer.

10.2.2 Introduction

Increasing necessity for renewable energy sources requires means to store the energy, as it cannot be easily generated on demand. Not only pumped-storage power plants and energy storage by electrochemical generation of hydrogen, but also the storage in large scale batteries is a possibility one could think of looking towards the future. As next-generation batteries, metal-air batteries might be the way to go in the future. Their big advantage is not only the high energy density, which is primarily important for electromotive applications, but also – and probably more importantly - the fact that less abundant elements like Co are not needed in stoichiometric amounts for insertion materials at the cathode. Though metal-air battery research is a common research topic nowadays, the performance of this type of battery still remains insufficient and a lot of work still needs to be done. Li-O_2[68, 72, 82, 92, 99, 113, 124, 125], Na-O_2[88, 126-128], and Mg-O_2[129-131] systems already were topic of research and looking towards further cations like potassium[132-134] and calcium seems reasonable, as the ORR product distribution depends on the cation.[47, 48, 72, 135, 136] The use of more abundant active materials than lithium for the anode may also be necessary for a wider application. Calcium was already proposed as interesting candidate, as it is one of the most abundant elements in the earth's crust and still has a sufficiently high theoretical energy density (Ca-air) to replace Li-ion batteries. Both ORR/OER[47, 48] and metal deposition[45, 137] were investigated in Ca-ion containing aprotic electrolytes.

The ORR and OER were investigated on several cathode materials. For the ORR in $Ca(ClO_4)_2$ containing DMSO on Pt, Rh, Glassy Carbon and Ru a one electron process was observed, while for Au a two electron process is found.[47] It was shown, that Au plays a special role in the mechanism, as on gold in Mg^{2+}, Ca^{2+}, Sr^{2+} and Ba^{2+} containing DMSO, the two electron process is dominating the ORR, which is not the case for Glassy Carbon and platinum electrodes.[48] This is of special interest, as the formation of O_2^- and further solution mediated disproportionation to O_2^{2-} and O_2 might lead to significant amounts of highly reactive singlet oxygen, which will decompose the electrolyte.[96, 98, 138] Upon reducing the relative amount of generated O_2^-, one might increase the reversibility and thus the cycle life of the battery. At this point, the current work starts with further investigation on the ORR and OER in $Ca(ClO_4)_2$ containing DMSO using techniques like DEMS to identify oxygen consumption/evolution and RRDE to further investigate the nature of the generated oxygen species during the ORR. The influence of the electrode surface structure was taken into account by using single crystalline electrodes on the one hand and rough electrodes on the other. A similar approach was also used to investigate the ORR/OER in case of Li^+ containing DMSO in our earlier work.[5] We found that mostly Li_2O_2 is formed on rough electrodes during the ORR and thus showed once again, that the surface structure strongly affects the electrochemical reactions. This work strongly focuses on the ORR/OER mechanism in Ca^{2+} containing DMSO and the influence of the surface structure (single crystal orientation on the one hand and high roughness factors on the other). It supplements a previous study in which already a transition from mixed O_2^- and O_2^{2-} formation to exclusively O_2^- formation was observed on smooth electrodes. [139] The study further showed that the blocking thin film mainly consist of $Ca(O_2)_2$, CaO_2 and CaO (identified by XPS) and is formed on Au and Pt electrodes. In other previous studies we have shown that reliable and clean double layer studies can be performed on Au(111) in aprotic solvents, e.g. pzc measurements.[140]

10.2.3 Experimental

Electrodes: The gold electrodes used in this study had a diameter of 1 cm resulting in a geometrical surface area of 0.785 cm^2, while RRDE disk electrodes had a diameter of 0.5 cm and 0.457 cm and thus a geometrical surface area of 0.196 cm^2 (exchange disk electrode) or 0.164 cm^2 (thin gap disk electrode) respectively. Ring electrodes were also made of gold, while the theoretical collection efficiency (N_0) was 0.25 for the exchange disk electrode and 0.22 for the thin gap disk electrode.

RRDE setup: The RRDE experiments were conducted in a usual H-Cell under argon atmosphere. The Au working electrode (WE), Au counter electrode (CE) and Ag reference electrode (RE) were connected to a bipotentiostat (TACUSSEL BIPAD B1), while electrode rotator was connected to a PINE rotation control. Counter electrode was a gold sheet and the reference electrode was a silver wire immersed into 0.1 M $AgNO_3$ containing DMSO. Disc currents were normalized to the geometrical surface area of the disk electrode ($A_{\mathrm{geo}}^{\mathrm{disk}}$); ring currents were normalized not only to the collection efficiency N_0 but also to the geometrical surface area of the disk electrode ($A_{\mathrm{geo}}^{\mathrm{disk}}$) for 1 to 1 comparability.

DEMS setup: DEMS measurements were conducted using a Dual Thin Layer flow through cell, where WE, CE and RE were connected to a homebuilt bipotentiostat. The electrolyte outlet was connected to a peristaltic pump (SPETEL Perimax). The CEs were gold wires and the RE was a silver wire immersed into 0.1 M $AgNO_3$ in DMSO. The RE was contacted to the working electrolyte via a Teflon tube (sealed with a rough glass bead) filled with the silver containing solution. The end of the glass bead was immersed into the working electrolyte, while the open end was immersed into the RE electrolyte. The size of the thin layer compartment of the WE and of the compartment of the porous Teflon membrane (serving as the interface to the vacuum) were defined by a Teflon spacer of 200 µm and 100 µm thickness and a diameter of 6 mm (electrode area of 0.283 cm^2), as in our previous study.[5] More detailed information about the DEMS setup and the Dual Thin Layer cell can be found elsewhere.[48, 109-112] The faradaic current in DEMS measurements was smoothed using the Savitzky-Golay method (100 mV window) to account for the periodic signal caused by the peristaltic pump.

AFM setup: A disc type of Au(111) single crystal(diameter: 10 mm and thickness: 3 mm) purchased from MaTecK GmbH was used as working electrode. Gold and platinum wires were used as counter and quasi-reference (Pt|PtO) electrodes, respectively. The standard sealed chamber (Agilent 5500) was purged with Ar before transferring the AFM cell. After the AFM-cell filled with electrolyte was loaded on the AFM, Ar was purged for around 10 min because the AFM-cell was exposed to the atmosphere during assembling and transfer. O_2 was purged during the experiment to maintain the concentration of oxygen in the electrolyte (100% oxygen saturation). Sharp silicon tips (PPP-CONTSC, tip radius <10 nm) were used with normal spring constants of 0.1±0.05 N/m. For AFM measurements the single crystals were prepared by flame annealing.

Electrode cleaning: Prior to any experiment, the electrodes were cycled in 0.5 M H_2SO_4 until the well-known shape of the cyclic voltammogram (CV) could be observed. In case of contaminations, the electrodes were cleaned further. The gold electrodes were oxidized in 0.5M H_2SO_4 until the surface was covered by gold oxide. Then the formed gold oxide was removed in concentrated hydrochloric acid. After the cleaning procedure, the voltammetry was checked again to exclude remained contamination.[33, 34]

Preparation of single crystals: The single crystals were cleaned as described above and annealed in a N_2-purged induction heat cell afterwards. After the annealing, the crystals cooled down in the same cell above N_2-saturated Milli-Q water.[33, 34] Upon reaching room temperature, the electrodes were characterized in H_2SO_4 once every day prior to an experiment to proof the setup. When the setup showed good performance, the electrodes were again prepared and transferred to the experimental setup.

The electrode roughening and the single crystal preparation procedures were the same as in an earlier publication.[5] The electrode roughness of polycrystalline electrodes equals one unless stated otherwise. The single crystals used for AFM experiments were prepared by flame annealing.

Chemicals: Calcium perchlorate tetrahydrate (99%, Sigma Aldrich) was dried (8h) under reduced pressure to obtain a white powder of anhydrous $Ca(ClO_4)_2$. Tetrabutylammonium perchlorate (≥99%, Sigma Aldrich), silver nitrate (99%, CHEMPUR), potassium bromide (99%, ACROS ORGANICS) and Dimethyl sulfoxide (99.7%, extra dry, over molecular sieve) were used as received. DMSO, $CaClO_4$ and $TBAClO_4$ were stored inside an *MBraun* glovebox under argon atmosphere. For purging and electrolyte saturation argon (99.999%, Air liquide), nitrogen (99.999%, Air liquide), oxygen (99.9995%, Air liquide), argon oxygen mixture (80%/20%, Air liquide) and argon hydrogen mixture (95%/5%, Air liquide) were used.

10.2.4 Results

Investigations in resting/quiescent solution

We already reported that the oxygen reduction reaction (ORR) in Ca^{2+} containing DMSO on Pt, Rh, Glassy Carbon and Ru leads to a large extend to the formation of soluble $Ca(O_2)_2$ whereas on gold electrodes, the oxygen reduction reaction leads to the formation of soluble CaO_2.[47] To further understand the effect of the electrode and the electrode surface structure concerning the ORR, experiments on gold single and poly crystals were conducted.

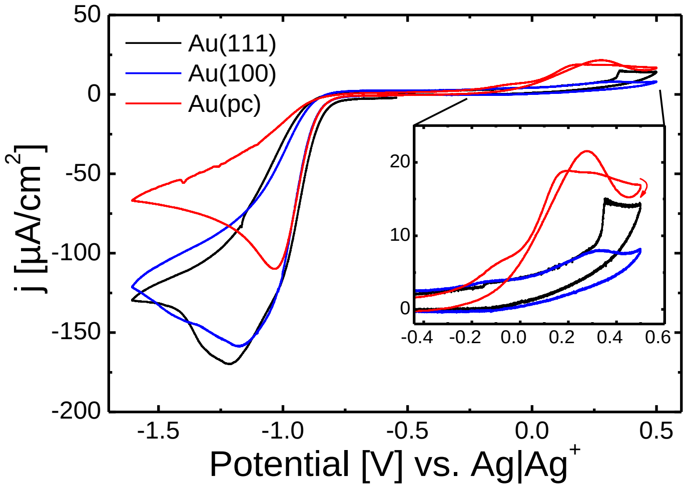

Figure 66 The first recorded cyclic voltammogram for single and poly crystalline gold electrodes at 10 mV/s in (20% O_2 + 80% Ar)-saturated 0.1 M $Ca(ClO_4)_2$ containing DMSO after immersion at -0.5 V vs Ag|Ag$^+$. The current is normalized to the geometrical surface area. Inset shows OER region more detailed. The poly crystal was prepared/annealed like the single crystals. Only the 1st sweep is shown because of probable changes in surface structure in subsequent scans (cf. remark SI A).

Figure 66 shows the first cyclic voltammogram of single and poly crystalline gold electrodes in (20% O_2 + 80% Ar)-saturated 0.1 M $Ca(ClO_4)_2$ containing DMSO vs Ag|Ag$^+$ at 10 mV/s after immersion at -0.5 V. Starting in cathodic direction, the absolute value of the current density increases to a maximum close to -1.0 V for the polycrystalline gold electrode. In case of Au(111) the feature at -1.0 V appears as a shoulder prior to a peak close to -1.25 V. In case of Au(100) no such feature close to -1.0 V is visible as the current increases to a maximum close to -1.15 V. After the maxima the current decreases, while in case of Au(111) and Au(100) a shoulder is visible in the decreasing current. Furthermore, the ORR onset in case of Au(111) is slightly shifted positive compared to Au(100) and Au(pc), which almost overlap during the ORR onset. After going to zero in anodic direction, the oxidation starts with a shoulder at -0.14 V, followed by a broad peak of low current in case of Au(100), a sharp peak of slightly larger current in case of Au(111) and a broad peak with a much larger current in case of Au(pc). After the change in sweep direction at 0.5 V, the current decays monotonously to zero in case of Au(111) and Au(100). In case of Au(pc) the current increases again to a maximum close to 0.25 V before it decreases to zero.

Calculating the theoretical ORR peak current density for this system with the Randles-Sevcik equation for reversible (or totally irreversible) processes (see SI) leads to 153.5 µA/cm^2 (or 85.5 µA/cm^2 for z_α=1, 120.9 µA/cm^2 for z_α=2) for a two electron process and for a one electron process 54.5 µA/cm^2 (or 42.7 µA/cm^2 for z_α=1), where z_α is the number of electrons transferred in the rds. The comparison with the experimental values which are larger than 100 µA/cm^2 indicates peroxide as main product. Combining this fact with the lower number of defects in single crystalline surfaces compared to poly crystalline surfaces, explains the observed differences in ORR and OER current: Thus, the nucleation of CaO_2 (or possibly CaO) is hindered at both Au(111) and Au(100) surfaces but facile at Au(pc) surfaces. This leads to a faster decay in ORR current at Au(pc) electrodes and a larger OER current due to increased deposition of CaO_2 on the electrode surface as compared to Au(111) and Au(100). This also explains the much higher oxidation charge of ca. 1860 $\mu C/cm^2$ at the polycrystalline surface as compared to the single crystal surfaces.

Atomic force microscopy (AFM) investigations

To further investigate the adsorbate/deposit an in situ AFM measurement was conducted in 0.1 M $Ca(ClO_4)_2$ containing DMSO on Au(111). Figure 67a shows the CV in the AFM cell.

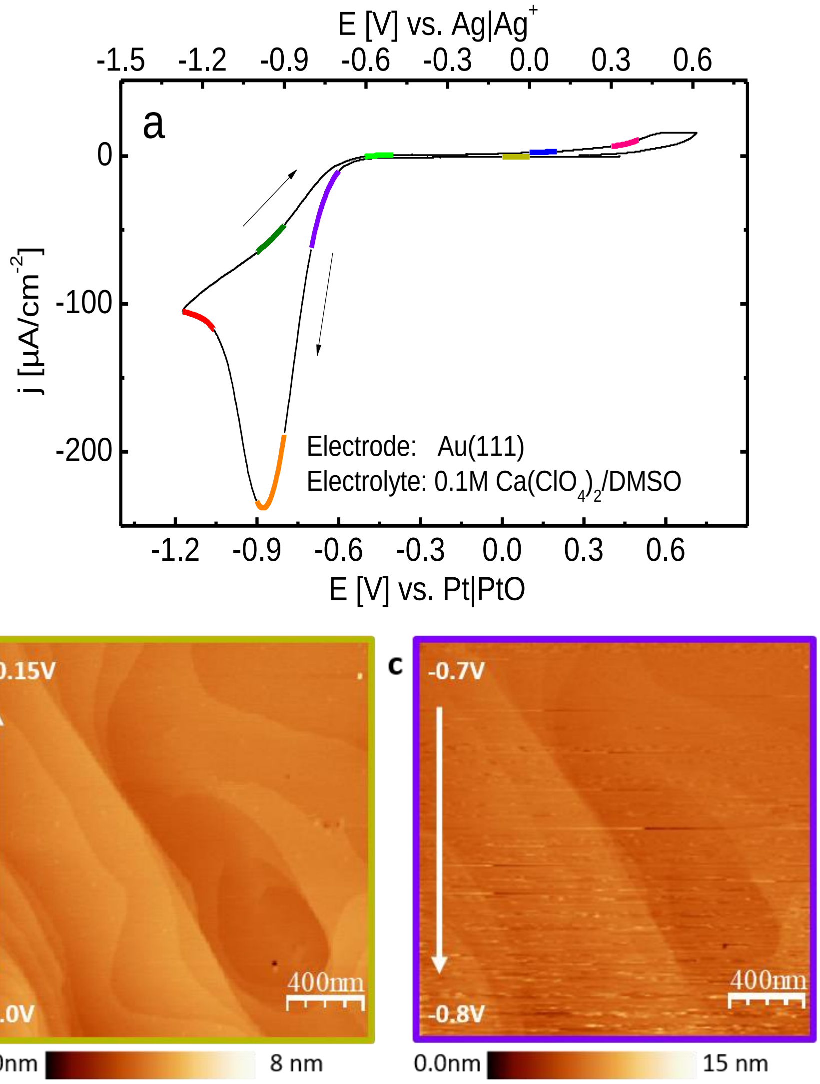

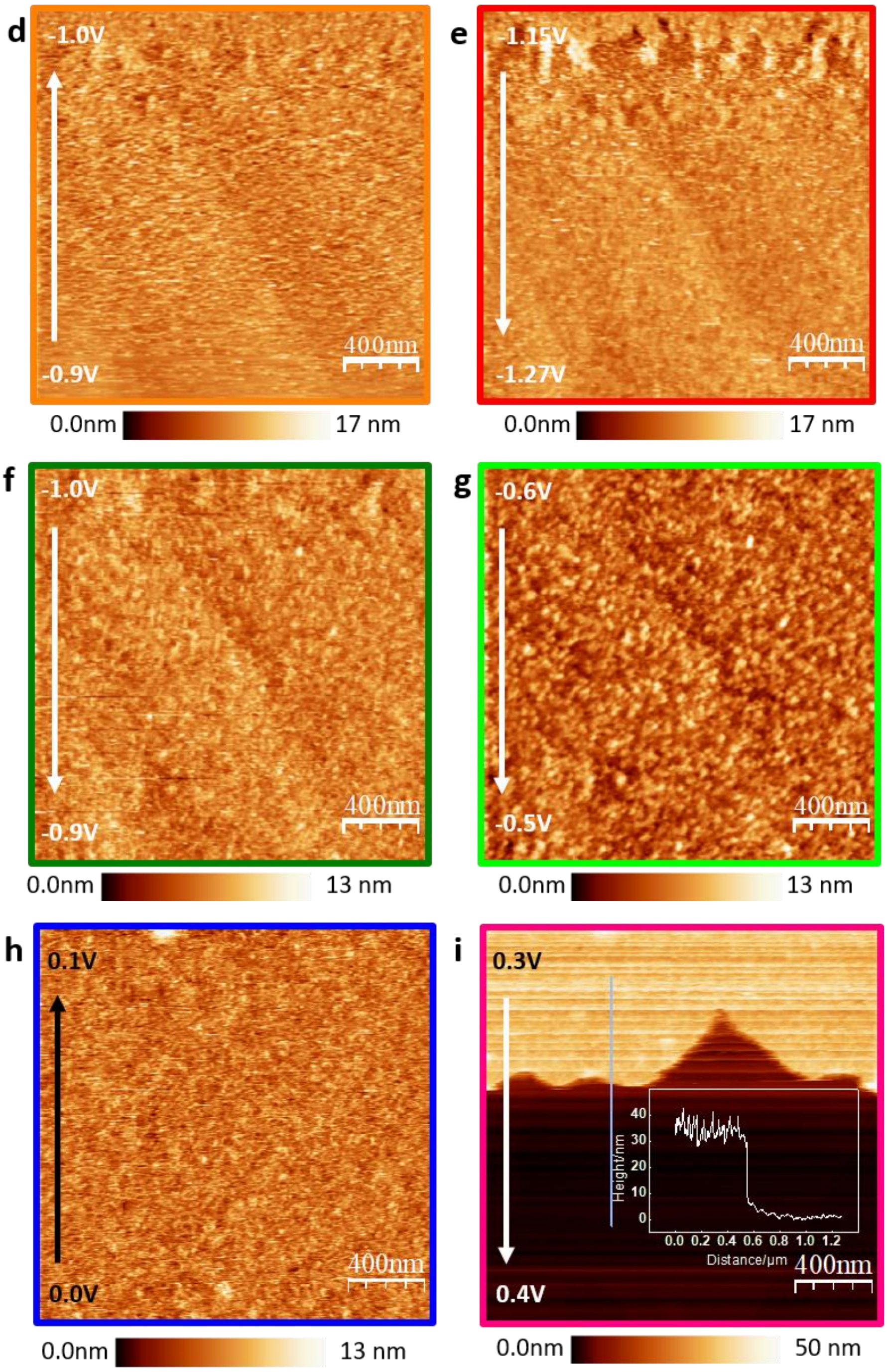

Figure 67 Voltammetry of Au(111) in an AFM-cell at 5 mV/s in 0.1 M $Ca(ClO_4)_2$ containing DMSO (100% oxygen saturated) (a). In situ AFM images show the topography on Au(111) in the indicated potential ranges upon discharge (b-e) and upon charge (f-i), all potentials refer to $Ag|Ag^+$. The inset image of (i) shows the height profile. The color code (AFM-frame and CV-line) denotes the actual potential region. The arrow in the AFM images indicate the scan direction. Integral and proportional gains were 6 and 7, respectively. Scan size was 2X2 μm^2 and the scan rate was 19 nm/s.

Figure 67b shows that prior to ORR large and clean terraces can be observed between 0.0V and -0.15 V vs. $Ag|Ag^+$. When the potential passed the onset of ORR, some particles are deposited on the surface appearing as noise in the Figure 67c and these particles grow to a dense layer upon sweeping more negative than -0.8 V vs. $Ag|Ag^+$ (Figure 67d-e). Then continuing in anodic direction after the negative potential limit of -1.27 V vs. $Ag|Ag^+$, the particles seem to grow continuously until a potential of -0.5 V vs. Ag|Ag$^+$ is attained. The apparent growth of the particles during the anodic scan indicates a further deposition of solid CaO_2 (that this is really CaO_2 will be shown below) from O_2^{2-} directly formed at the electrode or formed via disproportionation of the dissolved superoxide (formed at the most negative potentials). Ostwald ripening might also play a role. While sweeping the potential from -0.5 V to -0.1 V vs. Ag|Ag$^+$, the interaction between the AFM tip and the electrode surface was getting unstable and the tip was retracted. The subsequent images therefore were recorded at a different position. Figure 67h was recorded after re-approaching the tip. It is remarkable that the size of the particles is reduced at a more positive potential than -0.5 V vs. Ag|Ag$^+$. We assume that the dissolution of peroxide leads to the reduced size, but this may also be caused by the shift in the scanned area. Figure 67i shows that the deposited particles seem to quickly dissolve at the potential of OER without any appreciable charge flow and the inset figure shows that the height of the deposited layer is around 30 nm. Furthermore in a similar experiment (Figure 78), the potential was stopped at -0.65 V vs. Ag|Ag$^+$ (≈ -0.55 V vs. Pt|PtO) (after ORR) and images were taken every 3 minutes. After 6 minutes, the particles formed during ORR were gone during the scan. This observation further demonstrates the slow dissolution of the formed particles without oxidation and also explains that hardly any charge is flowing during the dissolution in Figure 67i. Note that the dissolution of the particles might have been accelerated by the scanning tip (e.g. by induced convection by moving AFM-tip). This measurement clarified, that a bulk layer of CaO_2 forms at the electrode in the absence of convection, but slowly dissolves without oxidation. However, at this point it is not yet clear whether the thick layer is the reason for the blockade of the electrode.

Investigations under flow-through conditions using Differential Electrochemical Mass Spectrometry

Differential Electrochemical Mass Spectrometry (DEMS) provides information about the product distribution, the consumption and generation of volatile species and furthermore the number of transferred electrons during ORR and OER after a calibration measurement.

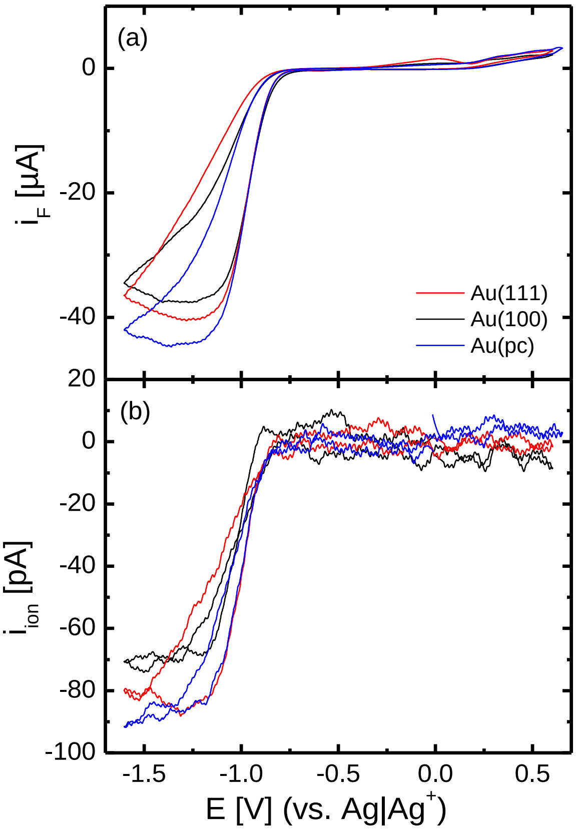

Figure 68 Cyclic voltammetry of single-/ and polycrystalline gold electrodes in (20% O_2 + 80% Ar)-saturated 0.4 M $Ca(ClO_4)_2$ containing DMSO at 10 mV/s and 5 µl/s flow rate using a thin layer flow through cell (a). Potential dependent ion current for mass 32 (O_2) for single-/polycrystalline gold electrodes (b).

Figure 68a) shows the cyclic voltammetry (second cycle) of polycrystalline and single crystalline Au electrodes in 0.4 M $Ca(ClO_4)_2$ containing DMSO saturated with (20% O_2 + 80% Ar)together with the ion current for mass 32 (O_2; Figure 68(b)). The absolute faradaic current increases to a plateau for the diffusion limited formation of predominantly CaO_2, indicated by the number of transferred electrons (Figure 69).

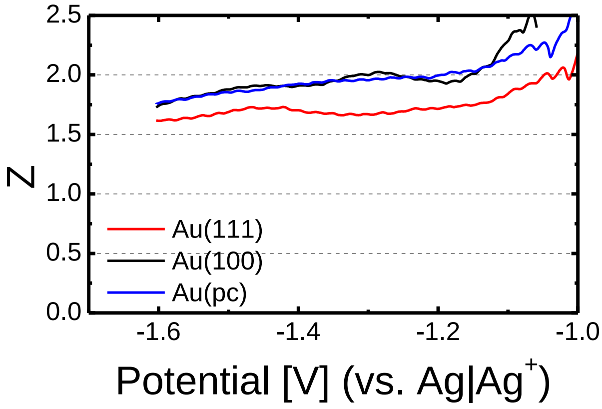

Figure 69 Potential dependent number of transferred electrons per O_2 during the ORR in cathodic direction for single-/ and polycrystalline gold electrodes in (20% O_2 + 80% Ar)-saturated 0.4 M $Ca(ClO_4)_2$ containing DMSO at 10 mV/s and 5 µl/s flow rate using a thin layer flow through cell.

The number of transferred electrons starts from $Z \approx 2$ (in case of Au(111) $Z \approx 1.7$) at -1.1 V and stays constant during the remaining cathodic sweep. This in combination with the fact, that almost no reoxidation current is observed, leads to the assumption, that predominantly soluble CaO_2 is formed during the ORR on all gold electrodes, as already suggested in ref. [47]. No strong effect of the single crystal surface structure is observed (only in case of Au(111), the number of transferred electrons during ORR is slightly lower compared to Au(100)/Au(pc); this effect might be due to a slight change in calibration constant of the Spectrometer). Comparing the ORR during cathodic and anodic sweep one observes a hysteresis, indicating a change in electrode activity, while for polycrystalline gold electrodes the hysteresis is smaller. This is plausible, as we assume the formation of an insoluble (adsorbed) CaO_2/CaO layer on the electrode surface (this will be discussed in detail in the RRDE chapter below). This hysteresis was already found when comparing gold with Glassy Carbon in Ca^{2+} containing DMSO.[47] As already observed in Figure 66, also under the conditions of Figure 68 the peroxide reoxidation is not finished at the end of the anodic scan, but continues after potential reversal.

The effect of electrode roughness is shown in Figure 70. Overall, the cyclic voltammetry for Au does not change much with increasing roughness. The hysteresis is reduced, indicating less blocking for rougher electrodes. In the OER region, an oxidation peak only is clearly visible for the highest roughness factor. For all electrode roughness factors, the maximum absolute (limiting) current during the ORR remains the same, indicating that the CaO_2 formation really is diffusion limited. The half wave potential of the ORR shifts positive with increasing electrode roughness due to the increasing effective rate constant; this will be further analyzed below.

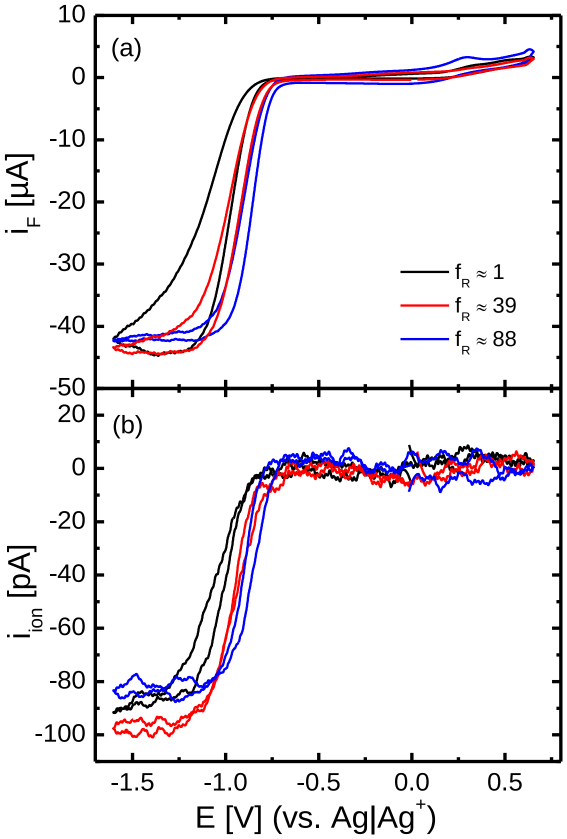

Figure 70 Cyclic voltammetry of roughened polycrystalline gold electrodes (a) in (20% O_2 + 80% Ar)-saturated 0.4 M $Ca(ClO_4)_2$ containing DMSO at 10 mV/s and 5 µl/s flow rate vs Ag|Ag$^+$ using a thin layer flow through cell. Potential dependent ion current for mass 32 (O_2) (b).

Figure 71 shows the potential dependent number of transferred electrons for the roughened gold electrodes. The number of transferred electrons constantly stays above a value of 1.7, indicating that the two-electron process is predominant during the whole ORR on gold surfaces.

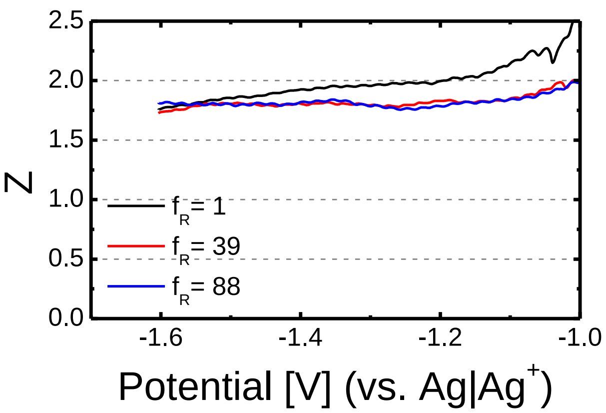

Figure 71 Potential dependent number of transferred electrons per O_2 during the ORR in cathodic direction for roughened gold electrodes in (20% O_2 + 80% Ar)-saturated 0.4 M $Ca(ClO_4)_2$ containing DMSO at 10 mV/s and 5 µl/s flow rate using a thin layer flow through cell.

Rotating Ring Disk Electrode (RRDE) investigations

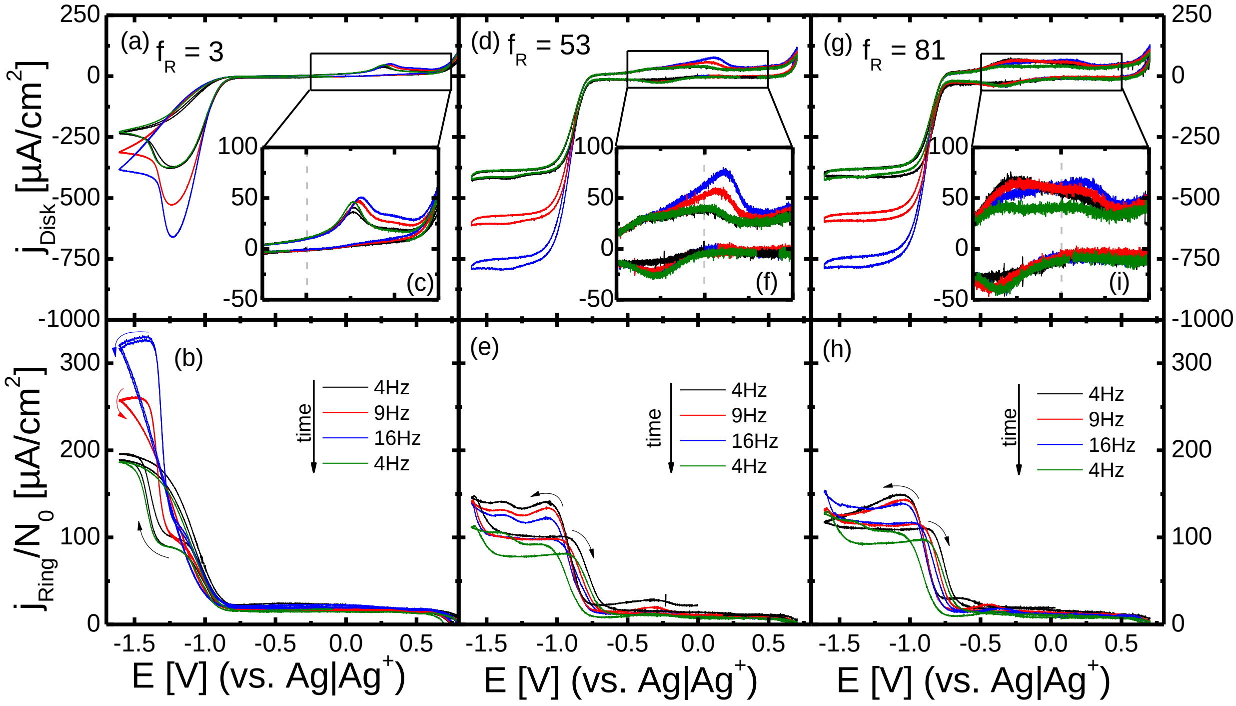

Figure 72 Cyclic voltammetry of roughened gold electrodes (exchange disk electrodes) in (20% O_2 + 80% Ar)-saturated 0.1 M $Ca(ClO_4)_2$ containing DMSO at 20 mV/s, E_{ring} = 0.4 V and 4-16 Hz rotation frequency vs Ag|Ag$^+$ using a usual H-cell. Disk current density is shown in (a), (d) and (g). The ring current ((b), (e) and (h)) is normalized to the collection efficiency N_0 and A_{geo}^{disk}. The anodic signal is magnified in (c), (f) and (i), while the dashed grey line denotes 0 V.

To demonstrate the effect of higher convection and different roughness factors, Figure 72 shows RRDE experiments for polycrystalline gold electrodes in (20% O_2 + 80% Ar)-saturated 0.1 M $Ca(ClO_4)_2$ containing DMSO. For higher roughness factors, the CV shape is similar to the DEMS case in the previous chapter; the ORR starts around -0.8 V in cathodic direction with peroxide formation. However, in case of the lowest electrode roughness (Figure 72(a)), the decreasing reduction current indicates a transition from peroxide to superoxide formation. This transition from the 2 e^- reduction to a 1 e^- reduction had been found before and explained by the formation of a CaO/CaO_2 adsorbate layer, which had also been characterized by XPS.[139] The ORR is accompanied by an increase in ring current, which is astonishingly low as long as peroxide is the main product. This is visible in Figure 72(b) as shoulder (≈ -1.2 V) in the ring current and in Figure 72(e, h) as plateau during ORR. The ring current due to O_2^- reoxidation at the lower potential limit corresponds to that expected from the disc current. The ring current caused by re-oxidation of the generated peroxide is not increasing with rotation frequency, but decreases with time. This will be addressed further below. During the anodic scan only a small current for the OER is observed at the disk electrode visible in Figure 72(c, f, i). With increasing electrode roughness, the overall current during the anodic scan increases, especially below 0 V. It is also notable that in Figure 72(c, f, i) the anodic peak above 0 V increases with increasing rotation frequency while in Figure 72(i) the current below 0 V decreases with increasing rotation frequency. (Also cf. remark B in the SI.)

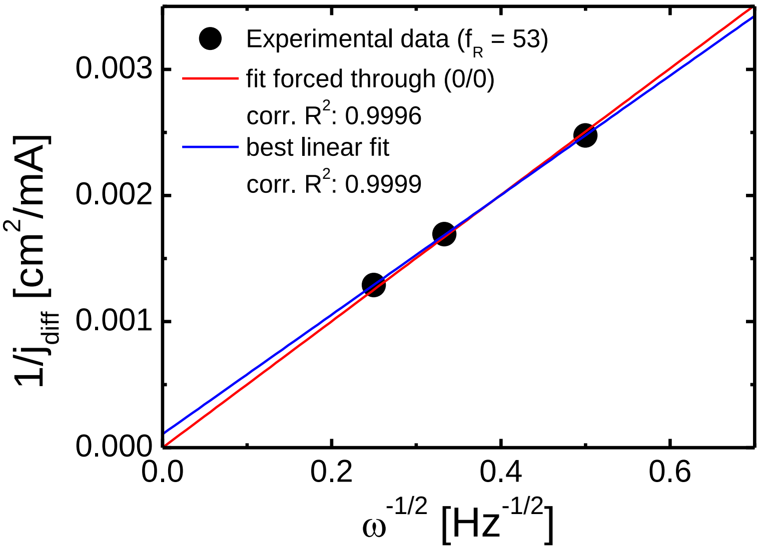

Figure 73 Plot of the inverse diffusion limited current (at -1.25 V for f_R = 53; Figure 72 (d)) vs the inverse square root of the rotation frequency (dots), linear fit forced through (0/0) (red line) and best linear fit (blue line) confirming diffusion limitation.

Figure 73 shows a plot of inverse limited ORR current vs inverse square root of rotation frequency taken from Figure 72(d). The plot shows that the ORR at electrodes with f_R ≥ 53 really is diffusion limited, as the fit deviates very little from a fit going through the origin. Using the dynamic viscosity of DMSO [141] a diffusion coefficient of $2.48 * 10^{-5}\ \mathrm{cm}^2/s$ is obtained from the slope. This value is close to those obtained by a non-electrochemical method for 0.1 M solutions of Li^+, Na^+, K^+, Rb^+, Cs^+ and TBA^+ in DMSO. [40, 41] Here, we used this method, in which the rate of diffusion of a volatile species through a thin, liquid layer between two membranes is determined by mass spectrometric detection for our 0.1 M Ca^{2+} containing DMSO. We obtained $D_{\mathrm{O}_2} = 2.18 * 10^{-5}\ \mathrm{cm}^2/\mathrm{s}$, which is in good agreement with the value obtained from electrochemical RDE measurements.

Concerning the decrease of peroxide formation rate during ORR at smooth electrodes and transition to the 1 electron superoxide formation, we had suggested that the electrode is slowly covered by an adsorbate (CaO_2 or CaO), which not only completely blocks peroxide formation, but also inhibits superoxide formation to some extent as it becomes a thin, closed layer.[139] To confirm this we conducted an RRDE experiment, where the Au electrode was first saturated with this CaO_2/CaO adsorbate by holding the potential at -1.6 V during the scan for 5 minutes at 9 Hz rotation frequency. As the CaO_2/CaO layer forms at this potential, superoxide formation becomes predominant as visual by the current decreasing to a constant value of -265 µA/cm^2, i.e. 50% of the initial current. To exclude a thick layer of CaO_2 deposit as being the reason for the inhibiting effects, the disk potential was then stepped to -0.75 V (just before ORR region) to dissolve possibly formed multilayers for 10 minutes (still at 9 Hz rotation frequency). After this procedure the Au surface is only covered with a CaO_2/CaO adsorbate layer (as the thick deposit is dissolved) and CVs were recorded starting in cathodic direction, consecutively opening the anodic limit from -0.75 V to +0.7 V (see Figure 79).

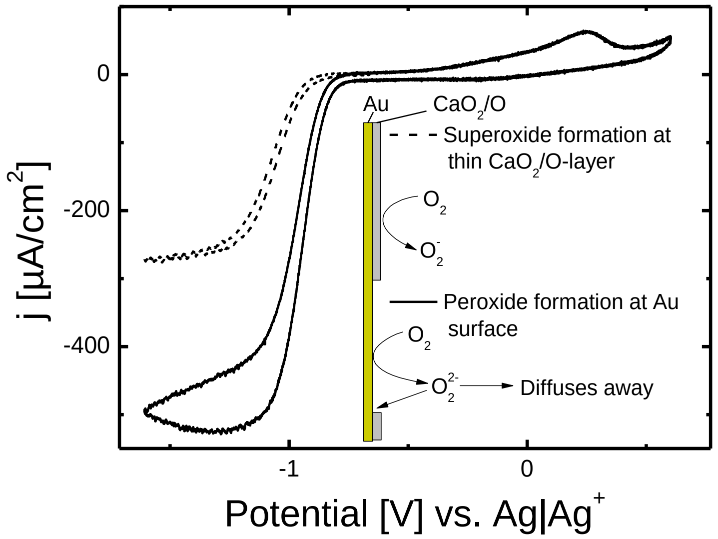

Figure 74 Voltammetry of a CaO_2/O covered (dashed line) and regenerated (solid line) Au (exchange disk) electrode in (20% O_2 + 80% Ar)-saturated 0.1 M $Ca(ClO_4)_2$ containing DMSO at 20 mV/s and 9 Hz rotation frequency vs Ag|Ag$^+$ using a usual H-cell. The disk current is normalized o the geometrical disk surface area. The disk electrode roughness was $f_R \approx 13$.

Figure 74 is an extract of Figure 79, showing the CV after the Au electrode is covered with this thin, but closed CaO_2/CaO film starting from the hold potential of -0.75 V in cathodic direction (dashed line) and a CV (solid line) after the electrode is regenerated during the consecutively opening of the upper potential limit to +0.7 V. (Simply cycling to positive potentials (above 0.3 V) to desorb the adsorbate layer also would have been sufficient). But the approach used here (Figure 79) further shows that the electrode begins to slowly reactivate as the upper limit reaches 0.3 V, which indicates 0.3 V as the potential required for CaO_2/CaO adsorbate oxidation. Note that in the first sweeps up to 0.4 V oxidation of this adsorbate is slow and remains incomplete, whereas in subsequent sweeps the maximum current is at 0.25 V (peak potential). This indicates a nucleation and growth behavior for the free sites, as it was observed earlier for Ca^{2+} - electrolytes on smooth Au electrodes[139] and for Na^+ - electrolytes on smooth Pt (but not on Au)[142]. As visualized in the schematic in Figure 74, on top of the CaO_2/CaO film oxygen is exclusively reduced to superoxide. The continuous reduction is astonishing, as a layer of Li_2O_2 almost completely inhibits further ORR on Au and Pt electrodes.[5] As the electrode is regenerated by oxidative stripping, so that oxygen has access to the gold surface, peroxide is formed as predominant product, thus confirming our suggestion. The ring current shown in Figure 79 confirms superoxide (being completely re-oxidized) or peroxide (being re-oxidized to a small extent) as the main product. A very similar approach for smooth gold electrodes showed a stronger suppression of superoxide formation (Figure 79 and [139]). This is explained by the influence of the rough surface leading to a more defective CaO_2/CaO adsorbate.

The decrease of peroxide formation and transition to superoxide formation is not observed in the DEMS measurements (Fig. 3, [47] and [48]). This is due to lower mass transport in the DEMS cell, while the large hysteresis concerning ORR for smooth electrodes in the DEMS cell already is an indication for the formation of the CaO_2/CaO film, as it is caused by the decrease in electrode activity.

Therefore we assume that the adsorbate layer formation is a slow reaction competitive to the formation of soluble peroxide. This experiment and the corresponding experiment on smooth gold[139] identify the adsorbate as reason for inhibition of peroxide formation, which persists after slow dissolution of the thicker CaO_2 bulk layer formed during ORR.

The normalized ring current during peroxide oxidation at the disk electrode (see Figure 72(b, e, h)) is much smaller than expected: it should be larger (oxidation of peroxide to oxygen) or at least as large (oxidation of peroxide to superoxide) as the ring current during superoxide formation. In the following we will show that this is due to sluggish oxidation kinetics by increasing the effective rate of peroxide oxidation at the ring electrode.

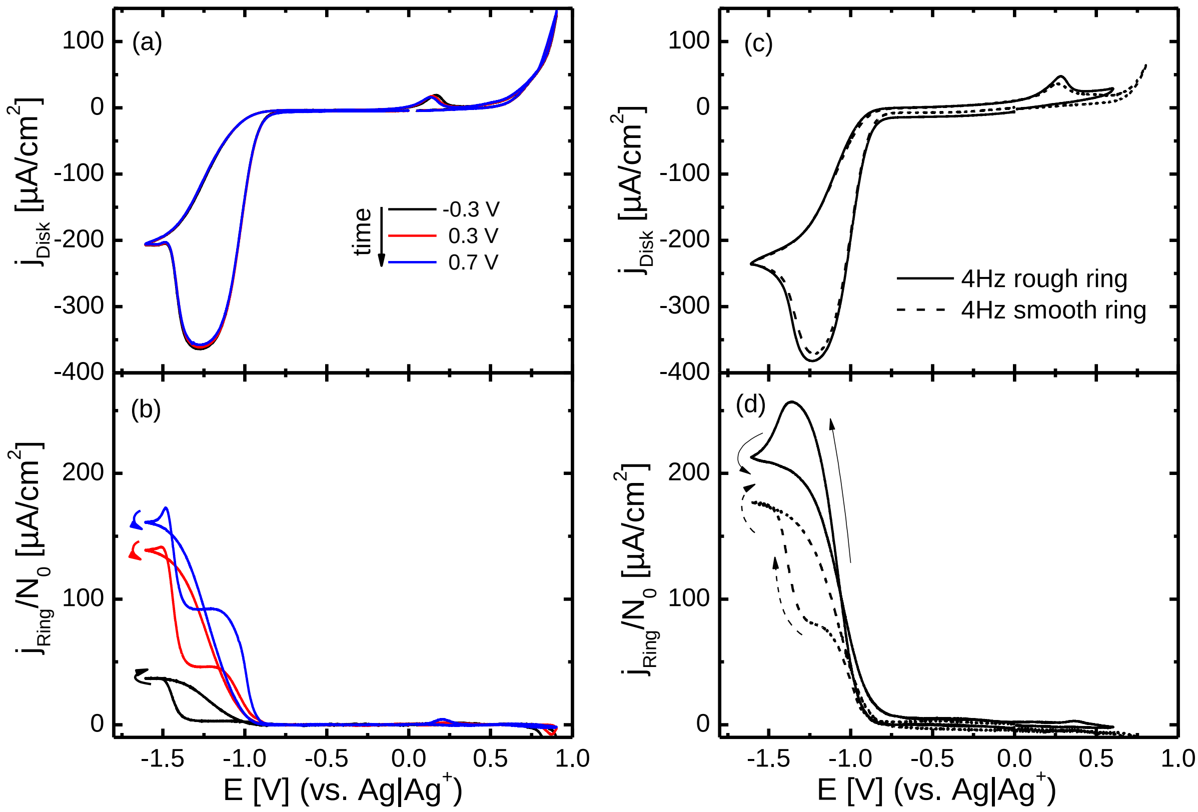

Figure 75 (a, b): Cyclic voltammetry of gold (thin gap disk electrode) in (20% O_2 + 80% Ar)-saturated 0.1 M $Ca(ClO_4)_2$ containing DMSO at 20 mV/s and 4 Hz rotation frequency vs Ag|Ag$^+$ in a usual H-Cell. The disk current (a) is normalized to the geometrical electrode surface area and the ring current (b) is normalized to the theoretical collection efficiency (N_0) and the geometrical WE surface area. The ring potential was varied as indicated by the color code. (c, d): Cyclic

voltammetry of gold (exchange disk electrode) in (20% O_2 + 80% Ar)-saturated 0.1 M $Ca(ClO_4)_2$ containing DMSO at 20 mV/s and 4 Hz rotation frequency vs Ag|Ag$^+$ in a usual H-Cell. The disk current (c) is normalized to the geometrical electrode surface area and the ring current (d) is normalized to the theoretical collection efficiency (N_0) and the geometrical WE surface area. The ring potential was 0.4 V. The electrode roughness of the disk electrodes in (c) were $f_R \approx 3$ for both, while the ring electrode was polished (dashed line) or roughened (solid line). The arrows (b, d) in indicate the sweep direction. Data is smoothed using Savitzky-Golay method with 25 points of window.

In the first experiment (see Figure 75(a, b)) the ring potential was increased from -0.3 V to +0.7 V. All ring currents increase with increasing ring potential, which indicates kinetic limitations. As already shown in [47] a minimum potential of 0.3 V is required to achieve oxidation of the superoxide at low potentials; higher ring potentials only lead to slightly more efficient re-oxidation. The necessity for such a high ring potential to achieve oxidation of superoxide which should be oxidized around -0.3 V was explained by the formation of a contact ion pair between Ca^{2+} and O_2^-. Anyway, superoxide oxidation is sufficiently fast at a ring potential of 0.3 V (or 0.4 V as used in the other RRDE measurements). However, oxidation of peroxide is not complete even at 0.7 V (note that the normalized ring current should ideally be the same as the disk current). This indicates a very sluggish peroxide oxidation kinetics; increasing the ring potential further would lead to stronger DMSO decomposition/gold dissolution and therefore is not an option. We used another approach in the second experiment, Figure 75(c, d): Here the ring electrode was roughened using the same method as for polycrystalline gold disk electrodes leading to a ring electrode roughness of $f_R \approx 32$. (The dependence on rotation rate is shown in Figure 80). Thus, the amount of detected peroxide is strongly increased: In Figure 75 the ring current now even resembles the shape of the ORR at the disk. This effect of kinetic limitation also explains the independence of the ring current on the rotation frequency (in Figure 72(e, h)), while the deactivation of the ring electrode with time can be explained by slow accumulation of decomposition products (e.g. from DMSO decomposition by singlet-oxygen) [96, 98, 138].

Qualitatively it is already obvious from the size of the peroxide formation current, which is much larger than the oxidation peak at the disc at 0.3 V that peroxide does not accumulate at the disc electrode (at least under convection) but rather dissolves. To confirm this more quantitatively, and to separate the superoxide and peroxide contributions, we use Figure 72 for $f_R = 3$ and introduce the superoxide share χ. Using the approach shown in the supporting information for the experiment in Figure 72(a-c), the obtained charge densities (referring to the geometrical surface area) are 6987 µC/cm^2 (4 Hz), 7998 µC/cm^2 (9 Hz) and 8332 µC/cm^2 (16Hz) (note that this only provides a rough estimate of the peroxide contribution). Comparing these values with the peroxide oxidation charge densities at the disk (evaluated from the anodic and cathodic scan prior to the steep increase in disk current close to the upper potential limit): 1045 µC/cm^2 (4 Hz), 1215 µC/cm^2 (9 Hz) and 1338 µC/cm^2 (16 Hz), it is obvious that most of the peroxide formed while the adsorbate layer is incomplete, is dissolving. The discrepancy between peroxide formation and oxidation charge is even much larger as exclusively peroxide is formed on roughened electrodes. The OER charge on smooth polycrystalline Au electrodes without convection is larger compared to the values under convection due to contribution of undissolved bulk CaO_2 to OER, which is mostly dissolved under convection.

In Figure 70 and Figure 72 one observes a positive shift of ORR half-wave potential with increasing electrode roughness. In the DEMS measurement, the shift in half wave potential will not be quantified, as the whole electrode was roughened in a hanging meniscus setup, while only the inner part of the electrode surface has contact to the electrolyte in the DEMS cell. Thus only the RRDE experiment is used for further evaluation to avoid uncertainties in electrode roughness. To quantify the half-wave potential shift, we start with the current density, which is given by the Koutecký-Levich equation:

$$\frac{1}{j} = \frac{1}{j_{\mathrm{D}}} + \frac{1}{j_{\mathrm{K}}} \tag{59}$$

with the diffusion limited current density j_{D} and kinetic current density j_{K}. For a given current density j being a fraction $1/x$ of the diffusion limited current j_{D} such as $j/2$ at the half wave potential, equation ((*59*) gives:

$$\frac{x}{j_{\mathrm{D}}} = \frac{1}{j_{\mathrm{D}}} + \frac{1}{j_{\mathrm{K}}} \tag{60}$$

After rearranging equation (60) and inserting the expression for i_{K} this leads to:

$$zF[k_0 f_{\mathrm{R}}]e^{-\frac{\alpha_{\mathrm{app}}FE}{RT}} = \frac{j_{\mathrm{D}}}{x-1} = b \tag{61}$$

Where k_0 is the rate constant per unit true surface area, f_{R} is the roughness factor and α_{app} is the apparent cathodic transfer coefficient. Converting the expression leads to

$$E = \frac{RTln(f_{\mathrm{R}})}{\alpha_{\mathrm{app}}F} + \frac{RTln(zFk_0/b)}{\alpha_{\mathrm{app}}F} \tag{62}$$

As j_{D} is independent of E and f_{R}, this gives the proportionality between the roughness factor and the potential for a constant current density j, such as the current at the half-wave potential ($x = 2$):

$$E_{1/2} = \frac{RT}{\alpha_{\mathrm{app}} F} ln(f_{\mathrm{R}}) + constants \tag{63}$$

Thus the apparent transfer coefficient (α_{app}) can be obtained from the slope of $E_{1/x}$ vs. $ln(f_{\mathrm{R}})$.

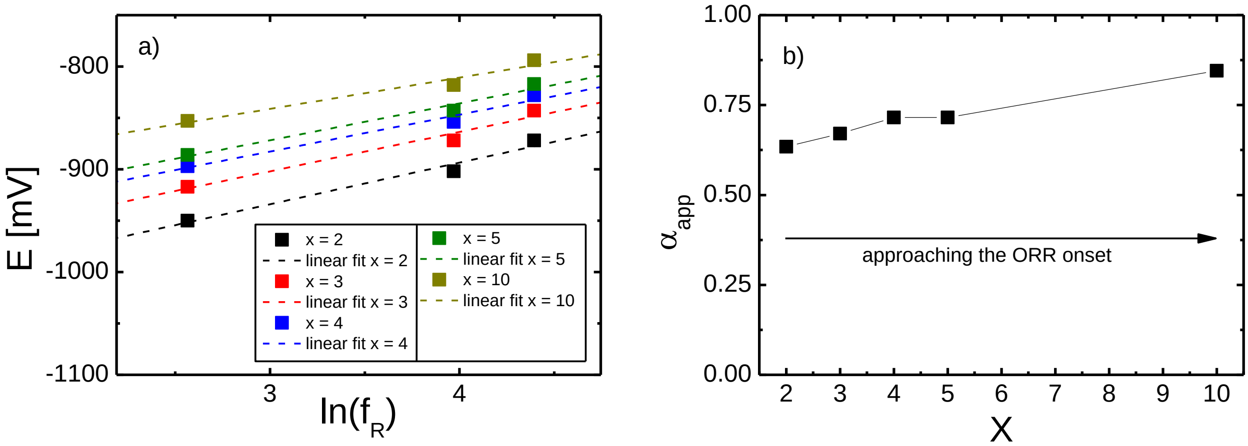

Figure 76 a): Plot of $E_{1/x}$ vs. ln(f_R) where squares show $E_{1/x}$ for i = i_D/x and dashed lines show linear fit. b): Plot of α_{app} vs. *x* (black dots). The arrow indicates approaching the ORR onset and thus the more kinetically controlled region. Measurements were conducted in 0.1 M $Ca(ClO_4)_2$ containing DMSO in an RRDE setup at 9 Hz rotation frequency and 20 mV/s sweep rate.

Figure 76a shows the plot of the logarithm of the roughness factor vs the ORR potential for i being a fraction $1/x$ of i_{D}. From the slopes, one obtains reasonable values for the apparent transfer coefficient α_{app} (see Figure 76b). Figure 76b further shows, that approaching the ORR onset, α_{app} approaches the value of 0.9, which indicates an initial, equilibrated 1 e^{-} step, followed by a slow process (e.g. slow formation of the CaO_2^+ ion-pair). This is in agreement with the observed Tafel slope of close to 60 mV/dec for rough electrodes (f_R = 53 and 81; see Figure 81. At larger overpotentials (or X = 2) α_{app} approaches 0.5 in agreement with the Tafel plot yielding a slope of 120 mV Figure 81. This could indicate a transition to a slow 1st electron transfer caused by partial blocking of the surface, in particular of active sites, in the course of the potential sweep. Also, chemical dissolution of the peroxide formed after the 2nd e- transfer might be too slow at large overall rates, causing such a blocking only at larger rates and thus higher overpotentials. A preliminary Tafel analysis for electrodes with low f_R yields Tafel slopes of 90 mV already during the ORR onset caused by the same reason.

10.2.5 Discussion

Collecting the results in this study, we are now able to suggest a consistent mechanism for the ORR mechanism in Ca^{2+}-containing DMSO on gold and how it changes with electrode roughness (see Figure 77).

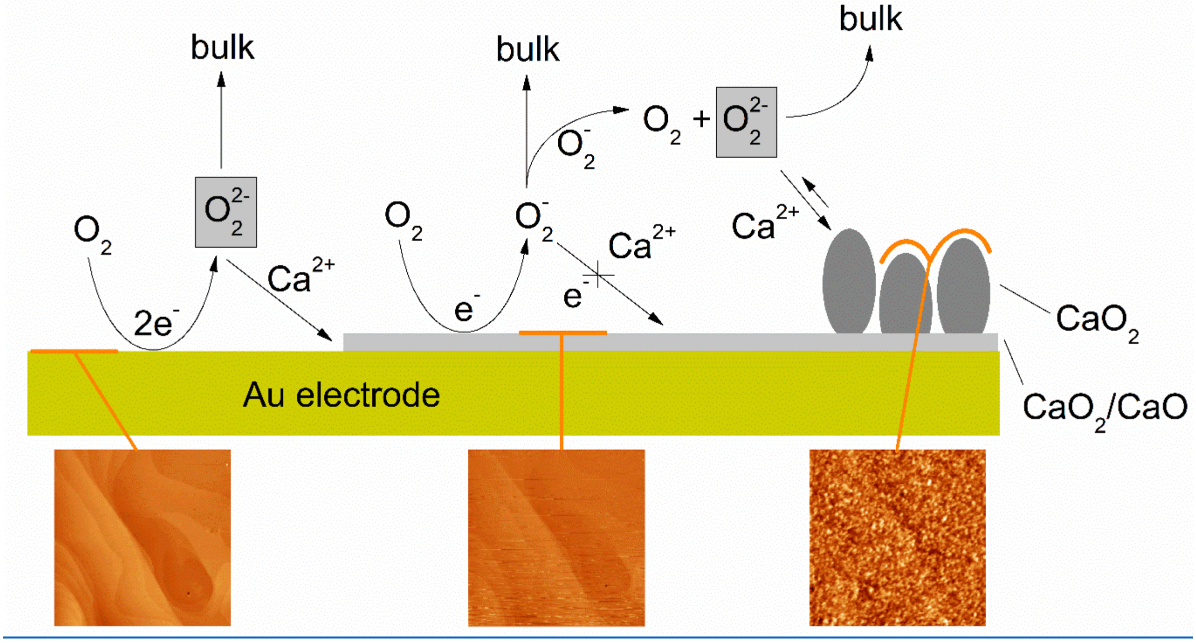

Figure 77 ORR/OER mechanism in Ca^{2+} containing DMSO on Au electrodes.

Regarding the voltammetry we will have a closer look at the ORR and OER separately and define the ORR region from -0.8 V to -1.6 V and the OER region from -0.5 V to 1.0 V vs Ag|Ag$^+$ respectively.

ORR:

The predominant product during ORR is slightly soluble peroxide formed via an initial 1 e^- reduction in equilibrium followed at least by a further 1 e^- reduction step, until a complete adsorbate layer of CaO_2/CaO is formed. Thereafter, superoxide is formed.

- It was already shown in earlier studies and confirmed in this study, that a two electron process accompanied with oxygen consumption is observed below -0.8 V in the investigated system.[47, 48]
- The formed peroxide is only slightly soluble: In the absence of convection it precipitates in a nucleation and growth mechanism at the surface, predominantly at defects; it can slowly dissolve as demonstrated e.g. in the AFM experiments. Under convection (which is more severe in the RRDE experiments than in the DEMS experiments) it is completely dissolved and transported to the ring electrode. There, its oxidation is slow and requires high potentials even at rough ring electrodes.

- Peroxide formation is initiated by a one electron process (most likely superoxide formation) as indicated by the Tafel slope obtained from the current voltage curves and – indirectly - from the shift of the half-wave potential of ORR with electrode roughness.
- In immediate contact with the Au surface is an adsorbed layer of CaO_2 or CaO [139], which is also stable after dissolution of bulk CaO_2 and which inhibits further reduction of O_2 to peroxide and therefore leads to the observed change in electrode activity (hysteresis) and transition from peroxide formation to superoxide formation. This assumption of an adsorbate blocking further peroxide formation stems from the small oxidation charge (typically below the charge of 390 $\mu C/cm^2$ (real surface area) corresponding to a monolayer) observed for oxidative stripping of the adsorbate in subsequent anodic sweeps at the RRDE and AFM after waiting for complete dissolution.
- After completion of the adsorbate layer soluble superoxide is the predominant product during ORR. At smooth Au, also superoxide formation is blocked 300 sec after potential stop at -1.6 V vs $Ag|Ag^+$, while on rough electrodes, the current for superoxide formation is larger and limited by diffusion without notable decay within 150 sec of observation after completion of the adsorbate layer.
- The transition of peroxide to superoxide formation is indicated by an increasing ring current in RRDE generator collector experiments, because peroxide oxidation at the ring electrode is limited by kinetics and not by diffusion (superoxide has faster oxidation kinetics).
- On smooth disk electrodes in RRDE experiments, the superoxide formation is also partially hindered by the CaO_2/CaO-adsorbate layer[139], while on rough electrodes this is not the case, indicating a more defective adsorbate and thus more facile conduction.
- The electrochemically formed, soluble peroxide and the peroxide possibly formed via disproportionation deposits on the electrode surface as particles, if no convection is present. The particle formation is clearly visible in AFM measurements without convection. So far it is unclear, if the deposit originates from soluble peroxide formed prior completion of the adsorbate layer, from peroxide formed via superoxide disproportionation or both.

OER:

The CaO_2/CaO-adsorbate oxidation starts at potentials from -0.5 V to 0.3 V depending on the degree of adsorbate layer completion.

- At smooth electrodes the adsorbate layer is formed during one cycle under the RRDE measurement conditions in this study, while the anodic peak associated with adsorbate layer oxidation is located around 0.3 V. Also for $f_R = 13$, after completion of the adsorbate layer, regeneration of the electrode by oxidative stripping of the adsorbate, starts at 0.3 V. For very rough electrodes, an anodic current can be observed starting from -0.5 V, which indicates easier oxidation of the incomplete adsorbate layer, as the layer is not finished during one cycle (indicated by diffusion limited peroxide formation during the ORR on rough electrodes).

- Oxidation of the adsorbate layer and of thicker peroxide layers occur at similar potentials.
- We had shown before, that oxidation of the superoxide CaO_2^+ (at the ring electrode after formation at the disc) requires overpotentials of more than 0.5 V. This had been ascribed to the stabilization of the superoxide by forming a contact ion pair with Ca^{2+}. This effect is much more drastic for peroxide oxidation, which requires overpotentials of 1.5 V at a smooth ring electrode. This is not really astonishing because the reversible thermodynamic potential of CaO_2/O_2 is about 1.5 V more positive than that of the superoxide $Ca(O_2)_2/O_2$.[139] Since superoxide formation can occur only around – 1 V (vs. Ag|Ag^+), and since peroxide formation involves superoxide as an intermediate, it is the reduction to peroxide which requires a large (negative) overpotential, whereas its reoxidation occurs close to the thermodynamic potential. The question remains whether a catalyst or another solvent could be found for a possible calcium/oxygen battery allowing the direct 2-electron reduction to peroxide at a more positive potential than to superoxide in Ca containing electrolytes.

10.2.6 Conclusions

In this work we investigated the influence of atomic surface structure and electrode roughness on the ORR in Ca^{2+} containing DMSO and thus shed some light on the mechanism of oxygen reduction on gold surfaces. As we have shown, the atomic surface structure has a minor influence on the ORR in presence of convection. We found peroxide as main product during ORR both on single crystalline and polycrystalline gold surfaces as indicated by the number of transferred electrons in DEMS measurements under convection. Concerning the influence of electrode roughness, we found that a rough gold surface allows for continuous peroxide generation under the typical measurement conditions, whereas at smooth electrodes it is soon replaced by superoxide formation. However, under longer ORR without intermediate OER (i.e. oxidative stripping of the blocking adsorbate) peroxide formation is not maintained neither on the rough electrodes; instead, diffusion limited superoxide formation is observed, whereas at the smooth electrode the OER is completely suppressed after some time.

The reason for this behavior is the formation of a CaO_2 or CaO adsorbate on gold electrodes that inhibits further peroxide formation during ORR as soon as it forms a closed layer; instead, superoxide is formed at defects of this layer. Its formation requires more time at rough electrodes because it competes with peroxide formation and is diffusion limited. (For a roughness of 50, its formation would thus take 50 times as long as for a roughness of 1.) At Au single crystal electrodes, on the other hand, its formation is much slower probably because nucleation sites are missing. At smooth electrodes, this adsorbate layer ultimately is sufficiently defect - free to also inhibit superoxide formation, whereas at rough electrodes such a poisoning could not be observed. On Pt electrodes, the behavior is somewhat different, as already shown in [47, 48]. This will be examined in more detail in a forthcoming paper.

The soluble peroxide and superoxide can be oxidized at a collector electrode in a generator collector arrangement (e.g. RRDE), but the kinetics of the reoxidation is slow for superoxide (due to stabilization in an ion pair with Ca^{2+}) and even slower for the peroxide. In the absence of convection, the formed peroxide (either via the 2nd electron transfer at the electrode surface or possibly via disproportionation of the superoxide in solution) further deposits as CaO_2 particles on top of the CaO_2/CaO adsorbate layer as indicated by AFM measurements in this study; these experiments also demonstrated that this peroxide can be dissolved.

Furthermore we found in DEMS and RRDE measurements a dependency of the half wave potential on electrode roughness as predicted by theory and showed a further RRDE approach to obtain reasonable values for the apparent transfer coefficient (α_{app}). Using this approach combined with the Tafel slopes we conclude an initial, equilibrated one electron process followed by a slow process (e.g. slow formation of the CaO_2^+ ion-pair). This proves the electrode roughness to be a valuable tool for investigations on kinetics.

10.2.7 Supporting information

Separation of superoxide and peroxide contribution

Assuming eq.(*64*-(*66* to hold, χ can be derived from the disk current i_{disk} and ring current i_{ring} via:

$$i_{\mathrm{disk}} = 2F\frac{dn_{\mathrm{O}_2}}{dt} - F\frac{dn_{\mathrm{O}_2}}{dt} * \chi \tag{64}$$

$$i_{\mathrm{ring}} = 2FN_{\mathrm{P}}\frac{dn_{\mathrm{O}_2}}{dt} * (1-\chi) + FN_{\mathrm{S}}\frac{dn_{\mathrm{O}_2}}{dt} * \chi \tag{65}$$

With N_{P} and N_{S} as collection efficiency of peroxide and superoxide. After converting the expression to

$$\frac{dn_{\mathrm{O}_2}}{dt} = \frac{i_{\mathrm{disk}}}{F(2-\chi)} = \frac{-i_{\mathrm{ring}}}{F(2N_{\mathrm{P}} + \chi N_{\mathrm{S}} - 2\chi N_{\mathrm{P}})} \tag{66}$$

One obtains the superoxide share

$$\chi = \frac{2(i_{\mathrm{ring}} + N_{\mathrm{P}} i_{\mathrm{disk}})}{i_{\mathrm{ring}} + 2N_{\mathrm{P}} i_{\mathrm{disk}} - N_{\mathrm{S}} i_{\mathrm{disk}}} \tag{67}$$

To further obtain N_P and N_S via

$$N_{\mathrm{P}} = \frac{i_{\mathrm{P}}^{\mathrm{ring}}}{i_{\mathrm{P}}^{\mathrm{disk}}} \tag{68}$$

$$N_{\mathrm{S}} = \frac{i_{\mathrm{S}}^{\mathrm{ring}}}{i_{\mathrm{S}}^{\mathrm{disk}}} \tag{69}$$

Were $i_{\mathrm{S}}^{\mathrm{disk}}$, $i_{\mathrm{S}}^{\mathrm{ring}}$, $i_{\mathrm{P}}^{\mathrm{disk}}$ and $i_{\mathrm{P}}^{\mathrm{ring}}$ are taken from the voltammogram as shown in Figure 82 assuming that $i_{\mathrm{S}}^{\mathrm{disk}}$, $i_{\mathrm{S}}^{\mathrm{ring}}$, $i_{\mathrm{P}}^{\mathrm{disk}}$ and $i_{\mathrm{P}}^{\mathrm{ring}}$ exclusively consist of superoxide/peroxide generation/oxidation respectively. The product of $i_{\mathrm{disk}}(E)$ and $(1 - \chi(E))$ gives the current contribution of peroxide. Integration of the peroxide formation current leads to the peroxide charge of 6987 µC/cm^2 (4 Hz), 7998 µC/cm^2 (9 Hz) and 8332 µC/cm^2 (16Hz).

Calculation of the theoretical peak current density

Theoretical peak current densities (j_{p}) were calculated using the Randles-Sevcik equation for a reversible process:

$$j_{\mathrm{p}} = 0.4463\ C\ z^{3/2}\ F^{3/2}\ (vD/RT)^{1/2} \tag{70}$$

And a totally irreversible process:

$$j_{\mathrm{p}} = 2.99 * 10^5 * zC\ (\alpha z_{\alpha}\ Dv)^{1/2} \tag{71}$$

With C as bulk concentration of oxygen, z as number of transferred electrons, z_{α} as number of transferred electrons during the rate determining step, α as transfer coefficient, F as Faraday constant, v as sweep rate, D as diffusion coefficient of oxygen, R as gas constant and T as temperature. The bulk concentration of oxygen (0.4 mM at 20% O_2) in our electrolyte was determined like in [40, 41].

Further remarks

SI A: Note that the voltammograms of the single crystalline electrodes were not stable upon continuous cycling. The ORR current decreased and the OER current increased with time, thus indicating, that crystallization of CaO_2 becomes more facile over time, which further indicates incomplete oxidation or changes in the surface structure.

SI B: The behavior of the anodic disk current in Figure 72 further indicates the formation of a thin layer. Starting with the rough electrode (see Figure 72 (i)), one observes a current below 0 V, which decreases with increasing rotation frequency/time, while the current above 0 V increases with rotation frequency/time. In the picture of an adsorbate that slowly forms a closed layer that absolutely makes sense, as with increasing rotation frequency more peroxide is generated and thus adsorbed on the electrode surface. So as one increases the rotation frequency, the layer becomes more complete, thus increasing the potential required for the oxidation of the adsorbate. For lower electrode roughness (see Figure 72 (c, f)) this transition is not observed, but the anodic peak current shifts to more positive potentials leading to the same conclusion.

Additional Figures

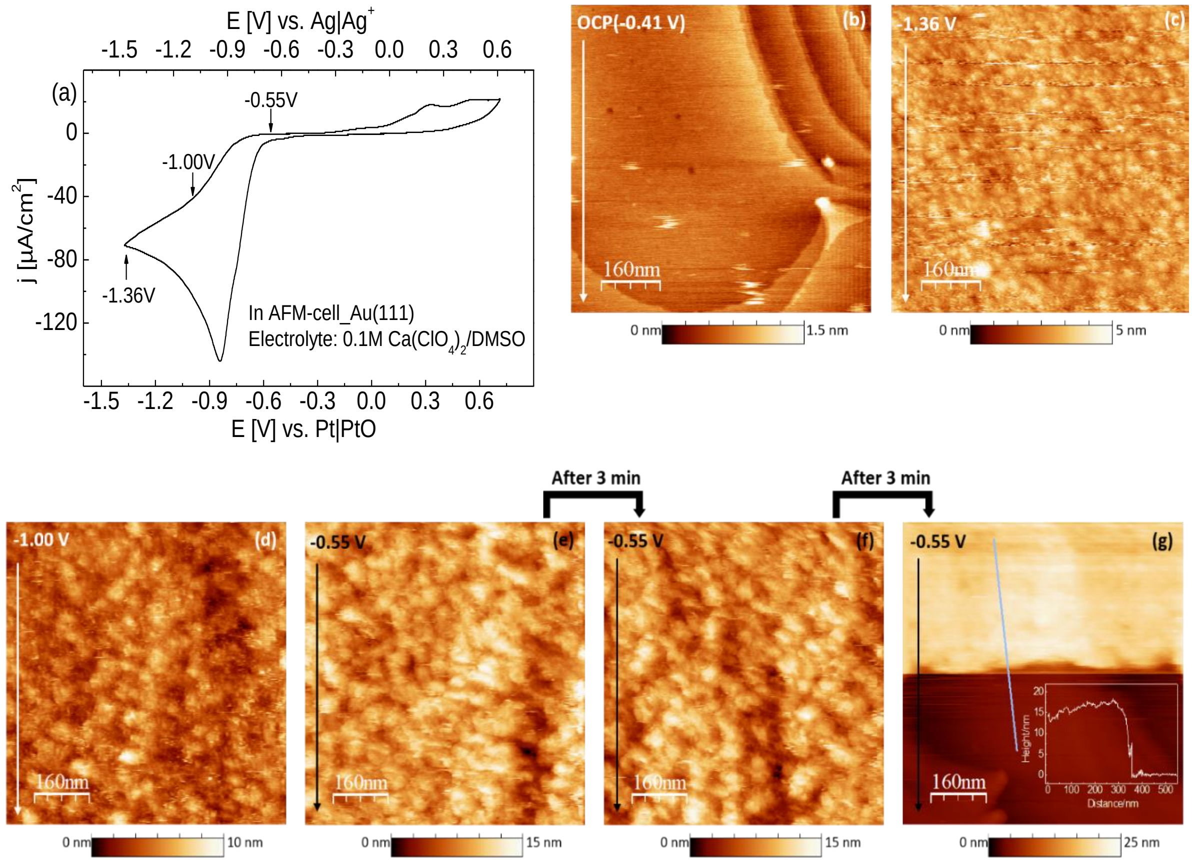

Figure 78 (a) CV on Au(111) in AFM-cell at 5 mV/s during AFM measurement. In situ AFM images showing the topography on Au(111) at OCP (b), -1.36 V vs. Pt|PtO (c), -1.00 V vs. Pt|PtO (d), -0.55 V vs. Pt|PtO (e)-(g). The inset image of (g) shows the height profile. To avoid the tip-induced influence on the electrochemical reaction we lifted up the AFM tip by 100 µm during ORR process and then re-approached it to the electrode surface after the ORR reaction. The arrow in the image represents the scan direction. A set point of AFM was 4nN, bias was 50 mV Integral and proportional gains were 8 and 9, respectively. Scan size was 800X800 nm² and scan rate was 3.08 nm/s.

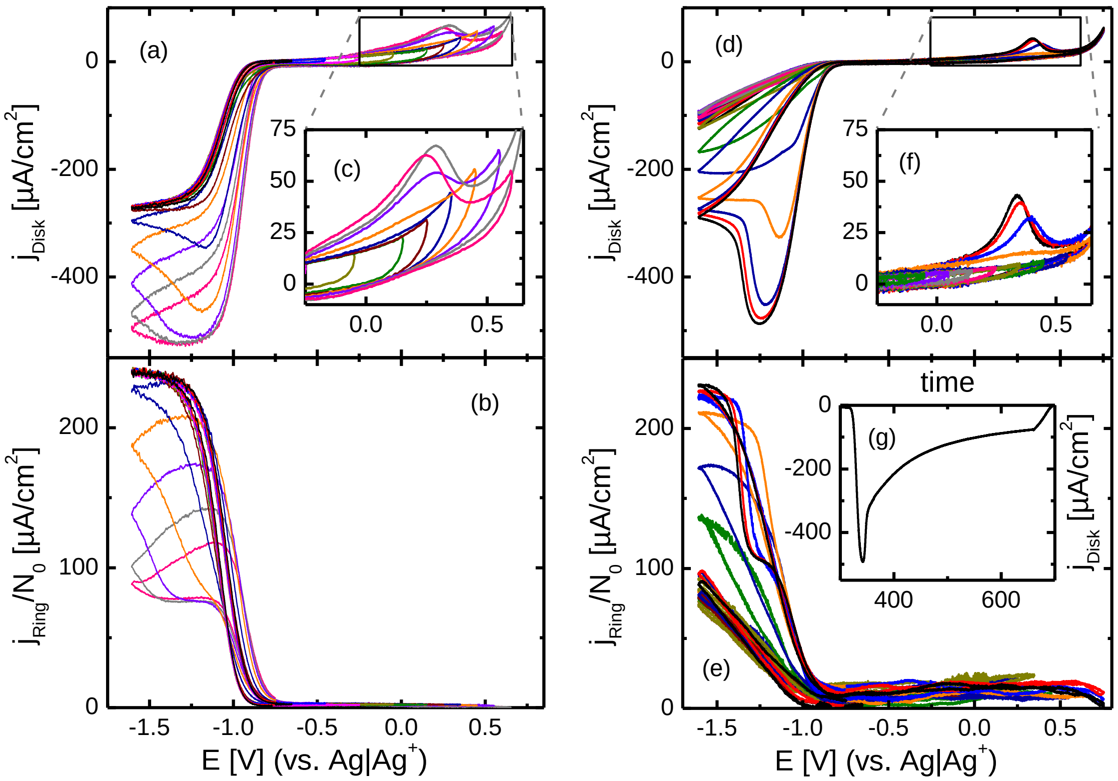

Figure 79 Cyclic voltammetry of roughened gold (left, at f_R = 13) and smooth gold (right, at f_R = 3, data from [139]) in (20% O_2 + 80% Ar)-saturated 0.1 M $Ca(ClO_4)_2$ containing DMSO at 20 mV/s, E_{ring} = 0.4 V and 9 Hz rotation frequency vs Ag|Ag$^+$ using a usual H-cell. Shown CVs are recorded after stopping the potential at -1.6 V for 5 min and jumping to -0.75 V for 10 min afterwards. The upper limit in this experiment is opened consecutively after each cycle until the disk electrode was regenerated by oxidative stripping of the CaO_2/CaO-adsorbate. Disk current density is shown in (a, d). The ring current (b, e) is normalized to the collection efficiency N_0 and the geometrical surface area of the disk electrode for 1 to 1 comparability. The anodic signal is magnified in (c, f). (g): The disk current transient at smooth Au during the 300 sec potential stop at -1.6V vs. Ag|Ag$^+$.

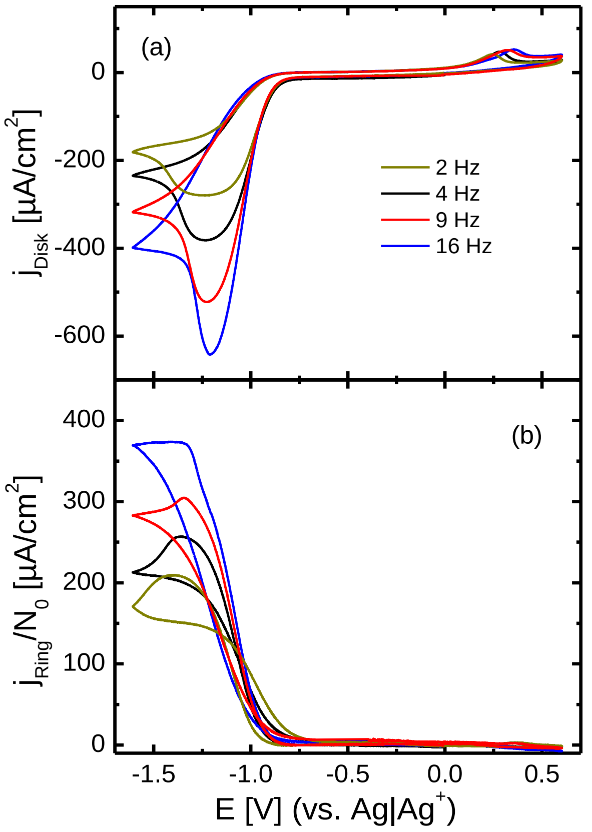

Figure 80 Cyclic voltammetry of gold (exchange disk electrode with $f_R \approx 3$) in (20% O_2 + 80% Ar)-saturated 0.1 M $Ca(ClO_4)_2$ containing DMSO at 20 mV/s, $E_{ring} = 0.4$ V and 9 Hz rotation frequency vs Ag|Ag$^+$ using a usual H-cell. Disk current density is shown in (a). The ring current (b) is normalized to the collection efficiency N_0 and the geometrical surface area of the disk electrode for 1 to 1 comparability. The ring electrode in this experiment is roughened leading to $f_R \approx 32$.

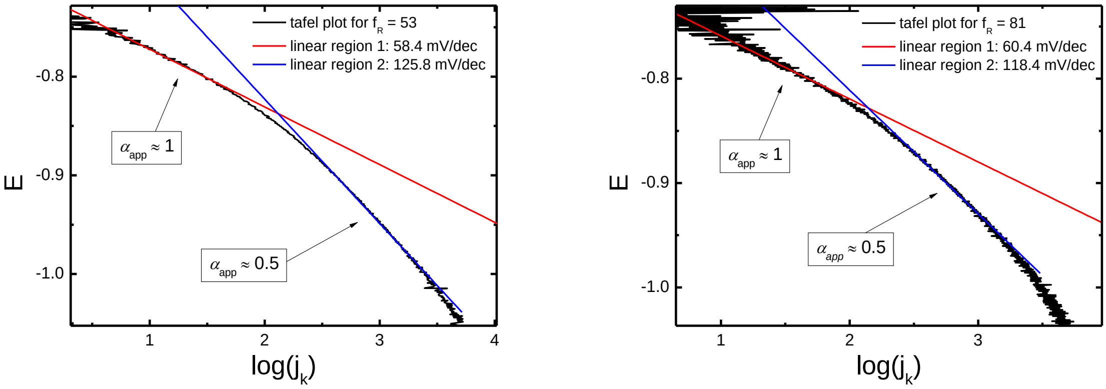

Figure 81 Tafel plot for f_R = 53 and 81. Tafel analysis refers to Figure 72d+g.

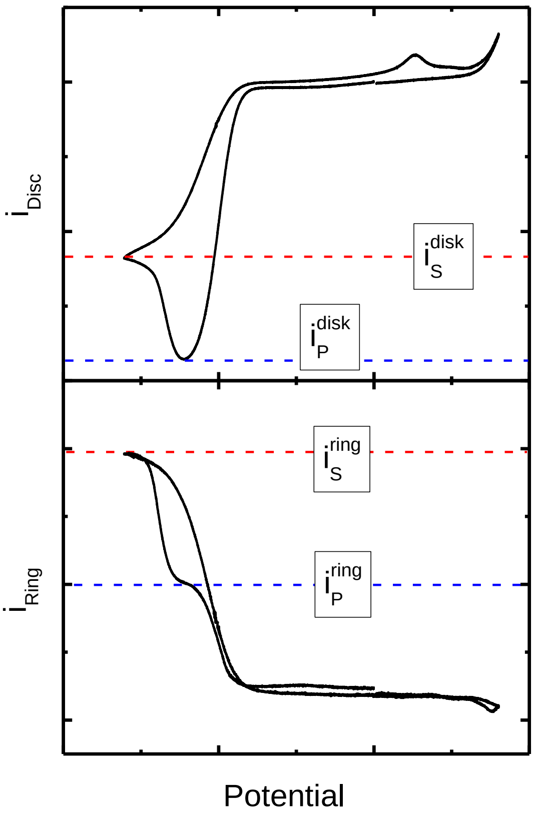

Figure 82 Exemplary determination of i_S^{disk}, i_S^{ring}, i_P^{disk} and i_P^{ring} from the voltammogram.

10.3 Towards a generalized ORR mechanism in M^{2+} containing DMSO – Oxygen reduction and evolution in Ca^{2+} containing DMSO on atomically smooth and rough Pt

10.3.1 Abstract

This study deals with the oxygen reduction reaction (ORR) and oxygen evolution reaction (OER) in Ca^{2+} containing dimethyl sulfoxide (DMSO) on atomically smooth Pt(111) and Pt(100) and rough Pt surfaces. As demonstrated by cyclic voltammetry and XPS, the bromine adlayer used to protect Pt single crystals against ambient air and solvent vapor is desorbed in DMSO and does not affect the following measurements.

Cyclic voltammetry, differential electrochemical mass spectrometry (DEMS) and rotating ring disk electrode (RRDE) investigations with variation of the electrode surface roughness and atomically surface structure show, that on Pt electrodes the CaO_2 adsorbate layer formation determines the ORR product distribution. On Pt electrodes calcium peroxide is formed on the clean electrode, whereas calcium superoxide is formed at the adsorbate covered electrode. We furthermore identified four key parameter, which strongly affect the ORR product distribution.

1. The electrode oxide interaction: A strong interaction increases superoxide contribution.
2. The alkaline earth metal oxide interaction: A strong interaction increases peroxide contribution.
3. The electrode surface area: A large electrode surface area increases peroxide contribution.
4. Electrode surface defects: Defects increase superoxide contribution.

Finally, reviewing earlier results of our group we provide a more general mechanism for the oxygen reduction alkaline earth metal cation containing DMSO, for a variety of electrode materials.

10.3.2 Introduction

The necessity of on-demand energy storage is an unquestionable fact nowadays, regardless of the final application. From large scale batteries, which are useful for stationary applications to applications in small portable devices, high energy density batteries are becoming more and more common. Lithium-ion batteries are the current state of the art, but suffer from environmental problems, as lithium is rare, very unevenly spread over the planet and lithium cation intercalation materials often require stoichiometric amounts of rare elements like cobalt. These problems are addressed in investigations on metal-air batteries and made this field become a topic one. However, especially regarding alkaline earth metal-air systems the performance is insufficient and a fundamental understanding of the underlying mechanisms is required. As Na-O_2[26, 88, 126-128] and K-O_2[132-134] systems drew attraction as alkaline metal alternatives to Li-O_2[5, 68, 72, 82, 92, 99, 113, 124, 125] systems, the Mg-O_2 [129-131] and Ca-O_2 [47, 48, 143-146]systems also experienced a raising interest. Na, K, Mg and Ca are very cheap and easily available materials, as their abundance in the earth crust is magnitudes larger compared to lithium. Furthermore DMSO has proven its ability to allow for highly reversible oxygen reduction and evolution in K^+ containing DMSO[132] and thus is expected to be somehow stable against the reactive superoxide anion.

As we already pointed out in several publications, calcium is a competitive candidate as anode material to lithium. The present study is a continuation of four previous studies [47, 48, 143, 144] of our group dealing with the oxygen reduction and evolution reaction in Ca^{2+} containing DMSO. Initially we found, that the ORR product distribution (superoxide and peroxide) strongly depends on the alkaline earth metal cation (Mg, Ca, Sr and Ba)[48] and the electrode material (Au, Pt, Rh, Ru and Glassy Carbon)[47]. The dependence on the cation in this context was attributed to the ion-pair formation between the alkaline earth metal cation and the oxide species. [48] Regarding the dependence on the electrode material, Au was found to play a special role, as on Au electrodes the oxygen reduction in Ca^{2+} containing DMSO is dominated by peroxide formation[47] [143, 144] contrary to the other electrode materials. [47] Addressing this observation, we conducted a series of experiments to investigate the oxygen reduction on Au electrodes of varying electrode roughness and surface structure, and found that the prevailing ORR mechanism on gold electrodes depends on the extent of adsorbate formation.[143] This CaO/CaO_2 adsorbate layer is formed via a (comparably slow) side reaction competing with the dominant formation of slightly soluble peroxide on Au electrodes. As soon as the adsorbate layer is complete, exclusively superoxide is formed on top of this adsorbate layer. [143] Instructive is the comparison to the Li case: the difference of the theoretical standard potentials for peroxide and superoxide formation (ΔE_0) is larger than 2 V for Ca^{2+}, while ΔE_0 is smaller than 0.5 V for Li^+[144]. Thus, Li - superoxide is formed at gold electrodes prior to peroxide (for kinetic reasons), but in presence of Ca^{2+} peroxide is directly formed in DMSO. In both cases the transfer of the second electron is hindered after formation of a blocking adlayer.

This, leads to the question if this CaO/CaO_2 adsorbate is the reason for the varying product distribution for different electrode materials. To address this question we moved to Pt as electrode material and investigated the ORR mechanism, while keeping in mind what we already learned from the ORR on Au electrodes.

This work intends to provide a deeper insight into the fundamentals of the ORR mechanism on a variety of electrode materials in DMSO containing alkaline earth metal cations. Thus, this work intends to shed new light on earlier studies.[47, 48, 143, 144] By varying the electrode roughness as in ref. [5, 143], we investigated the ORR and OER in Ca^{2+} containing DMSO via cyclic voltammetry, RRDE and DEMS methods. This once again proves the variation of the surface roughness to be a valuable tool for mechanistic investigations, especially as adsorbate formation plays a role, in addition to the importance of roughness in practical applications.

10.3.3 Experimental

Electrodes

In this study platinum electrodes of 1 cm diameter (geometrical surface area $(A_{\mathrm{geo}}) = 0.785\ \mathrm{cm}^2$) and RRDE disk electrodes of 0.5 cm diameter ($A_{\mathrm{geo}} = 0.196\ \mathrm{cm}^2$) were used. The ring electrodes were also made of platinum and show a collection efficiency (N_0) of 0.25.

Electrode cleaning

Before any experiment, the platinum electrodes were cycled in 0.5 M H_2SO_4 to show the well-known shape of the cyclic voltammogram (CV). If further cleaning was required, the platinum electrodes were immersed several times alternately into concentrated nitric acid and a solution of ammonia in water. The voltammetry was again checked afterwards to exclude remained contamination.

Single crystal preparation & bromide protection

The single crystals were cleaned as described above and annealed in an induction heat cell purged by N_2 (for Pt(111) and Pt(pc)) or 5% H_2 + 95% Ar (for Pt(100)) (see Figure 94). Afterwards, the crystals cooled down in the same cell above N_2-saturated Milli-Q water.[33, 34] Depending on the crystal thickness, the cooldown period varied between 4 and 6 minutes. Then a bromide solution was added to give a concentration of 20 mM KBr and the electrodes were contacted to this solution (still without any contact to ambient air); the adsorbing bromide protects the surface against ambient air and contaminants. They were characterized in H_2SO_4 (where bromide is also stripped at negative potentials concerning protected single crystals) once every day prior to an experiment to confirm cleanliness and surface order (see Figure 94). The electrodes were then again prepared and transferred to the cell containing the organic electrolyte. The general procedure to protect the Pt(hkl) single crystals against contaminants from ambient air and in particular from the vapor of the solvents by strongly, but reversibly adsorbing bromide is similar to ref. [35, 36], while here (as in ref. [35]) CO adsorption was unnecessary. (We demonstrate below that bromide is desorbed in the first sweep before the onset of ORR, multiple sweeps are not necessary.) This procedure is also similar to the original suggestion for single crystal preparation in ambient atmosphere and protection by iodine from Wieckowski [147, 148]. Further information on bromide adsorption and surface protection of Pt single crystals can be found in [5, 148, 149].

Further information to the electrode roughening procedures can be found elsewhere [5]. The electrode roughness of polycrystalline electrodes equals one unless stated otherwise.

RRDE setup

For the RRDE experiments, a Pt disc and a Pt ring electrode were used as working electrode (WE) and detector electrode (ring potential was 0.4 V vs. Ag|Ag$^+$) under argon atmosphere together with a Pt counter electrode (CE) and Ag reference electrode (RE, a silver wire immersed into 0.1 M $AgNO_3$ containing DMSO), all connected to a bipotentiostat (TACUSSEL BIPAD B1). The rotator was connected to a PINE rotation control. For a 1 to 1 comparability disc currents were normalized to the geometrical surface area of the disk electrode ($A_{\mathrm{geo}}^{\mathrm{disk}}$) and ring currents were normalized to N_0 and $A_{\mathrm{geo}}^{\mathrm{disk}}$.

DEMS setup

For DEMS measurements we used a dual thin Layer flow through cell. WE, CE (Pt wire) and RE (Ag wire immersed into 0.1 M $AgNO_3$ containing DMSO in a separated compartment) were connected to a homebuilt bipotentiostat. A peristaltic pump (SPETEL Perimax) was connected to the electrolyte outlet to ensure constant convection. The RE was contacted to the working electrolyte via a Teflon tube, which was sealed with a rough glass bead and filled with the silver containing solution. The sealed end was immersed into the working electrolyte, while the open end was immersed into the RE electrolyte. The thin layer WE and porous Teflon membrane (serving as interface to the vacuum) compartment is defined by a Teflon spacer of 200 µm and 100 µm thickness and a diameter of 6 mm (electrode area of 0.283 cm^2), as already reported earlier. [5] More detailed information about the DEMS setup and the dual thin Layer cell can be found elsewhere.[48, 110-112, 150]

Chemicals

Calcium perchlorate tetrahydrate (99%, Sigma Aldrich) was dried (8h) under reduced pressure to obtain a white powder of anhydrous $Ca(ClO_4)_2$. Tetrabutylammonium perchlorate (≥99%, Sigma Aldrich), silver nitrate (99%, CHEMPUR), potassium bromide (99%, ACROS ORGANICS) and Dimethyl sulfoxide (99.7%, extra dry, over molecular sieve) were used as received. DMSO, $CaClO_4$ and $TBAClO_4$ were stored inside an *MBraun* glovebox under argon atmosphere. For purging and electrolyte saturation argon (99.999%, Air liquide), nitrogen (99.999%, Air liquide), oxygen (99.9995%, Air liquide), argon oxygen mixture (80%/20%, Air liquide) and argon hydrogen mixture (95%/5%, Air liquide) were used.

10.3.4 Results

Single crystal investigations

Bromide Protection

For single crystal investigations with the sensitive Pt(hkl) in organic electrolytes, a method was required to effectively protect the surface after preparation to achieve a clean transfer to the electrolyte. As our system of interest is metal cation (M^{n+}) containing DMSO, we investigated the suitability of Br_{ads} as protecting agent for this special case. Br_{ads} was already proven to work as effective protecting reagent for Pt(hkl) single crystals[5, 35, 36] against ambient air in our system of interest, which also can be removed effectively. Here we further monitor the stripping behavior of adsorbed Br_{ads} in pure and Na^+ containing DMSO using XPS.

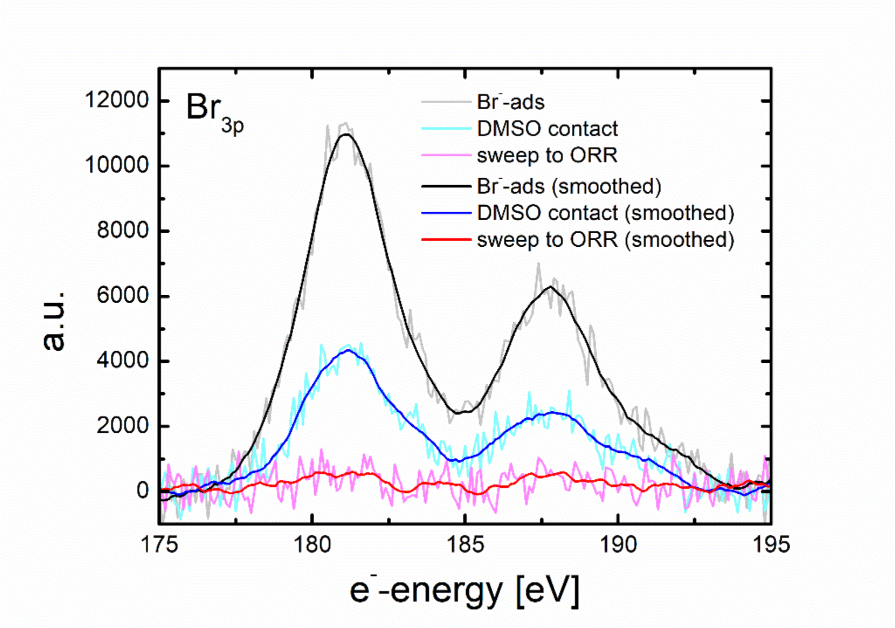

Figure 83 shows the XPS results of the Br_{3p} excitation for the cases of adsorbed bromide on Pt(111) (black), exposure to DMSO for 1 minute after bromide protection (blue) and Sweep from 0.0 V to -0.85 V (ORR onset) vs Ag|Ag^+ in 0.1 M $NaClO_4$ containing DMSO at 50 mV/s after bromide protection (red). Darker colours show smoothed spectra using Savitzky-Golay method.

Figure 83 shows the XPS spectra for the Br_{3p} excitation for three different cases:

- Freshly adsorbed bromide as described above (black) after preparation.
- Exposed to DMSO without potential control for 1 minute (blue) after fresh preparation and protection.
- After sweeping from 0.0 V to -0.85 V (onset of ORR) vs. Ag|Ag^+ in 0.1 M $NaClO_4$ containing DMSO at 50 mV/s (red), after a fresh preparation and protection.

A strong decrease in intensity of the Br_{3p} signal, and thus bromide coverage, is already visible in Figure 83 after simply contacting the protected crystal to pure DMSO at open circuit. After sweeping the potential into negative direction up to the ORR onset potential, the intensity is close to zero and hardly discernible from noise, indicating (at least nearly) complete removal of the Br_{ads} layer prior to the ORR onset. This is supported by the fact that integration of the charge transient between immersion of the protected electrode at 0.0 V vs. Ag|Ag^+ and the ORR onset leads to a value of approximately 115 $\mu C/cm^2$, which corresponds to about one monolayer Br_{ads} (assuming a 3×3 adlattice with $\Theta = 0.44$ [149]).

As we further observed that even iodide desorption in M^{n+} containing DMSO occurs spontaneously and is irreversible ($DMSO_{ads}$ replaces iodide and prevents iodide from re-adsorbing (Figure 95), and since the desorbed monolayer of bromide will dilute into 20-30 ml electrolyte as pointed out in ref. [36] (resulting at most in a concentration of $\frac{1\ \mathrm{nMol}}{20\ \mathrm{mL}} = 5 * 10^{-8}\ \mathrm{M}$), we assume that the protective layer will not influence the ORR, even during the first cycle. Thus all changes in the voltammetry will be caused by other effects which we will address later on in this study.

Investigations in quiescent solution

As found before for Au single crystalline electrodes [143], also on Pt we observe large currents indicative of a two electron process on annealed electrodes:

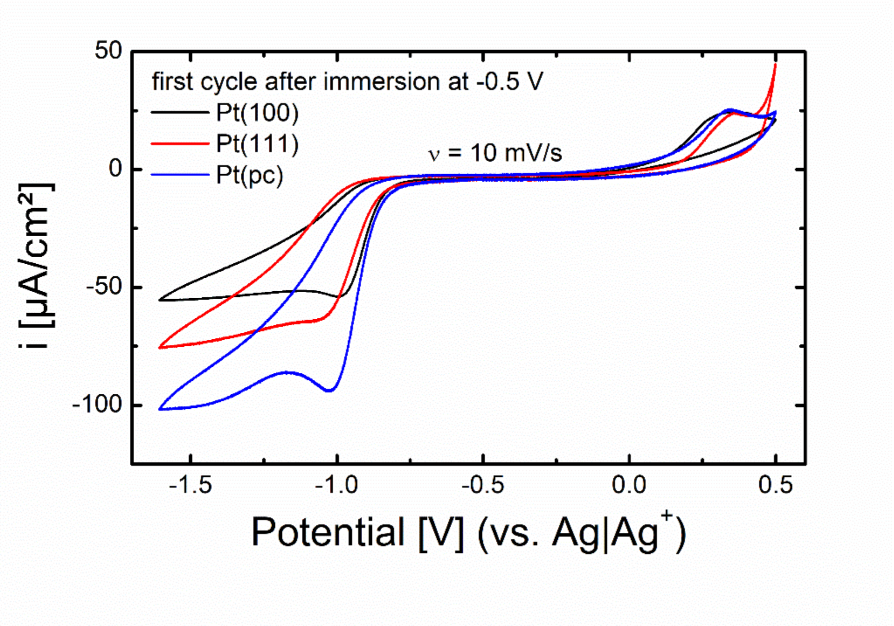

Figure 84 First cycle of Pt(100) (black), Pt(111) (red) and Pt(pc) (blue). Electrolyte: 0.1 M $Ca(ClO_4)_2$ in DMSO; ν = 10 mV/s; WE: Pt; CE: Pt-sheet; RE: Ag|Ag$^+$.

Figure 84 shows the first cycle of prepared, bromide-protected Pt electrodes. Only the first cycle is shown and used for further evaluations, as the voltammetry of the single crystalline electrodes strongly changes with the number of cycles, indicating that the single crystalline surface roughens. This roughening is most likely caused by the positive potential, which has to be applied to desorb and reoxidize oxide species formed during the ORR to oxygen. All electrodes show a similar ORR onset potential close to -0.8 V vs Ag|Ag$^+$. Furthermore, a peak of varying current density and peak potential is observed and followed by a minimum in current density after which the current density increases again.

Table 6 Theoretically calculated, absolute peak current densities from the Randles-Sevcik equation for an irreversible and reversible process. For the equations see SI.

Conditions	**irreversible ($\alpha = 0.5$)**			**reversible**	
	$z = 1;\ z_\alpha = 1$	$z = 2;\ z_\alpha = 1$	$z = 2;\ z_\alpha = 2$	$z = 1$	$z = 2$
$\boldsymbol{j_\mathrm{p}}$ **[μA/cm²]**	42.75	85.49	120.91	54.32	153.63

Comparing the experimental peak current densities with the theoretically calculated, absolute peak current densities (j_p) from the Randles-Sevcik equation for an irreversible and reversible process (see equation (77) + (78)), it becomes clear that j_p is below the expected current density for the two electron process. This is reasonable as we expect a mixture and/or more complex interplay between superoxide and peroxide formation. To fully understand the shape of the CV and the interplay between superoxide and peroxide formation during the ORR, further work on single crystalline Pt electrodes is required.

The OER is dominated by an increase in current density above 0.0 V vs Ag|Ag$^+$. It is notable that the current density starts to increase earlier in case of Pt(100) and Pt(pc) compared to Pt(111), while in case of Pt(111) the current density shows a steep increase prior to the upper potential limit.

DEMS investigations under convection

DEMS experiments under convection were performed to show the influence of mass transport on the one hand, and on the other to quantitatively determine the oxygen consumption, as monitored by mass spectrometry.

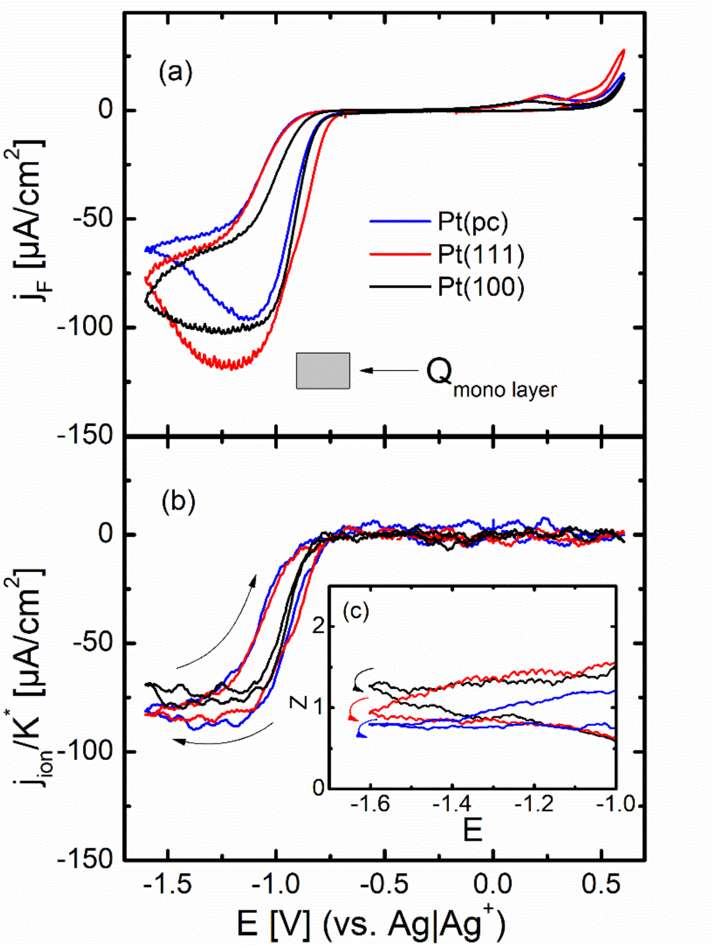

Figure 85 (a): First cycle of Pt(100) (black), Pt(111) (red) and Pt(pc) (blue). Electrolyte: 0.4 M $Ca(ClO_4)_2$ in DMSO; ν = 10 mV/s; flow rate was 5 µl/s, WE: Pt; CE: Pt-wires; RE: Ag|Ag$^+$. The grey box area represents the area corresponding to the theoretical charge for a monolayer of CaO_2 (assuming for simplicity the adsorption of 1 CaO_2 molecule per 1 Pt surface atom, which is certainly too high). (b): Corresponding MS-CV, where the ion current is normalized to the MS calibration constant for comparability. (c): Number of transferred electrons.

Figure 85 shows the increase in reduction current around -800 mV, which is accompanied by oxygen consumption and thus confirming oxygen reduction. The peak in the cathodic cycle of the CV (Figure 85 (a)) corresponds to a charge much larger than possible for adsorbate formation and is not visible in the MS ion current (Figure 85 (b)). It therefore points to a change of the number of electrons. Correlating the faradaic current with the MS ion current (after calibration as described in the SI), one obtains the number of transferred electrons (z, see Figure 85c). For Pt(111) and Pt(100) z starts at about 1.5 and decreases during the ORR. Annealed Pt(pc) shows the same trend, but with lower z. (The decrease of z below 1 is certainly due to an error in the calibration constant; from earlier results we know, that z is 1 or slightly above 1 at least at the very negative potential limit. [47, 48] Since a value of z below 1 is completely unreasonable, we assume that the true $z = 1.0$ for the plateau in z in Figure 85(c) and all values should be multiplied by 1.3.) The fact that $z = 1.5$ (or even z = 2) during early ORR and that z decreases during continuous oxygen reduction, is consistent with the observations on Au electrodes and indicates a peroxide contribution to the ORR current. The formed peroxide further seems to dissolve to large extent, as the peroxide contribution to the charge (showing up as the peak area in addition to the diffusion limited 1 electron process) exceeds the theoretical charge for a monolayer by far (cf. the grey box in Figure 85 (a)), does not inhibit further reduction and is much larger than the reoxidation charge in the anodic sweep around 0.3 V. Additionally it is notable, that the Pt(pc) electrode shows the largest hysteresis (together with Pt(111)) and a similar ORR onset as Pt(100) (while Pt(111) has the most positive ORR onset).

Effect of roughness

Influence on voltammetry

In this chapter we shed light on the influence of electrode roughness on oxygen reduction and reoxidation of deposited oxide species on Pt electrodes in 0.1 M $Ca(ClO_4)_2$ containing DMSO under convection.

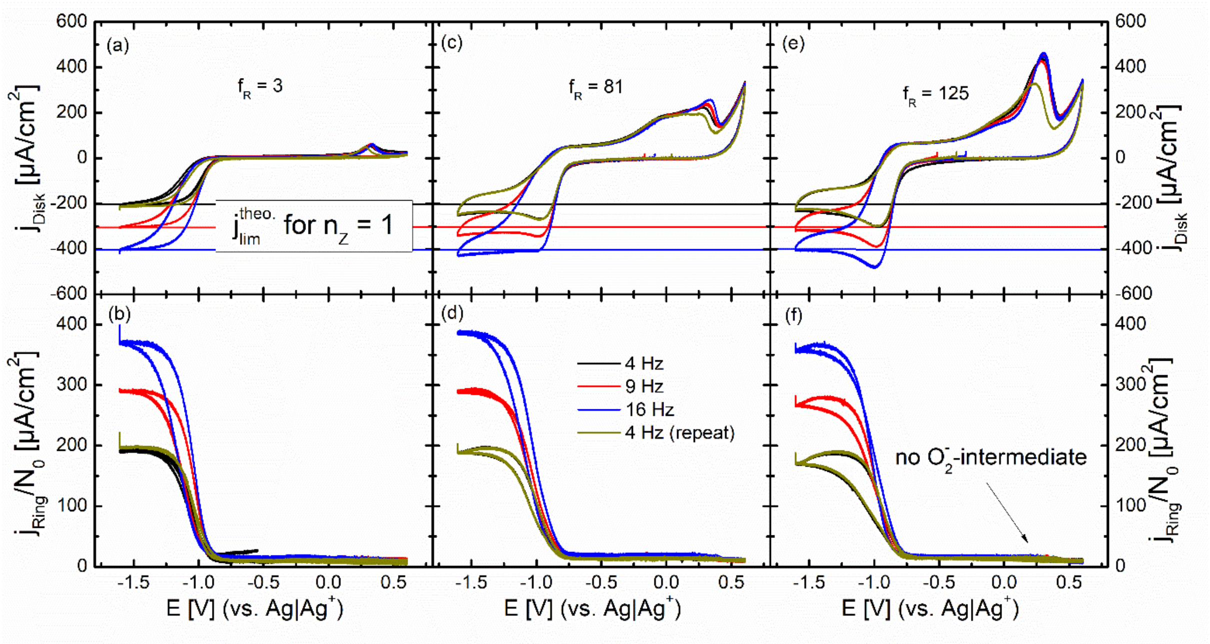

Figure 86 Stable voltammetric cycles of Pt rotating ring disk electrodes of varying disk electrode roughness. Electrolyte: 0.1 M $Ca(ClO_4)_2$ in DMSO; ν = 20 mV/s; ω = 4 Hz (black/yellow), 9 Hz (red) and 16 Hz (blue); WE: Pt(pc); WE2 (ring): Pt(pc) at 0.4 V; CE: Pt-sheet; RE: Ag|Ag$^+$. Disk electrode roughness (f_R) = 3 (a,b), 81 (c,d) and 125 (e,f). Disk current density is shown in (a, c, e) and ring current density in (b, d, f). Inset shows theoretical diffusion limited disk current density.

Figure 86 shows the steady state voltammetry of roughened Pt electrodes (typically 3rd or 4th cycle) in 0.1 M $Ca(ClO_4)_2$ containing DMSO. For low electrode roughness, the ORR starts close to -0.85 V vs Ag|Ag$^+$ and is dominated by superoxide formation, as indicated by a limiting current corresponding to the theoretical value for a one electron process. This is confirmed by the reversible reoxidation of the soluble species at the ring and further corroborates earlier investigations on Pt electrodes under convection [47, 48]. Concerning the rougher electrodes, the disk current density starts to deviate from the theoretical value for a one electron transfer. This deviation from the theoretical value is accompanied by a shift in ORR onset and half-wave potential in positive direction which is caused by the increasing effective rate constant (as the effective rate constant is the product of the rate constant and the electrode roughness) and increasing contribution of peroxide formation, which should occur at more positive potentials (as known from thermodynamic data [144]). The shift in half-wave potential is consistent with observations on Au electrodes.[143] Also the clearly visible increasing OER charge in the anodic scan, especially for f_R = 125, indicates an increasing contribution of adsorbed CaO_2 to the ORR product distribution with raising f_R. The absence of a ring current during peroxide reoxidation at the disk electrode even for f_R = 125 clearly indicates the absence of O_2^- as intermediate. Comparing the initial CV at 4 Hz and the repeated measurement, one observes a decrease in OER charge, which is most likely due to formation of blocking side products.

From a comparison of the disc current with the ring current, which is a measure of the amount of formed soluble species during the ORR, also the contribution of deposited, insoluble species formed at the disc was calculated. (For this calculation we carefully evaluated the first recorded cycle, where the voltammetry is least affected by the formation of side products or similar effects, which would become more pronounced with time.)

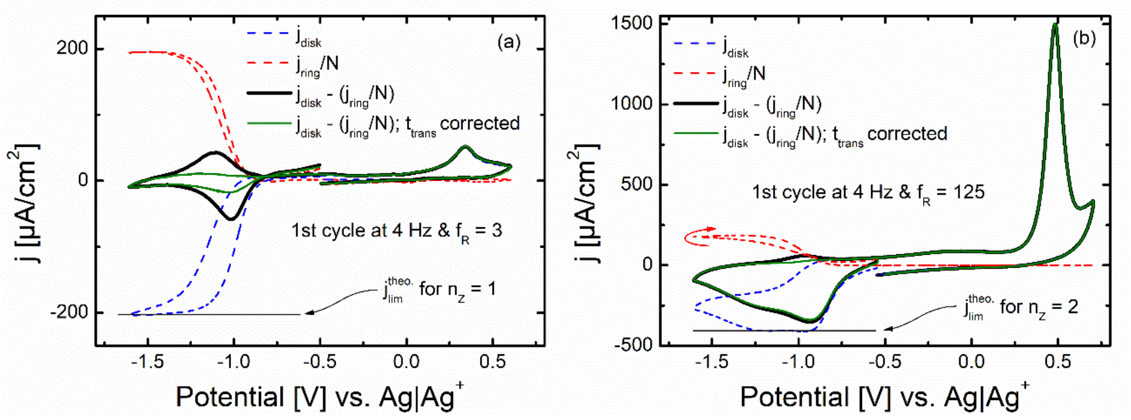

Figure 87 First voltammetric cycle of Pt rotating ring disk electrodes for low and high disk electrode roughness. Electrolyte: 0.1 M $Ca(ClO_4)_2$ in DMSO; v = 20 mV/s; ω= 4 Hz; WE: Pt(pc); CE: Pt-sheet; RE: Ag|Ag⁺. Disk electrode roughness (f_R) = 3 (a) and 125 (b). Only the first CV after electrode immersion is shown. Disk current density (blue, dashed) normalized ring current density (red, dashed) and difference between disk and normalized ring current density (black, straight line) with further correction for transfer time between disk and ring electrode (green, straight line). Limiting current for O_2^-/O_2^{2-}-formation ($i_{\text{lim}}^{\text{theo.}}$) is marked as black line ((a) for superoxide, (b) for peroxide). Rotation frequency was 4 Hz.

Figure 87 shows the first cycle for (a) the lowest and (b) the largest roughness, with the disk current density (blue) and the normalized ring current density (red). For low f_R the diffusion limited current is close to the value for the one electron transfer to form O_2^-.

Under the assumption that the ring current exactly corresponds to complete re-oxidation of soluble species (most likely O_2^-) formed at the disk, the experimental collection efficiency (N) is obtained via:

$$\boldsymbol{N} = \frac{\boldsymbol{i}_{\mathbf{ring}}}{\boldsymbol{i}_{\mathbf{disk}}} \tag{72}$$

i_{disk} is the disk current and i_{ring} is the ring current, N in this work is averaged over all rotation frequencies. To investigate solely the contribution of insoluble species to the disk current density, the normalized ring current density (j_{ring}/N) was subtracted from the disk current density resulting in the black curve.

The anodic current below -1.0 V in this CV is unreasonably large and caused by the delay between O_2^- formation at the disk electrode and detection at the ring electrode and thus an artifact. A correction for this delay leads to the CV for solely insoluble species (green). Though contributions of soluble species (O_2^-) were subtracted, a small negative current is observed, indicating the formation of insoluble oxide species or a small amount of dissolved peroxide (which is not detected at the ring). For large f_R, where the diffusion limited ORR current density approaches the value for two transferred electrons from -0.8 V to -1.25 V in cathodic direction, this negative current obtained after correction is much larger. Its charge closely corresponds to that of the oxidation peak in the subsequent cycle to within 10 %.

For the lowest roughness factor, the relative contribution of the insoluble species is too low and thus the error too large to allow for such a quantitative comparison. Therefore, as the diffusion limited currents indicate a large contribution of peroxide formation, this indicates a predominant formation of most likely adsorbed CaO_2; it is known, that bulk peroxide would quickly dissolve in DMSO. [143] Concerning the above assumption of complete re-oxidation of dissolved species at the disk, one might argue that peroxide requires higher oxidation potentials at the ring as observed before for Au electrodes.[143] However, the agreement between the charge of formation and re-oxidation of insoluble species suggests that the amount of dissolved peroxide is at least negligible. The fact that the fraction of the charge density calculated from anodic oxidation current over the charge density calculated from the ORR current for peroxide approaches unity for high electrode roughness indicates a reversible adsorbate system; its increase with roughness is a further argument for an adsorbate system. The formation of dissolved peroxide is also highly improbable, since we would additionally expect a shoulder in the ring current due to earlier (at more positive potentials) formation of peroxide at the disc electrode compared to superoxide, which leads to a small ring response prior to superoxide detection as observed for Au.[143]

It should be emphasized that for rough Pt electrodes the formed CaO_2 stays adsorbed on the surface until it is oxidized at positive potentials (approximately 0.4 V vs Ag|Ag$^+$) while for rough Au electrodes the formed CaO_2 is dissolved to a large extent[143]. In ref [143] a negative potential of -1.6 V had to be applied to rough Au electrodes to slowly (slow as compared to the formation of soluble peroxide) form an adsorbate, which leads to deactivation and exclusive formation of superoxide during continuous ORR after the completion of the adsorbate layer on Au electrodes. Thus, as the formed CaO_2 on Pt electrodes stays adsorbed on the surface and we observe continuous O_2^- formation, we conclude that similar to Au electrodes[143], the CaO_2 adsorbed on Pt electrodes leads to inhibition of further CaO_2 formation, but allows for O_2^- formation on top of the adsorbate. Note that in case of Au, electrodes can deactivate due to the completion of the adsorbate layer or due to formation of a thick, slowly dissolving CaO_2 layer.[143]

Concerning Figure 86, we already mentioned the deviation of the diffusion limited current density for rougher electrodes from the theoretical value for a one electron transfer and attributed this to the formation of CaO_2. As the relative amount of the CaO_2 adsorbate formation at a given potential during the ORR is larger at low rotation frequency, we would expect an increasing deviation from the theoretical behavior in a plot of the diffusion limited current density (i_{diff}^{-1}) against rotation frequency ($\omega^{-1/2}$) with decreasing ω, as long as the adsorbate layer formation is not finished during the cathodic scan.

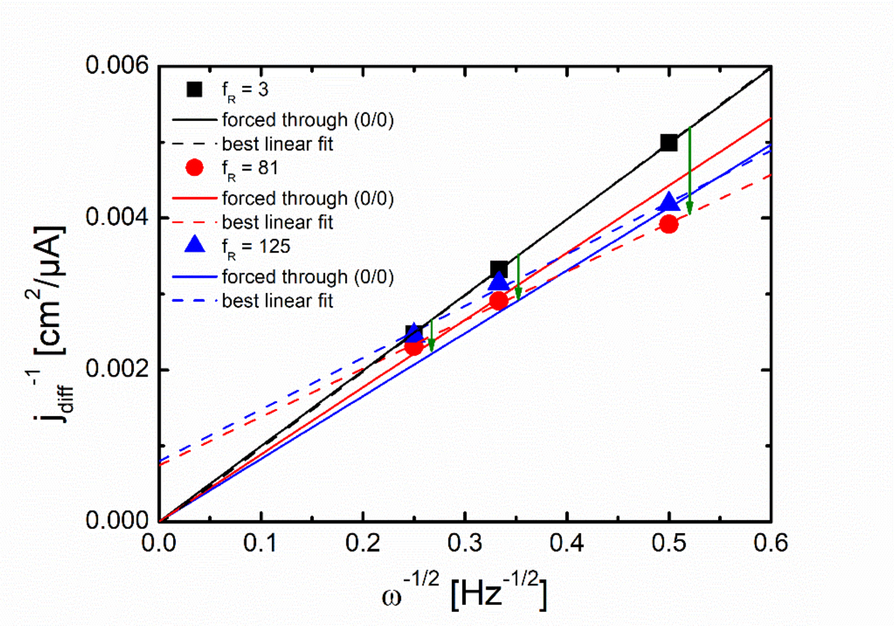

Figure 88 Plot of diffusion limited current density (i_{lim}^{-1}) against rotation frequency ($\omega^{-1/2}$) for f_R = 3 (black), 81 (red) and 125 (blue). Dashed line shows best linear fit and solid line shows linear fit forced through (0/0). Arrows highlight deviation from theoretical behavior for z = 1.

Figure 88 shows this plot, where the dashed lines denote the best linear fit and the solid lines denote a linear fit forced through (0/0). The arrows indicate the deviation from theoretical behavior, as expected. (As the amount of peroxide is limited by the electrode surface and deactivation of peroxide formation occurs within one cycle, the influence on the total ORR current is largest for smallest ω). Thus, we attribute those deviations to the difference in contribution of CaO_2 formation to the limiting current (j_{diff} as function of z, with z as function of E and ω). For f_{R} = 3 the contribution of peroxide formation is negligible and we can calculate the oxygen diffusion coefficient, which gives a value of $2.49 * 10^{-5}\ \mathrm{cm}^2/\mathrm{s}$, being in good agreement with the value obtained similarly on gold electrodes ($2.48 * 10^{-5}\ \mathrm{cm}^2/\mathrm{s}$) [143] and the value ($2.18 * 10^{-5}\ \mathrm{cm}^2/\mathrm{s}$)[143] obtained via diffusion through a thin electrolyte layer (for details see ref. [40, 41]).

Influence on product distribution and kinetics

As we already observed above, electrode roughness influences the product distribution. To get further insights, the total amount of generated CaO_2 was calculated for all CVs shown above following the procedure of Figure 87.

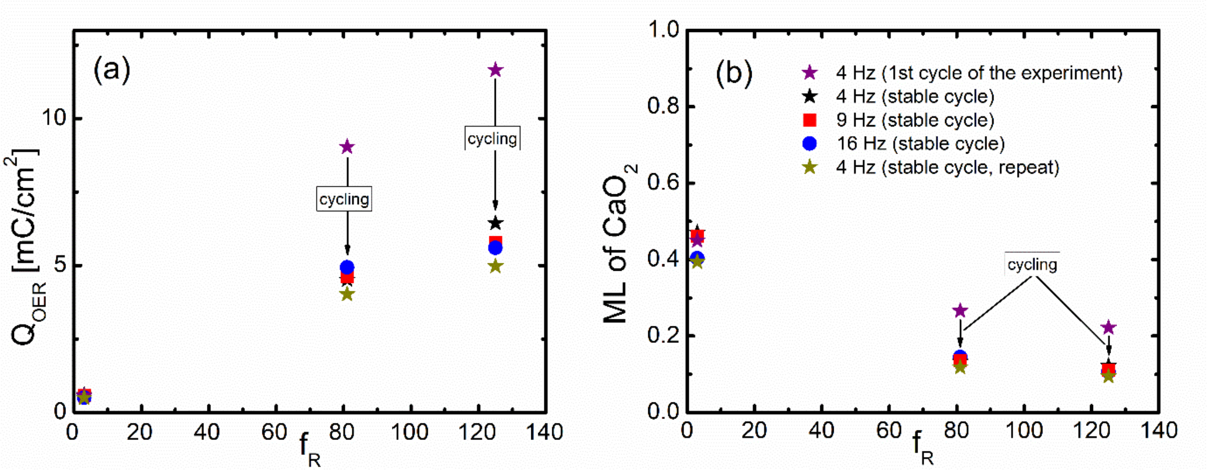

Figure 89 OER charges calculated via integration of anodic oxidation currents normalized to geometric surface area (a) and number of CaO_2 layers (b), both plotted against electrode roughness. Origin of calculated charges are Figure 86 and Figure 87.

Figure 89 shows the OER charges (a) and number of layers (b) adsorbed on Pt electrodes plotted against the electrode roughness. Note that the number of layers corresponds to the hypothetical assumption of a 1 to 1 adsorption, i.e. of one CaO_2 molecule per one Pt surface atom, which might be unreasonable, but allows for better comparability (e.g. to Li^+ [5]). The OER charges increase with electrode roughness, which is reasonable as more CaO_2 can be adsorbed with increasing real surface area. During cycling, the total amount of generated CaO_2 decreases with time. Possible reasons for this behavior are: (i) Smoothening the electrode with time during cycling, (ii) Accumulation of CaO_2 at the electrode (incomplete reoxidation) (iii) Formation of blocking side products. The first possibility can be excluded as a control experiment did show, that the surface roughness for the case of f_R = 125 only changed to f_R = 114 after the whole experiment, which doesn't fit to the extent of deactivation. The second possibility, accumulation of CaO_2 during consecutive cycles can be excluded because above it was shown that the adsorbed peroxide is completely reoxidized (reversible adsorbate system). Thus we assume the third possibility to be the most plausible as it is well-known that the formation of superoxide in consequence leads to significant amounts of highly reactive singlet oxygen, which will decompose the electrolyte. [96, 98, 138, 144]

The charges calculated in Figure 89a can be converted to numbers of CaO_2 layers via division by f_R and the theoretical charge for a monolayer at f_R = 1 assuming the adsorption of one CaO_2 molecule per one Pt surface atom. Those numbers of CaO_2 layers are shown in Figure 89b. Especially for large f_R one obtains values between 0.1 ML and 0.3 ML, which are similar to those obtained in DEMS experiments under convection for Li^+ containing DMSO on Pt electrodes[5]. Nevertheless, it is important to note, that the relative amount of adsorbed CaO_2 (formed within one voltammetric cycle) to soluble O_2^- is strongly increasing upon increasing the electrode roughness, which highlights the effect of electrode roughness on product distribution.

We further elucidated the Tafel slopes from the current voltage relation (see Figure 93) and obtained values around 100 mV/dec for all roughness factors indicating a rate determining transfer of the first electron in the whole potential range. We did not observe a transition of the Tafel slope from 60 mV/dec (α_{app} = 1) at low overpotentials to 120 mV/dec (α_{app} = 0.5) at larger overpotentials as found on Au electrodes[143]. The reason is certainly that on non-annealed Pt blocking occurs so fast that a large part of the current is due to the one electron reduction, which on Au is only observed at higher overpotentials.

10.3.5 Discussion

Mechanism of oxygen reduction on Pt electrodes – comparison to Au

Summarizing all our results on oxygen reduction in Ca-ion containing DMSO, we are able to propose a simplified oxygen reduction mechanism on annealed and rough Pt electrodes (see Figure 91). The ORR mechanism on Au electrodes, which was described in detail in previous studies, is shown in Figure 90 for comparison. [143, 144]

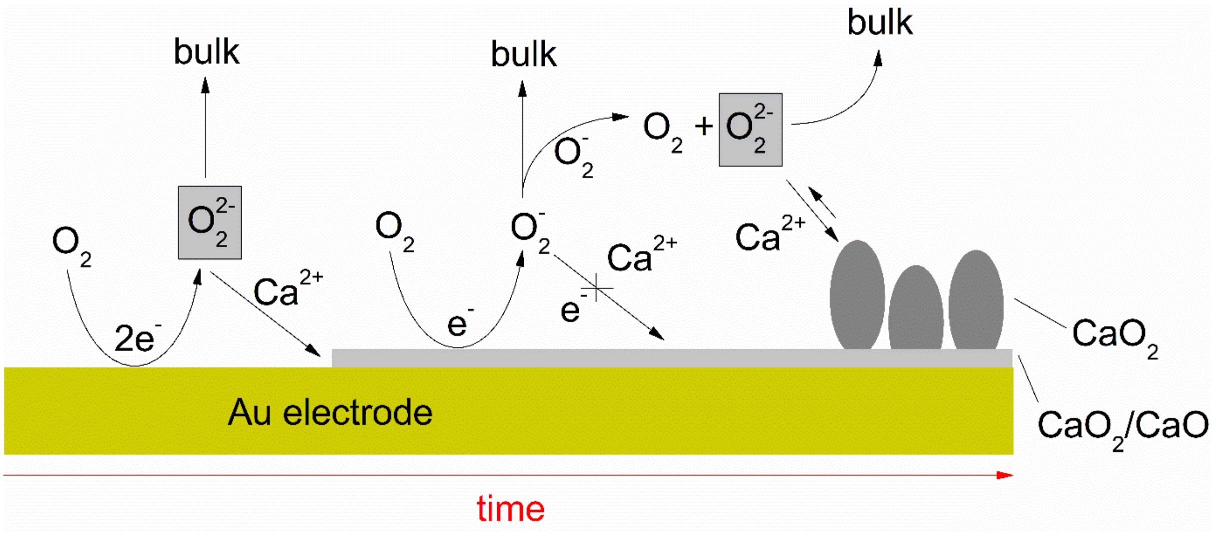

Figure 90 Simplified ORR mechanism on Au electrodes adapted from [143].

In earlier studies on Au electrodes [143, 144] it was found that on a bare Au electrode in $Ca(ClO_4)_2$ containing DMSO, oxygen is reduced to peroxide, which dissolves into the bulk electrolyte. This peroxide can form a thick bulk layer on the electrode during continuous ORR, which slowly dissolves as no more peroxide is formed (as the potential is swept out of the ORR region). In a competing, slow side reaction to the peroxide formation, a CaO/CaO_2 adsorbate is formed, which inhibits further peroxide formation. Astonishingly, though the adsorbate inhibits further peroxide formation, superoxide can still be formed on top or through the adsorbate.

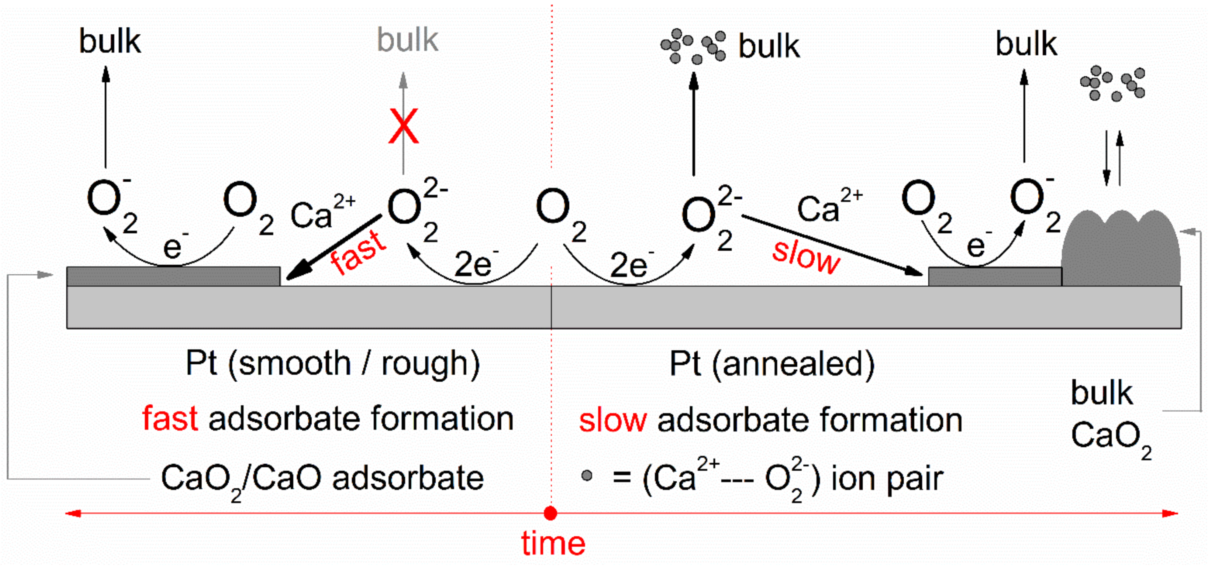

Figure 91 Simplified ORR mechanism on annealed (atomically smooth) and smooth/rough (at least atomically rough) Pt electrodes.

Regarding platinum electrodes, we earlier found that dominantly superoxide is formed.[47, 48] In the present study we found that on single crystalline electrodes the number of transferred electrons during oxygen reduction in a DEMS experiment under convection indicates a current contribution also of peroxide formation. Furthermore, in quiescent solution, we found that the current density during the ORR in an H-cell is larger than the theoretical value for a one electron transfer (both reversible and irreversible). Thus we conclude so far that at least on single crystalline electrodes, peroxide is formed on Pt electrodes as well.

The peroxide formed on single crystalline Pt electrodes in a DEMS experiment further seems to mostly dissolve, as the charge density exceeds the charge density of a theoretical monolayer (assuming the adsorption of 1 CaO_2 per 1 Pt surface atom) and only a comparably small oxidation current is observed. This suggests that the ORR mechanism on single crystalline Pt electrodes is similar to that on Au electrodes (cf. right side of Figure 91). So the formation of a thick CaO_2 bulk layer as well as the formation of an adsorbate which deactivates continuous peroxide formation have to be considered.

DEMS results on Pt single crystals under convection further show a decrease in the number of transferred electrons (and thus in peroxide contribution) at larger overpotentials during the oxygen reduction. This decrease in peroxide contribution might be the first indication of the formation of an adsorbate also on single crystalline Pt electrodes, as the transition from the two electron process to the one electron process is well known to be caused by the CaO_2 adsorbate referring to the Au system (note that CaO might also be formed as side product on Pt electrodes during ORR).

Regarding atomically rough Pt electrodes in an RRDE setup, we found that for low electrode roughness there is hardly any peroxide contribution visible. A peroxide contribution in this RRDE setup should be visible as:

1. A shoulder in the ring current (lower current as it is known that at least on Au electrodes the peroxide reoxidation kinetics are slow at the given ring potential).
2. A shoulder in the disc current (as the diffusion limited current should depend on the number of transferred electrons).

None of that is observed for the case of low electrode roughness. For larger electrode roughness, the disc current increases and exceeds the theoretical current for diffusion limited superoxide formation. This hints to the formation of peroxide also on rough Pt electrodes. Though we observed an increase in disc current, there was no shoulder in the ring current for rough Pt electrodes. This shows that the insoluble peroxide formed is not dissolved, i.e. deposited as bulk or adsorbed. As we know from the Au system that bulk CaO_2 can dissolve in DMSO (thus being expected to be partially detected at the ring electrode), we conclude that the formed peroxide is most probably directly adsorbed on the surface. This is further supported by a high reoxidation efficiency of the formed CaO_2. Furthermore the calculated charge densities for the formation and reoxidation of the calcium oxide species are in good agreement with the charge density for Li_2O_2 formation and reoxidation on Pt electrodes in DMSO[5], indicating that only a mono layer is formed. This layer inhibits further 2 e^- transfer, but allows for further superoxide formation and in consequence is the reason for the finding of dominant superoxide formation in ref. [47, 48] as there the electrode (with low f_R) was immediately covered by the adsorbate layer.

This leads to the conclusion that on atomically rough Pt electrodes the formation of the CaO_2 adsorbate is favoured over the formation of dissolving peroxide, whereas on atomically smooth Pt electrodes the adsorbate is formed in a slow, competing side reaction as it is observed on Au electrodes. This indicates, that the formed adsorbate is thermodynamically or kinetically less stable on atomically smooth Pt electrodes. As a consequence, smooth (annealed) Pt behaves similar to Au electrodes.

Mechanistic comparison to other electrode materials

As the adsorbate formation affects the product distribution not only on Au electrodes but also on Pt electrodes, we searched for factors that correlate with the kinetics of the adsorbate formation and trends of the product distribution. As the calculation of interaction energies is not part of this study, we used bond dissociation energies as simplified parameter. To further investigate influences of different divalent cations we used the relative bond dissociation energy (ΔBDE) which is calculated via:

$$\Delta BDE = BDE_{\mathrm{M-O}} - BDE_{\mathrm{electrode-O}} \qquad (\mathrm{M = Mg, Ca, Sr, Ba}) \tag{73}$$

In this study we used the BDE values from ref. [151]. As parameter for the product distribution we used the peroxide share (χ_{peroxide}), which is calculated from the number of transferred electrons during a DEMS experiment under convection (taken from earlier studies[47, 48]) during the ORR at -1.3 V vs. Ag|Ag$^+$. Assuming that only peroxide and superoxide formation contribute to the ORR current, z is given by

$$z = z_{\mathrm{peroxide}} * \chi_{\mathrm{peroxide}} + z_{\mathrm{superoxide}} * \chi_{\mathrm{superoxide}} \tag{74}$$

With the number of transferred electrons during peroxide formation ($z_{\mathrm{peroxide}} = 2$) and superoxide formation ($z_{\mathrm{superoxide}} = 1$) and

$$\chi_{\mathrm{peroxide}} + \chi_{\mathrm{superoxide}} = 1 \tag{75}$$

Equation (74) can be rearranged to give

$$\chi_{\text{peroxide}} = z - 1 \tag{76}$$

At the potential of -1.3 V vs. Ag|Ag$^+$ we would expect diffusion limited peroxide/superoxide formation (negative enough) and a low contribution of side reactions or other effects (positive enough). Note that roughness effects can be excluded as no roughened electrodes were used in ref. [47, 48]. Here we predict an increase of χ_{peroxide} with increasing (more positive values) ΔBDE, as the superoxide formation at the given potential requires a fast adsorbate layer completion and the peroxide contribution should be larger for more positive values of ΔBDE (weak electrode-oxide interaction and strong M-oxide interaction so that peroxide can leave the electrode vicinity, which leads to increased formation of peroxide).

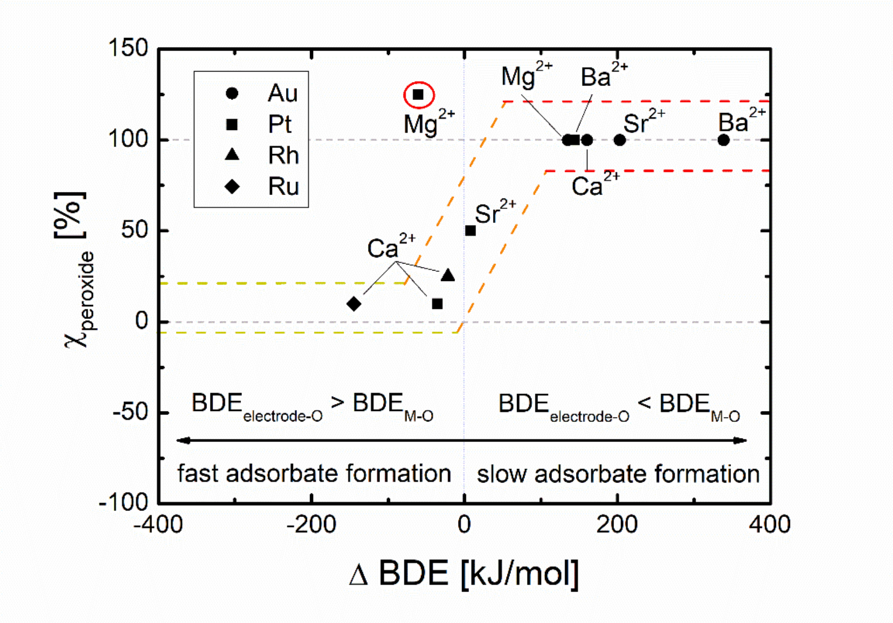

Figure 92 shows the plot of the peroxide contribution to the ORR current at -1.3 V vs Ag|Ag$^+$ in 0.4 M M^{2+} (M = Mg, Ca, Sr and Ba) containing DMSO ($\chi_{peroxide}$) vs. the relative bond dissociation energy (ΔBDE) for several electrode materials and divalent cations.

Figure 92 shows that the mentioned trend holds for all cations and electrode materials used in ref. [47, 48] . The only exception is magnesium, which one might attribute to the high charge density of Mg^{2+} or the different crystal structure of MgO compared to the other alkaline earth metal oxides. One might further argue, that the observed trend depends on the potential, where z (and share) was evaluated, which is partially true. So, if we use a potential which is too negative or stronger convection, we would observe a peroxide share of close to 0 % (z=1) in all cases (at this potential). This is effectively shifting the ($\Delta \mathrm{BDE}$) value where we observe the transition from peroxide to superoxide formation. However, the trend itself (being the important result) should stay unaffected as long as no additional effects are introduced. This trend finally hints a competition of the adsorbate formation and the ion pair formation

(ion pair formation was already proposed to be an important factor during the ORR)[48], finally determining the product distribution of the ORR.

10.3.6 Conclusion

We herein studied the effect of atomic roughness on the ORR and OER in Ca^{2+} containing DMSO. This involved the protection of the Pt single crystals during the transfer to the aprotic solution by an adsorbed layer of bromide, which – as we demonstrated by XPS and cyclic voltammetry – is completely stripped from the surface prior to the onset of oxygen reduction.

On both atomically smooth and rough Pt and Au electrodes initially Ca-peroxide is the main reduction product; superoxide is the main product after the completion of an adsorbate layer of CaO_2 (or CaO as side product). On Pt, this adsorbate layer is completed much faster than on Au. It is furthermore formed faster on atomically rough electrodes than on atomically smooth ones. In absence of convection the formation of a thicker bulk layer had been demonstrated on Au; the present study indicates that dissolved peroxide formation occurs on atomically smooth Pt electrodes as well. Note that the formation of bulk CaO_2 via disproportionation of superoxide somewhere in the electrolyte might also be possible, and in a battery may be even advantageous. However, under the conditions of the present study, this is not observed. (Disproportionation in the vicinity of the electrode would lead to an additional oxygen transport to the electrode showing up as an apparent 2-electron transfer in the diffusion limited currents.) It is noteworthy that superoxide can be formed on top or through the CaO_2 adsorbate layer, which allows for continuous discharge. However, the adsorbate might also cause an additional overpotential not only for the superoxide formation but also for the superoxide reoxidation

By varying the electrode roughness, we obtained a deeper understanding of the general ORR mechanism in M^{2+} containing DMSO. This and our former study on Au[143] identified the formation of the adsorbed alkaline earth metal oxide/peroxide as the limiting factor for continuous peroxide formation for several electrode materials (including even glassy carbon) in DMSO. Thus, the product distribution depends on the electrode surface–oxide interaction ($\Delta E_{\mathrm{M-O}}$). Referring to batteries a continuous discharge (with peroxide as main product) without deactivation is expected for electrode materials with low oxide interaction ($\Delta E_{\mathrm{M-O}}$ >> 0). Whereas for $\Delta E_{\mathrm{M-O}}$ << 0 we expect a fast adsorbate formation and thus a continuous discharge with superoxide as main product. This is exactly the trend we observe referring to earlier publications.[47, 48] Concerning battery applications peroxide is largely favored over superoxide due to its higher theoretical energy density ($z = 2$). Thus, electrode materials with extraordinarily positive $\Delta E_{\mathrm{M-O}}$ (like Au) are of special interest. Regardless of electrode material, the ORR product distribution in M^{2+} containing DMSO can be influenced by several factors:

- Electrode roughness: On rough electrodes the adsorbate layer completion requires more charge due to the increased real electrode surface area.
- Atomic surface structure: On atomically smooth electrodes (at least Au and Pt) the CaO_2/CaO adsorbate formation is hindered due to thermodynamic or kinetic instability of the Adsorbate on the atomically smooth surface or due to a kinetic hindrance.
- Additives: ORR mediators for example lead to an ORR at some distance of the electrode and thus should avoid the formation of the adsorbate to some extent; such a redox mediation was topic in an earlier study[144].

Regarding battery applications this study shows that:

1. minimizing the electrode oxide interaction
2. minimizing electrode surface defects/roughness (atomically smooth)
3. maximizing the real surface area of the electrode

are key points to maximize the contribution of dissolving peroxide to the ORR current and thus should increase the battery performance. Thus, this study encourages further experiments on e.g. gold nanoparticle electrodes, as those combine the mentioned key points.

10.3.7 Supporting information

Calculation of the theoretical peak current

In this study we used the Randles-Sevcik equation for a reversible process

$$j_{\mathrm{p}} = 0.4463 C_{\mathrm{O_2}} z^{3/2} F^{3/2} (v D_{\mathrm{O_2}}/RT)^{1/2} \tag{77}$$

And irreversible process

$$j_{\mathrm{p}} = 2.99 * 10^5 * z C_{\mathrm{O_2}} (\alpha z_\alpha D_{\mathrm{O_2}} v)^{1/2} \tag{78}$$

To estimate the theoretical peak current densities (j_{p}), with T as temperature, R as ideal gas constant, $D_{\mathrm{O_2}}$ as oxygen diffusion coefficient, v as sweep rate, F as faraday constant, α as transfer coefficient, z_α as number of transferred electron during the rate determining step, z as number of transferred electrons and $C_{\mathrm{O_2}}$ as bulk concentration of oxygen (0.4 mM at 20% O_2 saturation).[40, 41]

Tafel slopes of the ORR in 0.1 M $Ca(ClO_4)_2$ containing DMSO on Pt electrodes

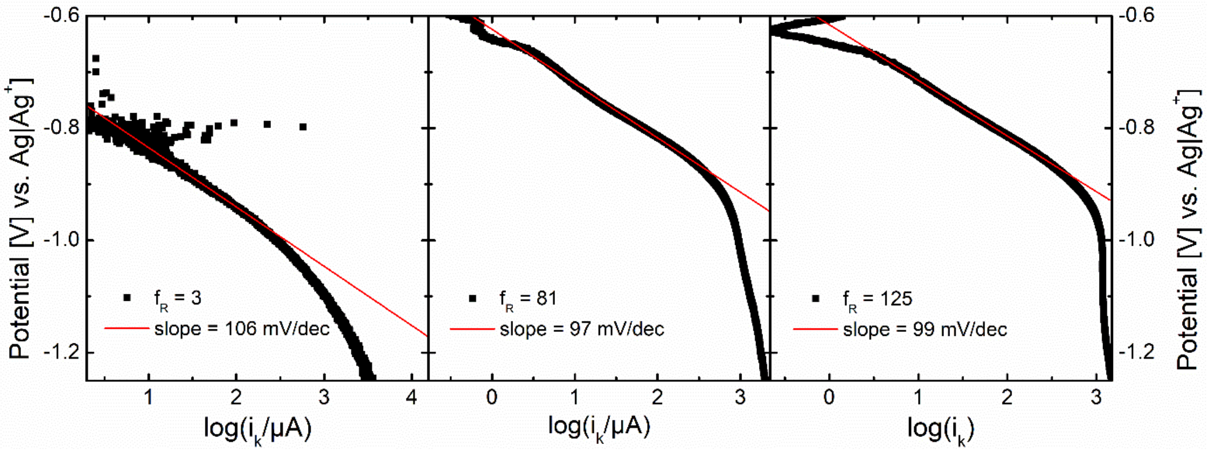

Figure 93 Tafel plots of potential against the logarithm of the absolute kinetic current (i_k) for f_R = 3, 81 and 125. Tafel analysis refers toFigure 86.

Induction setup and proof of protection concept

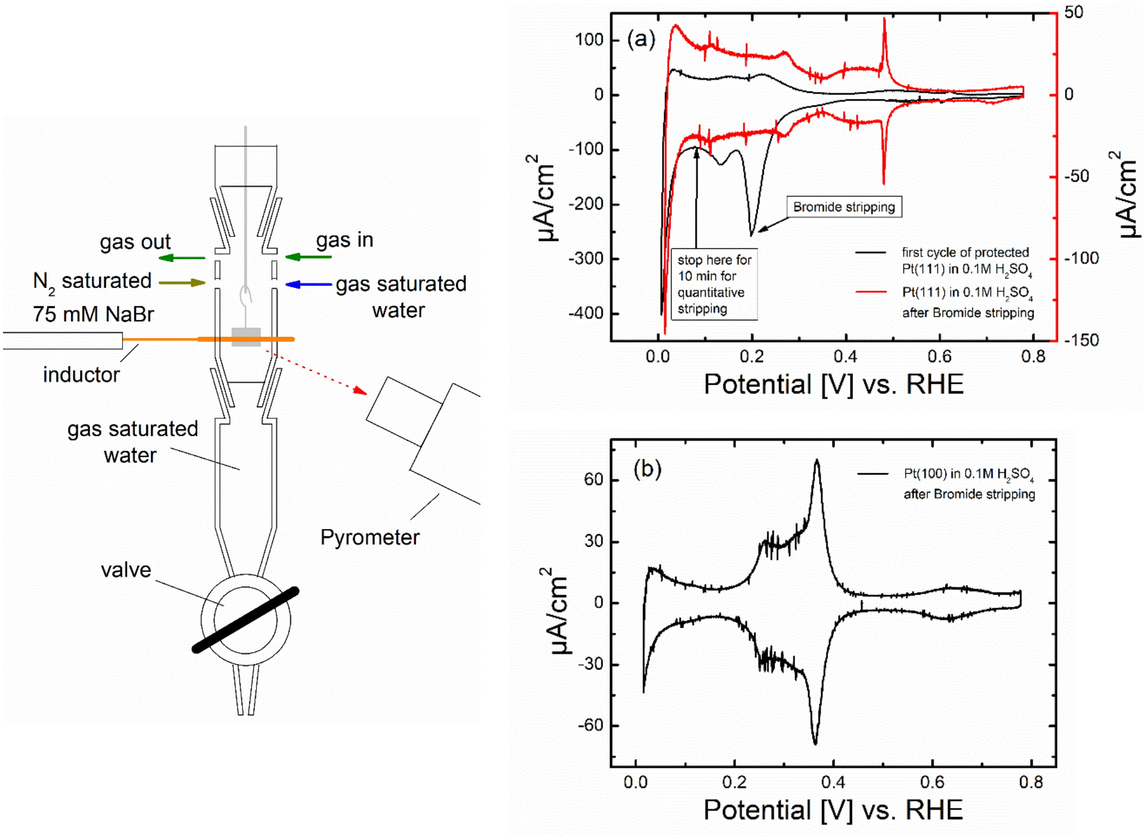

Figure 94 (left): Schematic picture of the induction/protection glass cell. (right): Voltammogram of a Br_{ads} modified Pt(111) electrode (black) and the same electrode after stripping of the adsorbate layer (red) (a). Voltammogram of the Pt(100) electrode after stripping of the Br_{ads} layer (b). The figures of the preservation prove were already shown in ref. [26].

In situ STM image of iodide on Pt(111) in DMSO

The Pt(111) single-crystal electrode was used as working electrode, while it was prepared by flame annealing and cooled down above Milli-Q water in an Ar atmosphere afterwards. After the cooling process, the Pt(111) electrode was dipped into 1mM KI/water for 2 min under Ar atmosphere. Adsorbed iodide on the Pt(111) surface makes it hydrophobic so that residual water can be removed easily. The Pt(111) electrode was then transferred to STM-cell. Afterwards the STM-cell was filled with DMSO. During operating the STM, the whole STM chamber was purged with Ar to preserve the clean surface.

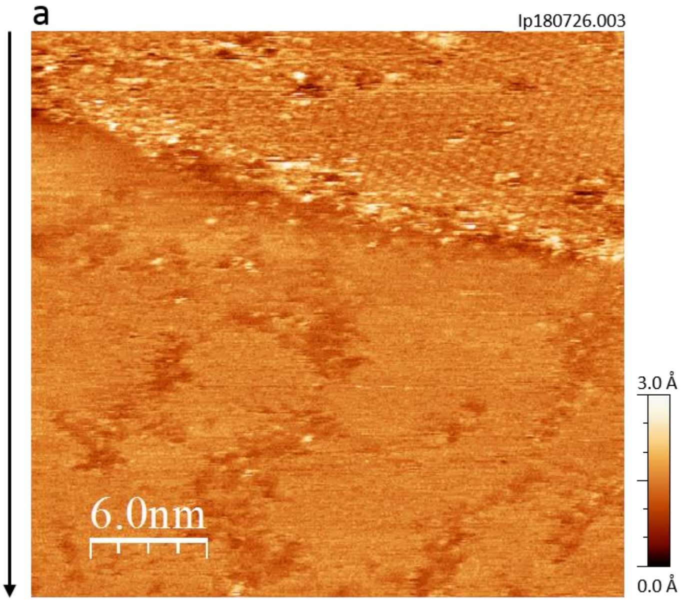

Figure 95 In situ STM image of iodide structure on Pt(111) in DMSO. The arrow indicates the scan direction. The bias voltage and set point were set as 25 mV and 1nA, respectively. The scan rate was 6.10 Hz and I/P gains were 0.3/0.4.

It was hard to preserve the atomic structure of iodine on Pt(111) in DMSO. As shown in Figure 95, the structure disappeared during the 1st scan of the STM. This behavior may correlate with a weaker interaction between the Pt(111) surface and iodide compared to the Pt(111) surface and DMSO.

11 References

[1] Y. Yamada, K. Usui, K. Sodeyama, S. Ko, Y. Tateyama, A. Yamada, *Nature Energy* **2016**, *1*, 16129.

[2] S. Wu, Y. Qiao, S. Yang, J. Tang, P. He, H. Zhou, *ACS Catalysis* **2018**, 1082.

[3] J. J. Leitch, J. Collins, A. K. Friedrich, U. Stimming, J. R. Dutcher, J. Lipkowski, *Langmuir* **2012**, *28*, 2455.

[4] I. Burgess, V. Zamlynny, G. Szymanski, J. Lipkowski, J. Majewski, G. Smith, S. Satija, R. Ivkov, *Langmuir* **2001**, *17*, 3355.

[5] A. Koellisch-Mirbach, T. Lohrmann, P. H. Reinsberg, H. Baltruschat, *Journal of Electroanalytical Chemistry (1959)* **2020**, *875*, 114560.

[6] W. J. Albery, S. Bruckenstein, *Transactions of the Faraday Society* **1966**, *62*, 1920.

[7] R. R. Bruckenstein, J. Gadde, *Journal of the American Chemical Society* **1971**, *93*, 793.

[8] O. Wolter, J. Heitbaum, *Berichte der Bunsengesellschaft für Physikalische Chemie* **1984**, *88*, 2.

[9] U. Schmiemann, U. Müller, H. Baltruschat, *Electrochimica Acta* **1995**, *40*, 99.

[10] F. J. Vidal-Iglesias, J. Solla-Gullon, J. M. Feliu, H. Baltruschat, A. Aldaz, *Journal of Electroanalytical Chemistry* **2006**, *588*, 331.

[11] T. Hartung, U. Schmiemann, I. Kamphausen, H. Baltruschat, *Analytical Chemistry* **1991**, *63*, 44.

[12] U. Schmiemann, H. Baltruschat, *Journal of Electroanalytical Chemistry* **1992**, *340*, 357.

[13] U. Müller, U. Schmiemann, A. Dülberg, H. Baltruschat, *Surface Science* **1995**, *335*, 333.

[14] R. Stadler, Z. Jusys, H. Baltruschat, *Electrochimica Acta* **2002**, *47*, 4485.

[15] T. Löffler, R. Bussar, E. Drbalkova, P. Janderka, H. Baltruschat, *Electrochimica Acta* **2003**, *48*, 3829

[16] T. Löffler, E. Drbalkova, P. Janderka, P. Königshoven, H. Baltruschat, *Journal of Electroanalytical Chemistry* **2003**, *550-551*, 81.

[17] F. Hernandez, J. Sanabria-Chinchilla, M. P. Soriaga, H. Baltruschat, in *Electrode Processes VII, Vol. 18* (Eds.: V.I. Birss, M. Josowicz, D. Evans, M. Osawa), Electrochemical Society Proceedings, Pennington, **2004**, p. 15.

[18] R. Bussar, M. Nielinger, H. Baltruschat, *Journal of Electroanalytical Chemistry* **2005**, *578*, 259.

[19] R. Stadler, H. Baltruschat, *to be submitted* **2005**.

[20] H. Baltruschat, R. Bussar, S. Ernst, F. Hernandez-Ramirez, in *In-situ Spectroscopic Studies of Adsorption at the Electrode and Electrocatalysis* (Eds.: S.-G. Sun, P. A. Christensen, A. Wieckowski), Elsevier, Amsterdam, **2007**, pp. 471

[21] H. Wang, H. Baltruschat, *Journal of Physical Chemistry C* **2007**, *111*, 7038.

[22] T. Löffler, R. Bussar, X. Xiao, S. Ernst, H. Baltruschat, *Journal of Electroanalytical Chemistry* **2009**, *629*, 1.

[23] A. A. Abd-El-Latif, E. Mostafa, S. Huxter, G. Attard, H. Baltruschat, *Electrochimica Acta* **2010**, *55*, 7951.

[24] E. Mostafa, A. A. Abd-El-Latif, H. Baltruschat, *ChemPhysChem* **2014**, *15*, 2029.

[25] S. Iqbal, C. Bondü, H. Baltruschat, *The Journal of Physical Chemistry C* **2015**, *119*, 20515.

[26] M. Hegemann, P. Bawol, A. Köllisch-Mirbach, H. Baltruschat, *Electrocatalysis* **2021**, 1.

[27] G. Eggert, J. Heitbaum, *Electrochimica Acta* **1986**, *31*, 1443.

[28] R. Imhof, P. Novak, *Journal of the Electrochemical Society* **1998**, *145*, 1081.

[29] C. J. Bondue, P. Königshoven, H. Baltruschat, *Electrochimica Acta* **2016**, *214*, 241.

[30] M. Heinen, Y. X. Chen, Z. Jusys, R. J. Behm, *Electrochimica Acta* **2007**, *53*, 1279

[31] Z. Jusys, H. Massong, H. Baltruschat, *Journal of the Electrochemical Society* **1999**, *146*, 1093.

[32] A. Wexler, *Journal of research of the National Bureau of Standards. Section A, Physics and chemistry* **1976**, *80A*, 775.

[33] L. A. Kibler, *Preparation and Characterization of Noble Metals Single Crystal Electrodes*, University of Ulm, **2003**.

[34] A. Cuesta, L. A. Kibler, D. M. Kolb, *Journal of Electroanalytical Chemistry* **1999**, *466*, 165.

[35] M. Ahmed, D. Morgan, G. A. Attard, E. Wright, D. Thompsett, J. Sharman, *The Journal of Physical Chemistry C* **2011**, *115*, 17020.

[36] T. A. Galloway, J. C. Dong, J. F. Li, G. Attard, L. J. Hardwick, *Chemical Science* **2019**, *10*, 2956.

[37] G. Binnig, C. F. Quate, C. Gerber, *Physical Review Letters* **1986**, *56*, 930.

[38] J. E. Sader, J. W. M. Chon, P. Mulvaney, *Review of Scientific Instruments* **1999**, *70*, 3967.

[39] C. P. Green, H. Lioe, J. P. Cleveland, R. Proksch, P. Mulvaney, J. E. Sader, *Review of Scientific Instruments* **2004**, *75*, 1988.

[40] P. H. Reinsberg, P. P. Bawol, E. Thome, H. Baltruschat, *Analytical chemistry* **2018**, *90*, 14150.

[41] P. P. Bawol, P. H. Reinsberg, H. Baltruschat, *Analytical chemistry* **2018**, *90*, 14145.

[42] T. Seguin, N. Hahn, K. Zavadil, K. Persson, *Frontiers in chemistry* **2019**, *7*, 175.

[43] N. N. Rajput, X. Qu, N. Sa, A. K. Burrell, K. A. Persson, *Journal of the American Chemical Society* **2015**, *137*, 3411.

[44] G. Srinivas, C. A. Howard, N. T. Skipper, S. M. Bennington, M. Ellerby, *Physica C-Superconductivity and Its Applications* **2009**, *469*, 2000.

[45] A. Ponrouch, C. Frontera, F. Barde, M. R. Palacin, *Nature Materials* **2016**, *15*, 169.

[46] T. Ouchi, H. Kim, X. H. Ning, D. R. Sadoway, *Journal of the Electrochemical Society* **2014**, *161*, A1898.

[47] P. Reinsberg, C. J. Bondue, H. Baltruschat, *Journal of Physical Chemistry C* **2016**, *120*, 22179.

[48] P. Reinsberg, A. A. Abd-El-Latif, H. Baltruschat, *Electrochimica Acta* **2018**, *273*, 424.

[49] Y. H. Kim, J. Calabrese, C. McEwen, *Journal of the American Chemical Society* **1996**, *118*, 1545.

[50] I. Burgess, C. A. Jeffrey, X. Cai, G. Szymanski, Z. Galus, J. Lipkowski, *Langmuir* **1999**, *15*, 2607.

[51] M. Petri, D. M. Kolb, *Physical Chemistry Chemical Physics* **2002**, *4*, 1211.

[52] G. J. Edens, X. Gao, M. J. Weaver, *Journal of Electroanalytical Chemistry and Interfacial Electrochemistry* **1994**, *375*, 357.

[53] E. Ito, H. Kang, D. Lee, J. B. Park, M. Hara, J. Noh, *Journal of Colloid and Interface Science* **2013**, *394*, 522.

[54] B. Lüssem, L. Müller-Meskamp, S. Karthäuser, R. Waser, *Langmuir* **2005**, *21*, 5256.

[55] P. Berenz, X. Xiao, H. Baltruschat, *Journal of Physical Chemistry B* **2002**, *106*, 3673.

[56] X. Y. Xiao, M. Nielinger, H. Baltruschat, *Electrochimica Acta* **2003**, *48*, 3093.

[57] M. Nielinger, P. Berenz, X. Y. Xiao, H. Baltruschat, *Surface Science* **2005**, *597*, 1.

[58] O. Hmam, A. Badia, *Advanced Materials Interfaces* **2022**, *9*.

[59] S. Iqbal, S. Wezisla, N. Podgaynyy, H. Baltruschat, *Electrochimica Acta* **2015**, *186*, 427.

[60] F. Hausen, M. Nielinger, S. Ernst, H. Baltruschat, *Electrochimica Acta* **2008**, *53*, 6058.

[61] I. Park, H. Baltruschat, *ChemPhysChem* **2021**, *7*, 1.

[62] I. Park, H. Baltruschat, *ChemElectroChem* **2022**, *9*.

[63] H. Angerstein-Kozlowska, B. E. Conway, A. Hamelin, L. Stoicoviciu, *Electrochimica Acta* **1986**, *31*, 1051.

[64] R. Sadeghi, S. Shahabi, *The Journal of Chemical Thermodynamics* **2011**, *43*, 1361.

[65] I. Park, H. Baltruschat, *Journal of the Electrochemical Society (Focus Issue on Nucleation Growth: Measurements, Processes, and Materials)* **2022**, *169*, 122501.

[66] A. I. Belova, D. G. Kwabi, L. V. Yashina, Y. Shao-Horn, D. M. Itkis, *The Journal of Physical Chemistry C* **2017**.

[67] Panasonic, **06.04.2020 (retrieved)**.

[68] C. Bondue, P. Reinsberg, A. A. Abd-El-Latif, H. Baltruschat, *Physical Chemistry Chemical Physics* **2015**, *17*, 25593.

[69] M. W. Chase, *Journal of Physical and Chemical Reference Data, Monograph 9, Vol. Monograph 9*, 4 ed., **1998**.

[70] N. Garcia-Araez, P. NovÃ¡k, *Journal of Solid State Electrochemistry* **2013**, *17*, 1793.

[71] Z. Peng, S. A. Freunberger, Y. Chen, P. G. Bruce, *Science* **2012**, *337*, 563.

[72] C. O. Laoire, S. Mukerjee, K. M. Abraham, E. J. Plichta, M. A. Hendrickson, *Journal of Physical Chemistry C* **2010**, *114*, 9178.
[73] D. Xu, Z.-l. Wang, J.-j. Xu, L.-l. Zhang, L.-m. Wang, X.-b. Zhang, *Chemical Communications* **2012**, *48*, 11674.
[74] W. Xu, J. Hu, M. H. Engelhard, S. A. Towne, J. S. Hardy, J. Xiao, J. Feng, M. Y. Hu, J. Zhang, F. Ding, M. E. Gross, J.-G. Zhang, *Journal of Power Sources* **2012**, *215*, 240.
[75] B. D. McCloskey, D. S. Bethune, R. M. Shelby, T. Mori, R. Scheffler, A. Speidel, M. Sherwood, A. C. Luntz, *The Journal of Physical Chemistry Letters* **2012**, *3*, 3043.
[76] K. M. Abraham, Z. Jiang, *Journal of the Electrochemical Society* **1996**, *143*, 1.
[77] C. O. Laoire, S. Mukerjee, K. M. Abraham, E. J. Plichta, M. A. Hendrickson, *Journal of Physical Chemistry C* **2009**, *113* 20127.
[78] Z. Peng, S. A. Freunberger, L. J. Hardwick, Y. Chen, V. Giordani, F. Bardé, P. Novák, D. Graham, J.-M. Tarascon, P. G. Bruce, *Angewandte Chemie International Edition* **2011**, *50*, 6351.
[79] A. Debart, J. Bao, G. Armstrong, P. G. Bruce, *Journal of Power Sources* **2007**, *174*, 1177.
[80] N. B. Aetukuri, B. D. McCloskey, J. M. García, L. E. Krupp, V. Viswanathan, A. C. Luntz, *Nat Chem* **2015**, *7*, 50.
[81] Y.-C. Lu, H. A. Gasteiger, Y. Shao-Horn, *Journal of the American Chemical Society* **2011**, *133*, 19048.
[82] W. Torres, N. Mozhzhukhina, A. Y. Tesio, E. J. Calvo, *Journal of the Electrochemical Society* **2014**, *161*, A2204.
[83] M. J. Trahan, S. Mukerjee, E. J. Plichta, M. A. Hendrickson, K. M. Abraham, *Journal of the Electrochemical Society* **2013**, *160*, A259.
[84] D. Sharon, V. Etacheri, A. Garsuch, M. Afri, A. A. Frimer, D. Aurbach, *The Journal of Physical Chemistry Letters* **2012**, *4*, 127.
[85] N. Mozhzhukhina, L. P. Méndez De Leo, E. J. Calvo, *The Journal of Physical Chemistry C* **2013**, *117*, 18375.
[86] E. J. Calvo, N. Mozhzhukhina, *Electrochemistry Communications* **2013**, *31*, 56.
[87] B. D. McCloskey, D. S. Bethune, R. M. Shelby, G. Girishkumar, A. C. Luntz, *Journal of Physical Chemistry Letters* **2011**, *2*, 1161.
[88] C. Xia, R. Black, R. Fernandes, B. Adams, L. F. Nazar, *Nature chemistry* **2015**, *7*, 496.
[89] D. Aurbach, B. D. McCloskey, L. F. Nazar, P. G. Bruce, *Nature Energy* **2016**, *1*, 16128.
[90] P. Reinsberg, A. Weiss, P. P. Bawol, H. Baltruschat, *Journal of Physical Chemistry C* **2017**, *121*, 7677.
[91] V. Gutmann, *Coordination Chemistry Reviews* **1976**, *18*, 225.
[92] C. J. Bondue, P. P. Bawol, A. A. Abd-El-Latif, P. Reinsberg, H. Baltruschat, *The Journal of Physical Chemistry C* **2017**, *121*, 8864.
[93] L. Johnson, C. Li, Z. Liu, Y. Chen, S. A. Freunberger, P. C. Ashok, B. B. Praveen, K. Dholakia, J.-M. Tarascon, P. G. Bruce, *Nature chemistry* **2014**, *6*, 1091.
[94] M. Marinaro, S. K. E. Moorthy, J. Bernhard, L. Jörissen, M. Wohlfahrt-Mehrens, U. Kaiser, *Beilstein Journal of Nanotechnology* **2013**, *4*, 665.
[95] N. Mozhzhukhina, F. Marchini, W. R. Torres, A. Y. Tesio, L. P. Mendez De Leo, F. J. Williams, E. J. Calvo, *Electrochemistry Communications* **2017**, *80*, 16.
[96] D. Córdoba, H. n. B. Rodríguez, E. J. Calvo, *ChemistrySelect* **2019**, *4*, 12304.
[97] N. Mahne, S. E. Renfrew, B. D. McCloskey, S. A. Freunberger, *Angewandte Chemie International Edition* **2018**, *57*, 5529.
[98] E. Mourad, Y. K. Petit, R. Spezia, A. Samojlov, F. F. Summa, C. Prehal, C. Leypold, N. Mahne, C. Slugovc, O. Fontaine, S. Brutti, A. Freunberger Stefan, *Energy & Environmental Science* **2019**, *12*, 2559.
[99] C. J. Bondue, P. Reinsberg, H. Baltruschat, *Electrochimica Acta* **2017**, *245*, 1035.
[100] C. J. Bondue, M. Hegemann, C. Molls, E. Thome, H. Baltruschat, *Journal of the Electrochemical Society* **2016**, *163*, A1765.

[101] C. J. Bondue, A. A. Abd-El-Latif, P. Hegemann, H. Baltruschat, *Journal of the Electrochemical Society* **2015**, *162*, A479.

[102] C. Liu, S. Ye, *The Journal of Physical Chemistry C* **2016**, *120*, 25246.

[103] S. Ganapathy, B. D. Adams, G. Stenou, M. S. Anastasaki, K. Goubitz, X.-F. Miao, L. F. Nazar, M. Wagemaker, *Journal of the American Chemical Society* **2014**, *136*, 16335.

[104] H.-C. Wang, S. Ernst, H. Baltruschat, *Physical Chemistry Chemical Physics* **2010**, *12*, 2190.

[105] E. Mostafa, H. Baltruschat, *Journal of Solid State Electrochemistry* **2013**, *17*, 1861.

[106] E. Mostafa, H. Baltruschat, *Electrocatalysis* **2014**, *5*, 75.

[107] P. Elumalai, H. N. Vasan, N. Munichandraiah, *Journal of Solid State Electrochemistry* **1999**, *3*, 470.

[108] A. Koellisch-Mirbach, I. Park, H. Baltruschat*, **In preparation**.

[109] H. Baltruschat, *Journal of the American Society for Mass Spectrometry* **2004**, *15*, 1693.

[110] A. A. Abd-El-Latif, H. Baltruschat, in *Encyclopedia of Applied Electrochemistry* (Eds.: G. Kreysa, K.-i. Ota, R. Savinell), Springer New York Dordrecht Heidelberg London, **2014**, pp. 507

[111] A. A. Abd-El-Latif, C. J. Bondue, S. Ernst, M. Hegemann, J. K. Kaul, M. Khodayari, E. Mostafa, A. Stefanova, H. Baltruschat, *TrAC Trends in Analytical Chemistry* **2015**, *70*, 4.

[112] H. Baltruschat, in *Interfacial Electrochemistry* (Ed.: A. Wieckowski), Marcel Dekker, Inc., New York, Basel, **1999**, pp. 577.

[113] Y. Wang, N.-C. Lai, Y.-R. Lu, Y. Zhou, C.-L. Dong, Y.-C. Lu, *Joule* **2018**, *2*, 2364.

[114] S. Trasatti, O. A. Petrii, *Journal of Electroanalytical Chemistry* **1992**, *327*, 353.

[115] Q.-S. Chen, J. Solla-Gullón, S.-G. Sun, J. M. Feliu, *Electrochimica Acta* **2010**, *55*, 7982.

[116] K. P. C. Yao, J. T. Frith, S. Y. Sayed, F. Barde, J. R. Owen, Y. Shao-Horn, N. Garcia-Araez, *The Journal of Physical Chemistry C* **2016**, *120*, 16290.

[117] L. Yang, J. T. Frith, N. Garcia-Araez, J. R. Owen, *Chemical Communications* **2014**, *51*, 1705.

[118] P. P. Bawol, J. H. Thimm, H. Baltruschat, *ChemElectroChem* **2019**, *6*, 6038.

[119] W. R. Torres, F. Davia, M. del Pozo, A. Y. Tesio, E. J. Calvo, *Journal of The Electrochemical Society* **2017**, *164*, A3785.

[120] S. Matsuda, K. Hashimoto, S. Nakanishi, *The Journal of Physical Chemistry C* **2014**, *118*, 18397.

[121] X. Gao, Y. Chen, L. Johnson, P. G. Bruce, *Nat Mater* **2016**, *15*, 882.

[122] T. Liu, J. T. Frith, G. Kim, R. N. Kerber, N. Dubouis, Y. Shao, Z. Liu, P. C. M. M. Magusin, M. T. L. Casford, N. Garcia-Araez, C. P. Grey, *Journal of the American Chemical Society* **2018**, *140*, 1428.

[123] S. Zhang, M. J. Nava, G. K. Chow, N. Lopez, G. Wu, D. R. Britt, D. G. Nocera, C. C. Cummins, *Chemical Science* **2017**, *8*, 6117.

[124] Z. Zhao, J. Huang, Z. Peng, *Angewandte Chemie* **2018**, n/a.

[125] Y. Yin, R. Zhao, Y. Deng, A. A. Franco, *The Journal of Physical Chemistry Letters* **2017**, 599.

[126] P. Hartmann, C. L. Bender, M. VraÄ�ar, A. K. DÃ¼rr, A. Garsuch, J. r. Janek, P. Adelhelm, *Nat Mater* **2013**, *12*, 228.

[127] D. Schröder, C. L. Bender, M. Osenberg, A. Hilger, I. Manke, J. Janek, *Scientific Reports* **2016**, *6*, 24288.

[128] Z. W. Seh, J. Sun, Y. Sun, Y. Cui, *ACS Central Science* **2015**, *1*, 449.

[129] T. Shiga, Y. Hase, Y. Kato, M. Inoue, K. Takechi, *Chemical Communications* **2013**, *49*, 9152.

[130] G. Vardar, E. G. Nelson, J. G. Smith, J. Naruse, H. Hiramatsu, B. M. Bartlett, A. E. S. Sleightholme, D. J. Siegel, C. W. Monroe, *Chemistry of Materials* **2015**, *27*, 7564.

[131] P. Reinsberg, C. Bondue, H. Baltruschat, *Electrochimica Acta* **2016**, *200*, 214.

[132] P. H. Reinsberg, A. Koellisch, P. P. Bawol, H. Baltruschat, *Physical Chemistry Chemical Physics* **2019**, *21*, 4286.

[133] W. Wang, N.-C. Lai, Z. Liang, Y. Wang, Y.-C. Lu, *Angewandte Chemie* **2018**, *130*, 5136.

[134] S. Sankarasubramanian, V. Ramani, *The Journal of Physical Chemistry C* **2018**, *122*, 19319.

[135] M. Moshkovich, Y. Gofer, D. Aurbach, *Journal of the Electrochemical Society* **2001**, *148*, E155.

[136] X. Ren, Y. Wu, *Journal of the American Chemical Society* **2013**, *135*, 2923.

[137] D. Wang, X. Gao, Y. Chen, L. Jin, C. Kuss, P. G. Bruce, *Nature Materials* **2017**, *17*, 16.

[138] N. Mahne, B. Schafzahl, C. Leypold, M. Leypold, S. Grumm, A. Leitgeb, G. A. Strohmeier, M. Wilkening, O. Fontaine, D. Kramer, C. Slugovc, S. M. Borisov, S. A. Freunberger, *Nature Energy* **2017**, *2*.

[139] P. P. Bawol, P. H. Reinsberg, A. Koellisch-Mirbach, C. J. Bondue, H. Baltruschat, *ChemRxiv (Preprint)* **2020**.

[140] A. S. Shatla, A. A. Abd-El-Latif, S. Ayata, D. Demir, H. Baltruschat, *Electrochimica Acta* **2020**, *334*, 135556.

[141] J. Lindberg, B. Endrődi, G. Åvall, P. Johansson, A. Cornell, G. Lindbergh, *The Journal of Physical Chemistry C* **2018**, *122*, 1913.

[142] M. Hegemann, H. Baltruschat, *In preparation* **2020**.

[143] A. Koellisch-Mirbach, I. Park, M. Hegemann, E. Thome, H. Baltruschat, *ChemSusChem* **2021**.

[144] P. P. Bawol, A. Koellisch-Mirbach, C. J. Bondue, H. Baltruschat, P. H. Reinsberg, *ChemSusChem* **2021**, *14*, 428.

[145] Y. T. Lu, A. R. Neale, C. C. Hu, L. J. Hardwick, *Chemical Science* **2021**, *12*, 8909.

[146] Y.-T. Lu, A. R. Neale, C.-C. Hu, L. J. Hardwick, *Frontiers in Energy Research* **2021**, *8*.

[147] A. Wieckowski, S. D. Rosasco, B. C. Schardt, J. L. Stickney, A. T. Hubbard, *Inorg. Chem.* **1984**, *23*, 565.

[148] D. Zurawski, L. Rice, M. Hourani, A. Wieckowski, *Journal of Electroanalytical Chemistry* **1987**, *230*, 221.

[149] G. N. Salaita, D. A. Stern, F. Lu, H. Baltruschat, B. C. Schardt, J. L. Stickney, M. P. Soriaga, D. G. Frank, A. T. Hubbard, *Langmuir* **1986**, *2*, 828.

[150] H. Baltruschat, *Journal of the American Society for Mass Spectrometry* **2004**, *15*, 1693.

[151] Y. R. Luo, *Comprehensive Handbook of Chemical Bond Energies*, CRC Press, Boca Raton, FL, **2007**.